

Revealing ultrastructural changes that determine the development of a CNS synapse

Dissertation
for the award of the degree
“Doctor rerum naturalium” (Dr. rer. nat.)
of the Georg-August-Universität Göttingen

within the doctoral program Sensory and Motor Neuroscience
of the Georg-August University School of Science (GAUSS)

Submitted by
Anika Hintze

Born in
Duderstadt, Germany

Göttingen, 2022

Members of the Thesis Advisory Committee

Prof. Dr. Carolin Wichmann

Institute for Auditory Neuroscience, InnerEarLab and Center for Biostructural Imaging of Neurodegeneration, University Medical Center, Göttingen

Prof. Dr. Thomas Dresbach

Institute of Anatomy and Embryology, University Medical Center, Göttingen

Dr. Benjamin Cooper

Department of Molecular Neurobiology, Max Planck Institute for Multidisciplinary Sciences, Göttingen

Members of the Examination Board

First Reviewer: **Prof. Dr. Carolin Wichmann**

Institute for Auditory Neuroscience, InnerEarLab and Center for Biostructural Imaging of Neurodegeneration, University Medical Center, Göttingen

Second Reviewer: **Prof. Dr. Thomas Dresbach**

Institute of Anatomy and Embryology, University Medical Center, Göttingen

Further members of the Examination Board

Dr. Benjamin Cooper

Department of Molecular Neurobiology, Max Planck Institute for Multidisciplinary Sciences, Göttingen

Prof. Dr. Silvio O. Rizzoli

Department of Neuro- and Sensory Physiology and Center for Biostructural Imaging of Neurodegeneration, University Medical Center Göttingen

Prof. Dr. Stefan Jakobs

Department of NanoBiophotonik, Max Planck Institute for Multidisciplinary Sciences, Göttingen and Clinic of Neurology, University Medical Center Göttingen

Prof. Dr. Frauke Alves

Institute of Diagnostic and Interventional Radiology, Clinic of Hematology and Medical Oncology, University Medical Center Göttingen and Max-Planck-Institute for Multidisciplinary Sciences

Date of oral examination: April 28th, 2022

Declaration

I hereby declare that this dissertation “Revealing ultrastructural changes that determine the development of a CNS synapse” is written independently with no other sources and aids than cited.

Anika Hintze

Göttingen, 14th March, 2022

Table of Contents

List of Figures	ix
List of Tables	xi
List of Abbreviations	xii
Abstract	xv
1 Introduction	1
1.1 Chemical synapses	1
1.2 Synaptic vesicle formation and cycle	2
1.2.1 Exocytosis pathway.....	3
1.2.2 Endocytosis pathway	4
1.3 The cytomatrix of the active zone	4
1.3.1 The role of RIM and RIM-BP at synapses	5
1.3.2 The vertebrate-specific protein Mover	6
1.4 Synaptic vesicle pools at conventional synapses	6
1.5 The role of presynaptic mitochondria in synaptic activity	8
1.6 The auditory system	10
1.6.1 The early auditory pathway.....	10
1.6.2 Otoferlin, a hair cell-specific protein involved in SV exocytosis	11
1.6.3 The cochlear nucleus.....	12
1.6.4 Developmental maturation of auditory synapses	14
1.6.5 Synapses on bushy cells	15
1.6.5.1 The structure of endbulbs	16
1.6.5.2 Influence of neuronal activity on endbulb structure.....	17
1.7 Hypotheses and Aims	19
2 Materials and Methods	21
2.1 Animals	21
2.2 Materials	22
2.2.1 Chemicals	22
2.2.2 Equipment.....	23
2.2.3 Solutions	24
2.3 Sample preparation for electron microscopy	25
2.3.1 High-pressure freezing (HPF) and freeze-substitution (FS).....	25
2.3.1.1 Vibratome slice preparation	25
2.3.1.2 High-pressure freezing (HPF).....	25
2.3.1.3 Freeze-substitution (FS)	25
2.3.2 Conventional embedding	27
2.4 Trimming of embedded samples	28
2.5 Formvar coating of slot and mesh grids	28
2.6 Sectioning and post-staining	28
2.7 Transmission electron microscopy (TEM)	29

2.7.1	Electron tomography	30
2.7.2	Generation of tomograms	31
2.7.3	Quality assessment of tomograms.....	31
2.7.4	Model rendering and three-dimensional (3D) analysis	32
2.7.5	Electron tomography of presynaptic mitochondria.....	33
2.8	Statistical analysis	34
3	Results.....	37
3.1	Ultrastructural changes at endbulb active zones upon maturation from pre-hearing to hearing.....	39
3.1.1	The density, size and distribution of synaptic vesicles are unaltered at endbulb of Held AZs	39
3.1.2	Refinement of the SV pool	42
3.1.2.1	The density of docked SVs is unaffected from the transition to hearing	42
3.1.2.2	The pool of membrane-proximal synaptic vesicles is comparable between P10 and P21.....	44
3.1.3	Summary.....	45
3.2	Presynaptic mitochondria within the AVCN.....	46
3.2.1	Mitochondria are highly variable in size and shape	46
3.2.2	Presynaptic mitochondria are larger after the onset of hearing at endbulbs of Held	47
3.2.3	Mitochondrial volumes increase at non-endbulb synapses from pre-hearing to young hearing mice.....	50
3.2.4	Mitochondria are larger at non-endbulb synapses compared to endbulb AZs of P10 mice.....	52
3.2.5	Mitochondria at endbulb synapses display a higher crista membrane density after the onset of hearing	53
3.2.6	Summary.....	54
3.3	Ultrastructural changes at endbulb active zones upon adulthood and lack of activity	56
3.3.1	The synaptic vesicle pool increases during development of wild-type active zones.....	56
3.3.2	Synaptic vesicle numbers decline in ageing <i>Otof</i> ^{-/-} mice.....	57
3.3.3	Synaptic vesicle numbers are comparable between wild-type and mutant mice at young ages	57
3.3.4	Active zones of adult <i>Otof</i> ^{-/-} endbulbs contain less morphologically docked synaptic vesicles	59
3.3.5	The density of membrane-proximal vesicles initially increases but declines towards adulthood at <i>Otof</i> ^{-/-} active zones.....	61
3.3.6	Sizes of synaptic vesicles decrease during development at <i>Otof</i> ^{-/-} endbulb active zones.....	62
3.3.7	Summary.....	64
3.4	<i>RIM-BP2</i> disruption alters the vesicle organization at endbulb active zones.....	65
3.4.1	<i>RIM-BP2</i> ^{-/-} endbulb active zones exhibit a different distribution of synaptic vesicles compared to wild-type	65
3.4.2	<i>RIM-BP2</i> ^{-/-} active zones contain less synaptic vesicles in membrane proximity.....	66
3.5	The lack of <i>Mover</i> has differentially effects on excitatory and inhibitory synapses	69
3.6	Summary	72

4 Discussion	73
4.1 Methodology	73
4.1.1 Sample preparation.....	74
4.1.2 The advantages of 3D electron tomography	75
4.1.3 The model system.....	76
4.2 The onset of hearing is not reflected by morphological changes on the level of individual endbulb of Held active zones	77
4.3 Structure of presynaptic mitochondria changes according to energy demands	78
4.3.1 Mitochondria become larger during maturation of the auditory system	79
4.3.2 Developmental maturation is associated with ultrastructural remodeling of mitochondria in endbulbs of Held.....	80
4.4 Spontaneous activity shapes the auditory pathway	83
4.4.1 Endbulb active zones of young wild-type and <i>Otof</i> ^{-/-} mice display a similar synaptic vesicle organization	84
4.4.2 Alterations of synaptic vesicle pools at endbulb of Held active zones of adult wild-type and <i>Otof</i> ^{-/-} mice	84
4.5 SV sizes differ between endbulbs of wild-type and <i>Otof</i>^{-/-} mice	85
4.6 Endbulb active zones contain a variable number of docked synaptic vesicles	87
4.6.1 The relationship between release probability and number of docked synaptic vesicles	87
4.6.2 Changes of release probability during development of endbulb AZs and lack of activity?	88
4.6.3 Release probability at endbulbs lacking presynaptic proteins	88
4.7 RIM-BP2 and Mover mediate tethering and docking of synaptic vesicles	89
5 Conclusion and Outlook	92
6 Bibliography	94
7 Supplemental Figures and Tables	114
Acknowledgements	xvii
List of publications	xix

List of Figures

Figure 1.1	Synaptic vesicle cycle.	2
Figure 1.2	The architecture of mitochondria.	8
Figure 1.3	The auditory pathway highlighting the first three synapses.	13
Figure 1.4	Endbulb of Held AZs after HPF/FS and conventional embedding.	16
Figure 2.1	Experimental workflow.	26
Figure 2.2	Preparation of sections for electron tomography.	29
Figure 2.3	Electron micrograph of an endbulb of Held terminal.	30
Figure 2.4	Single virtual sections of tomograms with different qualities.	32
Figure 3.1	Electron micrograph of a bushy cell (BC) and excitatory and inhibitory AZs.	38
Figure 3.2	SV pools at endbulbs of Held remain unaltered upon maturation in wild-type mice.	41
Figure 3.3	No difference in the number or density of morphologically docked SVs between P10 and P21.	43
Figure 3.4	The size of the membrane-proximal SV pool is comparable between P10 and P21.	44
Figure 3.5	Endbulb of Held AZ organization in pre-hearing and young hearing wild-type mice.	45
Figure 3.6	Mitochondria are variable in size and shape.	47
Figure 3.7	Mitochondrial ultrastructure changes upon maturation at endbulb synapses.	49
Figure 3.8	The ultrastructure of mitochondria at non-endbulb synapses is only slightly affected by maturation of the auditory system.	51
Figure 3.9	Mitochondria are larger at non-endbulb synapses compared to endbulbs at P10.	52
Figure 3.10	Mitochondria at endbulb terminals have a higher density of cristae compared to non-endbulb synapses at P21.	53
Figure 3.11	Changes of mitochondrial volume and CMs at endbulb and non-endbulb terminals upon maturation from pre-hearing to hearing.	55
Figure 3.12	SV densities increase at wild-type and decline at <i>Otof</i> ^{-/-} endbulb AZs upon adulthood.	58
Figure 3.13	Number and density of docked SVs is lower at <i>Otof</i> ^{-/-} AZs compared to wild-type of adult mice.	60
Figure 3.14	The density of membrane-proximal SVs is lower at adult <i>Otof</i> ^{-/-} endbulb AZs compared to wild-type.	62
Figure 3.15	Mean diameters averaged per tomogram for each condition.	63
Figure 3.16	SV pool changes upon development and lack of auditory input.	64
Figure 3.17	<i>RIM-BP2</i> deletion alters the axial SV distribution at the endbulb AZs.	66
Figure 3.18	Docked and membrane-proximal SVs at endbulb AZs of wild-type and <i>RIM-BP2</i> ^{-/-} mice.	67
Figure 3.19	Changes at endbulb AZs upon lack of <i>RIM-BP2</i> .	68

Figure 3.20	SV distribution at endbulb and inhibitory synapses of wild-type and <i>Mover</i> ^{-/-} mice.	70
Figure 3.21	Differences in SV pools at endbulb of Held AZs and inhibitory AZs of wild-type and <i>E2a-Mover</i> ^{-/-} mice.	71
Figure S1	Overall SV numbers do not correlate with the AZ areas.	114
Figure S2	The number of docked SVs and the size of the AZ area do not correlate.	115
Figure S3	Correlation between the density of all SVs and the density of docked SVs.	116
Figure S4	The density of membrane-proximal SVs correlates with the density of docked SVs at mutant AZs.	117
Figure S5	The frequency distributions of individual SV diameters.	118
Figure S6	The frequency distributions of individual diameters of morphologically docked SVs.	118
Figure S7	The frequency distributions of individual diameters of membrane-proximal SVs.	119

List of Tables

Table 2.1	Used mouse lines.	21
Table 2.2	Chemicals used for the experiments.	22
Table 2.3	Equipment used for this thesis.	23
Table 2.4	Solutions used in this study.	24
Table 2.5	Program for freeze substitution (FS).	26
Table 2.6	Epoxy-acetone infiltration series.	26
Table 2.7	Dehydration series of increasing ethanol concentration.	27
Table 2.8	Epoxy-ethanol infiltration series.	28
Table 2.9	Color code and analyzed parameters of the different investigated mouse models.	34
Table S1	Quantitative analysis of tomograms of wild-type P10 and P21.	120
Table S2	Quantitative analysis of tomograms of mitochondria at presynaptic AZs of P10 and P21 mice.	121
Table S3	Quantitative analysis of tomograms of wild-type AZs.	123
Table S4	Quantitative analysis of tomograms of <i>Otof</i> ^{-/-} AZs.	125
Table S5	Quantitative analysis of tomograms of P10 wild-type and <i>Otof</i> ^{-/-} mice.	127
Table S6	Quantitative analysis of tomograms of P21/22 wild-type and <i>Otof</i> ^{-/-} mice.	128
Table S7	Quantitative analysis of tomograms of 6M wild-type and <i>Otof</i> ^{-/-} mice.	129
Table S8	Comparison of the number of docked and membrane-proximal SVs.	130
Table S9	Quantitative analysis of tomograms of P22 wild-type and <i>RIM-BP2</i> ^{-/-} mice.	131
Table S10	Quantitative analysis of tomograms of adult wild-type and <i>Mover</i> ^{-/-} mice.	132

List of Abbreviations

-/-	Knockout
(m)EPSC	(Miniature) excitatory postsynaptic current
3D	Three-Dimensional
6M	6-month-old
ABR	Auditory brain stem responses
AMPA	α -amino-3-hydroxy-5-methyl-4-isoxazolepropionic acid
ANF	Auditory Nerve Fiber
ATP	Adenosine triphosphate
AVCN	Anteroventral cochlear nucleus
AZ	Active zone
BC	Bushy cell
<i>C. elegans</i>	<i>Caenorhabditis elegans</i>
Ca ²⁺	Calcium ions
CaCl ₂	Calcium chloride
CAST	CAZ associated structural protein
CAZ	Cytomatrix of the active zone
ChR2	Channelrhodopsin2
CM	Crista membrane
CME	Clathrin-mediated endocytosis
CN	Cochlear nucleus
CNS	Central nervous system
CO ₂	Carbon Dioxide
DCN	dorsal cochlear nucleus
DPOAE	distortion-product otoacoustic emissions
Eb	Endbulb of Held
ELKS	Glutamate (E), Leucine (L), Lysine (K) and Serine (S) rich protein
EM	Electron microscopy
Exc.	Excitatory
FIB-SEM	Focused ion beam-scanning electron microscopy
FS	Freeze substitution
GBC	Globular bushy cell
GluA	AMPA receptor
GluN	NMDA receptor
GluR2	Glutamate receptor 2

HC	Hair cell
HPF	High-pressure freezing
IHC	Inner hair cell
ILD	Interaural level differences
Inh.	Inhibitory
ITD	Interaural time differences
K ⁺	Potassium ions
KCl	Potassium chloride (KCl)
KW	Kruskal-Wallis
LSO	Lateral superior olive
MAC	Mitochondria-associated adherens complex
MgCl ₂	Magnesium chloride
MNTB	Medial nucleus of the trapezoid body
MSO	Medial superior olive
Munc18	Mammalian homologues of <i>C. elegans</i> UNC-18
Na	Sodium
NaCl	Sodium chloride
NaH ₂ PO ₄ ·H ₂ O	Sodium dihydrogen phosphate monohydrate
NaHCO ₃	Sodium hydrogen carbonate
NMDA	N-methyl-D-aspartate
non-eb	Non-endbulb synapses
ns	Not significant
NSF	N-ethylmaleimide-sensitive factor
O ₂	Oxygen
OHC	Outer hair cells
Otof	Otoferlin
<i>P</i>	Postnatal day
PBS	Phosphate buffered saline
<i>P_r</i>	Release probability
PSD	Postsynaptic density
RIM	Rab3 interaction molecule
RIM-BP	Rab3 interaction molecule-binding protein
RRP	Readily releasable pool
SBC	Spherical bushy cell
SBF-SEM	Serial block face-scanning electron microscopy
SEM	Standard error of the mean

SGN	Spinal ganglion neuron
SM	Sec1/munc18
SNAP	Synaptosome-associated protein
SNARE	Soluble NSF attachment receptor
SR	Spontaneous discharge rate
SV	Synaptic vesicle
syn	Non-endbulb synapses
T	Unpaired <i>t</i> -test
TW	Unpaired t-test with Welch's correction
VGCC	Voltage-gated calcium channel
Vglut	Vesicular glutamate transporter
W	Wilcoxon rank test
w/v	Weight/volume
wt	Wild-type

Abstract

Endbulbs of Held are synaptic contacts between auditory nerve fibers and bushy cells in the cochlear nucleus (CN) and represent the first central synapses of the auditory pathway. Endbulbs undergo functional and structural development that allows fast and reliable neurotransmission with high temporal precision. Its large terminal size and number of individual active zones (AZs) as well as its good accessibility make the endbulb of Held an ideal synapse to study structure-function relationships. While morphogenesis from small to large, highly branched terminals needs several weeks, functional maturation is completed shortly after hearing onset that occurs on postnatal day (P) 12 in mice. The developmental process is modulated by auditory nerve activity. Loss of this activity by depletion of otoferlin, an indispensable protein for synaptic transmission at inner hair cell ribbon synapses, results in smaller endbulbs. Synaptic transmission at endbulbs is further mediated by a plethora of proteins. Development from pre-hearing to adult stages in wild-type (wt) mice, the lack of auditory nerve activity and the lack of presynaptic proteins, such as Rab-interacting molecule (RIM)-binding protein 2 (BP2) and Mover are presumably reflected in structural changes at endbulb AZs. In my thesis, I addressed the ultrastructural consequences of these functional changes by using high-pressure freezing and freeze substitution prior to electron tomography of freshly sliced CNs. With this methodology, the morphological details of endbulb terminals like synaptic vesicle (SV) distribution and the structure of mitochondria can be examined with highest z resolution.

I found that SV pools were unchanged upon maturation from pre-hearing (P10) to hearing (P21) in wt but increased mitochondrial volume and crista membrane density suggest higher mitochondrial performance after the hearing onset. Endbulb AZs of six-months-old (6M) mice exhibited larger SV pools and a clustering of SVs within 5-15 nm from the AZ membrane compared to P10. SV densities at endbulb AZs were comparable between mice lacking *otoferlin* (*Otof*^{-/-}) and wt at P10 and P21/22. However, AZs of 6M *Otof*^{-/-} mice contained a considerably reduced number of SV compared to wt. This decrease also affected morphologically docked (0-2 nm) and membrane-proximal SVs (2-40 nm away from the AZ membrane) that were analyzed separately. While SVs of *Otof*^{-/-} mice were larger at P10, the docked SVs at 6M were significantly smaller than at wt. Upon *RIM-BP2* disruption, docked SVs and SVs in membrane proximity (2-20 nm) were decreased at endbulb AZs compared to wt. The lack of *Mover* resulted in reduced membrane-proximal SVs at endbulb AZs of adult mice and elevated numbers of docked SVs at inhibitory synapses.

These results suggest that the maturation from pre-hearing to hearing is accompanied by a higher energy demand in wt. Increased SV pool sizes upon further development towards adulthood might be required to support the temporally precise neurotransmission at endbulbs. The elevated SVs within 5-15 nm from the AZ membrane might thereby contribute to an efficient SV recruitment. At 6M *Otof*^{-/-} endbulb AZs, reliability of synaptic transmission might be reduced due to reduced numbers of docked and membrane-proximal SVs. Finally, Mover and RIM-BP2 seem to be involved in recruiting SVs to membrane proximity at endbulb of Held AZs. RIM-BP2 is also important for SV docking at endbulbs, while Mover seems to prevent SV docking at inhibitory synapses.

1 Introduction

The mammalian nervous system consists of the central nervous system (CNS), which is made up of the brain and the spinal cord, and the peripheral nervous system that connects the CNS with the rest of the body, including muscles and internal organs. Sensory receptors detect information from inside and outside the body like temperature, light, sound or changes in blood pressure, and levels of hormones. This sensory input is converted into electrical signals and transmitted to the brain where it gets integrated. The CNS responds by sending signals, for example, to muscles resulting in movements or to glands causing the production of secretions.

Neurons are the fundamental units of the nervous system that are responsible for receiving and transmitting these signals. Neurons communicate with one another via specialized sites called synapses. Two types of synapses can be distinguished: electrical and chemical synapses. In electrical synapses, two cells are connected via gap junctions that allow a direct pass of ions and other molecules from one cell to the other. However, neuronal communication mostly occurs via chemical synapses where the release of chemical messengers known as neurotransmitters is required for communication.

1.1 Chemical synapses

Chemical synapses consist of a presynaptic membrane that is separated from the postsynaptic membrane by the synaptic cleft. An incoming electrical signal in form of an action potential depolarizes the membrane of the presynaptic cell and causes the opening of voltage-gated calcium channels (VGCCs). VGCCs are clustered at the active zone (AZ) membrane, which is a specialized region where the release of neurotransmitters takes place. The entering of calcium ions (Ca^{2+}) initiates a signaling cascade that causes fusion of synaptic vesicles (SVs) with the presynaptic membrane, a process that is called exocytosis. The neurotransmitter molecules within the SVs are released into the synaptic cleft, diffuse and bind to receptor proteins located in the postsynaptic membrane. The receptor binding leads to changes in the membrane potential activating a signaling cascade in the postsynaptic cell, which can initiate an action potential (Kandel et al., 2012).

Both the presynaptic and postsynaptic membranes show a highly specialized molecular organization important for synaptic transmission, which is described in more detail in the following sections.

1.2 Synaptic vesicle formation and cycle

To maintain neurotransmission even with high rates of neurotransmitter release, synapses require a constant supply of SVs. Initially, SVs are formed as precursor vesicles by budding from the Golgi apparatus, where SV proteins are synthesized and inserted into the plasma membrane (reviewed in Hannah et al., 1999). Next, the vesicles are transported along microtubules down the axon by using kinesin-3 motor proteins KIF1A and KIF1B β (Nakamura et al., 2002; Okada et al., 1995). In the presynaptic nerve terminal, SVs are finally filled with neurotransmitter molecules (Farsi et al., 2016; Nelson & Lill, 1994).

After SV recruitment and subsequent priming, SVs fuse, release their neurotransmitters and fully collapse into the AZ membrane. A subsequent clearance of the release sites from fused SV membranes is required. Since the AZs are located far away from the protein synthesis machinery, the supply of SVs is primarily ensured by SV recycling. Therefore, SVs undergo endocytosis, reacidification and refilling with neurotransmitters for a new round of exocytosis. The SV cycle is illustrated in Fig. 1.1 and exocytosis and endocytosis pathways are described further in the following sections.

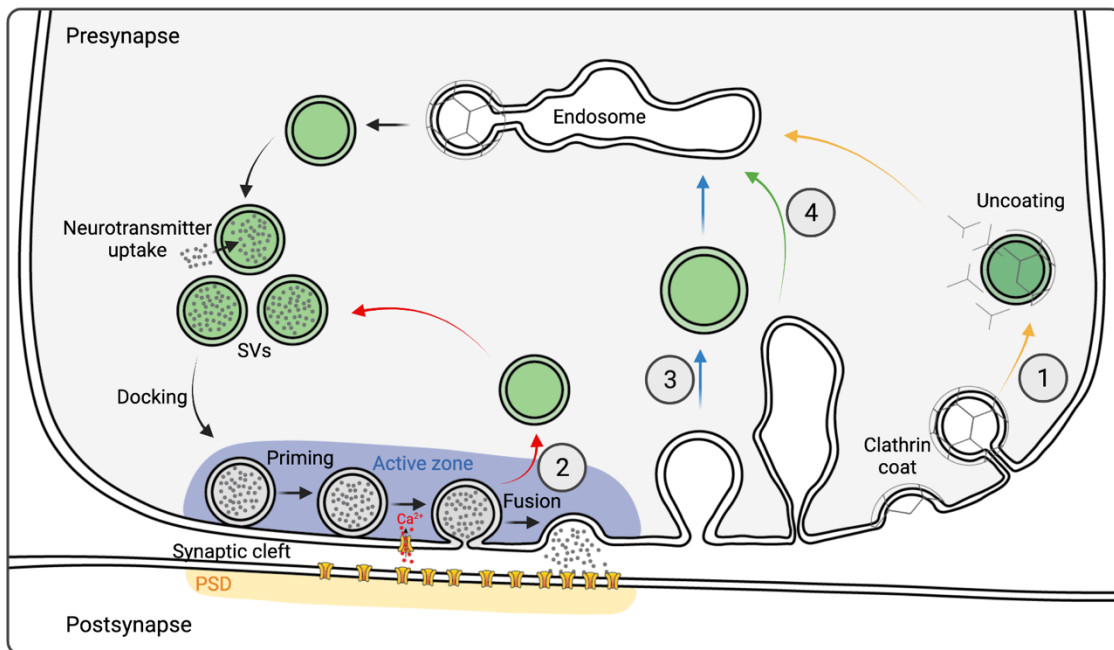


Figure 1.1: Synaptic vesicle cycle.

Synaptic vesicles (SVs) undergo a cycle of exocytosis and endocytosis to maintain neurotransmitter release at the presynapse. SVs are filled with neurotransmitters and translocated to the active zone where they become docked and primed to the plasma membrane. Upon arrival of an action potential and the resulting Ca^{2+} influx, primed SVs fuse with the plasma membrane and release neurotransmitters into the synaptic cleft. Neurotransmitters diffuse to postsynaptic receptors to mediate channel opening and ion influx into the postsynaptic terminal. Different mechanisms of vesicle membrane recycling by endocytosis are described: (1) Clathrin mediated endocytosis, (2) Kiss-and-run, (3) Ultrafast endocytosis and (4) Bulk endocytosis. Illustration created with Adobe Illustrator and BioRender.com.

1.2.1 Exocytosis pathway

The exocytosis of SVs occurs at the AZ membrane and is highly regulated by a plethora of conserved proteins. Prior to SV fusion with the AZ membrane, SVs undergo docking and priming. In the first step, SV docking is mediated by a loose tethering of SVs to the plasma membrane. Although the whole set of proteins involved in the tethering process has not been identified yet, it has been found that the Rab3-interacting molecule (RIM)-1 α is important for the tether formation. Fernandez-Busnadiego et al. observed an increase in the mean tether length by a reduced fraction of short tethers (0-5 nm) at synapses that lack RIM-1 α (Fernández-Busnadiego et al., 2013). The priming of SVs further involves the formation of the trimeric soluble N-ethylmaleimide-sensitive factor (NSF) attachment receptor (SNARE) complex whose main structures are highly conserved from yeast to humans (Fasshauer et al., 1998). The inhibition of vesicle priming by overexpressing the SNARE-related protein tomosyn in chromaffin cells reduced vesicle immobilization, fusion and release probability (P ; probability of a single vesicle to release its content in response to an action potential), demonstrating that immobilization of vesicles is a mandatory step to make them release competent (Yizhar & Ashery, 2008). The vesicular (V-) SNARE protein synaptobrevin thereby interacts with the target (T-) SNARE proteins syntaxin-1 and SNAP25 (synaptosome-associated protein of 25 kDa) on the plasma membrane and forms an α -helical SNARE complex (Poirier et al., 1998; Sutton et al., 1998). SNARE proteins interact with several other proteins like the mammalian homologues of *C. elegans* UNC-18 (Munc18-1) and synaptotagmin-1 (Gerst, 1999). Munc18-1, a member of the Sec1/munc18 (SM) protein family interacts with the SNARE complex by binding to syntaxin-1, a process that is suggested to enhance the fusion efficiency (Shen et al., 2007). The neuronal vesicular protein synaptotagmin-1 senses the Ca²⁺ influx caused by an incoming action potential (Brose et al., 1992). Upon Ca²⁺ binding, synaptotagmin-1 is thought to promote SV fusion by binding to phospholipids of the plasma membrane (Bai et al., 2002; Davis et al., 1999; Fernandez et al., 2001). After the fusion process, the recycling of SNARE proteins is mediated by NSF. The interaction with its cofactor α -SNAP leads to the disassembly of SNARE complexes on the plasma membrane prior to endocytosis to allow another round of fusion (Littleton et al., 2001). On the ultrastructural level, it has also been shown that at least the partial formation of SNARE complexes is required for SV docking and priming (Imig et al., 2014). Imig and colleagues used high-pressure freezing (HPF), freeze substitution (FS), and electron tomography of organotypic hippocampal slice cultures from mice lacking different components of the SNARE-complex (SNAP25, syntaxin-1 or synaptobrevin) and observed a reduction of docked SVs (Imig et al., 2014). SV docking was further characterized morphologically based on the identification of docking filaments with an average length of 22 nm that connect SVs with the plasma membrane (Cole et al., 2016). Electron tomography of cultures of dissociated rat

hippocampal neurons revealed that docked SVs have three or more docking filament connections that can vary in their orientation (Cole et al., 2016).

1.2.2 Endocytosis pathway

Fundamental research in the field of endocytosis over the last 50 years proposed different endocytic pathways (Fig. 1.1): (1) Clathrin-mediated endocytosis (CME) was first visualized in mosquito oocytes with electron microscopy (Roth & Porter, 1964) and is the oldest and best understood endocytic process in mammalian cells (reviewed in Mettlen et al., 2018). Clathrin molecules are recruited to the plasma membrane, form triskelia and induce invagination and formation of pits (Royle, 2006). The subsequent fission of the pits by dynamin and uncoating of clathrin results in the formation of new SVs. In contrast to CME that acts relatively slow with a range between 10 to 30 seconds (Milosevic, 2018), (2) kiss-and-run is a mechanism that supports fast kinetics of SV recycling (<1-2 seconds). In this process, SVs do not fully collapse into the plasma membrane and the fusion pore may reclose after transmitter release (Wen et al., 2017). (3) During ultrafast endocytosis, the membrane invaginates to form large endocytic vesicles that are delivered to endosomes. This process is suggested to occur after brief neuronal activity and during high-frequency stimulation (Soykan et al., 2017; Watanabe et al., 2013). Stimulation of *clathrin* knock-down hippocampal neurons in the presence of cationized ferritin, to mark internalization, resulted in the formation of ferritin-filled endosomes. However, these endosomes did not form coated pits suggesting that although membrane retrieval functions clathrin independently, the final step of the new SV generation from endosomes occurs in a clathrin dependent manner (Watanabe et al., 2014). (4) Activity-dependent bulk endocytosis is triggered by strong synaptic activity and is characterized by the internalization of large membrane areas (Clayton et al., 2008; Nguyen et al., 2012). The lack of dynamin1 and -3 in primary cortical neurons is associated with perturbed CME (Raimondi et al., 2011), but bulk endocytosis and the formation of new SVs from bulk endosomes have been observed upon stimulation with high potassium (K^+) concentrations suggesting that both processes run in a clathrin independent manner (Wu et al., 2014).

1.3 The cytomatrix of the active zone

In addition to the proteins important for exocytosis and endocytosis, a network of proteins is located at the cytomatrix of the AZ (CAZ; Schoch & Gundelfinger, 2006). Utilizing electron microscopy of chemically fixed synapses, the CAZ can be identified as an electron dense area close to the AZ. CAZ proteins comprise of multi-domain protein families involved in SV docking and priming as described above, such as RIMs, RIM binding proteins (RIM-BPs) and Munc13. Munc13 proteins are activated by RIMs (Deng et al., 2011) and are essential for SV priming

by enabling syntaxin-1 to form SNARE complexes as demonstrated in *C. elegans* or mice lacking Munc13 (Augustin et al., 1999; Richmond et al., 2001). By regulating this priming activity, Munc13 is involved in mediating short-term plasticity (Rosenmund et al., 2002). Furthermore, liprin- α , CAST (CAZ associated structural protein)/ELKS (glutamate (E), leucine (L), lysine (K), and serine (S) rich protein) as well as the large scaffold proteins piccolo and bassoon interact with each other to maintain the structural organization of the AZ and this way regulate the SV cycle (reviewed in Schoch et al., 2006; Schoch & Gundelfinger, 2006). Liprin- α family proteins interact with ELKS and RIMs as reported from conventional synapses (Stryker & Johnson, 2007; Wei et al., 2011; Zürner et al., 2011; Zürner & Schoch, 2009). The disruption of the liprin- α homologue Dliprin in *Drosophila* revealed abnormal AZ morphology and impaired synaptic transmission (Kaufmann et al., 2002) demonstrating a crucial role of liprin- α proteins in the assembly and organization of AZs.

The CAST/ELKS proteins interact with RIMs, piccolo, and bassoon and indirectly with Munc13 through RIM (Hida & Ohtsuka, 2010; Ko et al., 2003; Ohtsuka et al., 2002) whereby regulating the density of VGCCs (Dong et al., 2018).

Piccolo and bassoon are the largest members of the CAZ proteins showing functions in e.g. assembly of AZ scaffolds (Gundelfinger et al., 2015), SV clustering (Mukherjee et al., 2010), and presynaptic protein ubiquitination and degradation (Waites et al., 2013). Both proteins have been shown to promote SV replenishment, which affects the pool size of SVs that are available for immediate release, the so-called readily releasable pool (RRP) at endbulb of Held (Butola et al., 2017; Mendoza Schulz et al., 2014) and calyx of Held synapses (Parthier et al., 2018). Bassoon interacts with autophagy protein 5, an E3-like ligase, and plays a role in the regulation of presynaptic autophagy (Okerlund et al., 2017). Another interaction partner of bassoon is Mover, a vertebrate-specific phosphoprotein of SVs (Ahmed et al., 2013; Kremer et al., 2007).

1.3.1 The role of RIM and RIM-BP at synapses

RIMs are essential for SV docking and priming by forming a heterotrimeric complex with Munc13 and the small G-protein Rab3 or Rab27 (Gracheva et al., 2008; Kaeser et al., 2011; Koushika et al., 2001). They are important for dynamic changes in the strength of synaptic responses, termed short-term plasticity of neurotransmitter release (Schoch et al., 2002). Deletion of *RIMs* at the calyx of Held synapse results in reduced VGCC density and a smaller RRP that goes along with a reduced number of docked SVs (Han et al., 2011). Thus, Han and colleagues concluded that RIMs regulate SV release by recruiting VGCCs to AZs (Han et al., 2011). In addition to a direct binding of RIMs and VGCCs (Kaeser et al., 2011), VGCCs are linked to RIMs via RIM-BPs (Hibino et al., 2002).

RIM-BPs are involved in recruiting and organizing the topography of VGCCs (Grauel et al., 2016; Krinner et al., 2017). This function has been shown to depend on the interaction of RIM-BPs with bassoon (Davydova et al., 2014). Three isoforms exist in vertebrates, RIM-BP1, -2 and -3 (Mittelstaedt & Schoch, 2007; Wang et al., 2000). Although lack of the neuron specific *RIM-BP1* and *RIM-BP2* did not affect the Ca^{2+} current at the calyx of Held (Acuna et al., 2015), the absence of *RIM-BP1* and *RIM-BP2* reduced the number of VGCCs at ribbon-type AZs in the murine cochlea and retina (Krinner et al., 2017; Luo et al., 2017). Synaptic transmission is only slightly impaired by *RIM-BP* deletion at mammalian synapses (Acuna et al., 2015; Grauel et al., 2016; Krinner et al., 2017; Luo et al., 2017), while at *Drosophila* larval neuromuscular junctions Ca^{2+} influx is impaired, which results in strongly reduced P_r (Liu et al., 2011).

1.3.2 The vertebrate-specific protein Mover

In contrast to most other presynaptic proteins, Mover is not expressed in all species and synapses (Kremer et al., 2007; Wallrafen & Dresbach, 2018) suggesting its role in increasing functional heterogeneity of synapses. For the mouse calyx of Held it has been shown that *Mover* depletion results in a reduced P_r of selectively superprimed SVs (Pofantis et al., 2021). This contrasts with a study in the rat calyx of Held showing that Mover negatively regulates P_r by decreasing the Ca^{2+} sensitivity of the release machinery (Körber et al., 2015). In both studies, P_r was calculated by the ratio of the amplitude of an excitatory postsynaptic current (EPSC) and the size of the RRP, which in turn was determined from the intersection of the y axis and the regression fit of cumulative EPSCs induced by a 100-Hz train stimulation (Schneppenburger et al., 1999).

It is thought that Mover acts differently on synaptic transmission in different synapse types, which is supported by the fact that the expression of Mover strikingly differs between brain areas, within individual brain areas and between synapse types (Wallrafen & Dresbach, 2018).

1.4 Synaptic vesicle pools at conventional synapses

Despite their distance to the AZ membrane, SVs seem to form a homogeneous population since they appear identical under an electron microscope. Furthermore, no biochemical differences have been recognized that might identify different classes of SVs in a resting terminal. However, the idea that SVs differ functionally is around 70 years old (Birks & MacIntosh, 1961). Since then, various models of distinct functional and morphological SV pools were described. Three major functional SV pools were identified: a RRP, a recycling- and a reserve pool (reviewed in Denker & Rizzoli, 2010; Rizzoli & Betz, 2005). The classical model of the pool structure is based on the SV localization within the presynaptic terminal. The RRP is formed by SVs primed for immediate release upon stimulation. After tethering, SVs

dock and prime to the AZ membrane and represent the respective morphological, and functional correlate of the same process (Imig et al., 2014; Kaeser & Regehr, 2017; Schikorski & Stevens, 1997). While SV priming can be measured electrophysiologically by quantifying the RRP size (Rosenmund & Stevens, 1996), SV docking can just be evaluated morphologically. These SVs are in physical contact with the AZ membrane. Cole and colleagues suggest that a uniformly horizontal orientation of all docking filaments between SV and the presynaptic membrane could be indicative of fusion-competent primed SVs, which would allow the morphological distinction between docked and primed SVs (Cole et al., 2016).

The recycling pool is located adjacent to the RRP and consists of SVs whose release is maintained and continuously recycled under physiological stimulation. Finally, SVs of the reserve pool are thought to be located farther away from the AZ and are only released under high-frequency stimulation. However, ultrastructural studies in *Drosophila* larval neuromuscular junctions revealed a strong spatial intermixing of the recycling and the reserve pool (Denker et al., 2009).

A new model, introduced by Denker and Rizzoli, propose a further refinement of the pool model where recycling and reserve pool SVs have different mobilities. The highly mobile recycling pool contains SVs that undergo cycles of release several times till they eventually mature into reserve pool SVs that are bound to scaffolding molecules (Denker & Rizzoli, 2010).

Nowadays, also the RRP is no longer considered as a uniform pool of primed SVs. Instead, these SVs can switch between a more loosely and a more tightly primed state (Neher & Brose, 2018). Another subpool, the superprimed SV pool has been identified (Schlüter et al., 2006) and although both primed and superprimed SVs are docked at the AZ membrane and are release-competent, they show different kinetics of SV release (Schlüter et al., 2006; Taschenberger et al., 2016; Xue et al., 2018). At calyces of Held, Taschenberger and co-workers found that normally primed SVs have a low P_r of around 0.1 and are rapidly regenerated after SV depletion. Superprimed SVs show a higher P_r (around 0.5), but they regenerate slowly upon fusion (Taschenberger et al., 2016). Superpriming was reported to be enhanced upon high-frequency activity to regulate synaptic strength and plasticity. Further, this subpool of primed SVs is suggested to be responsible for the variance in synaptic strength between individual synapses (Taschenberger et al., 2016).

1.5 The role of presynaptic mitochondria in synaptic activity

Next to SVs, mitochondria are often found near AZs. This is not surprising since synaptic transmission is the main energy consumer in the CNS and mitochondria, known as the powerhouses of cells, serve as primary energy generators (Verstreken et al., 2005). They are known to regulate neurotransmission by Ca^{2+} buffering (Billups & Forsythe, 2002; David & Barrett, 2003; Jonas et al., 1999; Medler & Gleason, 2002; Tang & Zucker, 1997) and contribute to signaling processes, the regulation of cell proliferation, cell migration, cell viability, and neuronal morphology (Chandel, 2014). Mitochondria consist of an outer and an inner membrane that enclose the intermembrane space and the matrix (Fig. 1.2). Inner membranes possess the inner boundary membrane and the crista membranes (CMs) that form deep invaginations (Fig. 1.2; Vogel et al., 2006). The two functional domains of the inner membrane are connected by crista junctions, small neck-like membrane structures that are proposed to form barriers between the intracristal and the intermembrane space (Frey et al., 2002; Mannella et al., 1994, 2001).

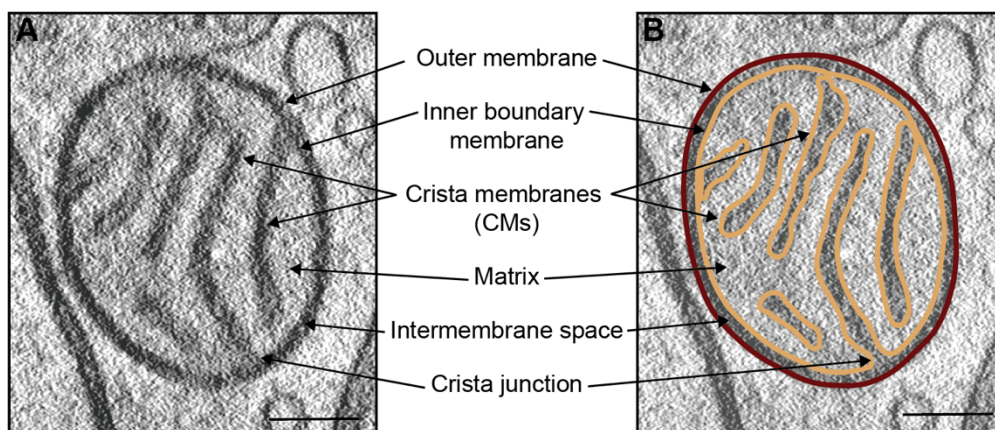


Figure 1.2: The architecture of mitochondria.

(A) Electron micrograph showing the compartments of a mitochondrion. (B) The same electron micrograph as in (A) showing the segmented mitochondrion. Mitochondria have a smooth outer membrane and a highly convoluted inner membrane with numerous invaginations, termed cristae. The crista membranes (CMs) point into the matrix of the organelle. Crista junctions connect the CMs with the inner boundary membrane. The mitochondrial outer and inner membrane are separated by an intermembrane space. Scale bars: 100 nm.

This compartmentalization reflects the functional specializations of the mitochondrial membranes. Protein import machineries e.g., are located at the outer and inner boundary membrane and makes them responsible for the communication with the cytosol. The CMs are specialized for oxidative phosphorylation and therefore harbor the protein complexes for the respiratory chain and the ATP (adenosine triphosphate) synthase (Gilkerson et al., 2003; Wiedemann & Pfanner, 2017; Wurm & Jakobs, 2006). Mitochondria are hallmark structures of nerve terminals, and their positioning seems to be important for synaptic function. It has been

found that the presence of presynaptic mitochondria at axonal AZs correlates with the size of synapses and SV density (Smith et al., 2016). The presence of mitochondria further maintains synaptic transmission during prolonged stimulation, while absence of a mitochondrion results in depletion of SV release (Sun et al., 2013). In addition, the mobilization of reserve pool SVs has been demonstrated to be disturbed at synapses that lack mitochondria due to an insufficient ATP supply (Verstreken et al., 2005). Given that, it seems surprising, that just roughly half of hippocampal presynaptic boutons have a mitochondrion nearby (Kang et al., 2008; Shepherd & Harris, 1998; Smith et al., 2016). A similar observation has been made for cultured cortical neurons (Chang et al., 2006). However, since neuronal morphology as well as synaptic strength changes in an activity-dependent manner, also the demand for mitochondrial supply can alter. Mitochondria form a rapidly changing, dynamic network that, dependent on local needs, involves fusion and fission events as well as bidirectional movements and anchoring at specific positions (reviewed in Rube & van der Bliek, 2004). In hippocampal neurons, around one third of axonal mitochondria are motile (Kang et al., 2008), but it has been proposed that the proportion of motile mitochondria can be modulated by changes in synaptic activity (Chang et al., 2006; Li et al., 2004; Macaskill et al., 2009). However, the effect of synaptic activity on mitochondrial movement and recruitment to synapses on the one hand differs between axons and dendrites (Chang et al., 2006) and on the other hand leads in contrary results. For instance, enhanced neuronal activity results in more stationary mitochondria at synapses of cortical neurons (Chang et al., 2006; Rintoul et al., 2003) and hippocampal dendrites (Li et al., 2004; Macaskill et al., 2009), whereas blocking action potential firing using the sodium channel blocker tetrodotoxin increases mitochondrial motility (Li et al., 2004). Further, developmental maturation of the nervous system that is associated with an increase in neuronal activity has been shown to decrease mitochondrial motility in cortical neurons (Lewis et al., 2016; Silva et al., 2021), which is paralleled by an increasing expression of syntaphilin, an axonal mitochondrial docking protein (Zhou et al., 2016). In contrast, there are also studies that demonstrate no affect in mitochondrial motility upon activity changes (Beltran-Parrazal et al., 2006; Faits et al., 2016; Smit-Rigter et al., 2016). This suggests that changes in mitochondrial motility are not the only mechanism to adjust to changes in the local need for energy supply or enhanced calcium signaling.

There is evidence that volume and ultrastructure of mitochondria are coupled to synaptic performance (Cserép et al., 2018; Ivannikov et al., 2013; Smith et al., 2016; Thomas et al., 2019). In hippocampal synaptosomes e.g., a higher presynaptic mitochondrial level is associated with higher levels of SV release (Ivannikov et al., 2013), which is consistent with a developmental increase in synaptic localization and mitochondrial volume to support the rise in firing rates at calyx of Held synapses (Thomas et al., 2019) as well as at CA1 hippocampal boutons (Smith et al., 2016). The comparison of high-performance and low-performance

neurons of glutamatergic as well as GABAergic boutons within the hippocampal formation has revealed that high-performance neurons show larger mitochondria with a higher CM density (CM surface area/mitochondrial volume) at axonal AZs (Cserép et al., 2018). A larger CM surface can harbor a higher number of respiratory chain and ATP synthase proteins resulting in an enhanced oxidative phosphorylation at high-performance neurons. Furthermore, the CM arrangement of high-performance mitochondria is more lamellar (Cserép et al., 2018), which has been shown to be beneficial for the assembly of respiratory chain supercomplexes (Cogliati et al., 2013) and results in an increased proton motive force, leading to higher ATP-producing capacity (Song et al., 2013).

1.6 The auditory system

The mammalian auditory system is responsible for the sense of hearing and is subdivided into the peripheral auditory system, which consists of the outer, middle and inner ear, and the central auditory system that is made up by different brain regions from the cochlear nuclei (CN) to the auditory cortex. Synapses of the auditory system are specialized for fast signal transmission with high temporal fidelity (Kopp-Scheinflug & Tempel, 2015; Moser et al., 2006; Trussell, 1999; Wichmann, 2015). To master this challenge, they rely on a fast and efficient SV cycle. Due to their good accessibility, the synapses of the early auditory pathway, the ribbon-type synapse, the endbulb and calyx of Held (Fig. 1.3) are ideal models to study CAZ proteins and structure-function relationships.

1.6.1 The early auditory pathway

Sound waves travel through the air-filled outer and middle ear to the liquid-filled inner ear containing the spiral shaped cochlea. The pressure waves cause vibrations of the extracellular fluid inside the cochlea, named perilymph, whose movement is further transmitted to the basilar membrane inside the cochlear duct, where the receptor organ for hearing is localized - the organ of Corti. Subsequently, these vibrations are detected by mechanosensory auditory hair cells (HCs), which are embedded into the tonotopically organized basilar membrane responding to certain frequencies. Due to its physical characteristics, different sound frequencies reach maximum amplitudes at specific positions. High-frequency sounds are transduced at the narrow and stiff base of the cochlea, while the more flexible apex is tuned for low frequencies (Liberman, 1982; Oghalai, 2004). This tonotopic organization is maintained throughout the auditory system, with each cell being maximally responsive for a characteristic frequency (Kandler et al., 2009).

Two types of auditory HCs are described, 3-4 rows of outer hair cells (OHCs) and one row of inner hair cells (IHCs). Both types are characterized by several rows of stereocilia at their

apical pole. The movement of this 'hair bundle' leads to opening of mechano-electrical transduction channels that in turn results in HC depolarization. In OHCs, the depolarization causes a synchronized electromotile contraction through which they can amplify the sound-induced vibrations of the basilar membrane (Brownell, 1990; Liberman et al., 2002; Zheng et al., 2000). OHC function can be measured by distortion-product otoacoustic emissions (DPOAEs; reviewed in Kim, 1986). In IHCs, depolarization leads to Ca^{2+} influx through VGCCs, resulting in SV fusion and glutamate release at ribbon synapses (Fig. 1.3). The exocytosis of neurotransmitters activates postsynaptic AMPA (α -amino-3-hydroxy-5-methyl-4-isoxazolepropionic acid) receptors on afferent boutons of the spiral ganglion neurons (SGNs) of the auditory nerve (Glowatzki & Fuchs, 2002; Schnee et al., 2011). SGNs are bipolar neurons and transmit the sound information to neurons of the CN in the auditory brainstem via their central processes, which are called auditory nerve fibers (ANFs). From there, the signals are further processed in different auditory brain regions including olivary nuclei, lateral lemniscus, inferior colliculus, medial geniculate nuclei, and auditory cortex. In order to study the auditory function of the cochlea as well as the brain pathway, auditory brain stem responses (ABRs) are used. Auditory stimuli with different sound pressure levels and frequencies are tested resulting in a pattern of ABR waves that are believed to be generated by different auditory structures (Hall, 2007).

1.6.2 Otoferlin, a hair cell-specific protein involved in SV exocytosis

Otoferlin, encoded by the *OTOF* gene, is a member of the ferlin protein family, that consists of six C_2 domains ($\text{C}_2\text{A-F}$) and a C-terminal transmembrane domain (Pangršič et al., 2012). It is localized at SVs associated with the ribbon (Roux et al., 2006) and at the membrane (Strenzke et al., 2016; Vogl et al., 2015) of mature IHCs. Mutations in the *OTOF* gene are associated with a genetic auditory synaptopathy called autosomal recessive nonsyndromic deafness (DFNB9; Rodríguez-Ballesteros et al., 2008; Yasunaga et al., 1999, 2000). More than 200 pathogenic *OTOF* mutations have been identified whereby most of them lead to profound deafness (Vona et al., 2020).

The functions of otoferlin at IHCs have been investigated using *otoferlin* knockout (*Otof^{-/-}*) or mutant mice. These mouse models are deaf as they do not show electrical activity in ABR measurements, but normal initial DPOAE levels (Reisinger et al., 2011; Roux et al., 2006; Wright et al., 2014). Otoferlin is crucial for late steps of exocytosis at IHCs since Ca^{2+} dependent SV release at IHCs is almost abolished, while they show normal numbers of SVs at their ribbon synapses (Roux et al., 2006). In addition, it has been reported that otoferlin is involved in SV tethering and priming (Pangršič et al., 2010; Vogl et al., 2015) as well as clearance of the AZ (Jung et al., 2015; Pangršič et al., 2010). Up to P3, exocytosis at IHCs, which results from non-sensory spontaneous activity is comparable between *Otof^{-/-}* and control

mice, but from P4 on it decreases and becomes undetectable at *Otof*^{-/-} IHCs. This is paralleled with a drastic decrease in synaptotagmin-2 expression (Beurg et al., 2010). An age-dependent degeneration of IHCs and OHCs has been shown that is more pronounced in *Otof*^{-/-} compared to wild-type (wt) mice. This goes along with a reduction in DPOAE amplitudes from 24 weeks of age on (Stalman et al., 2021). Whereas the number of ribbon synapses is initially greater at *Otof*^{-/-} IHCs compared to wt littermates, their number decreases markedly in the third and fourth postnatal week (Al-Moyed et al., 2019; Roux et al., 2006; Stalman et al., 2021). However, only after 48 weeks, a decrease in the number of SGNs is observed (Stalman et al., 2021). In contrast to IHCs, exocytosis at the endbulb of Held and other conventional synapses does not depend on otoferlin, but rather on synaptotagmin as Ca²⁺ sensor (Brose et al., 1992). However, the two proteins cannot simply replace each other's functions as demonstrated by Reisinger et al.: Exocytosis at IHCs lacking otoferlin could not be restored by overexpression of synaptotagmin-1. (Reisinger et al., 2011). Analog, synaptic transmission at chromaffin cells and hippocampal neurons lacking synaptotagmin-1 cannot be rescued by overexpression of otoferlin (Reisinger et al., 2011). In *Otof*^{-/-} mice the molecular composition at endbulb synapses is not altered and the auditory pathway is shaped until P3 by spontaneous activity, but auditory input is missing when the system is matured. *Otof*^{-/-} mice are therefore an appropriate model system to investigate how the lack of auditory input affects the function of the downstream auditory pathway.

1.6.3 The cochlear nucleus

Coming from the cochlea, each ANF bifurcates upon entering the CN (Fekete et al., 1984): The descending process projects to the dorsal CN (DCN), while the ascending process converge onto two cell types, stellate cells and bushy cells (BCs) within the anteroventral CN (AVCN; Fig. 1.3; Wu & Oertel, 1984). Stellate cells receive bouton-like glutamatergic inputs (Cant, 1981), while BCs are contacted by large synaptic endings, the so-called endbulbs of Held (Cant & Morest, 1979; Held, 1893; Ryugo & Fekete, 1982). Based on cytologic criteria established for cats, BCs can be subdivided into large spherical, small spherical and globular BCs (SBCs and GBCs; Brawer et al., 1974; Cant & Morest, 1979; Osen, 1969). SBCs are contacted by the largest endbulbs of Held, whereas GBCs receive several smaller so called "modified endbulbs" (Harrison & Irving, 1965; Rouiller et al., 1986). The number of these modified endbulbs has been shown to be highly variable with an average number of 22.7 per BC in cats (Spirou et al., 2005). SBCs and GBCs also differ in their projection pattern and due to the tonotopy by encoding different sound frequencies: SBCs innervate the medial superior olive (MSO) on both sides, the ipsilateral lateral superior olive (LSO) as well as the contralateral ventral nucleus of the lateral lemniscus and specifically for the large SBCs it has been shown that they encode mainly low frequencies (Smith et al., 1993). GBCs encode sounds of higher

frequencies and project to the contralateral medial nucleus of the trapezoid body (MNTB) to form the very large calyces of Held (Fig. 1.3; Brownell, 1975; Sento & Ryugo, 1989; Smith et al., 1991; Tolbert & Morest, 1982). By passing auditory information to these auditory nuclei, BCs are responsible for auditory processing and sound localization. Since MSO neurons receive information from both CNs, they can detect interaural time differences (ITD) to determine the origin of sound stimuli (Fitzpatrick et al., 1997; Yin & Chan, 1990). The LSO neurons not only receive excitatory input from the ipsilateral SBCs, but also inhibitory projections from MNTB neurons to detect interaural level differences (ILD; Glendenning et al., 1992; Sanes, 1990).

In mice, little low-frequency hearing (Ehret, 1974) and just few large SBCs (Willard & Ryugo, 1983; Webster & Trune, 1982) have been reported. Moreover, it has been shown that murine BCs cannot be clearly distinguished on cell body characteristics (Lauer et al., 2013), but morphological differences in inputs are described: SBCs receive input from 1-3 ANFs while GBCs are contacted by more than 3 ANFs (Cao & Oertel, 2010).

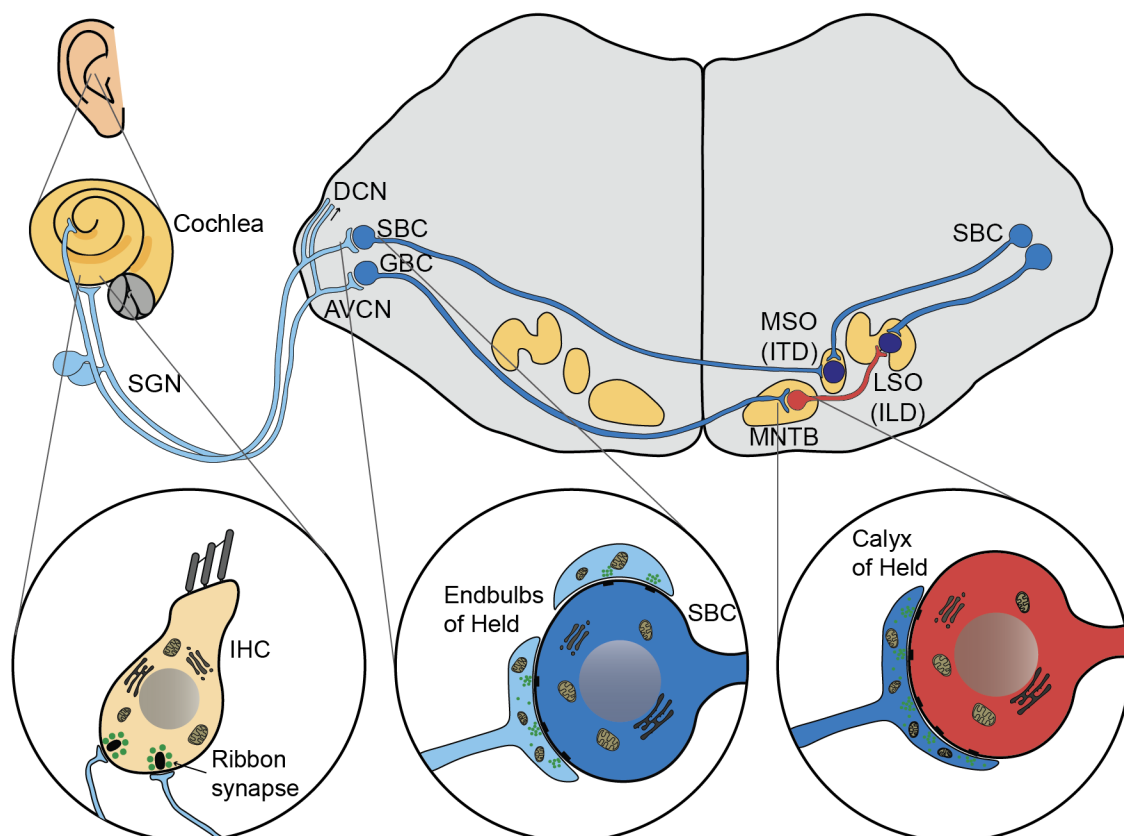


Figure 1.3: The auditory pathway highlighting the first three synapses.

Spiral ganglion neurons (SGNs) receive input from inner hair cells (IHCs) in the cochlea of the inner ear via their ribbon synapses. The central processes of SGNs, called auditory nerve fibers bifurcate upon entering the cochlear nucleus: The descending process projects to the dorsal cochlear nucleus (DCN), while the ascending process converges onto bushy cells (BCs) within the anteroventral cochlear nucleus (AVCN) and forms the endbulb of Held. Spherical BCs (SBCs) project to neurons of the ipsilateral lateral superior olive (LSO) as well as the contralateral and ipsilateral medial superior olive (MSO) and are important for interaural time differences (ITD). Globular BCs (GBCs) innervate neurons in the

(Figure 1.3 continued): contralateral medial nucleus of the trapezoid body (MNTB) where they form the calyx of Held synapse. The neurons of the MNTB are inhibitory and project to the LSO. LSO neurons use this inhibition and ipsilateral excitation from SBCs to compute interaural level differences (ILD). Blue axons indicate excitatory action, red indicates inhibitory action.

1.6.4 Developmental maturation of auditory synapses

Due to their functions in auditory processing, which are important not only for sound localization but also for sound perception (Zeng et al., 1999), a high precision of synaptic transmission at auditory synapses is required. The first three synapses of the auditory pathway, the IHC ribbon synapse, the endbulb as well as the calyx of Held, fulfill these requirements. Due to their accessibility and recognizability they represent ideal models to understand functional and dysfunctional auditory processing and the relationship between function and morphology. All three synapse types are known to undergo developmental maturation to evolve structural and functional properties that ensure a fast and reliable neurotransmission. A very important step in the maturation process is the onset of hearing, which occurs in mice around postnatal day (P)11/12 (Mikaelian & Ruben, 1965). Before that, non-sensory spontaneous activity already shapes the pathway (Babola et al., 2018; Sonntag et al., 2009; Tritsch et al., 2010) that undergoes functional and structural refinement around the onset of hearing. For IHCs it has been shown, for example, that coupling between Ca^{2+} influx and exocytosis is getting more tightly, indicated by a switch from Ca^{2+} -microdomains to Ca^{2+} -nanodomains (Wong et al., 2014). Morphologically, ribbon size and SV numbers increase, while SV diameters decrease during maturation (Michanski et al., 2019). Moreover, the expression of synaptotagmins, which are important for Ca^{2+} dependent SV release (also see section 1.2.1), vanishes during the first postnatal week, while a gradual increase of the HC-specific protein otoferlin is shown (Beurg et al., 2010; Reisinger et al., 2011; Safieddine & Wenthold, 1999; Uthaiyah & Hudspeth, 2010). Otoferlin likely acts as the Ca^{2+} sensor and is believed to take over this function of synaptotagmin (Johnson & Chapman, 2010; Michalski et al., 2017; Roux et al., 2006).

For the calyces of Held it has also been observed that Ca^{2+} sensitivity increases upon maturation due to changes in VGCC type and modality (Fedchyshyn & Wang, 2005; Iwasaki & Takahashi, 1998). Calyx terminals from P7 rats express a mixture of P/Q-, N- and R-type VGCCs, in contrast to calyces from P13 rats that express nearly exclusively P/Q-type channels (Iwasaki et al., 2000; Iwasaki & Takahashi, 1998). After hearing onset, calyces exhibit higher action potential kinetics as well as EPSC kinetics (Taschenberger & von Gersdorff, 2000). These changes go along with a decrease in P_r (Iwasaki & Takahashi, 2001; Taschenberger et al., 2002), but an unchanged quantal size (Iwasaki & Takahashi, 2001). In addition, it has been shown that the size of the RRP increases (Iwasaki & Takahashi, 2001; Taschenberger et al.,

2002; Taschenberger & von Gersdorff, 2000), while AZ sizes decrease upon maturation (Taschenberger et al., 2002).

For endbulbs of Held, it has been demonstrated that already at the pre-hearing stage P/Q channels reflect the dominant Ca^{2+} current. These channels are associated with the nanodomain modality indicating an efficient SV release (Lin et al., 2011; Oleskevich & Walmsley, 2002). Moreover, Yang and Xu-Friedman investigated delayed release that could affect auditory processing by disrupting the timing of evoked spikes. Using current clamp recordings from BCs and stimulation of ANFs, they observed spikes after ending the stimulation that were driven by delayed release of immature synapses. After the onset of hearing, delayed release occurred as well, but did not result in late spiking. The upregulation of K^+ conductance upon hearing onset was causing this effect, suggesting that postsynaptic activation of K^+ channels during spiking suppresses the subsequent effects of delayed release in hearing mice (Yang & Xu-Friedman, 2010). Further, a developmental switch of the glutamate receptor from NMDA (N-methyl-D-aspartate) to AMPA receptor mediated neurotransmission (Bellingham et al., 1998; Isaacson & Walmsley, 1995), as well as a switch in AMPA receptor subunits with a decrease in the GluR2 subunit is described (Gardner et al., 1999, 2001; Lawrence & Trussell, 2000; Wang et al., 1998).

1.6.5 Synapses on bushy cells

Two categories of chemical synapses were identified based on the morphological appearance: type I or asymmetric (later shown to be excitatory), and type II or symmetric (later shown to be inhibitory; Colonnier, 1968; Gray, 1959). Both synapse types can also be found in the AVCN contacting BCs. Synaptic terminals can also be categorized ultrastructurally into two groups based on the size of SVs within the AVCN (Lenn & Reese, 1966). Each of these groups in turn contains morphologically distinct types of synaptic terminals contacting BCs as described by Cant and Morest for cats using electron microscopy of chemically fixed tissue (Cant & Morest, 1979). The first group contains terminals with large, spherical SVs. These include endbulbs of Held and smaller bouton-like endings that form asymmetric contacts with BCs. The large endbulbs are irregular shaped and have multiple dome-shaped AZs within the same terminal. The second group, which contains terminals with small SVs, is further classified into subtypes based on the size and distribution of the terminals as well as on the shape of SVs. The most common subtype within this group has large terminals that form symmetrical (inhibitory) contacts with BCs and contain flattened SVs. Another subtype has small terminals that form symmetrical contacts and are filled with small pleiomorphic SVs. The last subtype contains small spherical SVs and forms asymmetrical contacts, but rather with dendrites than the soma of BCs (Cant & Morest, 1979).

Details of cell and specifically synapse structure are strikingly different after rapid freezing and freeze-substitution (Tatsuoka & Reese, 1989) or cryo-electron microscopy (Tao et al., 2018) from those in chemically fixed tissue. Membranes are shown to be smoother, and the electron density of cytoplasm, organelles and extracellular space appear to be greater (Korogod et al., 2015; Rostaing et al., 2006; Tatsuoka & Reese, 1989). In all synaptic terminals, SVs are round and have different diameters. The postsynaptic density (PSD), which appears as an electron-dense, fuzzy structure at asymmetric synapses in fixed tissue, appears as a fine filamentous structure in frozen tissue that differ in size and distribution between different types of synaptic terminals. Moreover, AZ membranes are flattened in frozen tissue (Fig 1.4, Tao et al., 2018; Tatsuoka & Reese, 1989).

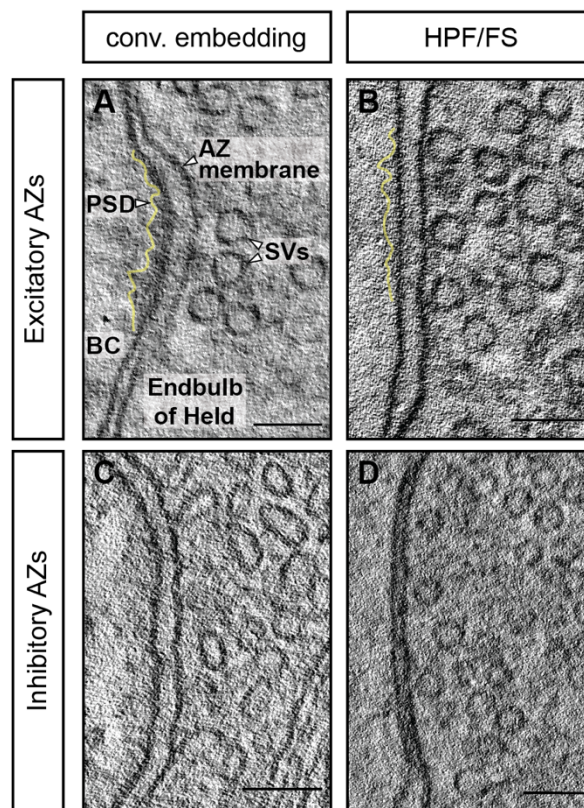


Figure 1.4: Endbulb of Held AZs after HPF/FS and conventional embedding.

(A) Chemical fixation, which is part of the conventional embedding protocol (see section 2.3.2) results in a crosslinking of proteins at the membrane of the postsynapse. This in turn leads to good visibility of the dome-shaped postsynaptic density (PSD; in yellow) at excitatory synapses. **(B)** With HPF/FS, PSDs (yellow) appear less electron-dense and flattened. **(C)** At inhibitory synapses of conventional embedded tissue, SVs appear flattened, and the PSD is less thick and electron-dense compared to that of excitatory synapses. **(D)** Using HPF/FS, SVs at inhibitory synapses are spherical and no fuzzy material at the postsynaptic membrane can be seen. Scale bars: 100 nm.

1.6.5.1 The structure of endbulbs

Next to the functional changes during maturation described in section 1.6.4, the morphogenesis of the endbulb of Held terminals is intensively studied in cats (Ryugo & Fekete,

1982) and mice (Limb & Ryugo, 2000). Endbulbs initially develop as a small and simple swelling at the end of an ANF that have contacted a BC. They gradually grow and develop branches and filipodia-like extensions to evolve a complex tree-like structure (Limb & Ryugo, 2000; Ryugo & Fekete, 1982). The morphogenesis is accompanied by ultrastructural changes of endbulbs that are described in detail for the cat (Ryugo et al., 2006). Early contacts between SBCs and endbulbs are characterized by a very irregular surface of the endbulb and somatic evaginations. In addition to PSDs, numerous *puncta adherentia* are found that represent short symmetrical membrane thickenings not associated with SVs. By the time when the ear canal opens (between P23 and P26 in cats; Ryugo et al., 2003), the membranes between SBCs and endbulbs flatten and *puncta adherentia* diminish. PSDs become larger, but decrease in number, which is accompanied by a developmental transformation of endbulbs into progressively smaller swellings and finer fibers by sequential branching. The progressive increase in SV density per μm^2 continues into adulthood (Ryugo et al., 2006).

The number and size of individual AZs per endbulb in cats and rats is highly variable: Serial-section reconstruction of endbulbs in P25 rats has revealed that each endbulb contains on average 155 AZs with a mean PSD size of $0.066 \pm 0.12 \mu\text{m}^2$ (Nicol & Walmsley, 2002). Furthermore, the mean number of SVs per AZ, especially the mean number of docked SVs has been shown to differ between endbulbs, but the density of SVs is similar (Nicol & Walmsley, 2002). Ryugo et al. estimated the number of AZs per endbulb in the cat AVCN that varies between around 200 to 2000 (Ryugo et al., 1996). However, this study demonstrates that this variability can at least partially be explained by differences in neuronal activity (Ryugo et al., 1996), which will be described in the next section.

1.6.5.2 Influence of neuronal activity on endbulb structure

ANFs, which are responsive for characteristic frequencies (see section 1.6.1) can be categorized by their spontaneous discharge rate (SR; Kiang et al., 1965; Liberman, 1982). Endbulbs from low SR fibers have complex terminals with smaller swellings and project to smaller SBCs compared to endbulbs from high SR fibers (Ryugo et al., 1996; Ryugo & Sento, 1991; Sento & Ryugo, 1989). On the ultrastructural level, endbulbs from low SR fibers have been found to contain fewer, but larger AZs with a lower number of SVs per AZ compared to endbulbs from high SF fibers. Nevertheless, the size of SVs has been shown to be similar in endbulbs from low and high SR fibers (Ryugo et al., 1996).

Interestingly, the effect of neuronal activity on endbulb morphology has also been addressed using deafness models. Endbulbs from deaf cats (Baker et al., 2010; Ryugo et al., 1997; Ryugo et al., 1998) and mice (Lee et al., 2003; Limb & Ryugo, 2000; McGuire et al., 2015; Wright et al., 2014; Youssoufian et al., 2008) are smaller and less branched. In the studied cats, congenital deafness results from a collapsed Reissner's membrane that usually separates

scala media from scala vestibuli in the cochlea (Ryugo et al., 2003). Baker and co-workers found larger but fewer PSDs in newborn deaf kittens compared to normal hearing kittens (Baker et al., 2010). At the age of 30 days, they observed that AZ numbers of deaf and hearing cats have equalized, but PSD length continued to increase into adulthood (Baker et al., 2010). Moreover, PSDs at endbulbs from deaf animals appear flattened compared to the dome-shaped PSDs from normal hearing cats (Baker et al., 2010; Ryugo et al., 1997). The SV density at endbulb AZs is higher in deaf cats throughout development (Baker et al., 2010) but the total number of SV per AZ is strikingly reduced in adult deaf cats compared to age-matched hearing cats (Ryugo et al., 1997). Ryugo and colleagues additionally obtained data from hearing impaired cats that are not profoundly deaf. These cats have intermediate endbulbs in terms of size and complexity compared to endbulbs from hearing and totally deaf cats, which further indicates a correlation of neuronal activity and endbulb structure in cats (Ryugo et al., 1998). In addition, congenitally deaf mice were analyzed regarding their endbulb structure and properties in several studies (Lee et al., 2003; McKay & Oleskevich, 2007; Oleskevich & Walmsley, 2002; Wright et al., 2014). *Deafness* mutant mice have a recessive mutation in the *transmembrane cochlear-expressed gene 1*, which manifests in morphological abnormalities of HCs and SGNs at early postnatal ages. When the ear canal opens, both, HCs and SGNs start to degenerate, while central connections remain intact (Keats et al., 1995; Pujol et al., 1983). Electrophysiological recordings and variance–mean analysis from *deafness* mice before hearing onset reveal a higher synaptic strength due to a higher quantal amplitude (average amplitude of the postsynaptic response to the transmitter content of an SV) compared to normal hearing mice (McKay & Oleskevich, 2007). After ear canal opening, synaptic transmission is enhanced due to an increase in P_r . However, the number of individual AZs and the RRP size are comparable between deaf and wt mice at both ages (McKay & Oleskevich, 2007; Oleskevich & Walmsley, 2002). Another model for congenital deafness is the *shaker-2* mouse that exhibits a recessive point mutation within the *MYO15* gene that encodes the unconventional myosin (Liang et al., 1999; Probst et al., 1998). As a result, HCs within the inner ear have abnormally short stereocilia with disrupted actin organization (Anderson et al., 2000; Beyer et al., 2000; Probst et al., 1998). The *shaker-2* mice exhibit larger PSDs and a reduction of SVs compared to normal hearing wt mice (Lee et al., 2003).

Otoferlin mutant mice also serve as a model of congenitally deafness. Mice lacking a normal copy of the *OTOF* gene show reduced cross-sectional areas of ANFs and smaller VCNs, but the tonotopic organization appears normal (Wright et al., 2014). Wright and colleagues also found smaller and less branched endbulbs in *otoferlin* mutant mice compared to hearing control mice (Wright et al., 2014). These findings could indicate that, as in deaf cats of *shaker-2* mice, changes also occur at the level of individual endbulb AZs. However, this has not been investigated so far.

1.7 Hypotheses and Aims

This study aimed to understand how functional changes of the endbulb of Held, a conventional central synapse, affect its morphology on the level of individual AZs. In order to do so, a systematic ultrastructural analysis was performed using electron tomography of high-pressure frozen tissue. Thereby, different aspects underlying functional changes of endbulbs were considered including development, lack of activity and disruption of presynaptic proteins. Structural parameters of AZs include SV densities and the size of AZs that were previously shown to negatively correlate with synaptic activity (Baker et al., 2010; Murthy et al., 2001; Redd et al., 2000; Ryugo et al., 1996). SVs docked to the AZ membrane represent the morphological correlate of the RRP and could indicate for the P_r of individual synapses (Maus et al., 2020; Murthy et al., 2001).

Mitochondria are characteristic organelles in endbulb terminals and their localization, size and structure near AZs may indicate increased energy consumption due to increasing neuronal activity upon maturation. At the calyx of Held, mitochondrial volume increase upon the onset of hearing (Thomas et al., 2019), but it is unknown so far if this is also reflected by changes of the mitochondrial ultrastructure.

The following objectives were addressed in this thesis:

1. In a first step I used wt mice at the age of P10 and P21 and compared their morphological SV pools in order to understand how maturation of the auditory system is reflected in the morphology of individual endbulb AZs. Functionally, this maturation process is associated with increased neuronal activity, thus a decrease in the AZ area and an increase of the number of SVs can be assumed, which was previously observed for the calyx of Held (Taschenberger et al., 2002; Thomas et al., 2019).
2. In addition to SV pools at individual AZs, I focused on presynaptic mitochondria and its compartments at excitatory synapses within the AVCN including endbulbs of Held upon maturation. The ultrastructure of neuronal mitochondria was previously shown to depend on neuronal activity (Cserép et al., 2018; Ivannikov et al., 2013; Smith et al., 2016; Thomas et al., 2019) and subsequently I aspired to elucidate if the transition from pre-hearing towards hearing also affect mitochondrial structure. Developmental gain in mitochondrial volumes and cristae density might support high firing rates required for auditory processing.
3. Endbulb AZs of mice lacking the HC-specific protein otoferlin were examined to understand how the lack of auditory input affects their ultrastructure while the molecular composition at these AZs is unaltered. In addition to *Otof*^{f/-} mice with comparable ages

to the wt mice (P10 and P22), I investigated if synaptic organization changes upon adulthood by analyzing endbulb AZs of 6-months-old (6M) wt and *Otof*^{-/-} mice.

4. In the next part of my thesis, I analyzed the effects of the CAZ protein RIM-BP2 on the organization of SV pools at endbulb AZs. At IHC ribbon synapses, RIM-BP2 was shown to facilitate SV release positively by regulating the number of VGCCs at IHCs (Krinner et al., 2017), while Ca²⁺ currents were unaltered at the calyx of Held lacking *RIM-BP2* (Acuna et al., 2015). This project is part of a published study that aimed to characterize the function of *RIM-BP2* at endbulbs by combining electrophysiological and ultrastructural analysis (Butola et al., 2021).
5. Finally, the role of the vertebrate-specific protein Mover at synapses projecting on BCs was investigated. Mover was shown to be present at a subset of synapses at different brain regions (Kremer et al., 2007; Wallrafen & Dresbach, 2018) and its function is not completely enlightened. In the AVCN, Mover was shown to be expressed more at inhibitory synapses contacting BCs compared to endbulbs. However, the amount of Mover per SV was higher in endbulbs than in inhibitory synapses (Wallrafen, 2019). Therefore, I investigated the role of Mover in the organization of SVs at both synapse types.

2 Materials and Methods

2.1 Animals

For this thesis, C57BL6/J (wild-type, wt) and *otofelin* knockout (*Otof*^{-/-}) mice in a C57BL6/N background (Reisinger et al., 2011) at postnatal day (P) 10, and P21/22, as well as six-months-old animals (6M) of either sex were used to study ultrastructural changes of endbulb active zones (AZs) upon developmental maturation and lack of activity. To characterize the role of Rab-interacting molecule (RIM)-binding protein 2 (BP2) on the endbulb ultrastructure, *RIM-BP2*-deficient mice with a C57BL6/N background (Grauel et al., 2016), as well as their wt littermates of either sex, were used at the age of P22. The effect of Mover was investigated using male *E2a-Mover* knockout mice (Akula et al., 2019) and their wt littermates at the age of 4M. All mice used for this thesis were housed at the Central Animal Facility of the University Medical Center in Göttingen (C57BL6/J wt, *E2a-Mover*^{-/-} and wt littermates) or the animal facilities of the Max Planck Institutes for Experimental Medicine (*Otof*^{-/-}) or Biophysical Chemistry (*RIM-BP2*^{-/-} and wt littermates). Mice were accommodated in groups in individually ventilated cage racks with ad libitum access to food and water. All experiments were performed in compliance with the national animal care guidelines and were approved by the animal welfare of the University of Göttingen and the State of Lower Saxony.

Details about the mouse lines are listed in Table 2.1.

Mouse line	Results shown in section	Age	Number of animals	Reference
C57BL6/J (wild-type, wt)	3.1/3.2/3.3	P10	4	available at Jackson's Laboratory
	3.1/3.2/3.3	P21	3	
	3.3	6M	3	
<i>Otof</i> ^{-/-} mice	3.3	P10	3	Reisinger et al., 2011
		P22	3	
		6M	3	
<i>RIM-BP2</i> ^{-/-} mice and littermate control mice (wt)	3.4	P22	3	Grauel et al., 2016
	4			
<i>E2a-Mover</i> ^{-/-} mice and littermate control mice (wt)	3.5	4M	5	Akula et al., 2019
	5			

Table 2.1: Used mouse lines.

2.2 Materials

2.2.1 Chemicals

Product	Company	Cat. No
10 nm gold particles	Plano	EM.GC10_4
1-hexadecene	Sigma-Aldrich	52276-5ML
Acetone, glass distilled	Carl Roth	5025.2
Calcium chloride (CaCl ₂)	Carl Roth	CN93.2
Chloroform	Sigma-Aldrich	288306-100ML
Disodium hydrogen phosphate dihydrate (Na ₂ HPO ₄ *2H ₂ O)	Sigma-Aldrich	71643-250G
EPON Agar pre-mix kit	Plano	R1140
Ethanol	Roth	T171.3
Formvar/ Vinylec	Plano	R1202
Glucose	Sigma-Aldrich	G8270-1KG
Glutaraldehyde	Sigma-Aldrich	G7651
Magnesium chloride (MgCl ₂)	Honeywell	M0250-500G
Molecular sieve (0.3 nm, type 564, beads)	Carl Roth	8487.2
Myo-inositol	Sigma-Aldrich	I7508-50MG
Osmium tetroxide, 4 % aqueous solution	EMS	19170
Osmium tetroxide, crystalline	EMS	19132
Paraformaldehyde (PFA)	Carl Roth	0335.1
Phosphate buffered saline (PBS) tablet	Sigma-Aldrich	P4417-100TAB
Potassium chloride (KCl)	Sigma-Aldrich	P5405-250G
Sodium cacodylate trihydrate	Carl Roth	5169.1
Sodium chloride (NaCl)	Sigma-Aldrich	S5886-500G
Sodium dihydrogen phosphate monohydrate (NaH ₂ PO ₄ *H ₂ O)	Sigma-Aldrich	71507-250G
Sodium hydrogen carbonate (NaHCO ₃)	AppliChem	141638
Sodium L-ascorbate	Sigma-Aldrich	A4034-100G
Sodium L-lactate	Sigma-Aldrich	71718-50G
Sodium pyruvate	Sigma-Aldrich	P2256-25G
Sucrose	Sigma-Aldrich	S0389-500G
Tannic acid	Sigma-Aldrich	403040
UranyleLess	EMS	22409

Table 2.2: Chemicals used for the experiments.

2.2.2 Equipment

Product	Company
Blades (for trimming)	Plano
Blades (for vibratome)	Campden Instruments
Copper slot (3.05 mm Ø) and 100 mesh (3.05 mm Ø) grids	Plano
Cryotrim 45°	DiAtome
EM AFS2	Leica Microsystems
EM UC7 ultramicrotome	Leica Microsystems
Embedding molds	Plano
Glass slides	Th. Geyer
Grid boxes	Plano
HPM100	Leica Microsystems
Incubator INCU-line	VWR
Instant adhesives (LOCTITE 401)	Henkel
JEM-1011	JEOL
JEM-2100	JEOL
Magnetic hot plate stirrer	Stuart
Micro scale CP124S	Sartorius
Orius SC1000 CCD camera	GATAN
pH-meter 1000L	VWR
Rotating wheel	UMG workshop
Sample holder half cylinder and middle plate	Leica Microsystems
Specimen carriers Type A and B	Leica Microsystems
Ultra 35° diamond knife	DiAtome
Vapor pressure osmometer	Wescor
VT 1200S vibratome	Leica microsystems

Table 2.3: Equipment used for this thesis.

2.2.3 Solutions

Solution	Concentration and treatment conditions
Anhydrous ethanol	Anhydrous beads are filled up to the level of 200 ml, volume further filled till 1000 ml, stored airtight under hood.
Cutting solution	(in mM) 50 NaCl, 26 NaHCO ₃ , 120 sucrose, 1.25 NaH ₂ PO ₄ *H ₂ O, 2.5 KCl, 20 glucose, 0.2 CaCl ₂ , 6 MgCl ₂ , 0.7 sodium L-ascorbate, 2 sodium pyruvate, 3 <i>myo</i> -inositol, and 3 sodium L-lactate. Osmolarity: around 310 mOsm, pH adjusted to 7.35.
Fixative 2 (for conventional embedding)	2 % glutaraldehyde (v/v) in 0.1 M cacodylate buffer. Used under the hood.
Formvar solution	1 % in water free chloroform (w/v), light protected (under the hood at room temperature)
Karlsson-Schultz buffer	4 % PFA, 2.5 % glutaraldehyde, 0.5 % NaCl in 0.1 M phosphate buffer, pH 7.4. Used under the hood.
Osmium tetroxide	2 % in acetone (w/v) (for freeze substitution) and 1 % (v/v) in cacodylate buffer (for conventional embedding). Used under the hood.
Phosphate buffer	0,36 g NaH ₂ PO ₄ *H ₂ O, 3,1 g Na ₂ HPO ₄ *2H ₂ O in distilled water, pH 7.4
Sodium cacodylate buffer	0.1 M in distilled water, pH 7.2-7.4. Used under the hood.
Tannic acid	0.1 % (w/v) tannic acid in acetone
Uranyl acetate	1 % (v/v) in distilled water. Under the hood.
Water free chloroform	500 ml glass bottle filled up to the 100 ml mark with CaCl ₂ powder and with Chloroform (w/v), till the 500 ml mark, stirred once well (stored airtight and light protected under the hood at room temperature)

Table 2.4: Solutions used in this study.

2.3 Sample preparation for electron microscopy

2.3.1 High-pressure freezing (HPF) and freeze-substitution (FS)

HPF and FS of freshly prepared slices of the anteroventral cochlear nucleus (AVCN) were used to study synaptic vesicle (SV) pools at individual endbulb of Held AZs in a near-to-native state. The following sections describe the single steps of this workflow.

2.3.1.1 Vibratome slice preparation

After anesthetization with carbon dioxide, animals were sacrificed by decapitation for immediate dissection of the brains. Parasagittal slices (150 μm) of AVCN were prepared as described previously (Butola et al., 2017; Mendoza Schulz et al., 2014; Yang & Xu-Friedman, 2008). Brains were immersed in ice-cold cutting solution containing 50 mM NaCl, 26 mM NaHCO_3 , 120 mM sucrose, 1.25 mM $\text{NaH}_2\text{PO}_4 \cdot \text{H}_2\text{O}$, 2.5 mM KCl, 20 mM glucose, 0.2 mM CaCl_2 , 6 mM MgCl_2 , 0.7 mM sodium L-ascorbate, 2 mM sodium pyruvate, 3 mM *myo*-inositol, and 3 mM sodium L-lactate, continuously aerated with carbogen (95 % O_2 , 5 % CO_2). The meninges were removed from the ventral part of the brainstem and a midsagittal cut separated hemispheres. After that, the forebrain was removed at the pons-midbrain junction. Brain blocks containing the brainstem and the cerebellum were glued onto the specimen plate of a VT 1200 S vibratome (Leica Microsystems) with the lateral sides facing upwards and the ventral side facing the blade. The specimen plate was then transferred to the buffer tray containing ice-cold cutting solution. Sections were cut at a blade feed rate of 0.02 mm/s with an amplitude of 1.50 mm. Slices containing the AVCN were trimmed and prepared for HPF (Fig. 2.1).

2.3.1.2 High-pressure freezing (HPF)

The slices of the AVCN were mounted onto type A specimen carriers (Leica Microsystems) with a diameter of 3 mm and a depth of 0.2 mm, filled with cutting solution. The flat side of the type B carriers (Leica Microsystems) was dipped in 1-hexadecene (Sigma-Aldrich) and placed onto the type A carrier (Fig. 2.1). Samples were frozen immediately using a HPM100 (Leica Microsystems) and transferred into liquid nitrogen for storage or further processing.

2.3.1.3 Freeze-substitution (FS)

FS was performed in an EM AFS2 (Leica Microsystems) as described previously (Chakrabarti et al., 2018; Wong et al., 2014) according to the program described in Table 2.5.

Temperature (°C)	Duration (h)	Solution
-90	92	0.1 % (w/v) tannic acid in acetone
-90	3	washing in acetone (3 times)
-90	7	2 % (w/v) osmium tetroxide in acetone
-90 → -20	14	
-20	17	
-20 → +4	2.4	
+4	3	washing in acetone (3 times)

Table 2.5: Program for freeze substitution (FS).

During the last washing step, samples were brought to room temperature, infiltrated in epoxy resin (Table 2.6) and embedded in fresh 100 % epoxy resin, put in embedding molds and polymerized at 70 °C for 48 h. The whole workflow is visualized in Fig. 2.1.

Duration (h)	Condition	Epoxy concentration (v/v)
0.5	On a rotating wheel at room temperature	1:1 epoxy resin in acetone
1.5		1:1 epoxy resin in acetone
Overnight		100 % epoxy resin
3-6		100 % epoxy resin

Table 2.6: Epoxy-acetone infiltration series.

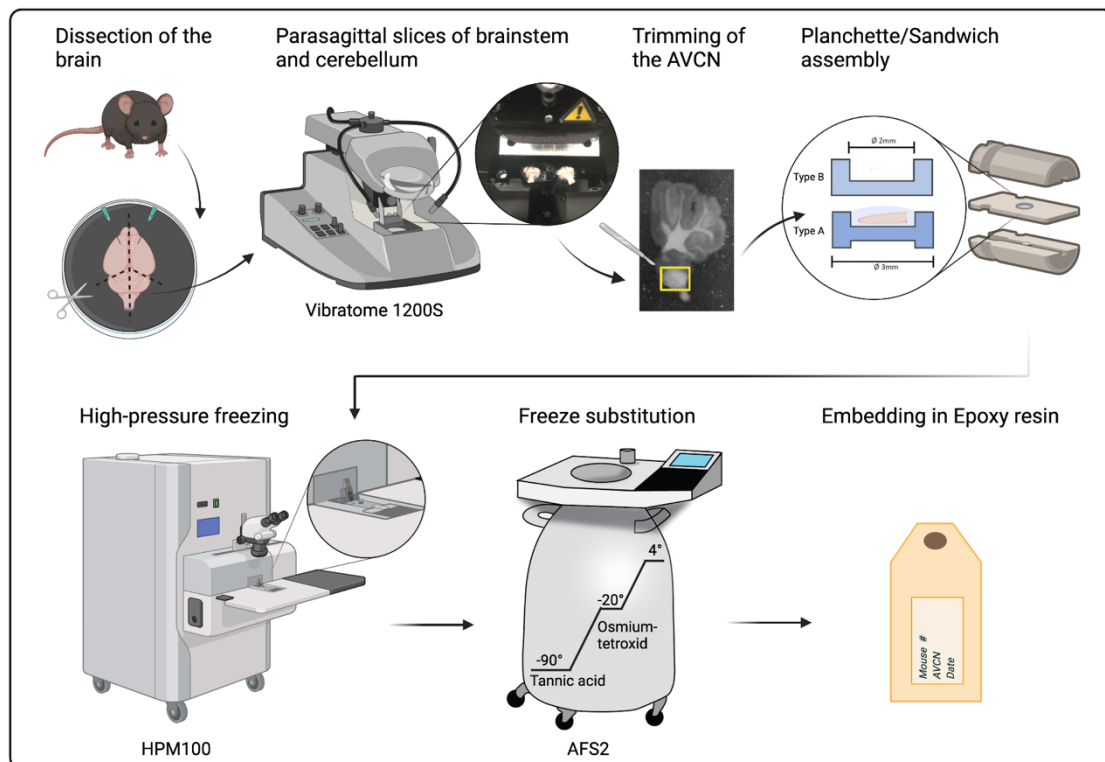


Figure 2.1: Experimental workflow.

(Figure 2.1 continued): After dissection of the brains, 150 μm parasagittal slices of brain blocks containing the brainstem and cerebellum were prepared with a vibratome. Slices containing the AVCN were trimmed and prepared for high-pressure freezing by assembling a sandwich with specimen carriers. Samples were frozen immediately and stored in liquid nitrogen until freeze substitution (FS) was performed. During FS samples were brought slowly to room temperature while incubated with 0.1 % tannic acid and 2 % (w/v) osmium tetroxide. At room temperature, slices were infiltrated in epoxy resin, put in embedding molds and polymerized at 70 °C for 48 h. AFS2 was prepared in Adobe Illustrator and the illustration was created with BioRender.com.

2.3.2 Conventional embedding

Conventional embedding was performed to study SV pools at endbulb AZs and inhibitory synapses of *E2a-Mover*^{-/-} and their wt littermate control (*E2a-Mover*^{+/+}) mice (section 3.5). Mice were euthanized by CO₂ inhalation and transcardially perfused with 0.9 % saline followed by perfusion with Karlsson-Schultz buffer (Karlsson & Schultz, 1965) by Dr. Rebecca Wallrafen (Institute of Anatomy and Embryology, University Medical Center Göttingen). Brains were removed and fixed for an additional hour in Karlsson-Schultz buffer. After preparation of the brainstem, 200 μm thick parasagittal slices containing the AVCN were prepared in PBS using the vibratome as described in section 2.3.1.1. Slices were fixed further overnight at 4 °C using fixative 2 (2 % glutaraldehyde in 0.1 M sodium cacodylate buffer, pH 7.2) and washed in sodium cacodylate buffer. Post-fixation was performed in 1 % osmium tetroxide for 1 h on ice, followed by washing steps in sodium cacodylate buffer, distilled water, and *en bloc* staining with 1 % uranyl acetate in water for 1 h on ice. After three washing steps in distilled water, slices were dehydrated in increasing ethanol concentrations on ice (Table 2.7). Finally, slices were infiltrated with epoxy resin (Table 2.8) and embedded in molds where the resin polymerized for 48 h at 70 °C.

Duration (min)	Ethanol concentration (v/v)
5	30 %
5	50 %
10	70 %
10	95 %
10	95 %
12	100 % (anhydrous ethanol)
12	100 % (anhydrous ethanol)
12	100 % (anhydrous ethanol)

Table 2.7: Dehydration series of increasing ethanol concentration.

Duration (h)	Condition	Epoxy concentration (v/v)
0.5	On a rotating wheel at room temperature	1:1 epoxy resin in ethanol
1.5		1:1 epoxy resin in ethanol
Overnight		100 % epoxy resin
3-6		100 % epoxy resin

Table 2.8: Epoxy-ethanol infiltration series.

2.4 Trimming of embedded samples

After polymerization, the epoxy blocks containing the samples were trimmed with a fine file (DiAtome, Switzerland) to remove the empty resin and to expose the region of interest within the tissue. Afterward, excess of epoxy resin at the sides was removed with the file and then carefully with a razor blade to get a small trapeze-shaped block face (Fig. 2.2).

2.5 Formvar coating of slot and mesh grids

Copper slot (3.05 mm Ø; Plano) and mesh (3.05 mm Ø; Plano) grids were coated with 1 % formvar in water-free chloroform as described previously (Chakrabarti, 2017) before they can be used for collecting slides of the trimmed samples. Therefore, a glass cylinder equipped with a tap at the bottom was filled with formvar solution and a clean glass object slide was placed into the cylinder. The tap was opened quickly and entirely to ensure an optimal drag force so that a thin layer of formvar was coated onto both sides of the slide. Afterwards, the edges of the slides were scratched on both sides using a razor blade. The slide was carefully immersed into a beaker filled with distilled water so that the cut formvar film floats onto the water surface. A silver to light yellow color represents a ~ 80-90 nm thick formvar film which was used for coating the grids. Using forceps, grids were placed on the formvar film with the shiny side facing up, and a little pressure was applied to ensure proper attachment of formvar with the grids. Formvar films covered with slot grids were picked up with a piece of parafilm, while for films with mesh grids the paper of the parafilm was used. Finally, the formvar films were placed onto petri dishes for drying and small holes were made in the grid-free areas of the films to release air bubbles.

2.6 Sectioning and post-staining

The surface of the trimmed samples was smoothed prior sectioning using a 45° cryotrim knife (DiAtome). To check the region and the structural preservation of the tissue, 70 nm ultrathin sections were cut with a 35° diamond knife (DiAtome) using an EM UC7 ultramicrotome (Leica

Microsystems) and collected on formvar-coated copper slot grids (3.05 mm \varnothing , 1 mm x 2 mm slot; Plano). For electron tomography, 250 nm semi-thin sections were prepared and collected on formvar-coated 100 mesh grids (3.05 mm \varnothing ; Plano; Fig. 2.2).

Post-staining was performed with UranylLess (EMS) for 20 minutes. After that, grids were washed 6 times on droplets of distilled water and dried with filter paper. Additionally, 10 nm gold particles (Plano) were applied on both sides of the mesh grids with the semithin sections that act as fiducial markers (Fig. 2.2).

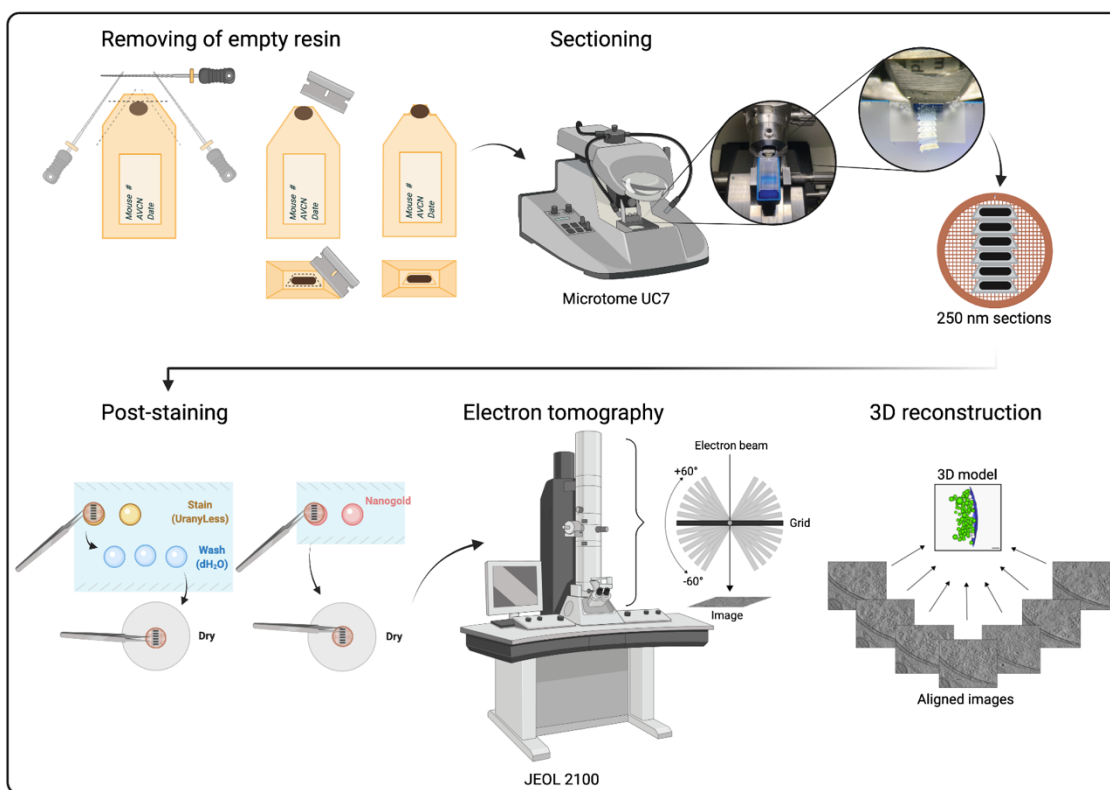


Figure 2.2: Preparation of sections for electron tomography.

Epoxy blocks were trimmed to remove excessive epoxy resin. After smoothing the block face, 70 (not shown) and 250 nm slices were prepared with an ultramicrotome, and sections were put on formvar-coated grids. Post-staining was performed with UranylLess and mesh grids were incubated with nanogold particles. After prescreening the samples (not shown), single tilt series of AZs were recorded mostly from -60° to $+60^\circ$. Tomograms were generated using the IMOD package etomo and segmentation was done using 3dmod (Kremer et al., 1996). Illustration created with BioRender.com.

2.7 Transmission electron microscopy (TEM)

To check the presence of BCs with contacting endbulb terminals within the sections, 2D electron micrographs were taken at 80 kV using a JEM1011 TEM (JEOL, Freising, Germany) equipped with a Gatan Orius 1200A camera (Gatan, Munich, Germany) using the Digital Micrograph software package. In addition, the tissue quality was checked which included the preservation of the tissue and the absence of freezing artefacts like tissue distortion due to ice crystal formation or poor freezing.

2.7.1 Electron tomography

After prescreening the grids, endbulb of Held AZs of the AVCN were chosen by the appearance of a large presynaptic terminal contacting a BC with an asymmetric (denoted as postsynaptic density (PSD)) synaptic site. In high-pressure frozen samples, PSDs appear less electron-dense compared to chemical fixed synapses (see also section 1.6.5). Thus, only asymmetric synapses with a clearly visible synaptic cleft at 0° and a clearly identifiable PSD were analyzed. Moreover, just tomograms of AZs within large synaptic terminals that are typical for endbulbs of Held as shown in Fig. 2.3 and 2.4 were generated.



Figure 2.3: Electron micrograph of an endbulb of Held terminal.

Electron micrograph obtained from an ultrathin section of the AVCN of a P10 wt mouse. The big terminal represents an endbulb of Held (eb) that contacts a bushy cell (BC). Black boxes highlight potential active zones. Scale bar: 500 nm.

Electron tomography was essentially performed as described previously (Chakrabarti et al., 2018; Wong et al., 2014). Large synaptic terminals on bushy cells (Fig. 2.3, 2.4) were identified, and single tilt series from endbulb AZs were acquired at 200 kV using a JEM2100 TEM (JEOL, Freising, Germany) mostly from -60° to $+60^\circ$ with a 1° increment at 15,000 \times magnification, using the Serial-EM software package (Mastrorarde, 2005). In rare cases, a grid bar came into the visual field at higher angles and the tilt series were acquired only from -40° or to -40° . When the quality of these tomograms, described in section 2.7.3 was sufficient, they were included into the analysis.

2.7.2 Generation of tomograms

Tomograms were generated using the IMOD package *etomo* (Kremer et al., 1996). For detailed introduction and tutorial see <https://bio3d.colorado.edu/imod/doc/tomoguide.html>. The raw tilt series were saved as *.mrc file that was loaded into *etomo* as a single stack. Pre-processing steps recognized and removed X-rays and other camera artifacts that produced very low or high values and negatively influenced the contrast. Next, a coarse alignment step was performed to pre-align the images for the following generation of the fiducial model. For this, gold beads that were applied to the grids as described in section 2.6, were marked on a view near zero tilt that were traced by the program *Beadtrack* through the entire stack. The fine alignment step resolved tilt displacements between the images and refined the projection angles. The tomogram positioning aimed to flatten the reconstruction. The sample tomogram thickness was thereby set to 1,000, and three sample tomograms were created (near the top, middle, and bottom of the stack), in which the top and bottom boundaries of the biological tomogram were defined. In the next steps, the final aligned stack was made, and the tomogram was generated. Finally, the tomogram was trimmed in z-plane to exclude blurry virtual sections. The workflow of trimming, sectioning, post-staining, electron tomography and tomogram generation is illustrated in Fig. 2.2.

2.7.3 Quality assessment of tomograms

In order to assess whether the tomograms could be used for quantification, they were subjected to a further quality control (Fig 2.4). (i) Although the freezing quality of the sample was checked already before (see section 2.7), minor freezing artefacts were only identified in the tomograms. (ii) Only tomograms with parallel pre- and postsynaptic membrane were considered to allow the distance measurements of SVs to the AZ membrane. (iii) To distinguish between excitatory and inhibitory AZs, the presence or absence of a PSD throughout the tomogram was examined.

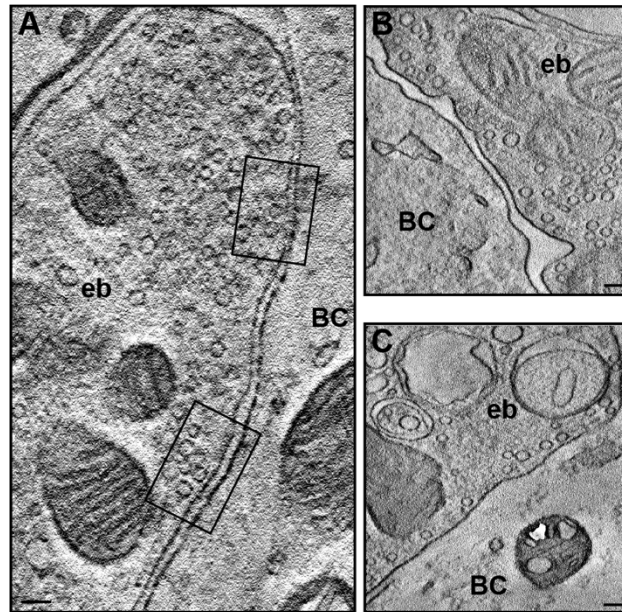


Figure 2.4: Single virtual sections of tomograms with different qualities.

(A) Tomogram of an endbulb terminal with a good structural preservation. No distortion of the tissue due to freezing artifacts can be observed and the pre- and postsynaptic membrane are parallel. The active zones (black boxes) were defined due to the PSDs, that are difficult to recognize in a single virtual section but could be identified in the tomogram. This tomogram was used for quantification. **(B)** The structural preservation in this tomogram is good, but the membranes do not run parallel which prevents a reliable quantification of distances. **(C)** The bright, large, round structures in the endbulb terminal indicate a bad structural preservation. In addition, the postsynaptic membrane is missing which makes demarcation of the active zone impossible. eb, endbulb of Held; BC, bushy cell. Scale bars: 100 nm.

2.7.4 Model rendering and three-dimensional (3D) analysis

Tomograms were segmented semi-automatically using 3dmod (Kremer et al., 1996), with a pixel size of 0.95 nm. For a detailed introduction, see also <https://bio3d.colorado.edu/imod/doc/3dmodguide.html>. The presynaptic AZ membrane was defined as part of the presynaptic membrane that was opposed to the PSD, and the PSD was determined along a clear synaptic cleft. Previous studies did comparable approaches on conventionally embedded endbulbs of Held (Butola, 2017) and calyces of Held (Taschenberger et al., 2002), demonstrating that the measurement of the membrane along the PSD extent is a valid approximation for the presynaptic AZ size. The AZ membrane of an AZ was assigned as a *closed* object and manually segmented every 15 virtual sections for five consecutive virtual sections using the *sculpt* drawing tool and then interpolated across the Z-stack using the *interpolator* tool of 3dmod. The AZ area was generated by meshing the contours (Helmprobst et al., 2015), and the total surface area of this object was then divided by two to calculate the presynaptic AZ area.

SVs were reconstructed using “*scattered*” objects at its maximum projection, and the sphere size was adjusted for each SV. The number of SVs was presented as the total number per AZ as well as SV density by normalizing the SV number to the size of the respective AZ area. The smallest distances from the outer leaflet of the SV membrane to the inner leaflet of the AZ membrane were measured, and SVs in physical contact with the AZ membrane were defined as morphological docked SVs (0-2 nm distance) and were annotated in a different color to distinguish them from the rest of the SV pool. All SVs within 200 nm perpendicular to the AZ membrane were quantified and divided into bins. To analyze the SV distribution upon maturation and further development in wt and upon lack of activity on endbulb AZs (sections 3.1 and 3.3), 5 nm bins were used up to 40 nm, and 40 nm bins were used for SVs farther away from the AZ membrane (40-80 nm; 80-120 nm; 120-160 nm; 160-200 nm). To analyze the effect of *RIM-BP2* disruption, 20 nm bins were used (section 3.4), and the effect of knocking out *Mover*, 40 nm bins were used (section 3.5). The number of SVs in the respective bins was normalized to the AZ area, or in the case of the *Mover* study, the relative SV number per AZ was calculated. The radii of the SVs were determined with the program *imodinfo* of the IMOD software package, and the average diameter per tomogram was calculated.

The effect of *Mover* disruption was not just investigated on the ultrastructure on endbulb AZs, but also on AZs of inhibitory terminals contacting BCs. At inhibitory AZs, SVs appeared to be flattened and were annotated as *closed* objects using the *sculpt* drawing tool and segmented manually. The analyzed parameters for all the mouse models used in this thesis are summarized in Table 2.9.

2.7.5 Electron tomography of presynaptic mitochondria

For section 3.2, I performed electron tomography of presynaptic mitochondria at the endbulb of Held terminals and at other excitatory synapses within the AVCN. I used the samples prepared for the project described in section 3.1. Dependent on the size of the endbulb terminal, single tilt series were recorded at 8,000 to 12,000x magnification that resulted in pixel sizes of 1.648-1.188 nm. The mitochondrial outer membranes were manually segmented every 15 virtual sections using the *sculpt* drawing tool and then interpolated across the Z-stack using the *interpolator* tool of 3dmod. Similarly, the crista membranes (CM) were manually segmented on every 5th virtual section, and when they split up, two objects were created, and the *combine* tool was used to allow precise measurement of their surface area. Mitochondrial volumes, the individual CM surface areas and CM inner volumes were measured using the *info* tool. The individual surface areas and inner volumes were summed up to determine the total area and inner volume of the cristae. The CM density was calculated by dividing the total CM surface area by the mitochondrial volume. The crista shape factor, which measures the lamellarity of

CMs, was calculated by dividing the total CM surface area by the total inner volume of the cristae.

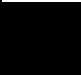




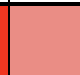






	C57BL6/J (wt)			<i>Otof</i> ^{-/-}			<i>RIM-BP2</i> ^{-/-} and littermate controls (wt)		<i>E2a-Mover</i> ^{-/-} and littermate controls (wt)			
	P10	P21	6M	P10	P22	6M	wt	KO	exc.		inh.	
									wt	KO	wt	KO
Color code used in figures												
AZ area		✓			✓		✓					
SV number		✓			✓		✓			✓		
SV density		✓			✓		✓					
Rel. SV number										✓		
Docked SVs	0-2 nm			0-2 nm			0-2 nm		0-2 nm			
Membrane-proximal SVs	2-40 nm			2-40 nm			2-20 nm		2-40 nm			
SV distribution (bins)	5 nm (until 40 nm) 40 nm			5 nm (until 40 nm) 40 nm			20 nm		40 nm			
SV diameter		✓			✓		✓		✓			
Mitochondrial ultrastructure	✓	✓										

Table 2.9: Color code and analyzed parameters of the different investigated mouse models.

2.8 Statistical analysis

The sample size analyzed in section 3.1 and 3.3 was the following (*N*, number of mice; *n*, number of AZs/SVs:

wt P10: *N* = 4, *n* = 24 AZs; wt P21: *N* = 3, *n* = 22 AZs; wt 6M: *N* = 3, *n* = 29 AZs;

Otof^{-/-} P10: *N* = 3, *n* = 22 AZs; *Otof*^{-/-} P22: *N* = 3, *n* = 23 AZs; *Otof*^{-/-} 6M: *N* = 3, *n* = 23 AZs

All SVs:

wt P10: *N* = 4, *n* = 1101 SVs; wt P21: *N* = 3, *n* = 1190 SVs; wt 6M: *N* = 3, *n* = 1842 SVs;

Otof^{-/-} P10: *N* = 3, *n* = 1078 SVs; *Otof*^{-/-} P22: *N* = 3, *n* = 1508 SVs; *Otof*^{-/-} 6M: *N* = 3, *n* = 911 SVs

Docked SVs:

wt P10: *N* = 4, *n* = 85 SVs; wt P21: *N* = 3, *n* = 67 SVs; wt 6M: *N* = 3, *n* = 86 SVs;

Otof^{-/-} P10: *N* = 3, *n* = 60 SVs; *Otof*^{-/-} P22: *N* = 3, *n* = 56 SVs; *Otof*^{-/-} 6M: *N* = 3, *n* = 42 SVs

Membrane-proximal SVs:

wt P10: $N = 4$; $n = 292$ SVs; wt P21: $N = 3$; $n = 283$ SVs; wt 6M: $N = 3$; $n = 420$ SVs;

Otof^{-/-} P10: $N = 3$, $n = 195$ SVs; *Otof*^{-/-} P22: $N = 3$, $n = 354$ SVs; *Otof*^{-/-} 6M: $N = 3$, $n = 248$ SVs

For investigating presynaptic mitochondria (section 3.2), the sample size was the following (N , number of mice; n , number of tomograms):

wt P10: $N = 3$, $n = 19$ tomograms of non-endbulb terminals with 20 AZs and 31 mitochondria (24 mitochondria for analyzing the ultrastructure) and $n = 12$ tomograms of endbulb terminals with 18 AZs and 82 mitochondria (23 mitochondria for analyzing the ultrastructure);

wt P21: $N = 3$, $n = 13$ tomograms of non-endbulb terminals with 15 AZs and 34 mitochondria (23 mitochondria for analyzing the ultrastructure) and $n = 15$ tomograms of endbulb terminals with 18 AZs and 65 mitochondria (29 mitochondria for analyzing the ultrastructure)

To investigate the role of RIM-BP2 at endbulb AZs (section 3.4) the sample size was the following:

RIM-BP2^{+/+} (wt): $N = 4$, $n = 26$ AZs;

RIM-BP2^{-/-}: $N = 3$, $n = 28$ AZs

The role of Mover (section 3.5) was investigated using the following sample size:

E2a-Mover^{+/+} (wt): $N = 5$, $n = 34$ endbulb AZs and $n = 9$ inhibitory synapses;

E2a-Mover^{-/-}: $N = 5$, $n = 33$ endbulb AZs and $n = 13$ inhibitory synapses

Data were analyzed using *Excel*, *Igor Pro 8.1* (Wavemetrics), and *GraphPad Prism 9.3.1* (GraphPad Software). Normal distribution was assessed with the Jarque-Bera test and equality of variances was assessed with the *F*-test in normally distributed data. For normally distributed data, two-tailed unpaired *t*-test (T), or, when not normally distributed, the Wilcoxon rank test (W) was used for two-sample tests. For more than two datasets, one-way ANOVA with post-hoc correction by Tukey's test was used to detect differences for normally distributed data. For not normally distributed data, Kruskal-Wallis (KW) test followed by Dunn's test was used. For analyzing SV diameters, the mean of the averaged SV diameters per AZ were compared. To compare variances in Fig. 3.13D and 3.14E, *F*-test was performed by Prof. Dr. Mehmet Gültas (Department of Animal Sciences, Georg-August-University Göttingen) using *R* version 4.0.3 and the corresponding *p*-values were corrected for multiple comparisons. Statistical significance of correlations was determined using the Spearman non-parametric correlation test. Statistically significant differences are reported as * $p < 0.05$, ** $p < 0.01$, *** $p < 0.001$ and **** $p < 0.0001$.

In section 3.3, data from wt and *Otof^{fl}* were compared for each age group by two-sample tests. In addition, the different age groups were compared separately for wt and *Otof^{fl}* using ANOVA or KW test with the respective post-hoc correction. In sections 3.1, 3.2, 3.4, 3.5 just two-sample tests were used.

Graphs were created with *GraphPad Prism 9.3.1* (GraphPad Software) and figures were assembled with Adobe Illustrator or with Biorender.com.

3 Results

Endbulbs of Held represent one of the largest synaptic terminals in the CNS and contain several hundred AZs (Nicol & Walmsley, 2002; Ryugo et al., 1996). They are formed by auditory nerve fibers (ANFs) that transmit auditory information to bushy cells (BCs) in the anteroventral cochlear nuclei (AVCN). Upon maturation from pre-hearing to hearing, endbulbs undergo functional refinement to evolve a reliable and temporal precise neurotransmission (see section 1.6.4).

How does these changes translate into morphology at the individual AZ? Structural changes that go along with this functional refinement have not been investigated so far and were subject of the first part of my thesis (section 3.1) which is based on the following paper:

Hintze A, Gültas M, Semmelhack EA, Wichmann C. [Ultrastructural maturation of the endbulb of Held active zones comparing wild-type and otoferlin-deficient mice.](#)
iScience. 2021 Mar 8;24(4):102282. doi: 10.1016/j.isci.2021.102282.

In the second part (section 3.2), I focused on presynaptic mitochondria at endbulb terminals and other excitatory synapses within the AVCN and compared ultrastructural parameters between pre-hearing and young hearing mice.

In a next step (section 3.3), I included adult mice and deaf *otoferlin*-deficient (*Otof*^{-/-}) mice into the analysis in order to investigate synaptic vesicle (SV) pool changes of individual endbulb AZs upon adulthood and lack of auditory input. As the first part, this part of the thesis is based on Hintze et al., 2021.

In the fourth part of this thesis, I performed electron tomography to understand the role of RIM-BP2 on the AZ organization at endbulbs of Held. The results are presented in section 3.4. and I contributed with the data depicted in Figure 18 of the publication:

Butola T, Alvanos T, Hintze A, Koppensteiner P, Kleindienst D, Shigemoto R, Wichmann C, Moser T. [RIM-Binding Protein 2 Organizes Ca²⁺ Channel Topography and Regulates Release Probability and Vesicle Replenishment at a Fast Central Synapse.](#)
J Neurosci. 2021 Sep 15;41(37):7742-7767. doi: 10.1523/JNEUROSCI.0586-21.2021.

I mainly focused on the excitatory endbulbs of Held, that similarly to other central synapses, show a clear postsynaptic density (PSD; Fig. 3.1; García-Hernández et al., 2017; Nicol and Walmsley, 2002; O'Neil et al., 2011; Redd et al., 2000). In order to determine the number and distribution of SVs at individual AZs as well as the ultrastructure of presynaptic mitochondria in a near-to-native state, high-pressure freezing and freeze substitution (HPF/FS) of acutely sliced AVCN followed by electron tomography was performed.

In addition to endbulbs, BCs receive inhibitory input (Gómez-Nieto & Rubio, 2011; Keine & Rübtsamen, 2015; Kuenzel, 2019; Lauer et al., 2013; Spirou et al., 2005, see also section 1.6.5) whose presynaptic terminals are considerably smaller (Gulley & Reese, 1981; Spirou et al., 2005) and AZs do not exhibit an elaborate PSD (Colonnier, 1968; Harris & Weinberg, 2012; Tao et al., 2018). After chemical fixation, inhibitory synapses contain a mixture of round and flattened SVs (Lauer et al., 2013; Spirou et al., 2005; Tolbert and Morest, 1982), whereby the proportion of flattened SVs correlates with the osmolarity of the buffer that was used for fixation (Valdivia, 1971). However, after rapid freezing and cryo-electron microscopy (Tao et al., 2018) or FS (Tatsuoka & Reese, 1989), this effect is not observed and SVs stay spherical. This is also the case in my samples of the AVCN (Fig. 1.4). Consequently, all tomograms were subjected to rigorous quality checks before quantification to determine the freezing quality and the presence or absence of a PSD in order to distinguish between excitatory and inhibitory AZs. Furthermore, only AZs from large terminals were considered and the presence of parallel pre- and postsynaptic membranes with a regular synaptic cleft served as a required criterion to enable a reliable quantification of SV distances to the AZ membrane (Fig. 3.1, see also section 2.3.7).

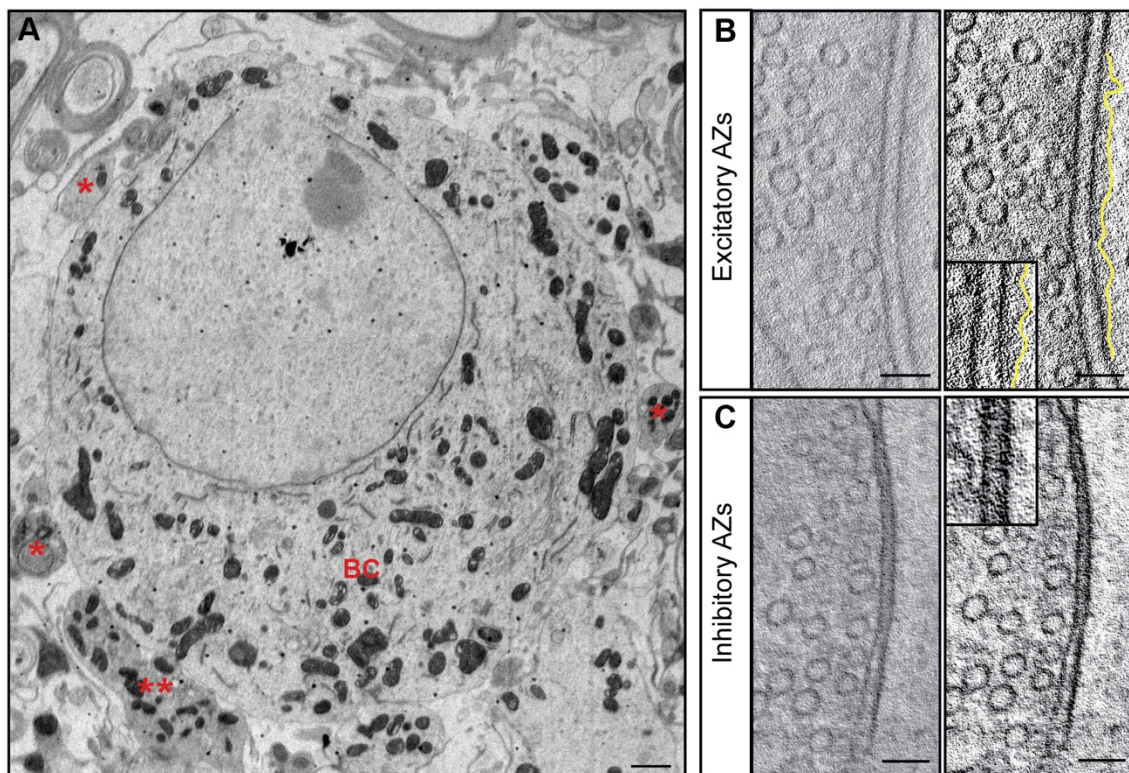


Figure 3.1: Electron micrograph of a bushy cell (BC) and excitatory and inhibitory AZs.

(A) Electron micrograph of a BC with several presynaptic contacts (*). The large terminal represents an endbulb of Held (**). Scale bar: 1 μ m. (B) Left: Example virtual section of an excitatory AZ with a PSD appearing fuzzy in HPF/FS samples. The corresponding tomogram was included into the analysis. Right: Enhanced contrast of the same section, where the outline of the PSD is highlighted (yellow line). See also inset. Scale bars: 100 nm. (C) Left: Virtual section of an asymmetrical contact, lacking the

(Figure 3.1 continued): PSD. Right: Enhanced contrast of the same section as left. As also seen in the inset, a typical PSD is not present. This inhibitory AZ was excluded from the study after inspection of the whole tomogram. Scale bars: 100 nm. Figure modified from Hintze et al., 2021.

In the last part of my thesis, I present ultrastructural investigations of adult mice lacking the presynaptic protein Mover (section 3.5). In contrast to the other parts, electron tomography of chemically fixed tissue was performed. Endbulb AZs and inhibitory synapses contacting BCs were analyzed, which were easy to distinguish from the excitatory terminals due to chemical fixation.

3.1 Ultrastructural changes at endbulb active zones upon maturation from pre-hearing to hearing

Maturation of synapses results in functional changes that I assume to be reflected also on the level of SV pool organization. To investigate this, individual AZs of endbulb of Held synapses of pre-hearing (P10) and young hearing (P21) wt mice were analyzed. I analyzed parameters that describe the morphology of these AZs including their size (measured by the AZ area), and the number and size of SVs. Moreover, I evaluated the distribution of SVs with a specific focus on morphologically docked and membrane-proximal SVs. Most of the data obtained in this part is published in Hintze et al., 2021.

3.1.1 The density, size and distribution of synaptic vesicles are unaltered at endbulb of Held AZs

The morphological parameters assessed at individual endbulb AZs of P10 and P21 wt mice are visualized in Fig. 3.2A,B. As described in section 2.7.4, the AZ membrane was defined due to the visibility of the opposing PSD. I found that the reconstructed AZ areas were highly variable, but not different between the age groups (Fig. 3.2C). Surprisingly, the total number of SVs within 200 nm from the AZ membrane was just slightly, but not significantly higher after the onset of hearing (Fig. 3.2D; wt P10: 45.88 ± 4.25 SVs vs. wt P21: 54.09 ± 5.94 SVs; $p = 0.2608$). Since tomograms were generated from 250 nm semithin-sections, which do not include the whole endbulb AZ, I normalized the SV numbers to the respective AZ area within each tomogram and found that the SV densities (SV numbers per μm^2 AZ) were comparable between P10 and P21 (Fig. 3.2E). All details about values and statistics can be found in Table S1. Since both, the AZ area and the SV numbers are highly variable, I checked if there is a relationship between these parameters. However, the number of SVs did not correlate with the AZ area, neither for P10 nor for P21 endbulbs of Held (Fig. 3.2F; wt P10: $r = 0.3246$; $p = 0.1217$; wt P21: $r = 0.1937$; $p = 0.3878$, Spearman test). This finding is in line with a lack of correlation between SV number and AZ size in electron tomograms of cultured hippocampal

neurons (Siksou et al., 2007), but contrasts with studies of endbulbs in rats where the slope of the linear regression fit revealed a density of 144 SVs per μm^2 PSD area (Nicol and Walmsley, 2002).

In the classical model (see section 1.4), SV pools are determined via their distance to the AZ membrane, assuming that the distance correlates to the availability of a vesicle to fuse with the AZ membrane upon an incoming signal. This approach is commonly used in morphological studies of synapses (Fernández-Busnadiego et al., 2013; Imig et al., 2014; Maus et al., 2020; Sätzler et al., 2002; Thomas et al., 2019). To resolve the spatial distribution of SVs in membrane proximity, I used 5 nm bins (0-40 nm). For SVs farther from the AZ membrane, 40 nm bins were used (Fig. 3.2B,G). As shown in Fig. 3.2G, I found an accumulation of SVs near the AZ membrane (0-5 nm), although the SV density was comparable between P10 and P21. However, the SV density was significantly higher within 5-10 nm from the AZ membrane after the onset of hearing (Fig 3.2G; wt P10: 13.00 ± 3.04 SVs/ μm^2 vs. P21: 29.83 ± 6.18 SVs/ μm^2 , $**p = 0.0021$), while within 35 and 40 nm, the SV density was lower at P21 compared to P10 (Fig 3.2G; wt P10: 19.69 ± 3.00 SVs/ μm^2 vs. P21: 12.66 ± 2.94 SVs/ μm^2 , $*p = 0.0454$). The SV density within the other bins was not significantly affected upon maturation (Fig 3.2G). All values and statistics can be found in Table S1.

SV sizes have been shown to change upon synapse development and a wide range of SV diameters might argue for a defective SV formation or immaturity as shown e.g. for cochlear ribbon (Strenzke et al., 2016) and hippocampal (Imig et al., 2014) synapses as well as for *Drosophila* neuromuscular junctions (Stevens et al., 2012). Therefore, I measured the sizes of SVs and compared the mean diameters at individual AZs but did not find a significant change between P10 and P21 (Fig. 3.2H; Table S1).

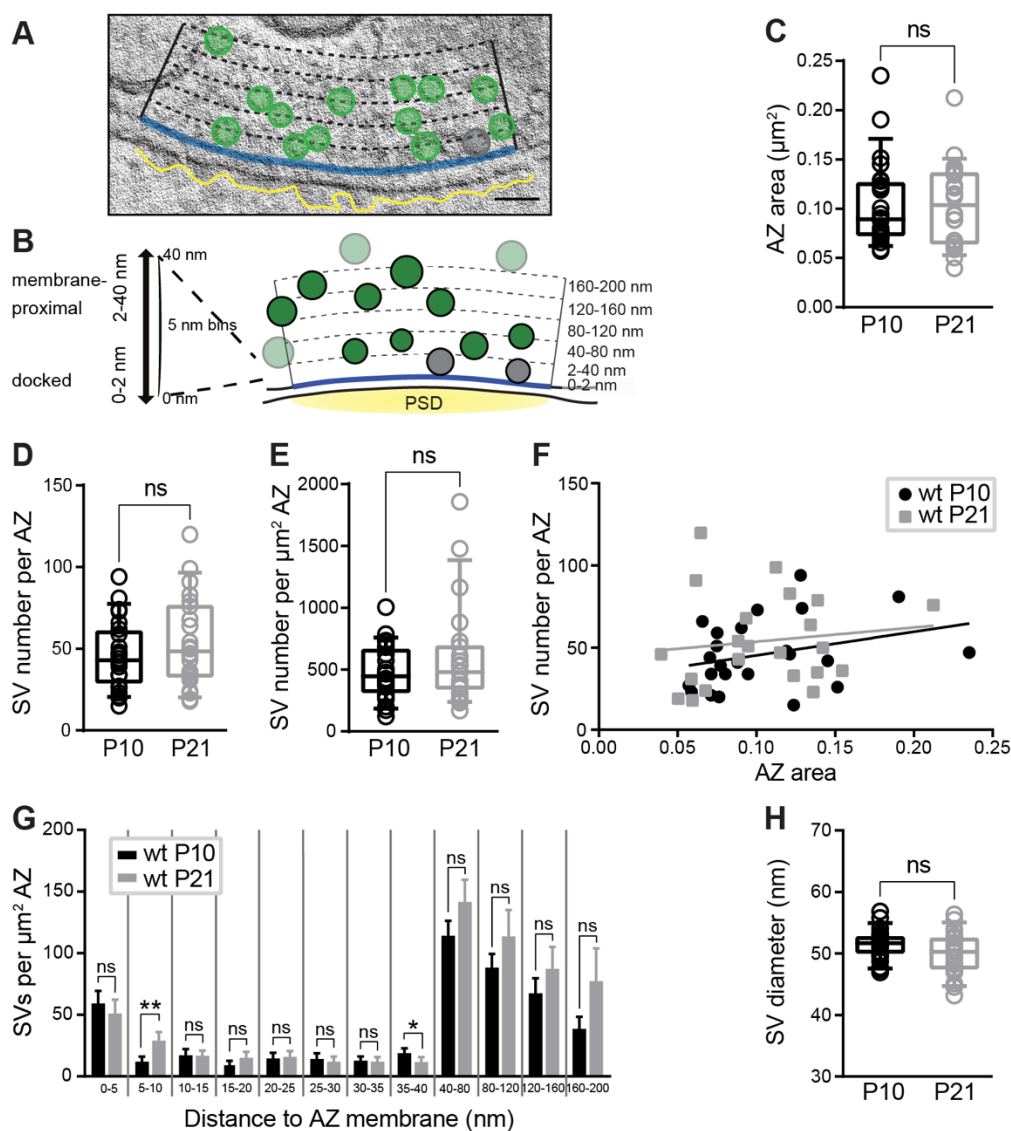


Figure 3.2: SV pools at endbulbs of Held remain unaltered upon maturation in wild-type.

(A) The segmentation of SVs (green) within 200 nm from the AZ membrane (blue) and docked SVs (gray) is shown on top of a virtual section of the tomogram of an endbulb AZ. The outline of the PSD is highlighted in yellow. Scale bar: 100 nm. (B) The scheme of an AZ depicts the bins used to analyze the distribution of SVs. SVs outside of this area (transparent green) were excluded. (A) and (B) are taken from Hintze et al., 2021. The data for the remaining panels are taken from Hintze et al. but were evaluated separately for this thesis. (C) The size of the AZ area does not change upon maturation from pre-hearing to young hearing mice. (D) The total number of SVs per AZ stays constant from P10 to P21. (E) Normalized to the size of AZ area, the SV number is unaltered upon maturation of endbulbs. (F) The number of SVs does not correlate to the AZ area neither at P10 nor at P21 (see text for details). The continuous line is the linear regression fit to the data. (G) The SV distribution at individual AZs reveals that the density of SVs within 5-10 nm from the AZ membrane is higher, while the density within 35 to 40 nm is lower after the onset of hearing. In all other bins, the SV density remains unaltered between the age groups. Data are presented as box and whisker plots that indicate median, lower/upper quartiles, 10–90th percentiles (C-F) or as bar graph that represent mean \pm SEM (G). (H) Upon maturation at wt endbulbs, the SV size, measured by their diameter does not change. ns, not significant; $*p < 0.05$; $**p < 0.01$. wt P10 ($N = 4$; $n = 24$) in black, wt P21 ($N = 3$; $n = 22$) in gray (N , number of animals; n , number of AZs). For all values and statistics, see Table S1.

3.1.2 Refinement of the SV pool

Analogous to previous studies performing HPF/FS and electron tomography (Imig et al., 2014; Maus et al., 2020; Watanabe et al., 2013), two sub-populations of SVs were analyzed separately, whose definitions are based on different properties of the SVs. (1) Morphologically docked SVs (0-2 nm from the presynaptic AZ membrane) reduce upon stimulation, as demonstrated for example in experiments that combined optogenetic stimulations with rapid freezing and electron tomography (Watanabe et al., 2013). They represent the morphological correlate of the RRP (see section 1.4; Schikorski & Stevens, 2001, Imig, 2014, reviewed in Kaeser & Regehr, 2017), and are in focus of research as a correlate for synapse strength (Murthy et al., 2001). (2) Membrane-proximal SVs (2-40 nm from the presynaptic AZ membrane) were identified as a specific population of SVs connected to the AZ membrane via a single long tether with a maximum length of 45 nm (Cole et al., 2016; Fernández-Busnadiego et al., 2010, 2013; Siksou et al., 2007, 2009).

3.1.2.1 The density of docked SVs is unaffected from the transition to hearing

First, I focused on morphological docked SVs (Fig. 3.3A). At wt endbulbs of Held, the total number of docked SVs (Fig. 3.3B) as well as their density (Fig. 3.3C) remained unaltered during maturation from pre-hearing to young hearing mice. The mean diameters of the docked SVs were comparable between P10 and P21 (Fig. 3.3D). The values and statistics can be found in Table S1. I generated top views of the tomogram models showing only the AZ membrane and docked SVs and found that docked SVs were located in the center, but also near the end of the reconstructed AZ membrane (Fig. 3.3E). Consistent with previous findings for rat endbulb AZs, the number of docked SVs was highly variable (between 0 and 14; Fig. 3.3B,F; Nicol & Walmsley, 2002). At P10, most endbulb AZs had two (26 %) to three (21 %) docked SVs, while the majority of AZs at P21 (around 27 %) showed zero docked SVs (Fig. 3.3F). However, the comparison of variances, done by Prof. Dr. Mehmet Gültas (Department of Animal Sciences, Georg-August University Göttingen) revealed no difference between the two age groups (Table S1; $p = 0.5117$; F -test).

Using serial sectioning, Nicol and Walmsley observed an excellent linear correlation of the number of docked SVs and the PSD area as well as of docked and undocked SVs and rat endbulb AZs (Nicol & Walmsley, 2002). Similar to the number of all SVs, the number of docked SVs did not scale with the area of the AZ in my study (Fig. 3.3G; P10: $r = 0.1006$; $p = 0.6400$; P21: $r = 0.0086$; $p = 0.9698$, Spearman test). However, the density of docked SVs correlated well with the density of all SVs within 200 nm from the AZ membrane (Fig. 3.3H; P10: $r = 0.7545$; **** $p < 0.0001$; P21: $r = 0.6690$; *** $p = 0.0007$, Spearman test), demonstrating that the density of docked SVs scaled to the overall SV density.

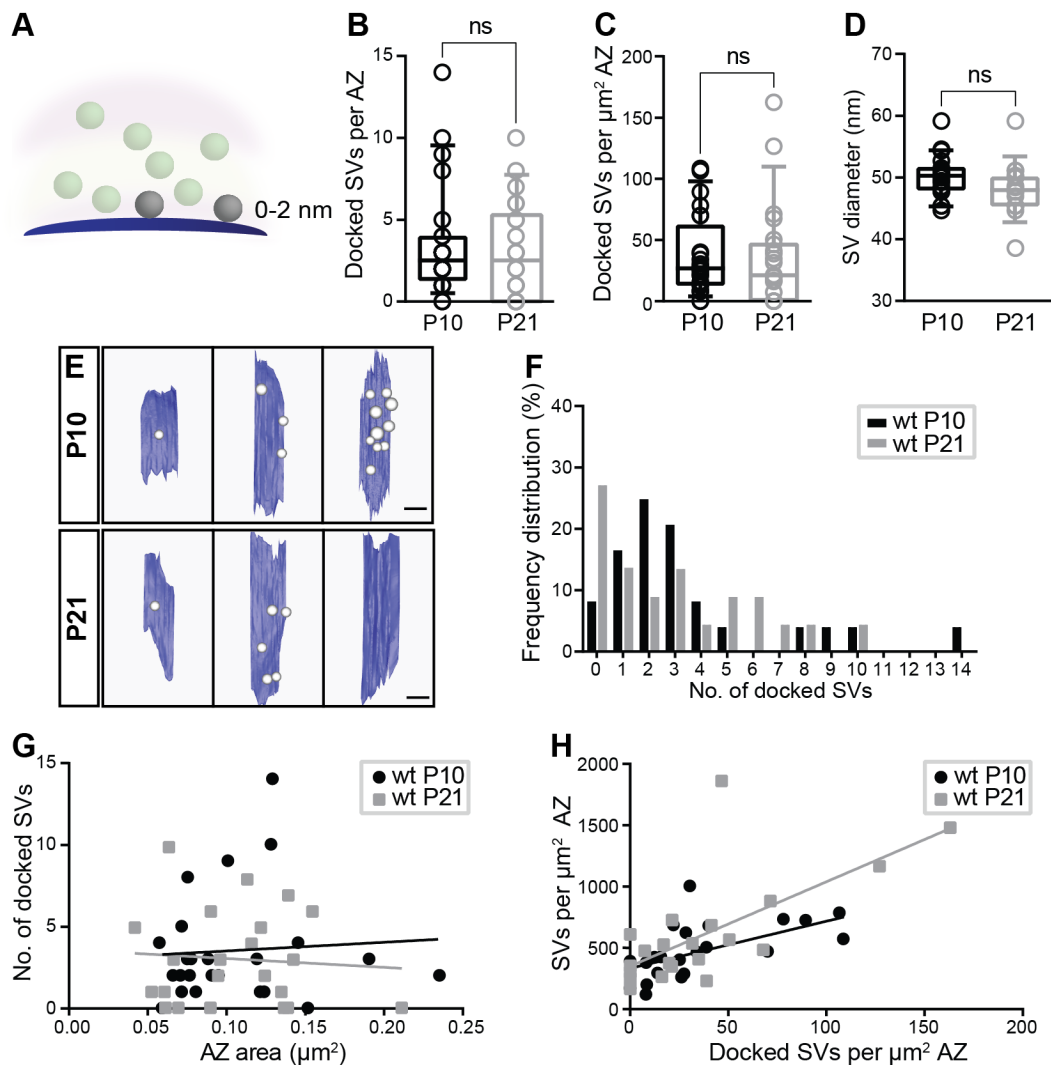


Figure 3.3: No difference in the number or density of morphologically docked SVs between P10 and P21.

(A) Scheme highlighting the morphologically docked SVs. **(B)** The number of docked SVs per AZ is comparable between P10 and P21. **(C)** The number of docked SVs normalized to the AZ area is similar before and after the hearing onset. **(D)** SV diameters are comparable between the groups. See also Table S1. Data are presented as box and whisker plots that indicate median, lower/upper quartiles, 10-90th percentiles. **(E)** Top views of representative tomogram models of endbulb AZ membranes with docked SVs from pre-hearing and young hearing mice. Scale bars: 100 nm. **(F)** Frequency distribution showing the number of docked SVs. **(G)** Plot showing that the number of docked SVs does not correlate with the AZ area. **(H)** The density of docked SVs correlates with the density of all SVs at the AZ (see text for details). The continuous line in **G** and **H** represents the linear regression fit to the data. **(A)** and **(E)** and the data for the graphs **(B-D)** and **(F-H)** are taken from Hintze et al., 2021 but were evaluated separately for this thesis. ns, not significant.

3.1.2.2 The pool of membrane-proximal synaptic vesicles is comparable between P10 and P21.

The membrane-proximal pool comprises SVs within 2-40 nm from the AZ membrane (Fig. 3.4A). Although I observed significant differences of SV numbers in some bins in membrane proximity (Fig. 3.2G), the overall number and density of the membrane-proximal SVs were comparable between P10 and P21 (Fig. 3.4B,C). Also, the mean diameters of these SVs were similar (Fig. 3.4D). All values and statistical details are listed in Table S1. According to the slight right shift in the frequency distribution in Fig 3.4E, it seems that more AZs contain more SVs within 2-40 nm at P21. However, the comparison of variances showed that there is no significant difference (Table S1; $p = 0.6716$; F -test).

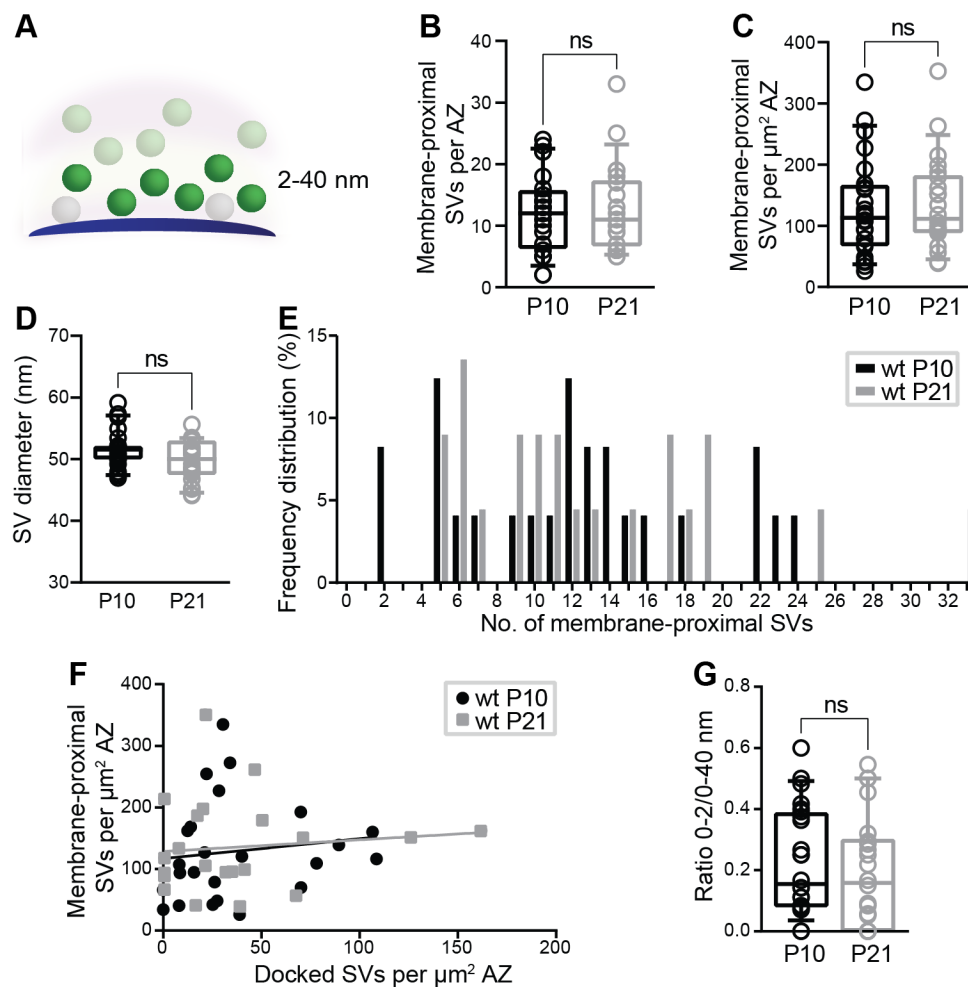


Figure 3.4: The size of the membrane-proximal SV pool is comparable between P10 and P21.

(A) Scheme highlighting the membrane-proximal SVs. (B) The number of membrane-proximal SVs per AZ is similar between P10 and P21. (C) The density of membrane-proximal SVs is comparable before and after the hearing onset. (D) SV diameters of this pool are comparable between the groups. See also Table S1. Data are presented as box and whisker plots that indicate median, lower/upper quartiles, 10-90th percentiles. (E) Frequency distribution showing the number of membrane-proximal SVs per AZ. (F) Plot showing that the density of docked SVs does not correlate with the density of membrane-proximal SVs (see text for details). The continuous line represents the linear regression fit to the data.

(Figure 3.4 continued): **(G)** The ratio of docked and membrane-proximal SVs is unaltered between the age groups. **(A)** and the data for the graphs **(B-G)** are taken from Hintze et al., 2021 but were evaluated separately for this thesis. ns, not significant.

Surprisingly, the density of docked and membrane-proximal SVs did not correlate (P10: $r = 0.3122$; $p = 0.1374$; P21: $r = 0.2230$; $p = 0.3185$, Spearman test) as shown in Fig. 3.4F, suggesting that SVs of the membrane-proximal pool did not form a simple substitute for the docked SVs, which fuse after arrival of an action potential. Furthermore, the ratio of docked and membrane-proximal SVs remained the same before and after the onset of hearing (Fig. 3.4G).

3.1.3 Summary

Although the onset of hearing is a substantial step in the maturation process where non-sensory spontaneous activity is refined towards sensory driven activity, this process is not reflected morphologically at individual endbulb of Held AZs. The AZ areas, the SV densities as well as the SV sizes of P10 and P21 mice were comparable. Also, the density of morphologically docked and membrane-proximal SVs did not change from P10 to P21. Only SVs within two specific distances in membrane proximity showed age-dependent changes. While the density of SVs within 5-10 nm from the AZ membrane increased upon hearing onset, the SV density within 35-40 nm decreased. I conclude that already shortly before the hearing onset, the early auditory system is well trained and prepared for the auditory input that the organization of endbulbs AZs can retain upon maturation. The SV density seems to be sufficient to pass on the signals reliably. The main findings of this part are illustrated in Fig. 3.5.

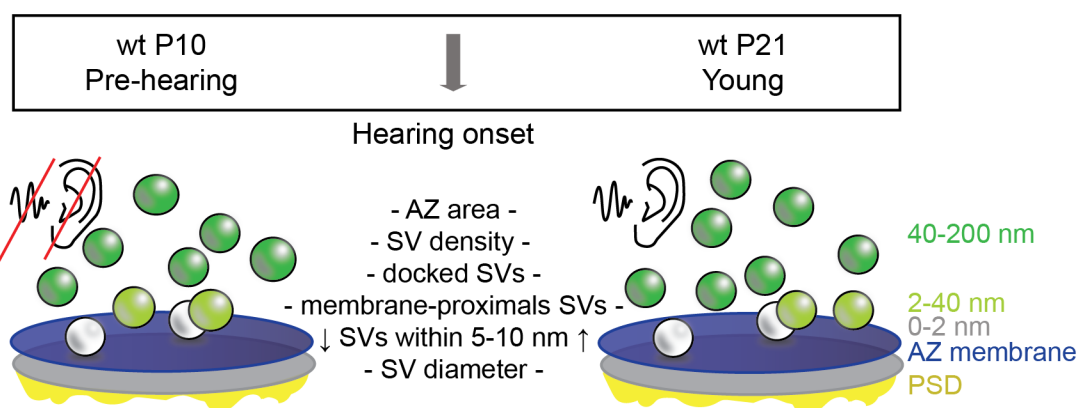


Figure 3.5: Endbulb of Held AZ organization in pre-hearing and young hearing wild-type mice.

3.2 Presynaptic mitochondria within the AVCN

In a second step, I questioned whether the maturation of the auditory system has broader effects on synapse attributes. The increase in neuronal activity during the transition from pre-hearing to hearing might come along with a higher energy demand, which could be manifested in ultrastructural changes of presynaptic mitochondria. This is part of a collaborative study with Dr. Felix Lange and Prof. Dr. Stefan Jakobs (Research Group Mitochondrial Structure and Dynamics, Max Planck Institute for Multidisciplinary Sciences).

As already described in section 1.5, it has been shown that in comparison to neurons with low activity, highly active neurons contain larger mitochondria with a higher crista membrane (CM) density and a more lamellar arrangement of the cristae, which is suggested to be beneficial for oxidative phosphorylation (Cogliati et al., 2013; Song et al., 2013). To date, it is not clear whether similar changes occur during hearing onset in the AVCN. Therefore, I used the samples from wt P10 and wt P21 mice prepared for the analysis of the AZs and recorded new tomograms at 8,000 to 12,000× magnification that allowed me to reconstruct mitochondria located in vicinity to endbulb AZs. In addition, I generated tomograms from other excitatory synapses within the AVCN to analyze if potential findings on ultrastructural changes of mitochondria are specific for endbulb of Held synapses or rather a general feature of the maturation process within the early auditory pathway. In addition to the comparison between P10 and P21 at endbulbs and smaller bouton-like terminal synapses that I termed non-endbulb synapses, I also compared the synapse types within the age groups.

3.2.1 Mitochondria are highly variable in size and shape

Mitochondrial networks at synapses are highly dynamic and can change depending on local needs. This includes changes in shape and size by fission and fusion as well as anchoring to specific positions or movements of mitochondria (Rube & van der Bliek, 2004).

My tomograms revealed that mitochondria were highly variable in their size and shape, especially in the endbulb terminals (Fig. 3.6). Here one needs to consider that with tomograms of 250 nm slices, only portions of mitochondria could be recorded instead of whole mitochondria. Therefore, changes in the shape might simply be a result of different cutting planes throughout the mitochondria. Nonetheless, with this method I collected data about the relation of the recorded mitochondrial volumes and their distance to the AZ membranes, questioning whether mitochondria are located closer to AZs after the onset of hearing. Therefore, I also reconstructed the corresponding AZ areas. For some of the mitochondria, I

was able to clearly identify and segment the single CMs. Crista junctions (Fig. 1.2) were not analyzed since I could only very rarely identify them with certainty.

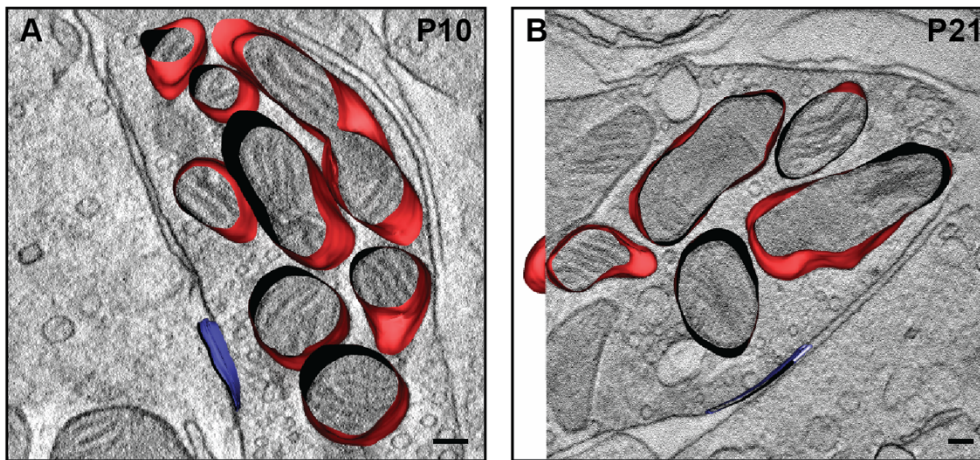


Figure 3.6: Mitochondria are variable in size and shape.

(A,B) 3D model with the z-view of a tomogram showing presynaptic mitochondria (red) within an endbulb terminal of a P10 (A) and a P21 (B) wt mouse. The AZ membrane is shown in blue. Both images show the diversity of mitochondrial sizes and shapes and illustrates that just a portion of the mitochondria can be analyzed with electron tomography of 250 nm slices. Scale bars: 100 nm.

3.2.2 Presynaptic mitochondria are larger after the onset of hearing at endbulbs of Held

First, I focused on presynaptic mitochondria within endbulb terminals and investigated their ultrastructure in P10 and P21 mice. The comparison of all reconstructed mitochondria (Fig. 3.7A,B) revealed that mitochondria had significantly larger volumes at endbulbs of young hearing mice compared to pre-hearing mice (Fig. 3.7C; eb P10: $5.18 \pm 0.30 \cdot 10^6 \text{ nm}^3$ vs. eb P21: $11.61 \pm 0.80 \cdot 10^6 \text{ nm}^3$; **** $p < 0.0001$). Consistent with the results in section 3.1, the AZ areas at endbulbs were comparable between the age groups (Fig. 3.7D). In a next step, I determined the mean shortest distance of the reconstructed mitochondria to the AZ. In calyx terminals, mitochondria were sometimes found to be arranged in mitochondrion-associated adherens complexes (MACs) and anchored to the plasma membrane on average 200 nm from synapses (Rowland et al., 2000). This complex formation was also described for endbulb terminals in chemically fixed tissue (Cant & Morest, 1979; Lauer et al., 2013; Tolbert & Morest, 1982b). In the high-pressure frozen tissue used in this study, the contrast is lower compared to chemically fixed tissue and the identification of MACs was not possible. However, a close distance of mitochondria to AZs could indicate their presence. A closer distance could further point to a higher and more reliable ATP supply that is particularly important to maintain SV release upon stimulation (Sun et al., 2013). The distances of mitochondria to the AZ membrane were highly variable in endbulb terminals but not significantly different between P10 and P21

mice (Fig. 3.7E). The surface area and density of CMs as well as a lamellar organization of cristae were shown to correlate with respiratory and ATP generating capacity of mitochondria (Cogliati et al., 2013; Song et al., 2013). Thus, changes in these parameters would indicate altered energy demands at AZs. Fig. 3.7F,G show higher magnifications of Fig. 3.7A,B with the reconstruction of CMs. Single CMs were not clearly identifiable in all segmented mitochondria. The subset of mitochondria with segmented CMs was separately analyzed to be able to relate their volume with the CM surface area. Despite the low number which I could include in this analysis, I still observed a significant increase in the volume after hearing onset (Fig 3.7H; eb P10: $5.97 \pm 0.60 \cdot 10^6 \text{ nm}^3$ vs. eb P21: $11.49 \pm 0.15 \cdot 10^6 \text{ nm}^3$; **** $p < 0.0001$). The surface area of the CMs was also significantly greater at endbulb mitochondria of the young hearing mice (Fig. 3.7I; eb P10: $0.19 \pm 0.02 \cdot 10^6 \text{ nm}^2$ vs. eb P21: $0.44 \pm 0.05 \cdot 10^6 \text{ nm}^2$; *** $p = 0.0001$). The ratio of CM surface area and mitochondrial volume, which represents the CM density increased significantly from P10 to P21 (Fig 3.7J; eb P10: 0.0313 ± 0.0018 vs. eb P21: 0.0362 ± 0.0015 ; * $p = 0.0123$). The crista shape factor (CM surface area/CM lumen volume) that describes the lamellarity of cristae appeared similar between P10 and P21 (Fig. 3.7K). Taken together, the increase in the surface area of CMs and their density indicate higher needs for mitochondrial functions at endbulb AZs after the hearing onset. However, the crista shape factor contrasts with these findings and indicates similar lamellar shapes of cristae before and after hearing onset. All values and statistics can be found in Table S2.

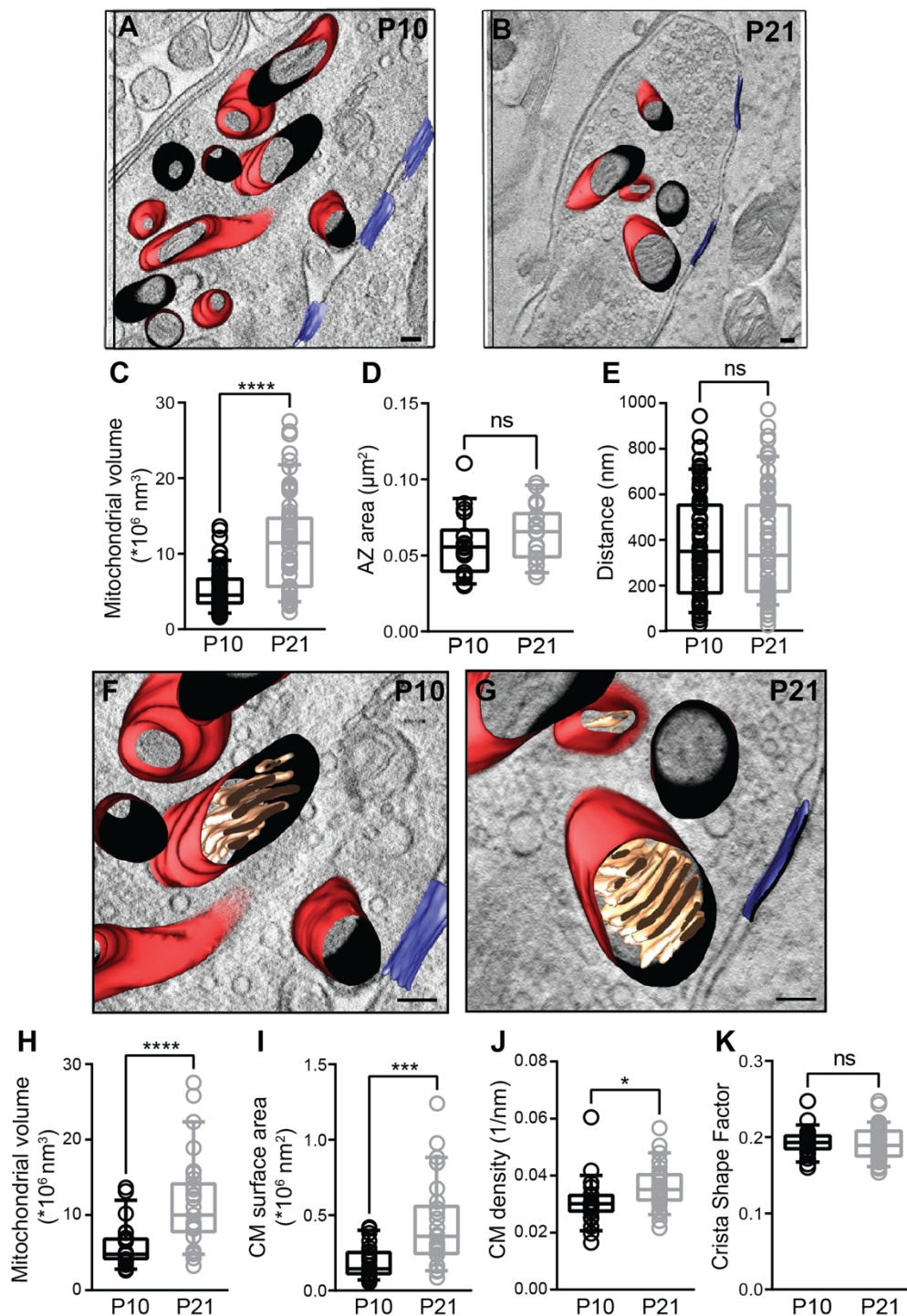


Figure 3.7: Mitochondrial ultrastructure changes upon maturation at endbulb synapses.

(A,B) 3D model with the z-view of a tomogram showing AZ membranes (blue) and presynaptic mitochondria (red) within an endbulb terminal of a P10 **(A)** and a P21 **(B)** wt mouse. Scale bars: 100 nm. **(C)** Comparing all mitochondria within the two groups, their reconstructed volume is larger after the onset of hearing. **(D)** The sizes of the AZ areas reconstructed in the tomograms are comparable between the age groups. **(E)** The shortest distance of the organelles to the AZ membrane is similar between endbulbs from P10 and P21 mice. **(F,G)** Higher magnifications of **(A)** and **(B)** showing examples of mitochondria in which the cristae could be reconstructed. Scale bars: 100 nm. **(H)** The volume of the mitochondria in which the CMs could be reconstructed is increased at endbulbs from P21 compared to P10 mice. **(I)** The sum of surface areas of CMs is larger after the onset of hearing. **(J)** The CM density (CM surface area/ mitochondrial volume) also increases upon maturation. **(K)** The crista

(Figure 3.7 continued): shape factor (CM surface area/CM lumen volume) indicates no difference in the organization of the cristae. Box and whisker plots present median, lower/upper quartiles, 10–90th percentiles. ns, not significant; * $p < 0.05$; *** $p < 0.001$, **** $p < 0.0001$. wt P10 ($N = 3$; $n = 82/23$) in black wt P21 ($N = 3$; $n = 65/29$) in gray. (N : number of animals; n : number of mitochondria (all/with segmentation of CMs)). For details about values and statistics, see Table S2.

3.2.3 Mitochondrial volumes increase at non-endbulb synapses from pre-hearing to young hearing mice

To understand if the findings on changes in mitochondrial structure are specific to endbulb terminals, I analyzed the same mitochondrial parameters in excitatory, non-endbulb terminals. Therefore, tomograms of bouton-like terminals contacting dendrites within the AVCN were recorded and AZs were identified based on the presence of a PSD (Fig. 3.8A,B). Larger volumes were found after the onset of hearing comparing all reconstructed mitochondria within these synaptic terminals (Fig 3.8C; syn P10: $7.74 \pm 0.81 \cdot 10^6 \text{ nm}^3$ vs. syn P21: $9.87 \pm 0.85 \cdot 10^6 \text{ nm}^3$; * $p = 0.0167$). Comparable to the results from endbulb synapses, the reconstructed AZ areas were similar between the age groups (Fig 3.8D). The shortest distance of mitochondria to the AZ membrane was also unchanged (Fig. 3.8E). Higher magnification of Fig. 3.8A,B are shown in Fig. 3.8F,G in which the CMs were segmented. With a lower number of mitochondria, the difference in mitochondrial volume did not reach statistical significance (Fig. 3.8H). Although I observed a significant increase in CM surface area during maturation at non-endbulb synapses (Fig 3.8I; syn P10: $0.23 \pm 0.03 \cdot 10^6 \text{ nm}^2$ vs. syn P21: $0.30 \pm 0.03 \cdot 10^6 \text{ nm}^2$; * $p = 0.0424$), the CM density was not significantly increased (Fig. 3.8J). The CMs of mitochondria of P10 synapses were found to be shaped similarly to those of P21 synapses as shown by the comparable crista shape factor (Fig. 3.8K). Taken together, mitochondria at non-endbulb synapses tended to increase in volume and had greater CM surface areas upon maturation. However, the effect was not as pronounced as in endbulb synapses. All values and statistical details can be found in Table S2.

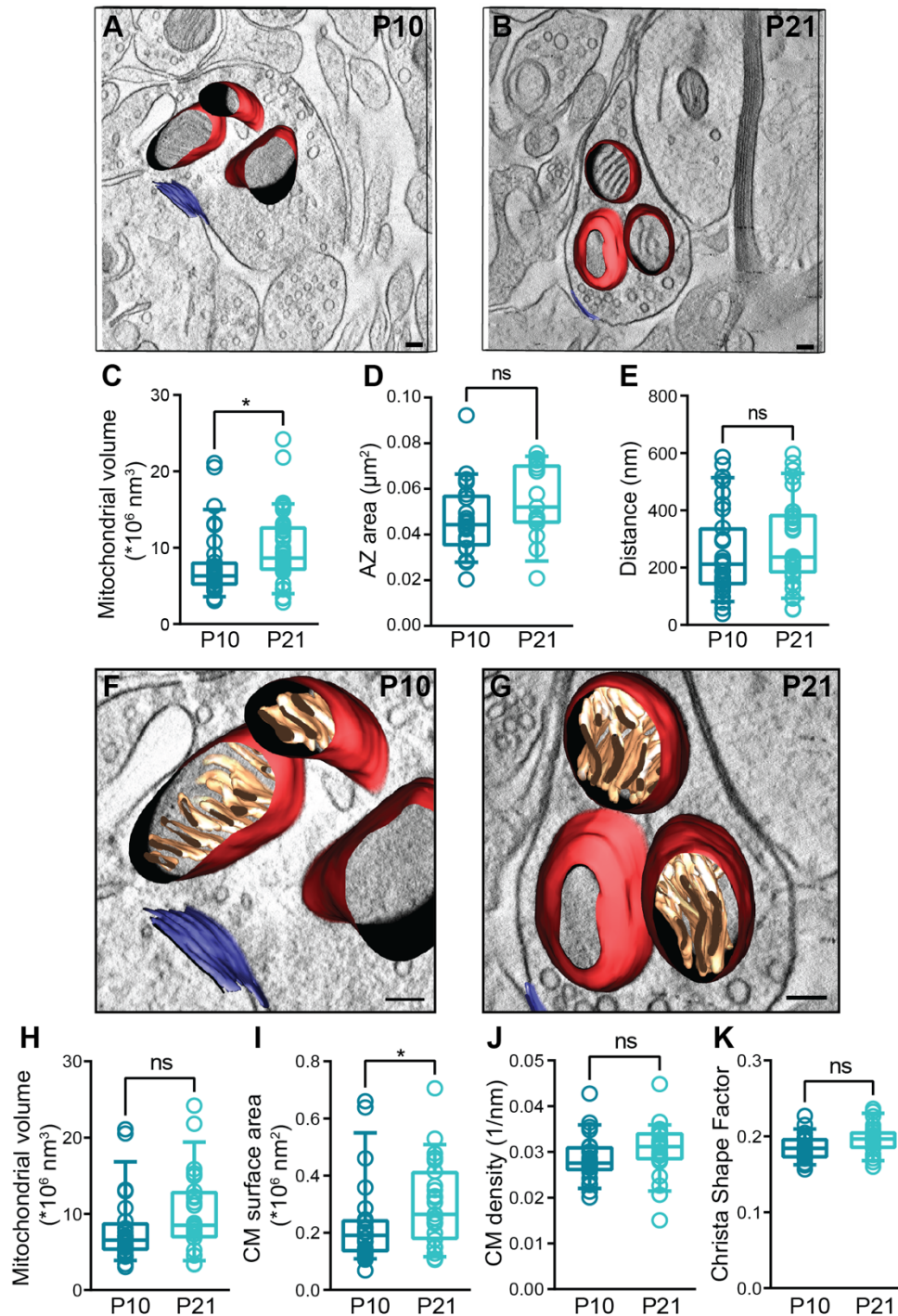


Figure 3.8: The ultrastructure of mitochondria at non-endbulb synapses is only slightly affected by maturation of the auditory system.

(A,B) 3D model showing the z-view of a tomogram to reveal AZ membranes (blue) and presynaptic mitochondria (red) within a non-endbulb terminal of a P10 (A) and a P21 (B) wt mouse. Scale bars: 100 nm. (C) The volumes of all analyzed mitochondria are larger at P21. (D) The reconstructed AZ areas are similar between the age groups. (E) The shortest distance of the mitochondria to the AZ membrane is the same between P10 and P21. (F,G) Higher magnifications of (A) and (B) showing examples of mitochondria in which the cristae could be reconstructed. Scale bars: 100 nm. (H) The volumes of this subset of mitochondria is not significantly different between the groups. (I) The sum of surface areas of the CMs is larger after the onset of hearing. (J) The CM density (CM surface area/ mitochondrial volume) is comparable between P10 and P21. (K) The lamellarity of the cristae is similar as verified by the crista shape factor (CM surface area/CM lumen volume). Box and whisker plots present median, lower/upper

(Figure 3.8 continued): quartiles, 10-90th percentiles. ns, not significant; * $p < 0.05$; wt P10 ($N = 3$; $n = 31/24$) in dark blue and wt P21 ($N = 3$; $n = 34/23$) in light blue. (N : number of animals; n : number of mitochondria (all/with segmentation of cristae)). For details about values and statistics, see Table S2.

3.2.4 Mitochondria are larger at non-endbulb synapses compared to endbulb AZs of P10 mice

In a last step, I compared mitochondrial parameters between endbulb synapses and non-endbulb synapses before and after the onset of hearing, taking the data from section 3.2.2 and 3.2.3. Interestingly, mitochondrial volumes were larger at non-endbulb synapses at the pre-hearing stage (Fig. 3.9A; eb P10: $5.18 \pm 0.30 \cdot 10^6 \text{ nm}^3$ vs. syn P10: $7.74 \pm 0.81 \cdot 10^6 \text{ nm}^3$; *** $p = 0.0007$). The AZs tended to be larger at endbulb terminals, but the difference did not reach statistical significance (Fig. 3.9B). The mean shortest distance of mitochondria to the AZ membrane was significantly higher at endbulbs compared to non-endbulb terminals (Fig. 3.9C; eb P10: $372.3 \pm 25.9 \text{ nm}$ vs. syn P10: $251.8 \pm 27.3 \text{ nm}$; ** $p = 0.0018$).

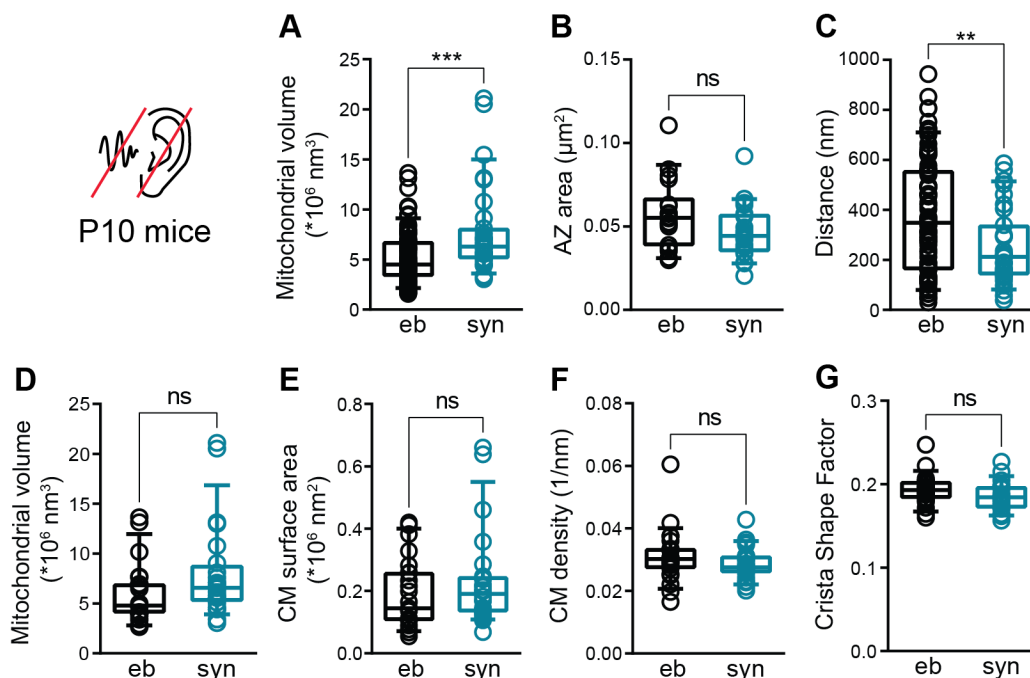


Figure 3.9: Mitochondria are larger at non-endbulb synapses compared to endbulbs at P10.

(A) Considering all analyzed mitochondria, their volumes are larger at non-endbulb synapses compared to endbulbs at pre-hearing mice. (B) The reconstructed AZ areas are similar between the synapse types. (C) The shortest distance of the mitochondria to the AZ membrane is higher at endbulb synapses. (D) The volume of the mitochondria in which the CM could be segmented, are not significantly different between endbulbs and non-endbulbs. (E) The sum of the CM surface areas is larger at mitochondria of non-endbulb synapses. (F) The CM density (CM surface area/mitochondrial volume) is comparable between the groups at the age of P10. (G) The crista shape factor (CM surface area/CM lumen volume) is the same between mitochondria of the two groups. Box and whisker plots present median, lower/upper quartiles, 10–90th percentiles. ns, not significant; ** $p < 0.01$; *** $p < 0.001$. Values and statistics see Table S2.

Comparing the volumes of the mitochondria where I was able to reliably segment the cristae, non-endbulb mitochondria still showed a trend to increased volumes, but the difference did not reach significance (Fig. 3.9D). The surface area of the cristae (Fig. 3.9E) as well as their density (Fig. 3.9F) was found to be comparable between endbulb and non-endbulb mitochondria at P10. The crista shape factor was also similar between the groups (Fig. 3.9G). All values and statistics are listed in Table S2.

3.2.5 Mitochondria at endbulb synapses display a higher crista membrane density after the onset of hearing

At P21 mice, mitochondrial volumes (Fig. 3.10A), AZ areas (Fig. 3.10B) and the shortest distance of mitochondria to the AZ membrane (Fig. 3.10C) were comparable at endbulb and non-endbulb terminals. The low number of mitochondria in which I was able to segment the CMs revealed similar volumes at endbulb and non-endbulb synapses (Fig. 3.10D), which is a sign for the robustness of these data. The CM surface area was also comparable between mitochondria in endbulb and non-endbulb mitochondria (Fig. 3.10E). However, the CM density was found to be significantly higher at mitochondria of endbulb terminals (Fig. 3.10F; eb P21: 0.0362 ± 0.0015 vs. syn P21: 0.0304 ± 0.0012 ; $**p=0.0046$). Finally, the crista shape factor revealed that the cristae were similar in their organization (Fig. 3.10G). All values and statistics can be found in Table S2.

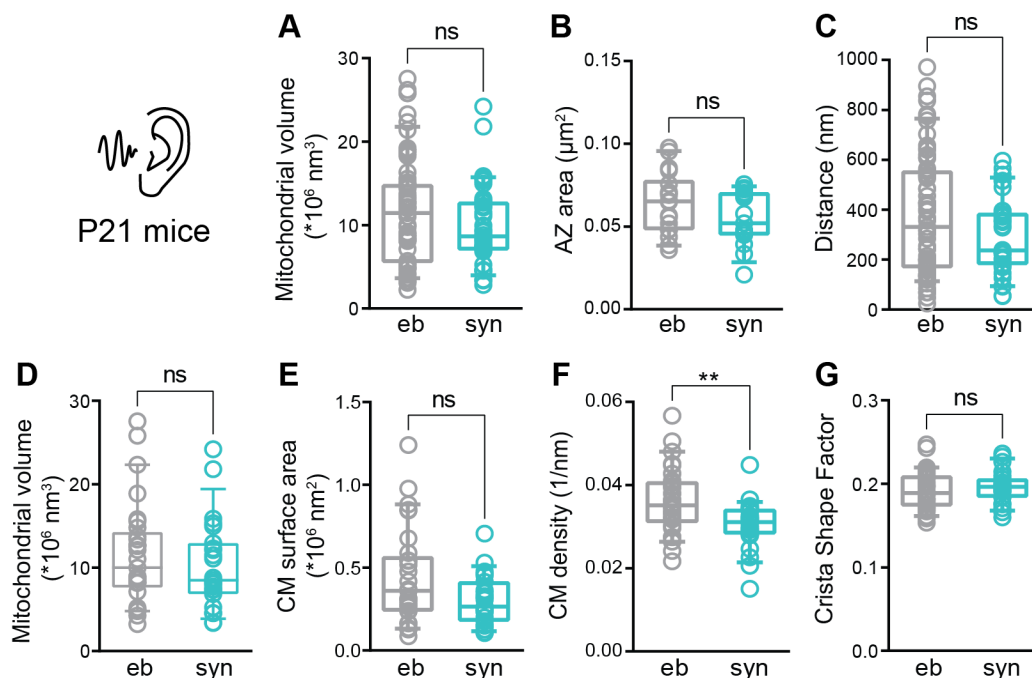


Figure 3.10: Mitochondria at endbulb terminals have a higher density of cristae compared to non-endbulb synapses at P21.

(A) Comparing all mitochondria analyzed in these groups, their volumes are comparable between the synapse types at P21. (B) The sizes of the reconstructed AZ areas are similar between endbulb and non-endbulb synapses. (C) The shortest distance of the mitochondria to the AZ membrane at endbulbs

(Figure 3.10 continued): is comparable to that of non-endbulb synapses. **(D)** The volumes of the mitochondria in which the CM could be segmented, are the same between endbulbs and non-endbulbs. **(E)** The sum of the CM surface areas is comparable between mitochondria of both groups. **(F)** The CM density (CM surface area/mitochondrial volume) is higher at mitochondria of endbulbs compared to that of mitochondria of non-endbulb synapses after the onset of hearing. **(G)** The crista shape factor (CM surface area/CM lumen volume) is the same between mitochondria of the two groups. Box and whisker plots present median, lower/upper quartiles, 10–90th percentiles. ns, not significant; ** $p < 0.01$. Values and statistics see Table S2.

3.2.6 Summary

The main findings of this part are summarized in Fig. 3.11. The reconstructed volumes of mitochondria at endbulb of Held synapses were considerably higher in young hearing mice compared to P10 mice. At non-endbulb synapses, a similar trend could be observed, but the effect was less pronounced. In the pre-hearing age, mitochondria were larger at non-endbulb synapses compared to endbulbs. However, the distinct developmental increase in mitochondrial volumes at endbulb terminals and the only slight increase at non-endbulb synapses resulted in comparable mitochondrial volumes at P21. Overall, the distances between mitochondria and AZ membrane were comparable between P10 and P21 at both, endbulb and non-endbulb synapses. However, the distances at non-endbulb synapses were significantly smaller at P10, which could be a result of the difference in the size of the terminal, since the endbulb terminals I took for analysis were considerably larger compared to the analyzed non-endbulb terminals. At P21, no difference in the distances was observed between the synapse types.

Consistent with the larger mitochondrial volumes after the onset of hearing, the surface area of cristae also increased during maturation at endbulb and non-endbulb synapses. The CM density was only increased at mitochondria of endbulb synapses. The surface area and density of CMs were comparable between the synapse types at P10, while the CM density was larger at mitochondria of endbulbs compared to non-endbulbs at P21 despite a comparable mitochondrial volume and CM surface area. These differences resulted from the pronounced increase in the surface area of cristae during maturation at endbulbs, whereas only a slight increase in the CM surface area was observed for mitochondria at non-endbulb synapses. Finally, the crista shape factor was found to be similar in all age groups, suggesting that the shape of CMs was not affected by the maturation process and comparable between mitochondria of different excitatory synapses within the AVCN.

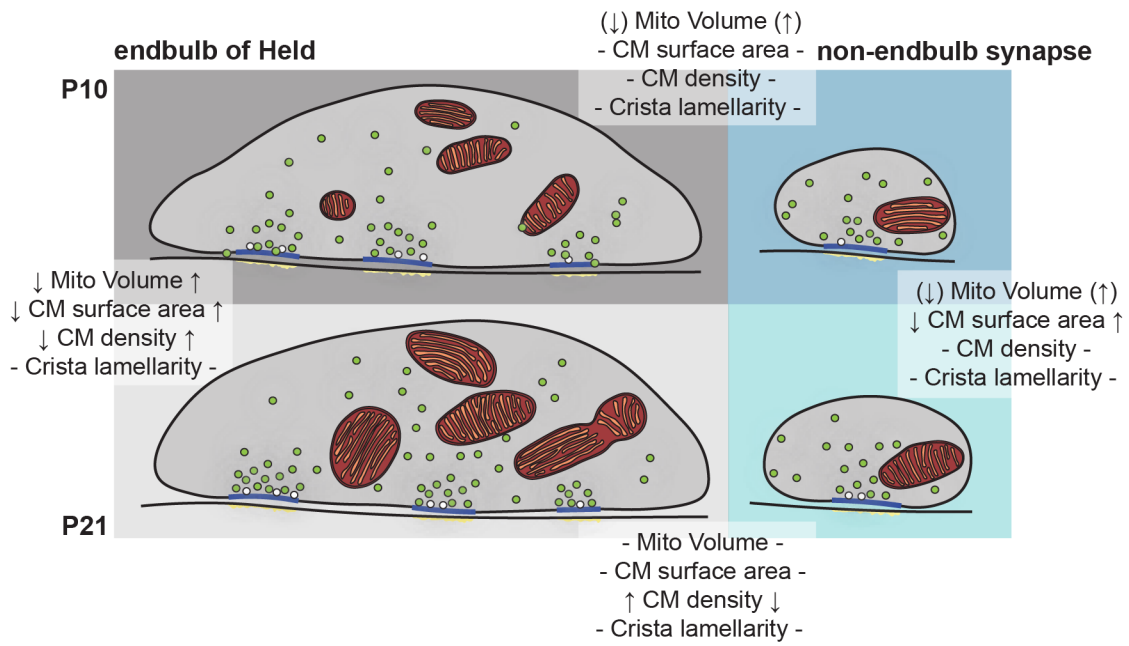


Figure 3.11: Changes of mitochondrial volume and CMs at endbulb and non-endbulb terminals upon maturation from pre-hearing to hearing.

3.3 Ultrastructural changes at endbulb active zones upon adulthood and lack of activity

While mitochondrial structure appears to change from P10 to P21, I could not observe structural changes in the SV pool organization between these ages as described in section 3.1. Functional maturation at murine BCs was described to be completed by P18 (Müller et al., 2019), but structural complexity was observed to increase until the eighth postnatal week (Limb & Ryugo, 2000). Therefore, I assumed that structural changes on the level of endbulb AZs might occur upon adulthood. To approach this question, I analyzed SV pools at individual endbulb of Held AZs of 6-months-old (6M) wt mice.

To understand the impact of neuronal activity on the endbulb of Held ultrastructure, I additionally determined the organization of individual AZs of congenitally deaf *Otof*^{-/-} mice that do not receive auditory input from ANFs. Exocytosis at ribbon synapses of these mice was presented to be almost depleted (Roux et al., 2006), but otoferlin as a molecular component is not required at endbulb synapses. However, *Otof* disruption in mice was described to result in smaller and less branched endbulbs compared to normal hearing mice (Wright et al., 2014). According to the data obtained from wt mice, I determined the same morphological parameters from *Otof*^{-/-} mice of different ages (Fig. 3.12A). Here, Esther A. Semmelhack contributed significantly in tomogram acquisition and analysis of the P10 and P22 *Otof*^{-/-} mice. The parameters were compared between the age groups of the two genotypes (wt P10 vs. wt P21 vs. wt 6M and *Otof*^{-/-} P10 vs. *Otof*^{-/-} P21 vs. *Otof*^{-/-} 6M) and between genotypes of the same age (wt P10 vs. *Otof*^{-/-} P10, wt P21 vs. *Otof*^{-/-} P22 and wt 6M vs. *Otof*^{-/-} 6M). The wt P10 and wt P21 data used in section 3.1 were reused for the comparisons in the following sections, as it was done in Hintze et al., 2021. Most of this part is published in Hintze et al., 2021, as individually indicated.

3.3.1 The synaptic vesicle pool increases during development of wild-type active zones

First, I focused on developmental changes in wt endbulbs. The reconstructed AZ membranes were equally sized, but it seemed that the variability between individual AZ areas decreased towards adulthood (Fig. 3.12B). As shown in section 3.1.1 and Fig. 3.2D, the total number of SVs within up to 200 nm away from the AZ membrane tend to increase slightly from P10 to P21 in wt. This tendency could further be observed towards adulthood. (Fig. 3.12C). After normalization to the respective AZ areas, a significant increase of the SV density could be observed comparing P10 and 6M wt endbulb AZs (Fig. 3.12D; wt P10: 477.4 ± 44.1 SVs/ μm^2 vs. wt 6M: 801.5 ± 65.7 SVs/ μm^2 ; ** $p = 0.0026$), indicating that morphological SV pool changes still proceed after hearing onset.

To determine the spatial distribution of SVs per AZ area, the same binning was used as in section 3.1.1 in order to subdivide the SV in different subpopulations. The accumulation of SVs within 5-10 nm from the AZ membrane that already increased from P10 to P21 was even more pronounced towards adulthood (Fig 3.12E; wt P10: 13.00 ± 3.04 SVs/ μm^2 ; wt 6M: 41.31 ± 5.71 SVs/ μm^2 , $**p = 0.0002$). In addition, the SV density within 10-15 nm increased significantly from P10 to 6M (Fig 3.12E; wt P10: 18.01 ± 4.17 SVs/ μm^2 ; wt 6M: 31.66 ± 3.85 SVs/ μm^2 , $*p = 0.0171$). The density of SVs within 80 to 200 nm away from the AZ membrane showed a steady rise towards adulthood as well (Fig 3.12E). This means that the overall increase in the SV density is mainly caused by SVs in membrane proximity and by SVs that are further away from the AZ membrane. All values and statistics can be found in Table S3.

3.3.2 Synaptic vesicle numbers decline in ageing *Otof*^{-/-} mice

In a next step, I compared the morphological parameters at individual endbulb AZs from congenitally deaf *Otof*^{-/-} mice throughout development. While the AZ areas were comparable between all age groups (Fig. 3.12B), the total number of SVs showed a slight increase from P10 to P21 but decreased significantly towards adulthood (Fig. 3.12C; *Otof*^{-/-} P22: 66.64 ± 8.73 SVs vs. *Otof*^{-/-} 6M: 39.61 ± 4.68 SVs, $*p = 0.0163$). Similar results were observed for the SV density (Fig. 3.12D). This reduction in the SV density is mainly resulted from SVs within 120-200 nm from the AZ membrane, since I observed a significant decrease of SVs within these distances between P22 and 6M mutant mice (Fig. 3.12E). Whereas SVs within 5-15 nm increased initially during the transition from P10 to P22, their density slightly decreased upon adulthood (Fig. 3.12E). All values and statistics are listed in Table S4.

3.3.3 Synaptic vesicle numbers are comparable between wild-type and mutant mice at young ages

The comparison of genotypes revealed that SV numbers and densities are similar at P10 and, surprisingly, also at P21/22, suggesting that the lack of auditory input did not affect these parameters at these early stages (Fig. 3.12C,D; Tables S5-S7). At adult wt and mutant mice, clear opposing effects could be observed that resulted in a strong decline of SV numbers and densities at AZs of 6M *Otof*^{-/-} mice compared to AZs of age-matched wt mice (Fig. 3.12C,D; wt 6M: 63.52 ± 5.63 SV vs. *Otof*^{-/-} 6M: 39.61 ± 4.68 SVs; $**p = 0.0020$ and wt 6M: 801.5 ± 65.7 SV/ μm^2 vs. *Otof*^{-/-} 6M: 431.3 ± 46.4 SVs/ μm^2 ; $****p < 0.0001$). Closer inspection of the SV pools showed that there were significant changes in the SV distribution comparing wt and *Otof*^{-/-} at the age of P10 (within 35-40 nm and 160-200 nm; Fig. 3.12E;

Table S5) and P21/22 (within 25-30 nm; Fig. 3.12E; Table S6). At 6 months of age, the decline of SV densities was made up by SVs in close membrane proximity (0-15 nm) and by SVs within 40-200 nm from the AZ membrane (Fig. 3.12E; Table S7).

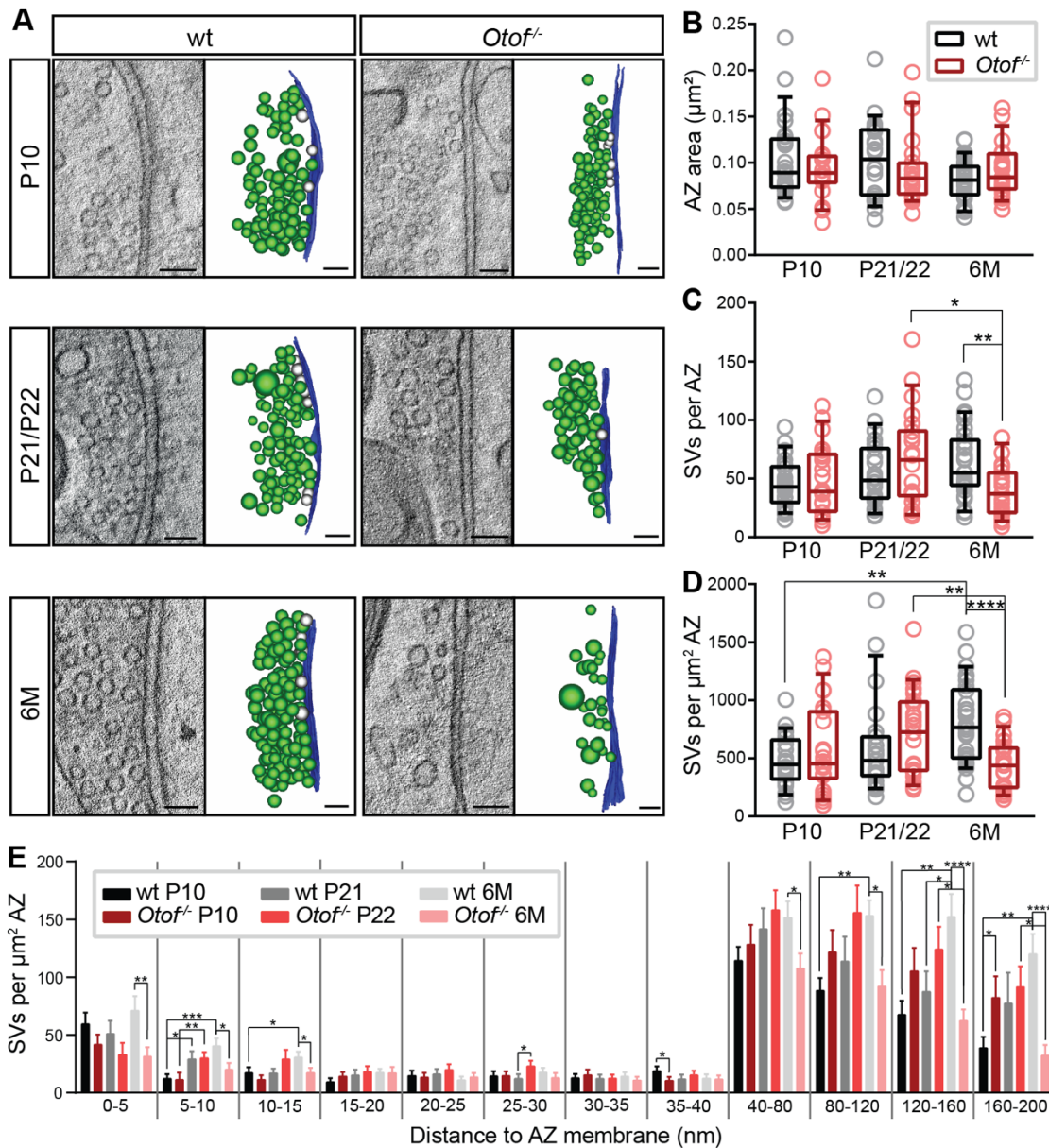


Figure 3.12: SV densities increase at wild-type and decline at *Otof*^{-/-} endbulb AZs upon adulthood.

(A) Single virtual sections and corresponding models of representative tomograms of AZs from P10, P21/22 and 6M wt and *Otof*^{-/-} mice showing the AZ membrane (blue), SVs (green), and morphologically docked SVs (gray). Scale bars: 100 nm. **(B)** AZ size determined by following the PSD extent in each tomogram is similar in all groups. **(C)** The number of SVs within 200 nm of the AZ membrane are reduced in 6M *Otof*^{-/-} mice compared to *Otof*^{-/-} P22 and wt 6M. **(D)** The density of SVs increases from wt P10 to wt 6M and is decreased at 6M *Otof*^{-/-} AZs compared to *Otof*^{-/-} P22 and wt 6M. **(E)** Graph showing the density of SVs divided into bins of 5 and 40 nm from the AZ membrane. Data are presented as box and whisker plots that indicate median, lower/upper quartiles, 10–90th percentiles (B-D) or as bar graph that represent mean ± SEM (E). ns, not significant; **p* < 0.05; ***p* < 0.01; ****p* < 0.001; *****p* < 0.0001. wt P10 (*N* = 4; *n* = 24), *Otof*^{-/-} P10 (*N* = 3; *n* = 22), wt P21 (*N* = 3; *n* = 22), *Otof*^{-/-} P22 (*N* = 3; *n* = 23), wt 6M (*N* = 3; *n* = 29) and *Otof*^{-/-} 6M (*N* = 3; *n* = 23), (*N*, number of animals; *n*, number of AZs). For all values and statistical details, see Tables S3-S7. Figure modified from Hintze et al., 2021.

In section 3.1.1, Fig. 3.2F, I already showed that the overall SV number did not correlate with the AZ area at wt endbulbs before and shortly after hearing onset. The same was true for wt 6M and *Otof*^{f/f} P10 AZs (Fig. S1; wt 6M: $r = 0.3023$; $p = 0.1108$; *Otof*^{f/f} P10: $r = 0.0300$; $p = 0.8947$), while at *Otof*^{f/f} P22 and *Otof*^{f/f} 6M endbulb AZs, the SV number correlated with the size of the AZ, indicated by a p -value < 0.05 (Fig. S1; *Otof*^{f/f} P22: $r = 0.5599$; $**p = 0.0067$; *Otof*^{f/f} 6M: $r = 0.4658$; $*p = 0.0251$; Spearman test).

3.3.4 Active zones of adult *Otof*^{f/f} endbulbs contain less morphologically docked synaptic vesicles

As in wt, I analyzed the morphologically docked (Fig. 3.13A) and membrane-proximal SVs (Fig. 3.14A) separately in order to compare their number and distribution with the wt condition. Even though *otof*erlin is not expressed at endbulb AZs, the lack of auditory input might cause degenerative or compensatory changes, such as adaptation of SV numbers at endbulbs. The lack of activity might specifically influence docked and membrane-proximal SVs. However, the number of docked SVs remained constant during development at both, wt and mutant AZs (Fig. 3.13B), which could also be observed after normalization to the AZ area (Fig. 3.13C). Comparing genotypes, the number and density of docked SVs was significantly lower at adult *Otof*^{f/f} AZs compared to wt (Fig. 3.13B,C; Table S7; wt 6M: 2.97 ± 0.51 SV vs. *Otof*^{f/f} 6M: 1.83 ± 0.56 SVs; $*p = 0.0379$ and wt 6M: 37.00 ± 7.15 SV/ μm^2 vs. *Otof*^{f/f} 6M: 22.06 ± 6.95 SVs/ μm^2 ; $*p = 0.0317$). All values and statistics can be found in Tables S3-S7. Consistent with the observations made in the first part, also at wt 6M as well as at the mutant AZs, the number of docked SVs was highly variable. At *Otof*^{f/f} P22 e.g., their number ranged from zero to 16. (Fig. 3.13B,D). However, most AZs of wt and *Otof*^{f/f} endbulbs of all age groups contained zero to three docked SVs (Fig. 3.13D) as also shown in representative AZ top-views of 3D models (Fig. 3.13E). The variances of the number of docked SVs were not significantly different for any of the comparisons, suggesting that the frequency distribution is similar in all groups (Table S8).

The number of docked SVs did not correlate with the sizes of AZ at all ages of both genotypes (Fig. S2). As reported in section 3.1.2.1, Fig. 3.3H, the density of docked SVs was found to correlate well with the density of all SVs within 200 nm from the AZ membrane at wt P10 and wt P21 AZs. The same was found for wt 6M and *Otof*^{f/f} AZ of all ages (Fig. S3; wt 6M: $r = 0.6158$; $***p = 0.0004$; *Otof*^{f/f} P10: $r = 0.7622$; $****p < 0.0001$; *Otof*^{f/f} P22: $r = 0.4880$; $*p = 0.0182$; *Otof*^{f/f} 6M: $r = 0.5993$; $**p = 0.0025$; Spearman test). This linear relationship indicates that the docked SV density scales the density of SVs within 200 nm in all groups.

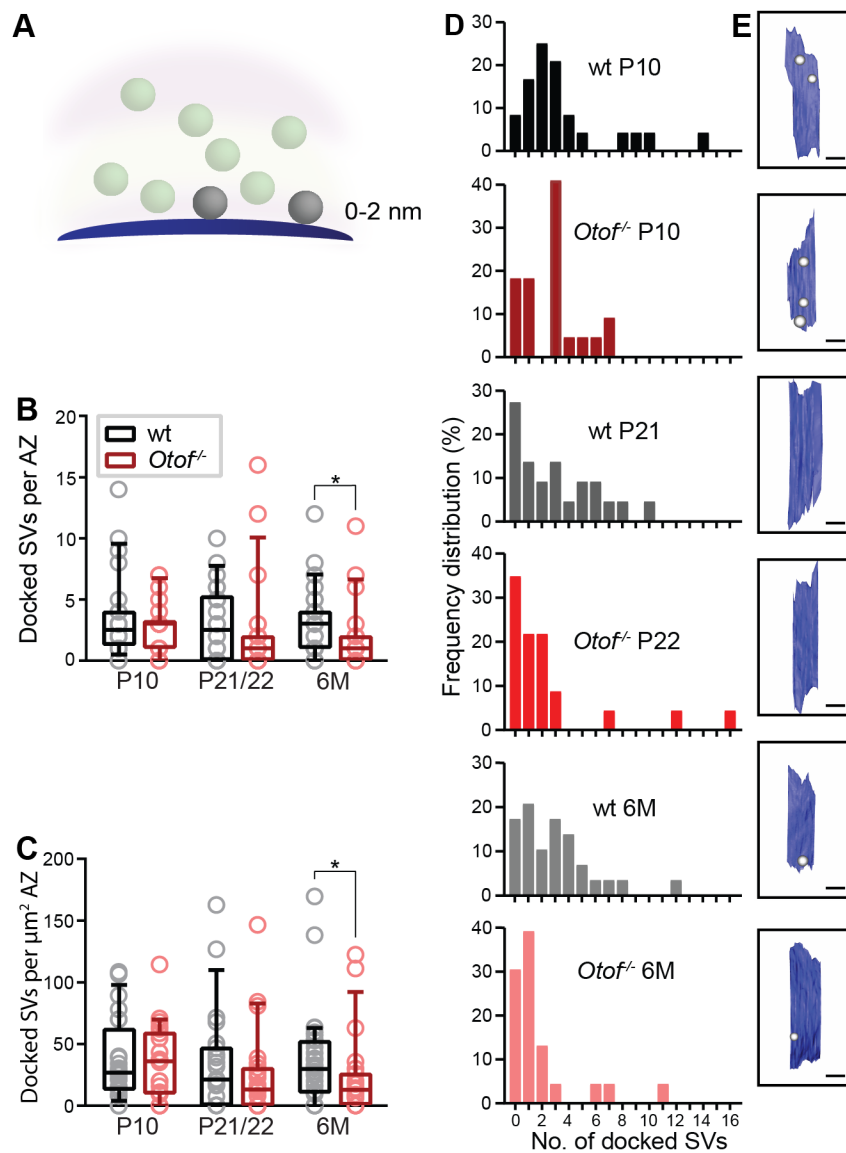


Figure 3.13: Number and density of docked SVs is lower at *Otof*^{-/-} AZs compared to wild-type of adult mice.

(A) Scheme highlighting the docked SVs. **(B)** The total number of docked SVs per AZ is lower at 6M *Otof*^{-/-} compared to 6M wt. **(C)** The density of docked SVs also differs between wt and *Otof*^{-/-} at 6 months of age. Data are presented as box and whisker plots that indicate median, lower/upper quartiles, 10-90th percentiles. Values and statistics see Table S3-S7. **(D)** Histograms showing the relative frequency of AZs with 0 to 16 docked SVs at wt P10, P21 and 6M as well as at *Otof*^{-/-} P10, P22 and 6M AZs. **(E)** Top views of representative 3D models of AZ membranes with their most frequently number of docked SVs. Scale bars: 100 nm. ns, not significant; * $p < 0.05$. Figure modified from Hintze et al., 2021.

3.3.5 The density of membrane-proximal vesicles initially increases but declines towards adulthood at *Otof*^{-/-} active zones

The total number of membrane-proximal SVs was comparable between the age groups at AZs of wt endbulbs (Fig. 3.14B, Table S3). Normalized to the AZ area, their number increased significantly from P10 to 6M (Fig. 3.14C; wt P10: 128.5 ± 16.6 SVs/ μm^2 vs. wt 6M: 184.1 ± 13.4 SVs/ μm^2 ; * $p = 0.0266$). At *Otof*^{-/-} AZs, the total number and density of membrane-proximal SVs increased from P10 to P22 (Fig. 3.14B,C, Table S4; *Otof*^{-/-} P10: 8.86 ± 1.13 SVs vs. *Otof*^{-/-} P22: 15.39 ± 2.11 SVs; * $p = 0.0104$ and *Otof*^{-/-} P10: 103.8 ± 14.6 SVs/ μm^2 vs. *Otof*^{-/-} P22: 162.9 ± 14.6 SVs/ μm^2 ; ** $p = 0.0081$), while the density decreased upon further development (Fig. 3.14C; *Otof*^{-/-} P22: 162.9 ± 14.6 SVs/ μm^2 vs. *Otof*^{-/-} 6M: 117.5 ± 10.8 SVs/ μm^2 ; * $p = 0.0490$). Comparing both genotypes, significantly fewer SVs within 2-40 nm per μm^2 AZ were observed at 6M *Otof*^{-/-} endbulb AZs compared to age-matched wt (Fig. 3.14C, Table S7; wt 6M: 184.1 ± 13.4 SVs/ μm^2 vs. *Otof*^{-/-} 6M: 117.5 ± 10.8 SVs/ μm^2 ; *** $p = 0.0003$). The ratio of docked and membrane-proximal SVs of wt synapses appeared to be independent of maturation, while the ratio declined during the transition from P10 and P22 at *Otof*^{-/-} AZs with no further decrease upon adulthood (Fig. 3.14D, Table S3; *Otof*^{-/-} P10: 0.23 ± 0.03 vs. *Otof*^{-/-} P22: 0.11 ± 0.03 ; * $p = 0.0168$ and *Otof*^{-/-} P10: 0.23 ± 0.03 vs. *Otof*^{-/-} 6M: 0.12 ± 0.03 ; * $p = 0.0308$). All values and statistics can be found in Table S3-S7. The frequency distribution showed that wt histograms were shifted slightly to the right indicating that the number of AZs containing a higher number of membrane-proximal SVs increased upon development (Fig. 3.14E), which is in line with the increase of this SV subpopulation during development to adulthood at endbulb AZs of wt mice. This shift was not visible in the histograms for the *Otof*^{-/-} AZs (Fig. 3.14E). The comparison of the variances revealed a significantly broader distribution of membrane-proximal SVs in *Otof*^{-/-} P22 compared to P10 and 6M (Table S8). One reason for this significant difference could be the high variability of the SV count in this group with some AZs containing more than 25 membrane-proximal SVs, whereas none of the other *Otof*^{-/-} groups contained more than 22 SVs within this subpopulation (Fig. 3.14E).

As shown in section 3.1.2.2, Fig. 3.4F, the density of docked SVs did not correlate with the density of membrane-proximal SVs at wt P10 and wt P21 AZs. The same was observed for wt 6M synapses (Fig. S4). In contrast, the densities of the two SV pools showed a correlation at AZs of mutant endbulbs of all ages, which might indicate a simple scaling in the number of docked and membrane-proximal SVs (Fig. S4: *Otof*^{-/-} P10: $r = 0.5125$; * $p = 0.0147$; *Otof*^{-/-} P22: $r = 0.4285$; * $p = 0.0414$; *Otof*^{-/-} 6M: $r = 0.4580$; * $p = 0.0280$; Spearman test).

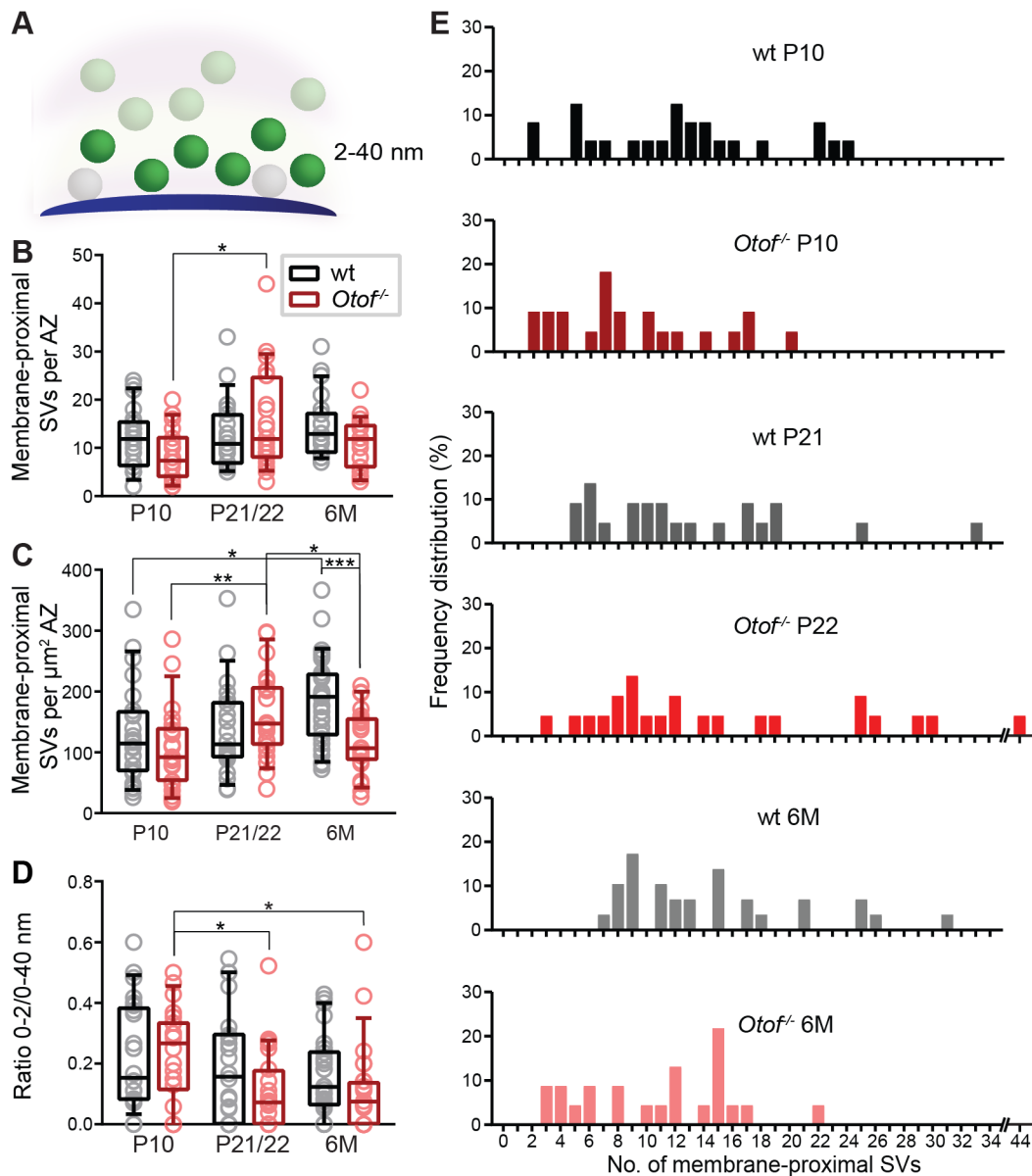


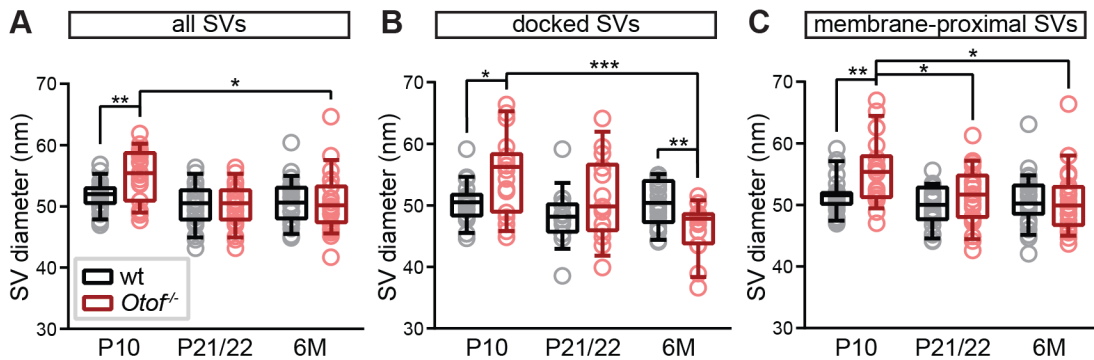
Figure 3.14: The density of membrane-proximal SVs is lower at adult *Otof*^{-/-} endbulb AZs compared to wild-type.

(A) Scheme highlighting the membrane-proximal SVs. **(B)** The number of membrane-proximal SVs per AZ increases during maturation of *Otof*^{-/-} endbulb AZs. **(C)** The density of SVs within 2-40 nm from the AZ membrane increases during development of wt endbulb synapses while it decreases at *Otof*^{-/-} AZs from P22 to 6M. **(D)** The ratio of docked and membrane-proximal SVs decreases at *Otof*^{-/-} AZs. Data are presented as box and whisker plots that indicate median, lower/upper quartiles, 10–90th percentiles. Values and statistics see Tables S3-S7. **(E)** Histograms showing the relative frequency of AZs with 0 to 44 SVs within 2-40 nm at wt and *Otof*^{-/-} of all ages. ns, not significant; * $p < 0.05$; ** $p < 0.01$; *** $p < 0.001$. Figure modified from Hintze et al., 2021.

3.3.6 Sizes of synaptic vesicles decrease during development at *Otof*^{-/-} endbulb active zones

At wt endbulbs of Held, an increase in SV sizes has been shown from P20 to P44 (Antunes 2020) and in mice with conductive hearing loss, SVs appeared smaller compared to hearing

controls (Clarkson et al., 2016). Therefore, I compared SV diameters in both genotypes and all age groups (Fig. 3.15, Tables S3-S7). For statistical analysis, I averaged the SV diameters per AZ and compared the means (Fig. 3.15). For visualizing the frequency distribution of SV sizes, the individual SV diameters were divided into 5 nm bins (Fig. S5-S7).



(A) The mean diameters of all SVs decrease in *Otof*^{-/-} mice from P10 to 6M. At P10, SVs are bigger at *Otof*^{-/-} AZs than at wt AZs. (B) Docked SVs are bigger at *Otof*^{-/-} AZs at P10 but smaller at 6 months of age compared to wt. (C) Membrane-proximal SVs are bigger at *Otof*^{-/-} AZs than at wt AZs but decrease with age. The distributions of SV diameters of all groups are shown in Fig. S5-S7. For all values and statistical details, see Tables S3-S7. Data are presented as box and whisker plots that indicate median, lower/upper quartiles, 10–90th percentiles. ns, not significant; * $p < 0.05$; ** $p < 0.01$; *** $p < 0.001$. Figure modified from Hintze et al., 2021.

In contrast to the findings from Antunes et al., SVs in this study appeared to be equally sized during development of wt mice (Fig. 3.15A). However, the development of *Otof*^{-/-} endbulb AZs was accompanied by a decrease of SV diameters (Fig. 3.15A, Table S4; *Otof*^{-/-} P10: 54.87 ± 0.90 nm vs. *Otof*^{-/-} 6M: 50.63 ± 1.03 ; * $p = 0.0128$). A separate analysis of docked and membrane-proximal SVs revealed that this decrease appeared in both populations, but the docked SVs showed the strongest effect (Fig. 3.15B; *Otof*^{-/-} P10: 54.99 ± 1.52 nm vs. *Otof*^{-/-} 6M: 46.23 ± 1.03 ; *** $p = 0.0003$). When comparing both genotypes, significantly larger SVs were found at *Otof*^{-/-} P10 compared to age-matched wt (Fig. 3.15A, Table S5; wt P10: 51.46 ± 0.50 nm vs. *Otof*^{-/-} P10: 54.87 ± 0.90 nm; ** $p = 0.0022$). Again, this change could be shown for both analyzed SV populations (Fig. 3.15B,C). Finally, at 6 months of age, docked SVs at *Otof*^{-/-} endbulb AZs were significantly smaller compared to wt (Fig. 3.15B, Table S7; wt 6M: 50.29 ± 0.76 nm vs. *Otof*^{-/-} 6M: 46.23 ± 1.03 ; ** $p = 0.0035$). The frequency distributions of the individual SV diameters are shown in Fig. S5-S7. In addition to the histograms showing all groups, the single comparisons with a significantly different mean diameter are shown. These graphs show that not just the mean of the averaged diameters per AZ was different, but also the graphs representing all diameters were shifted towards larger or smaller SVs.

3.3.7 Summary

Development of wt and *Otof*^{-/-} endbulb AZs is accompanied by changes in SV densities. Whereas the maturation from pre-hearing to young hearing did not affect the SV pools (section 3.1), the development to adulthood result in an increase of the SV density. Specifically, a subpopulation of the membrane-proximal SVs within 5 to 15 nm from the AZ membrane increased noticeably. In addition, SVs 80 to 200 nm away from the membrane showed a distinct increase in their density. At *Otof*^{-/-} AZ, the transition from P10 to P22 resulted in a slight increase of the SV density that mainly resulted from SVs within 5-20 nm from the AZ membrane. Upon adulthood, the overall SV density, but mainly within 120-200 nm clearly decreased. The opposite effects lead to the drastic ultrastructural differences between adult mutant AZs compared to age-matched wt, that also includes the density of docked SVs. Finally, SV sizes were not affected by developmental maturation of wt AZs, while SV diameters, especially of the docked SVs decreased at *Otof*^{-/-} AZs. I can conclude that the lack of auditory input does not influence the ultrastructure of individual endbulb AZs of young mice, but the morphological SV pools in adult animals are strikingly altered. The main findings are illustrated in Fig. 3.16.

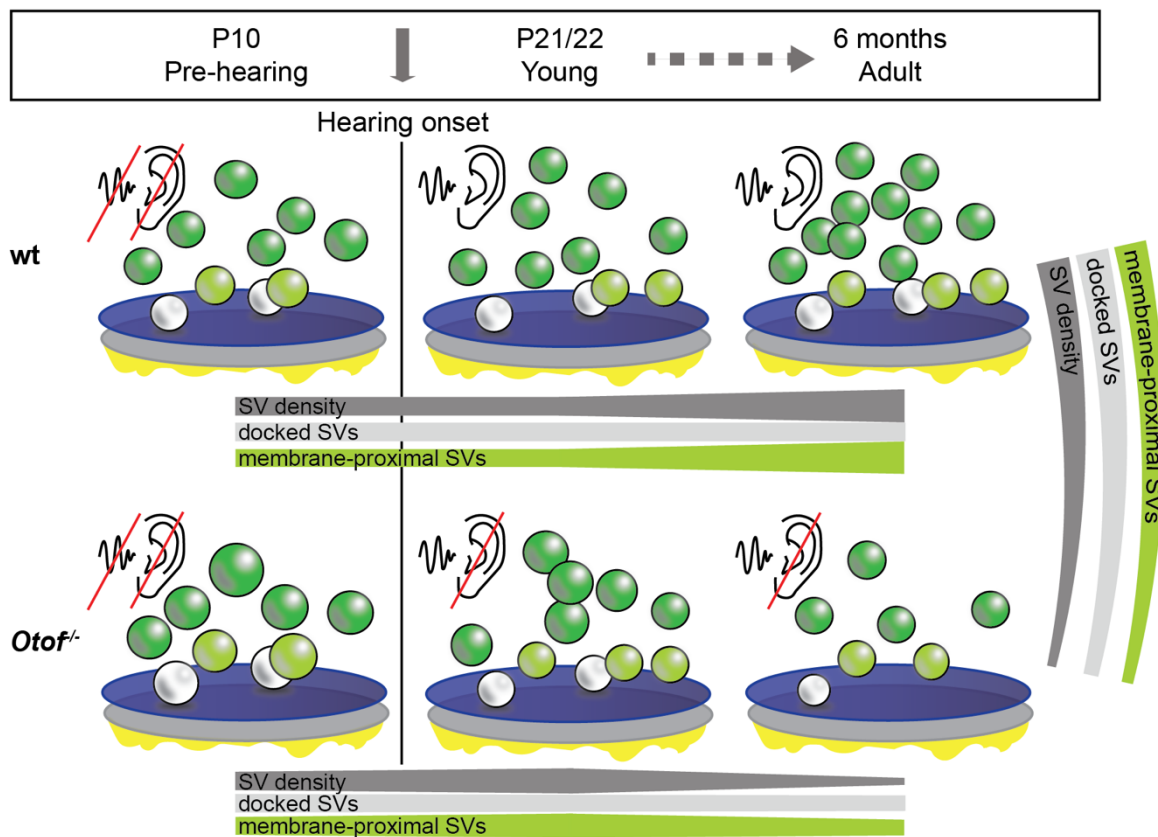


Figure 3.16: SV pool changes upon development and lack of auditory input.

3.4 *RIM-BP2* disruption alters the vesicle organization at endbulb active zones

Besides developmental maturation and activity changes, also the lack of presynaptic proteins could impact the SV pools at endbulb AZs. As described in section 1.3, a plethora of presynaptic proteins is involved in the structural organization of AZs as well as in SV exocytosis and endocytosis. The role of some of these proteins, including piccolo (Butola et al., 2017) and bassoon (Mendoza Schulz et al., 2014) on endbulb AZs were already investigated. This part of the thesis aims to characterize the role of RIM-BP2 on the organization of endbulb AZs of P22 mice. Together with Theoharis Alvanos (Institute for Auditory Neuroscience, University Medical Center Göttingen), I performed HPF/FS of freshly sliced AVCN of *RIM-BP2*-deficient (*RIM-BP2*^{-/-}) mice and their wt littermates. According to the parts before, electron tomography was used to obtain the morphological parameters. This part of the thesis is published in Butola et al., 2021.

3.4.1 *RIM-BP2*^{-/-} endbulb active zones exhibit a different distribution of synaptic vesicles compared to wild-type

Electron tomograms and 3D reconstruction (Fig. 3.17A) revealed significantly larger AZ areas in *RIM-BP2*^{-/-} endbulbs (Fig. 3.17B; wt: $0.0820 \pm 0.0052 \mu\text{m}^2$ vs. *RIM-BP2*^{-/-}: $0.1031 \pm 0.0039 \mu\text{m}^2$; ** $p = 0.0022$). The number (Fig. 3.17C) and density (Fig. 3.17D) of SVs per AZ were similar between the genotypes. To determine the spatial distribution of SVs within 200 nm from the AZ membrane, a 20 nm binning was used. Docked SVs (0 to 2 nm distance) were analyzed separately and showed a significantly lower density at *RIM-BP2*^{-/-} AZs (Fig. 3.17E; wt: $27.52 \pm 5.24 \text{ SVs}/\mu\text{m}^2$ vs. *RIM-BP2*^{-/-}: $14.64 \pm 4.77 \text{ SVs}/\mu\text{m}^2$; * $p = 0.0152$). A significantly lower SV density was also found for SVs within 2 to 20 nm (Fig. 3.17E; wt: $109.1 \pm 12.8 \text{ SVs}/\mu\text{m}^2$ vs. *RIM-BP2*^{-/-}: $68.16 \pm 9.22 \text{ SVs}/\mu\text{m}^2$; ** $p = 0.0056$) and for SVs within 40 to 60 nm from the AZ membrane (Fig. 3.17E; wt: $83.25 \pm 8.23 \text{ SVs}/\mu\text{m}^2$ vs. *RIM-BP2*^{-/-}: $53.59 \pm 5.36 \text{ SVs}/\mu\text{m}^2$; ** $p = 0.0042$). The SV density of the membrane-proximal pool, as defined in the previous part was significantly lower at *RIM-BP2*^{-/-} compared to wt AZs (Table S9; wt: $167.7 \pm 15.2 \text{ SVs}/\mu\text{m}^2$ vs. *RIM-BP2*^{-/-}: $117.8 \pm 10.5 \text{ SVs}/\mu\text{m}^2$; ** $p = 0.0041$). The measurement of SV diameters revealed that SVs at wt and *RIM-BP2*^{-/-} AZs exhibited comparable sizes (Fig. 3.17F). All values and statistical details can be found in Table S9.

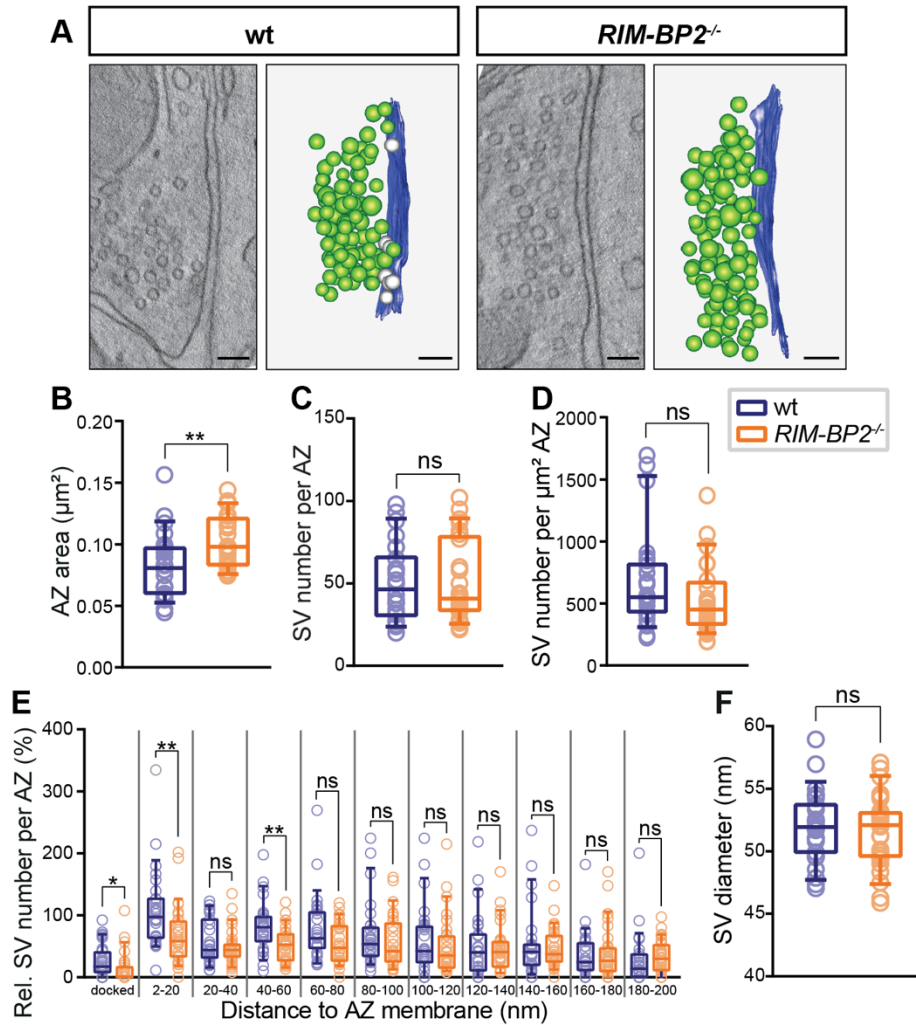


Figure 3.17: *RIM-BP2* disruption alters the axial SV distribution at the endbulb AZs.

(A) Single virtual sections and corresponding 3D models of representative tomograms of wt and *RIM-BP2*^{-/-} AZs showing the AZ membrane (blue), SVs (green), and morphologically docked SVs (gray). Scale bars: 100 nm. **(B)** The AZ area is larger at *RIM-BP2*^{-/-} endbulb synapses. **(C)** The total number of SVs is the same at mutant and wt AZs. **(D)** The SV number normalized to the AZ area is unaffected from the lack of *RIM-BP2*. **(E)** The density of docked SVs (0–2 nm) and SVs within 200 nm from the AZ membrane divided into 20-nm bins. The density of docked as well as SVs within 2–20 and 40–60 nm is lower at mutant AZs, while the densities of SVs in the other bins are comparable. **(F)** The mean of the averaged SV diameter per AZ is comparable between wt and *RIM-BP2*^{-/-}. Box and whisker plots present median, lower/upper quartiles, 10–90th percentiles. ns, not significant; **p* < 0.05; ***p* < 0.01. wt (*N* = 4; *n* = 26) in blue and *RIM-BP2*^{-/-} (*N* = 3; *n* = 28) in orange (*N*: number of animals; *n*: number of AZs). For details about values and statistics, see Table S9. Figure modified from Butola et al., 2021.

3.4.2 *RIM-BP2*^{-/-} active zones contain less synaptic vesicles in membrane proximity

The distribution of docked SVs and SVs within 2–20 nm from the AZ membrane were analyzed in more detail. Fig. 3.18A depicts examples of top views of the 3D models generated from the tomograms showing the AZs with only their docked SVs and I quantified the percentage of AZs

with zero to eight docked SVs. Whereas most wt AZs (27 %) contained two docked SVs, 50 % of the analyzed *RIM-BP2*^{-/-} AZs showed zero docked SVs (Fig. 3.18B). Further, as RIM-BP2 is involved in the recruitment and organization of VGCCs (Grauel et al., 2016; Krinner et al., 2017), the effects of *RIM-BP2* deletion on the lateral distribution of the docked SVs was investigated. Although the AZ areas captured in the tomograms might not allow an exact definition of the AZ center, I set a central point within the generated top views and measured the distances of all docked SVs from the center (Fig. 3.18C). The quantification revealed that docked SVs were further away from the center at *RIM-BP2*^{-/-} AZs, which could speak for a broader distribution over the AZs area (Fig. 3.18D).

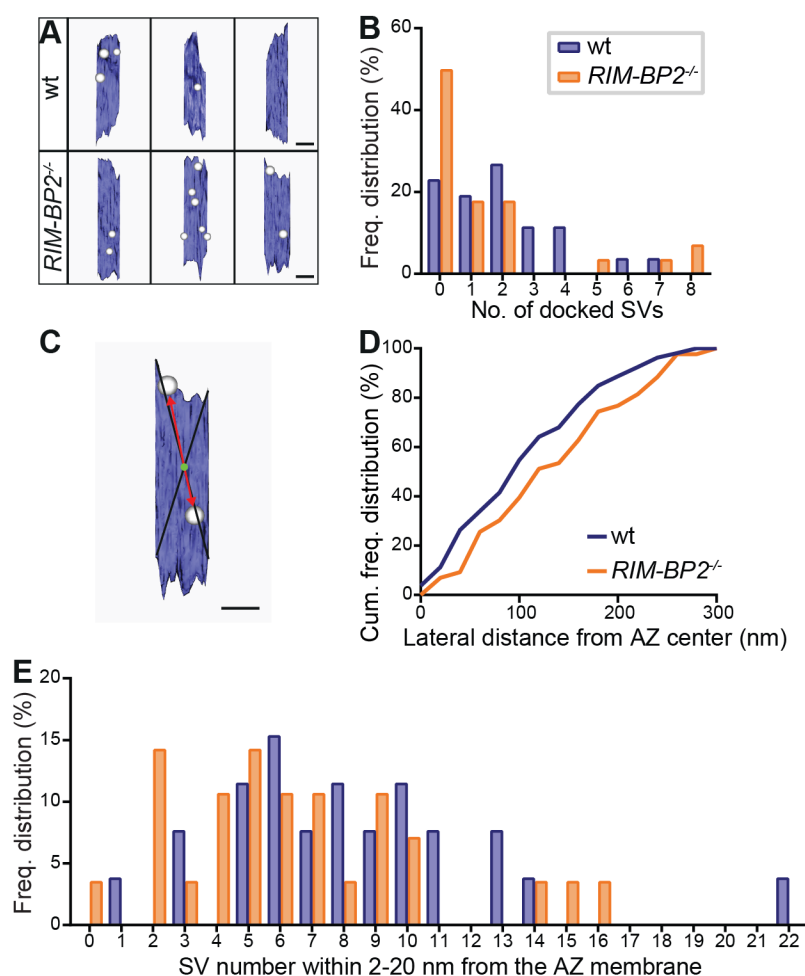


Figure 3.18: Docked and membrane-proximal SVs at endbulb AZs of wild-type and *RIM-BP2*^{-/-} mice.

(A) Top views of representative tomogram models of wt and *RIM-BP2*^{-/-} AZs with docked SVs. Scale bars: 100 nm. (B) Frequency distribution of the number of docked SVs. (C) Top view of a tomogram model demonstrating the measurement of the lateral distances of docked SVs from the assumed AZ center. Scale bar: 100 nm. (D) Cumulative distribution of the lateral distances of docked SVs to the center of the reconstructed AZ. (E) Frequency distribution of the SV number within 2–20 nm from the AZ membrane. Figure modified from Butola et al., 2021.

To analyze SVs in membrane proximity in more detail, the proportion of SVs within 2 to 20 nm from the AZ membrane were quantified and a shift towards fewer SVs at mutant AZs was observed. Most wt AZs (15 %) contained six SVs within this distance, while most mutant AZs showed only two or five SVs (Fig. 3.18E). These results allow me to conclude that RIM-BP2 could be involved in docking of SVs to the AZ at endbulb of Held synapses and in the recruitment of SVs to the membrane by organizing SVs in membrane proximity. The main findings of this part are summarized in Fig. 3.19.

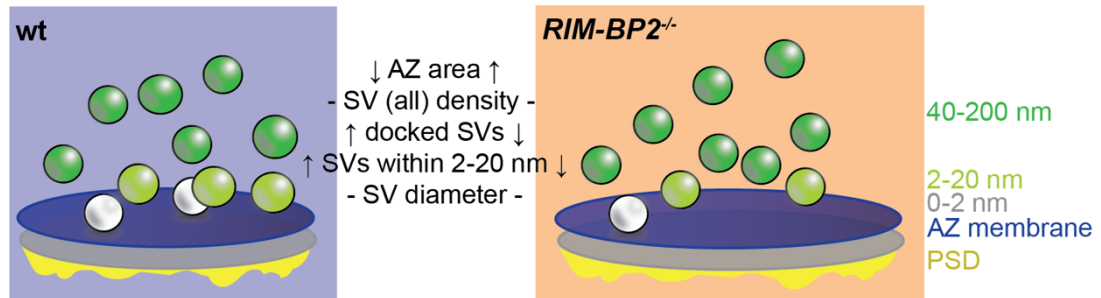


Figure 3.19: Changes at endbulb AZs upon lack of RIM-BP2.

3.5 The lack of *Mover* has differentially effects on excitatory and inhibitory synapses

Mover is a vertebrate-specific protein but in contrast to other presynaptic proteins, it is present only in a subset of synapses (Kremer et al., 2007; Wallrafen & Dresbach, 2018). In the AVCN, *Mover* was shown to be expressed at endbulbs of Held and inhibitory synapses contacting BCs (Mendoza Schulz et al., 2014). In order to get more insights into the role of *Mover* on the organization of synapses, I performed electron tomography of endbulb of Held AZs as well as of inhibitory synapses (Fig. 3.20A). For this part of the thesis, adult male *E2a-Mover*^{+/+} (wt) and *E2a-Mover*^{-/-} (*Mover*^{-/-}) mice were perfused by Rebecca Wallrafen (Institute of Anatomy and Embryology, University Medical Center Göttingen) and AVCN were conventionally embedded as described in section 2.3.2.

The total numbers of SVs within 200 nm from the AZ membrane were quantified and compared between wt and mutant mice for both, excitatory and inhibitory synapses. In addition, the SV numbers at endbulb AZs and inhibitory synapses were compared for wt and *Mover*^{-/-} mice. Fig. 3.20B shows that the disruption of *Mover* did not affect the SV number, neither at endbulb AZs nor at inhibitory synapses. However, the SV number was significantly different at endbulb AZs compared to inhibitory synapses of wt mice (Fig. 3.20B; wt exc.: 31.74 ± 2.24 SVs vs. wt inh.: 57.44 ± 8.53 SVs; * $p = 0.0169$) and of *Mover*^{-/-} mice (*Mover*^{-/-} exc.: 36.50 ± 2.18 SVs vs. *Mover*^{-/-} inh.: 54.77 ± 5.53 SVs; ** $p = 0.0065$). Interestingly, the distribution of SVs at endbulb AZs was altered when *Mover* was absent. While the percentage of docked SVs (0-2 nm distance) was found to be unchanged, the fraction of membrane-proximal SVs within 2-40 nm was significantly reduced at *Mover*^{-/-} AZs compared to wt (Fig 3.20C; wt: 31.96 ± 2.06 % vs. *Mover*^{-/-}: 24.52 ± 1.72 %; ** $p = 0.0073$). Since the percentage of SVs within 40 to 80 nm from the AZ was significantly increased at endbulb synapses from *Mover*^{-/-} mice (Fig 3.20C; wt: 24.17 ± 1.13 % vs. *Mover*^{-/-}: 28.57 ± 1.24 %; * $p = 0.0145$), the SVs seem to be shifted towards greater distances. The other bins were unaffected by the disruption of *Mover*. The proportion of docked SVs relative to all SVs within 40 nm of the AZ membrane was comparable between wt and *Mover*^{-/-} mice (Fig. 3.20D). During the reconstruction of the tomograms, it appeared that the spherical SVs at endbulb AZs were bigger at *Mover*^{-/-} mice compared to wt. However, the statistical comparison of the mean of the averaged SV diameters per tomogram showed that there was no significant difference (Fig. 3.20E).

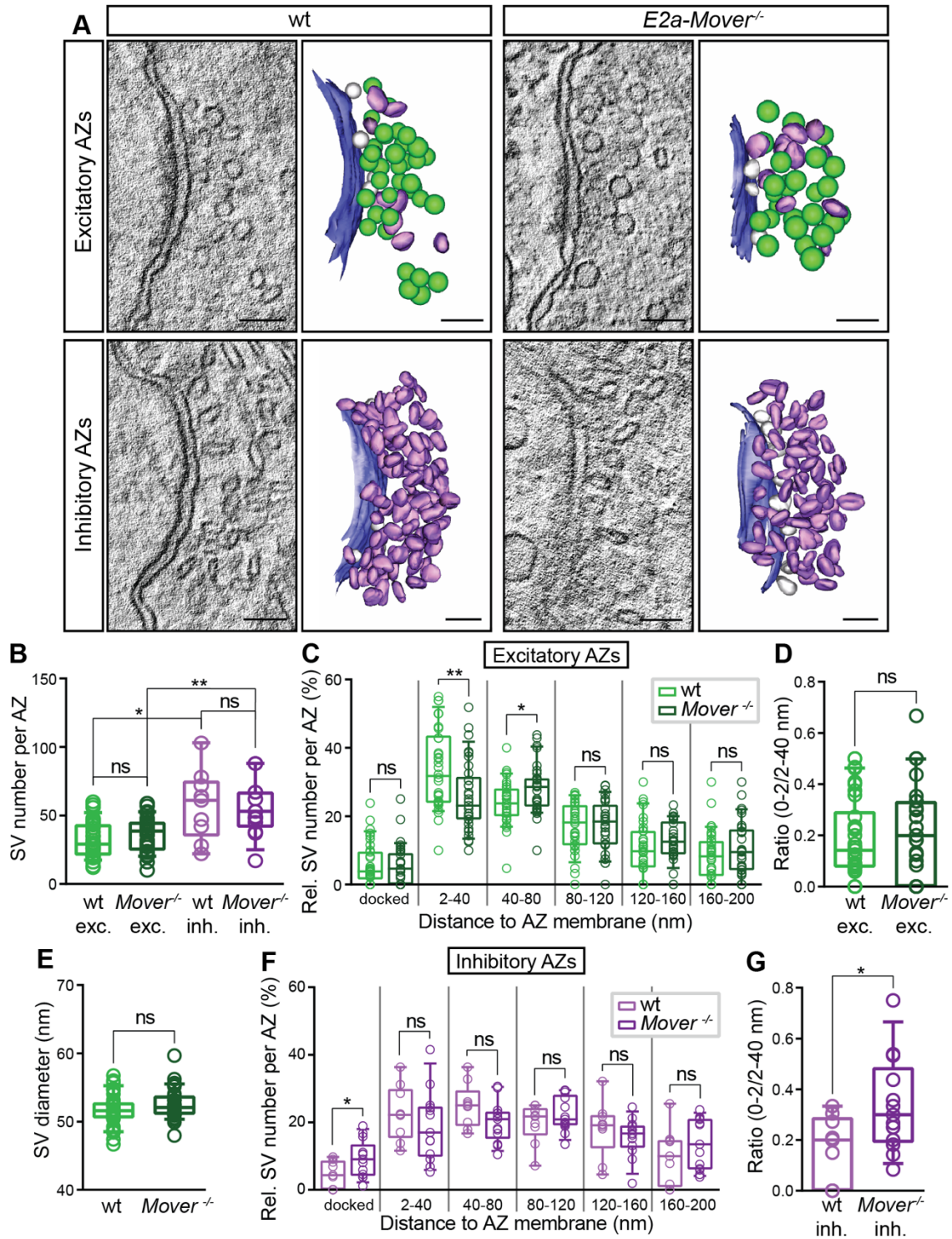


Figure 3.20: SV distribution at endbulb and inhibitory synapses of wild-type and *Mover^{-/-}* mice.

(A) Single virtual sections and corresponding models of representative tomograms of wt and *Mover^{-/-}* endbulb and inhibitory AZs showing the AZ membrane (blue), spherical SVs (green), flattened SVs (purple) and morphologically docked SVs (gray). Scale bars 100 nm. (B) The number of SVs per AZ in endbulb and inhibitory synapses is similar in wt compared to *Mover^{-/-}* mice, but it is greater at inhibitory compared to endbulb AZs of wt as well as of *Mover^{-/-}* mice. (C) The relative number of SVs of the membrane-proximal pool (2-40 nm distance) is lower at *Mover^{-/-}* endbulb AZs, but higher within 40 to 80 nm compared to wt. (D) The ratio of docked to membrane-proximal SVs is comparable between wt and mutant AZs. (E) The SVs at endbulb synapses are equally sized measured by their diameter.

(Figure 3.20 continued): **(F)** At inhibitory synapses, the relative number of docked SVs is greater in the mutant compared to wt. All other bins are unaffected from the lack of *Mover*. **(G)** The ratio of docked and membrane-proximal SVs is higher at inhibitory synapses of *Mover*^{-/-} mice compared to wt. Box and whisker plots present median, lower/upper quartiles, 10–90th percentiles. ns, not significant; **p* < 0.05; ***p* < 0.01. wt (*N* = 5; *n* = 34 endbulb AZs in light green and *n* = 9 inhibitory AZs in dark green); *Mover*^{-/-} (*N* = 5; *n* = 33 endbulb AZs in light purple and *n* = 13 inhibitory AZs in dark purple). For details about values and statistics, see Table S10.

At inhibitory synapses the lack of *Mover* resulted in a different SV distribution. While the fractions of all undocked SVs were similar between wt and *Mover*^{-/-}, the percentage of docked SVs was increased at *Mover*^{-/-} AZs (Fig. 3.20F; wt: 4.68 ± 1.34 % vs. *Mover*^{-/-}: 9.21 ± 1.52 %; **p* = 0.0364). This difference in the number of docked SVs resulted in a significantly higher ratio of docked and membrane-proximal SVs (Fig. 3.20G; wt: 0.1632 ± 0.0448 vs. *Mover*^{-/-}: 0.3365 ± 0.0518 ; **p* = 0.0199).

These results suggest that *Mover* does not influence SV docking at endbulb AZs but could potentially be involved in recruiting SVs to the AZ to prepare them for docking. At inhibitory synapses, *Mover* potentially prevents SV docking at wt AZs. Details about values and statistics can be found in Table S10 and the findings are summarized in Fig. 3.21.

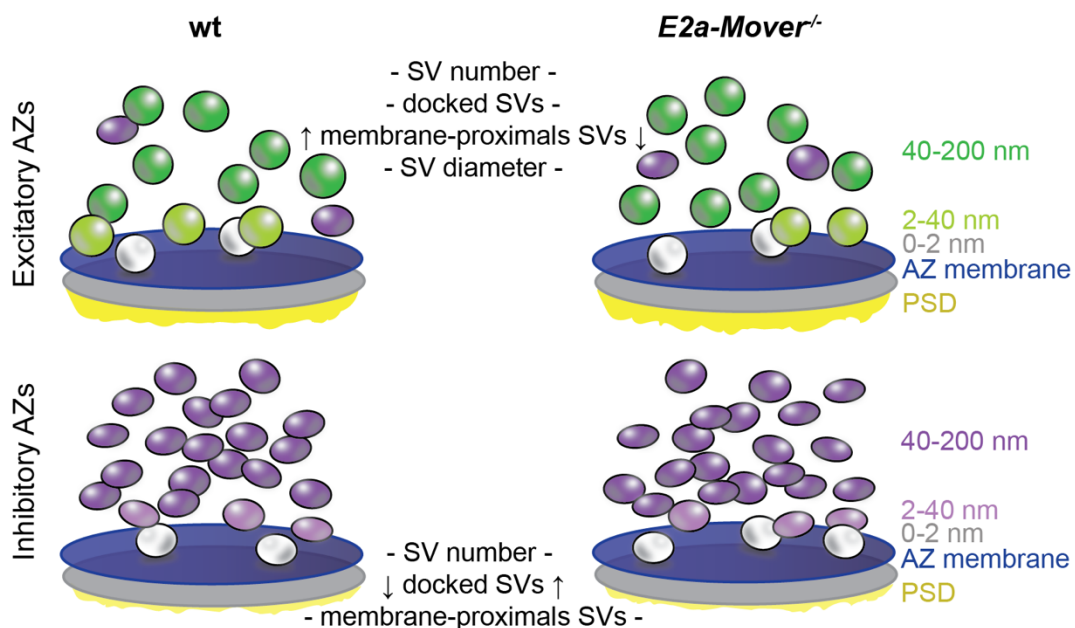


Figure 3.21: Differences in SV pools at endbulb of Held AZs and inhibitory AZs of wild-type and *E2a-Mover*^{-/-} mice.

3.6 Summary

This is the first study that systematically investigated the ultrastructure of murine endbulb of Held AZs using electron tomography in order to examine the morphology of endbulbs due to functional changes. These functional changes include the normal maturation from pre-hearing to young hearing mice and further development to adult stages by analyzing wt mice. While the SV organization at endbulb AZs was largely unaffected by maturation from pre-hearing to hearing, I observed significant changes in presynaptic mitochondria. A higher mitochondrial volume and CM density indicate higher mitochondrial performance at P21 compared to P10. These maturation-related changes in mitochondrial structure occurred not only in endbulb terminals but also in smaller excitatory synapses in the AVCN, albeit to a smaller degree.

The development to adulthood is accompanied by increased SV pools at endbulb AZs. This increase was mainly caused by SVs within 5-15 nm of the AZ membrane and SVs within 80-200 nm, whereas the density of docked SVs remained unchanged during the development of endbulb AZs in wt

The consequences of a lack of auditory input on the organization of endbulb AZs were studied using *Otof*^{-/-} mice. During the transition from P10 to P22, the density of membrane-proximal SVs increased, while the overall SV density was not affected, even compared to age-matched wt mice. Upon adulthood, SV densities and SV sizes significantly decreased. Most dramatic changes were revealed by comparing adult endbulb AZs of wt and *Otof*^{-/-} mice, including reduced numbers and sizes of morphologically docked SVs. These results suggest a less reliable neurotransmission at endbulbs of adult *Otof*^{-/-} mice.

The absence of the presynaptic proteins RIM-BP2 and Mover significantly impaired the number of SVs in membrane proximity, suggesting that both proteins are involved in recruiting and tethering SVs to the AZ membrane of endbulbs. RIM-BP2 seems further be involved in SV docking at endbulb AZs, while Mover seems to prevent docking at inhibitory synapses on BCs.

4 Discussion

Synapses represent the key element for signal transduction and plasticity in the brain via their function in synaptic transmission. To better understand the underlying processes of synaptic transmission, a quantitative morphological analysis of synaptic structures is required. Furthermore, a detailed description of synaptic morphology helps to define structural correlates of functional aspects of synaptic transmission.

The organization and size of synaptic vesicles (SVs), the key organelles of synaptic transmission, are two structural parameters that allow to draw conclusions about synaptic function. SVs can be categorized in different pools based on their location at active zones (AZs) or their mobilities (Denker & Rizzoli, 2010). With purely morphological analyses, only the morphologically docked SVs (defined as SVs within zero to two nm from the AZ membrane in the present study) can be clearly correlated to a distinct functional pool, the readily releasable pool (RRP; Imig et al., 2014; Kaeser & Regehr, 2017; Schikorski & Stevens, 1997). In addition, non-docked SVs within 40 nm from the AZ membrane (membrane-proximal SVs) were shown to be connected to the AZ membrane via tethers of a maximum length of 45 nm (Cole et al., 2016; Fernández-Busnadiego et al., 2010, 2013; Siksou et al., 2007, 2009).

Synapse function is further influenced by mitochondria and vice versa. Synaptic terminals with or without mitochondria differ in synapse size, density and release of SVs (Smith et al., 2016; Sun et al., 2013). By producing ATP and buffering Ca^{2+} , mitochondria maintain synaptic transmission and they were shown to be involved in mobilizing SVs (Verstreken et al., 2005). In this thesis, I focused on AZs of the endbulb of Held synapse, a classical conventional excitatory synapse. I performed a comprehensive structural analysis in order to investigate the morphological consequences of (i) the maturation process from pre-hearing (P10) to young hearing (P21) mice, (ii) the effect of ageing and (iii) lack of activity due to missing auditory input as well as the disruption of the presynaptic proteins (iv) RIM-BP2 and (v) Mover.

4.1 Methodology

A major part of this thesis deals with the structure of individual AZs and the organization of the SV pool with a particular focus on morphologically docked and membrane-proximal SVs. In order to analyze these structural parameters under close-to-physiological conditions and with a high z-resolution, I used high-pressure freezing (HPF) and freeze substitution (FS) of freshly sliced tissue prior to electron tomography. To compare my data with results from earlier studies that investigated the structure of synapses using different experimental approaches, some methodological aspects need to be considered including the sample preparation for electron microscopy, the image acquisition mode as well as different quantifications of morphological SV pools.

4.1.1 Sample preparation

Investigating the ultrastructure of synapses including endbulbs of Held has a long tradition, especially using chemically fixed tissue followed by electron microscopy (e.g. Cant & Morest, 1979; Clarkson et al., 2016; García-Hernández et al., 2017; Nicol & Walmsley, 2002; Ryugo et al., 1996, 1997, 2006). Studies comparing aldehyde fixation and rapid freezing of brain tissue demonstrate that chemical fixation can cause tissue shrinkage and distortion. These effects depend on the fixative composition and concentration (Hillman & Deutsch, 1978) and on the brain region (Kalimo, 1976). On the level of individual synapses, chemical fixation was shown to influence SV shape and distribution: SVs of chemically fixed inhibitory synapses appeared flattened while they are round after rapid freezing and FS (Fig. 1.4; Korogod et al., 2015; Tatsuoka & Reese, 1989). The combination of HPF/FS and electron tomography of hippocampal neurons revealed larger presynaptic terminals with a resulting lower SV density compared to perfusion or immersion fixed samples (Rostaing et al., 2006). Albeit, the overall SV density and AZ size were found to be comparable between chemically fixed and high-pressure frozen synapses of the murine somatosensory cortex, the distribution of SVs was different: The density of SVs within 30 nm from the presynaptic membrane was shown to be higher, while the density between 30 and 60 nm was lower in high-pressure frozen compared to chemically fixed synapses (Korogod et al., 2015). This finding might be a consequence of aldehyde-induced SV release as suggested by Smith and Reese (Smith & Reese, 1980). The use of different aldehydes for perfusion fixation resulted in an increase of spontaneous quantal release and exocytosis of SVs at the frog neuromuscular junction (Smith & Reese, 1980). However, in hippocampal neurons, fast fixation with 2 % glutaraldehyde did not deplete the RRP significantly (Rosenmund & Stevens, 1997). This finding indicates that the speed of fixation and the resulting immobilization of synaptic structures influences the effect of aldehydes on synaptic SV pools, in particular on morphologically docked SVs. In addition to the presynaptic changes, also the PSDs appear different depending on the fixation protocol. After HPF/FS they exhibited fine filamentous structures rather than a thick electron dense structure (Fig. 1.4; Rostaing et al., 2006; Tatsuoka & Reese, 1989).

Taken together, aldehyde fixation is a very useful tool to preserve synaptic structures for light and transmission electron microscopy as well as to gain beautiful overviews of larger cellular structures with large volume 3D reconstructions of data obtained from serial imaging, focused ion beam (FIB)- or serial block face (SBF)- scanning electron microscopy (SEM; e.g. Denk & Horstmann, 2004; Michanski et al., 2019; Thomas et al., 2019). Moreover, it induces changes on the shape of SVs, the crosslinking of proteins and the curvature of AZ, simplifying the distinction between excitatory and inhibitory synapses and the definition of the borders of the AZ membrane. However, to capture the distribution of SVs in a near-to native state, especially

the docked and membrane-proximal SVs, chemical fixation can only give a rough idea and might not reveal the full picture.

HPF followed by FS allows a more natural view of synaptic ultrastructure and different SV pools can be distinguished due to their distance to the AZ membrane more reliably. However, difficulties of preserving large volumes of brain tissue were described resulting in structural alterations and the formation of ice crystals comparing regions at the border and in the center of brain slices (Korogod et al., 2015; Rostaing et al., 2006). To exclude such problems, the tomograms I used for the analysis underwent a rigorous quality check to ensure the following criteria (see also section 2.7.3): a good structural preservation without freezing artefacts, the presence of a PSD to distinguish between excitatory and inhibitory synapses and the distinction between endbulbs and other excitatory synapses on BCs. To assure the last point, just tomograms of AZs of big synaptic terminals were recorded.

4.1.2 The advantages of 3D electron tomography

In order to study the distribution of SVs at AZs, a 3D approach is of advantage and will give an accurate overview of the synapse morphology. In previous studies, serial EM images were used to analyze the ultrastructure and the density of docked SVs at endbulb of Held (Nicol & Walmsley, 2002) and calyx of Held synapses (Han et al., 2011; Sätzler et al., 2002; Taschenberger et al., 2002; Thomas et al., 2019). With this technique, a large field of view can be imaged that allows volume measurements of the presynaptic terminal and postsynaptic cells, organelles like mitochondria and the determination of the number and distribution of individual AZs. However, EM images represent 2D projections through a volume that is determined by the section thickness. Sections are typically between 50 and 70 nm thick, therefore a precise analysis of SV sizes and distances to the AZ membrane is not possible.

The z-resolution in electron tomography is depending on the minimum and maximum tilt angle, the tilt increment, the resulting number of images in the tilt series, and the magnification used for image acquisition (Koster et al., 1997). Since the lack of presynaptic proteins resulted in different SV densities within very specific distances from the AZ membrane (Imig et al., 2014; Siksou et al., 2009), it is important to analyze the SV organization as precise as possible. The comparison of SV distributions at AZs of the different groups analyzed in this thesis revealed e.g., that particularly SVs within 5 to 15 nm from the AZ membrane were elevated upon development of wt endbulb of Held synapses and decreased upon the lack of activity (Fig. 3.12E). These differences in the nanometer range would most likely not have been resolvable with serial imaging. On the other hand, with electron tomography of 250 nm slices, it was not possible to image entire AZs. The reconstructed AZ areas measured in this study were therefore only used to determine SV densities.

4.1.3 The model system

The structure of endbulbs has been studied in several species including mice (García-Hernández et al., 2017; Lauer et al., 2013; Limb & Ryugo, 2000), rats (Clarkson et al., 2016; Nicol & Walmsley, 2002), monkeys (Gómez-Nieto & Rubio, 2011) and cats (Baker et al., 2010; Cant & Morest, 1979; Ryugo et al., 1996, 1997, 2006; Sento & Ryugo, 1989). However, to understand relationships between structure and function, it is important to investigate both species by species, since different species not just differ in size of the respective brain structure, but also in their hearing range. As described in chapter 1.6.1, the auditory pathway is organized in a tonotopic manner and different bushy cells (BCs) are responsive to different frequencies. Spherical BCs (SBCs) mainly encode sound of low frequencies, while globular BCs (GBCs) encode sounds of higher frequencies (Smith et al., 1991, 1993). In mice, (i) the subtypes of BCs cannot be definitely identified based in cell body characteristics as described for cats (Lauer et al., 2013) and (ii) just a few large SBCs can be found (Webster & Trune, 1982; Willard and Ryugo, 1983) since they have little low-frequency hearing (Ehret, 1974). Structure-function relationships were investigated for cats throughout development (Ryugo et al., 2006) and in rats upon maturation from pre-hearing to hearing (Taschenberger et al., 2002). In mice, the morphogenesis of endbulb during development (Limb & Ryugo, 2000) and functional changed upon hearing onset (McKay & Oleskevich, 2007) were well described, but structural investigations on the level of endbulb AZs are missing to date.

In addition, different murine deafness models including synaptopathy and ear-plugging were used to reveal structural and functional changes at endbulbs due to lack of auditory input. In the following, I will compare data I obtained from deaf mice lacking otoferlin (*Otof*^{-/-}; Reisinger et al., 2011) with these other models. It is important to keep in mind that the onset of deafness and the underlying deafness mechanisms are diverse and might potentially lead to different results. Another important factor that needs to be considered is the possibility of age-related degeneration of auditory nerve fibers (ANFs) and ribbon synapses in the 6-months-old (6M) mice I used in this study. C57BL6 mice show progressive hearing loss from three months of age, initially affecting the basal and middle regions of the cochlea (Kujawa & Liberman, 2019; Stamatakis et al., 2006). This age-related hearing loss results from a mutation in the gene encoding cadherin23, a protein of tip-links that connect adjacent stereocilia of HCs (Noben-Trauth et al., 2003).

Finally, I will relate my results to a very similar synapse, the calyx of Held, which is comparable to the endbulb of Held in several structural and functional aspects. Both synapses are part of the auditory pathway and therefore tuned for highly precise, fast and efficient firing (Lin et al., 2011). Morphologically, they share the huge presynaptic terminal that carries hundreds of individual AZs, resembling typical central synapses (Nicol & Walmsley, 2002; Ryugo et al., 1996; Wichmann, 2015). However, one important difference between endbulbs and calyces is

their respective number of terminals projecting on the postsynaptic cell. BCs receive auditory input from several endbulbs (Spirou et al., 2005), meaning that synaptic integration is necessary (Golding & Oertel, 2012). MNTB principal cells are mono-innervated (Hoffpauir et al., 2006) suggesting a purely sign-inverting relay where firing properties of the GBCs are transmitted with high speed and fidelity to the LSO (Joris & Trussell, 2018).

4.2 The onset of hearing is not reflected by morphological changes on the level of individual endbulb of Held active zones

Comparing P10 and P21 wt mice, I wanted to understand how maturation of the auditory system affects structural changes at endbulb synapses. Functionally, maturation was shown to be completed by P18 in murine BCs as processing of auditory information was mature-like at this age (Müller et al., 2019). It is characterized by enhanced reliability and improvement of timing of signal transmission (Bellingham et al., 1998; Wu & Oertel, 1987) due to a developmental switch from NMDA to AMPA receptor mediated neurotransmission (Bellingham et al., 1998; Isaacson & Walmsley, 1995), and a switch in AMPA receptor subunits (Gardner et al., 1999, 2001; Lawrence & Trussell, 2000; Wang et al., 1998).

Surprisingly, the hearing onset did not have an impact on the SV pool within a distance of 200 nm across the AZ area as shown by the unaltered SV number and density per AZ (Fig. 3.2D,E). These findings are inconsistent with observations of endbulbs in the nucleus magnocellularis (nMag), the CN analogue in the chick (Brenowitz & Trussell, 2001). Brenowitz and Trussell reported an improvement of reliable and temporal accurate neurotransmission after hatching partly due to a larger SV pool (Brenowitz & Trussell, 2001). The maturation of the rat calyx of Held was described to be accompanied with a decrease in SV numbers (Thomas et al., 2019). However, normalized to the also decreasing AZ areas, the SV densities were found to increase from P7 to P21 (Thomas et al., 2019).

The number and density of docked SVs at endbulb AZs from pre-hearing mice were similar to those of young hearing mice. This is in line with results from Thomas and colleagues who compared calyx of Held synapses of P7 and P21 mice (Thomas et al., 2019), but contrasts findings from Taschenberger et al.: Comparing calyces of P5 and P14 rats, they found a decreasing number of docked SVs (Taschenberger et al., 2002). In addition, the latter study showed a positive correlation of the AZ area and the number of docked SVs for both ages (Taschenberger et al., 2002), which was also described for endbulbs of P25 rats (Nicol & Walmsley, 2002). Nicol and Walmsley used serial reconstructions of fixed tissue to reconstruct whole AZs of a single endbulb (Nicol & Walmsley, 2002). In my analysis, I could not observe a linear relationship between the overall SV number within 200 nm from the AZ membrane and the AZ area or the number of docked SVs and the AZ area. Electron tomography of

hippocampal AZs also revealed a lack of correlation between overall SV number and AZ size (Siksou et al., 2007), suggesting that an explanation for the missing correlation might be the method I used. HPF/FS in combination with electron tomography provides a high z-resolution, which allows to determine SV docking in an unbiased way (Chakrabarti et al., 2018; Imig et al., 2014; Maus et al., 2020; Siksou et al., 2007, 2009; Watanabe et al., 2013), but lacks the capability to reconstruct whole AZs due to a limited section thickness of 250 nm (Chakrabarti et al., 2018; Imig et al., 2014; Maus et al., 2020). In addition, I analyzed AZs from different endbulb terminals and pooled data of three to four mice, which might result in a high variability of the parameters and a lack of correlation between AZ size and number of (docked) SVs. For the density of docked SVs and the density of all SVs within 200 nm, I observed a linear relationship, which could argue for a simple scaling of these parameters although not whole AZs with the complete SV pool can be analyzed.

Consistent with findings from Nicol and Walmsley comparing different endbulb terminals (Nicol & Walmsley, 2002), a high variability of the number of docked SVs per AZ was found in the present study. To assess the variability in SV docking in more detail, the frequency distribution of AZs with the respective number of docked SVs was analyzed. I did not find a difference in the frequency distribution between the two age groups, but I could show that most P21 AZs did not contain a docked SV, although they had an associated SV cluster. This finding could indicate that multivesicular release occurs less likely after the onset of hearing. This hypothesis was raised by Taschenberger et al. who also observed a lack of docked SVs at some calyx AZs of hearing P14 rats (Taschenberger et al., 2002). In line with this, the probability for SV release (P_r) was found to decrease during maturation (Iwasaki & Takahashi, 2001; Taschenberger et al., 2002; Taschenberger & von Gersdorff, 2000) and calculation according to a binomial model (Oertner et al., 2002) revealed that 62 % of the release events were multivesicular in the pre-hearing rats, but only 14 % after the hearing onset (Taschenberger et al., 2002). These findings raise the general question, whether the number of docked SVs is a direct readout for P_r .

4.3 Structure of presynaptic mitochondria changes according to energy demands

The SV distribution seemed not to be altered, but I hypothesize that metabolic activity in endbulbs might change during maturation. Therefore, I analyzed mitochondria, which are essential organelles for cellular processes including synaptic transmission due to their ATP production. Mitochondria were observed to be anchored in nerve terminals near AZs from various CNS regions including hippocampus (Spacek & Harris, 1998), thalamic nuclei (Lieberman & Spacek, 1997) and auditory brainstem (Cant & Morest, 1979; Lauer et al., 2013;

Perkins et al., 2010; Rowland et al., 2000; Tolbert & Morest, 1982b). Therefore, it is not surprising that mitochondrial function, positioning and architecture was studied in regard to synaptic function and changes in activity (Cserép et al., 2018; Ivannikov et al., 2013; Smith et al., 2016; Sun et al., 2013; Verstreken et al., 2005). Ca^{2+} buffering was described to positively impact short-term plasticity like post-tetanic potentiation in crayfish neuromuscular junctions (Tang & Zucker, 1997), rat calyx of Held (Billups & Forsythe, 2002) and rat hippocampal neurons (Lee et al., 2007). However, stimulation of murine hippocampal neurons revealed that mitochondria did not affect the basal and evoked Ca^{2+} concentrations and blocking of mitochondrial Ca^{2+} buffering did not impair SV release. Instead, mitochondrial ATP supply was required to maintain synaptic transmission (Sun et al., 2013). Consistent with these observations, Ivannikov and colleagues presented that inhibition of mitochondrial function in hippocampal synaptosomes decreased SV release due to reduced presynaptic ATP levels (Ivannikov et al., 2013).

4.3.1 Mitochondria become larger during maturation of the auditory system

The maturation from pre-hearing to hearing was discussed to be associated with an increase in mitochondrial volume at calyces of Held and minor terminals contacting MNTB principal cells (Thomas et al., 2019). The analysis of stalks and swellings, two compartments of the calyx that differ in coupling rate of SVs and Ca^{2+} buffering (Fekete et al., 2019), revealed no difference in mitochondrial volumes, suggesting that mitochondrial volumes increased as a result of development (Thomas et al., 2019). This increase in total mitochondrial volume per calyx resulted from larger mitochondria as determined by measuring mitochondrial diameters. An increase in mitochondrial number could also contribute to the observed higher total mitochondrial volume at P21, but due to fission and fusion of the organelles, absolute numbers were difficult to determine (Thomas et al., 2019). Thomas and colleagues performed SBF-SEM on transcardially perfused samples that allowed the reconstruction of whole calyx terminals with their containing mitochondria. Electron tomography of 250 nm slices used in the present study does not allow the reconstruction of whole mitochondria. Thus, individual volumes of reconstructed parts of mitochondria were compared between wt P10 and P21 as well as between endbulb terminals and non-endbulb terminals. In line with the observations for the calyx, the reconstructed volumes of mitochondria in endbulbs of Held were significantly larger at P21 compared to P10 (Fig. 3.7C). At non-endbulb synapses, the same effect was detected (Fig. 3.8C), suggesting that the increase in mitochondrial volumes is not specific for the large synaptic terminals like the endbulb or calyx of Held. These non-endbulb synapses project on dendrites within the AVCN, but their origin and target were not specified. Several smaller inputs from various sources on e.g. SBCs were described including small bouton-like inputs from ANFs and inputs from other parts of the CN (reviewed in Kuenzel, 2019). Not just ANFs, but

also intrinsic connections within the CN were described to follow the tonotopic organization (Wickesberg & Oertel, 1988), indicating that also the non-endbulb synapses depend on the activity of the auditory system. Surprisingly, and similar to the findings for the minor terminals, representing calyceal collaterals described by Thomas et al., mitochondria at non-endbulb synapses had greater individual volumes compared to those of endbulbs at the age of P10 (Fig. 3.9A). The strong increase in mitochondrial volumes at endbulbs and the relative slight increase at non-endbulb terminals, resulted in comparable mitochondrial volumes at P21 (Fig. 3.10A). An increase in mitochondrial volumes was also shown during the development of hippocampal neurons that was accompanied with an increase in the abundance of mitochondria at synaptic boutons (Smith et al., 2016). In endbulbs from cats, the average mitochondrial size did not change, but an increase in mitochondrial volume fraction was observed with age (Ryugo et al., 2006). The comparison of high- and low-performance glutamatergic and GABAergic hippocampal neurons revealed higher individual volumes of mitochondria at synapses with higher activity (Cserép et al., 2018), indicating, that not just the development *per se*, but also neuronal activity influences mitochondrial size. This is consistent with findings from cats: Ryugo and colleagues estimated that endbulbs from high SR fibers contained 50 % greater mitochondria compared to endbulbs from low SR fibers (Ryugo et al., 1996).

4.3.2 Developmental maturation is associated with ultrastructural remodeling of mitochondria in endbulbs of Held

The CM morphology of chemically fixed mitochondria was described to depend on the metabolic state of mitochondria. When respiratory activity and ADP concentration were low, mitochondria showed the orthodox configuration with homogeneously narrow cristae and a low intracristal volume. Mitochondria were found in the condensed state with wider cristae and a smaller matrix volume under fast respiratory conditions and high ADP levels (Hackenbrock, 1966; Mannella, 2006; Smith et al., 2016).

With SBF-SEM and a used section thickness of 50-70 nm, as Thomas and colleagues have done, it is not possible to analyze mitochondrial inner architecture. Here, electron tomography provides the advantage of a high resolution of 1.188 to 1.648 nm (dependent on the magnification I used for the tomogram recording), which allows the accurate visualization and segmentation of crista membranes (CM). With this technique, structural aspects like crista junctions were recognized for the first time (Mannella et al., 1994). Using high-pressure frozen tissue further allows to analyze mitochondria without possible fixation artifacts. Although Perkins et al. found that inner architecture of cryofixed mitochondria in brown adipocytes was similar to that of chemically fixed mitochondria, crista volumes were more sensitive to chemical fixation than the surface area (Perkins et al., 1998).

Cristae are described as pleomorphic membranes, ranging from tubular structures to sheet-like lamellae and it is supposed that tubular cristae merge to form large lamellae (Perkins et al., 1997). In contrast to Perkins and colleagues, who noticed both, tubular and lamellar compartments of cristae in mitochondria from different brain regions (Perkins et al., 2001), I only observed lamellar organized cristae. However, synaptic mitochondria were described to have fewer tubular segments compared to mitochondria of other neuronal compartments (Perkins et al., 2001). The shape of CMs was described to regulate respiratory chain supercomplex stability and assembly, impacting the respiratory efficiency (Cogliati et al., 2013). A high grade of lamellarity is expressed by a high crista shape factor that represents the ratio of CM surface area and crista lumen volume (Cserép et al., 2018). In simulation experiments, a higher surface-to-volume ratio was shown to induce a high proton motive force that represents the driving force for ATP synthesis, while the rate of ATP synthesis was dependent on the surface area of CMs only (Song et al., 2013). The ATP synthase was found to be arranged in rows of dimers that were specifically enriched at strongly curved rims of cristae (Davies et al., 2011). Taken together these findings indicate that compared to tubular cristae, lamellar cristae with their increased surface area and greater surface-to-volume ratio are beneficial for a high energy demand. Cellular compartments where a higher capacity for ATP generation and respiration is required, CMs of mitochondria might therefore be more lamellar organized, such as in synapses.

Cserép and colleagues indeed described that CMs in mitochondria of high-performance synapses were more lamellar organized compared to that of low-performance synapses. In addition, highly active synapses contain mitochondria with a higher CM density (Cserép et al., 2018). The surface area of CMs increased clearly upon maturation from pre-hearing to hearing at endbulb synapses. In relation to the mitochondrial volume, the difference was smaller, but still significant (Fig. 3.7). In non-endbulb synapses, the surface area of cristae was higher after the onset of hearing indicating increased mitochondrial function. However, the CM density was comparable between P10 and P21 due to the only minor difference in mitochondrial volume (Fig. 3.8). These differences in the mitochondrial ultrastructure indicate that excitatory synapses contacting BCs have a higher capacity for respiration and ATP generation after the onset of hearing, which might be required for a higher synaptic activity and a reliable neurotransmission. The differences were more pronounced at endbulb synapses where the energy demand might be higher to sustain high-frequency firing due to sound-evoked activity. Synaptic inputs on dendrites of BCs were suggested to modulate auditory processes (Koert & Kuenzel, 2020). The minor changes on mitochondrial structure in the dendritic inputs could indicate that their modulatory function is less dependent on increasing mitochondrial function. However, the aim of the present study was to analyze if changes in mitochondrial structure is specific for endbulbs. Therefore, the non-endbulb terminals on dendrites were not specified

and contain most likely a mixture of excitatory inputs of various sources and targets leading to variable structural parameters. Surprisingly, I did not observe differences in the crista morphology between the age groups and synapse types; already before the onset of hearing CMs were found to be organized in lamellae.

Changes in mitochondrial sizes and their CM density could be a result of an exchange of mitochondria e.g. by retrograde transport of small mitochondria and the anterograde transport of larger mitochondria with a higher CM density. However, this mechanism would result in a lack of mitochondrial support including ATP supply and Ca^{2+} buffering during the time of mitochondrial trafficking and is therefore rather unlikely. As described in section 1.5, mitochondria are highly motile and could move to regions where the energy demand increases. Studies investigating the correlation between mitochondrial motility and neuronal activity provide contrasting results: While increased neuronal activity due to developmental maturation or pharmacological manipulations resulted in more stationary mitochondria in axonal synapses (Chang et al., 2006; Lewis et al., 2016), mitochondrial motility increased in dendritic synapses of cortical neurons (Chang et al., 2006). Although anchoring of mitochondria to the plasma membrane near AZs is described in endbulbs Held (Cant & Morest, 1979; Tolbert & Morest, 1982a), mitochondrial motility alone is possibly not sufficient to adjust to local energy demands. The other mechanism that could underlie the change in mitochondrial structure is the remodeling of mitochondrial shape in response to the local needs. This dynamic remodeling dependent on cellular functions and activity was described for non-neuronal tissue (reviewed in Cogliati et al., 2016) and different excitatory and inhibitory neurons (Cserép et al., 2018).

As mentioned earlier, mitochondria are sometimes anchored to the plasma membrane. Thereby, they are arranged in so-called mitochondria-associated adherens complexes (MACs; Spirou et al., 1998) that were initially described in the spinal cord (Gray, 1963). Besides the mitochondrion positioned near the presynaptic membrane, a MAC consists of an electron dense mitochondrial plaque that is linked to a *punctum adherens* by filaments and a vesicular chain interposed among the filaments. CMs of MAC mitochondria were found to be lamellar organized and were often oriented roughly perpendicular to the mitochondrial plaque (Perkins et al., 2010; Spirou et al., 1998). In comparison to non-MAC mitochondria, MAC mitochondria showed a higher CM density and a higher density of crista junctions at calyx terminals (Perkins et al., 2010). These findings, together with the observation that MACs are located adjacent to synapses (Rowland et al., 2000), suggest that especially MAC mitochondria are important for synaptic function through ATP synthesis and Ca^{2+} buffering. MACs were identified and described using serial sectioning (Rowland et al., 2000) or electron tomography (Perkins et al., 2010) of chemically fixed tissue. In the high-pressure frozen tissue, it was not possible to identify these structures due to a lower contrast, but it would be interesting to analyze if the presence of MACs is developmentally regulated in endbulb terminals.

4.4 Spontaneous activity shapes the auditory pathway

Spontaneous activity influences neuronal connectivity and synaptic development and shapes neuronal pathways during maturation (reviewed in Kerschensteiner, 2014). In the auditory system, this spontaneous non-sensory activity is generated by supporting cells located near inner hair cells (IHCs; Tritsch et al., 2007). The release of ATP initiates the release of K^+ which in turn depolarize groups of IHCs, inducing glutamate release and excitation of SGNs (Tritsch et al., 2007; Wang et al., 2015). In the present study, deaf *Otof*^{-/-} mice were used to investigate how sensory deprivation affects endbulb of Held AZs. At mouse IHCs, exocytosis is dependent on otoferlin from P4 on (Beurg et al., 2010; see chapter 1.6.2). However, the maturation process might still occur since in immature mice lacking the vesicular glutamate transporter 3 (VGLUT3), spontaneous activity is preserved (Babola et al., 2018). As *Otof*^{-/-} mice, *Vglut3*^{-/-} mice are profoundly deaf, and exocytosis is abolished at their IHCs. SGNs of *Vglut3*^{-/-} mice showed enhanced excitability enabling them to get directly activated by K^+ released by supporting cells (Babola et al., 2018). Deletion of *otoferlin* reduced, but not fully abolished the frequency of spontaneous and high K^+ -induced excitatory postsynaptic currents (EPSCs), as measured in P9 mice using single bouton recordings at IHC afferent fibers (Takago et al., 2019). Assuming that these functional changes are reflected morphologically, the lack of otoferlin might result in structural deficits on subsequent centers of the auditory pathway after the onset of hearing.

Although CN volumes were found to be reduced by 46 % in otoferlin mutant mice, the circuits were well established and showed their normal pattern of connectivity (Wright et al., 2014). Similar observations were made in mice lacking *Vglut3* (Babola et al., 2018) as well as *jerker* mice (Cao et al., 2008) that have a mutation in the *ESPN* gene which encodes the actin-bundling protein espin of stereocilia in HCs (Zheng et al., 2000). In humans, mutations in this gene cause non-syndromic deafness and vestibular disorders (Donaudy et al., 2006; Naz et al., 2004). Homozygous *jerker* mice are deaf and show circling and head-shaking behavior (Grüneberg et al., 1941; Steel & Bock, 1983). In all three mouse models, the tonotopic organization of the auditory pathway was preserved (Babola et al., 2018; Cao et al., 2008; Wright et al., 2014) indicating that it develops independently of activity before or after the onset of hearing.

4.4.1 Endbulb active zones of young wild-type and *Otof*^{-/-} mice display a similar synaptic vesicle organization

Despite the residual activity in *Otof*^{-/-} mice reported by Takago et al., it seems surprising at first glance that I could not observe differences in the overall organization of AZs between endbulbs of wt and *Otof*^{-/-} mice shortly after hearing onset. However, at second glance, the findings made

by Wright et al. could explain this puzzle. They investigated functional properties like spontaneous miniature (m) EPSCs of BCs of deaf otoferlin mutant mice and hearing controls at the age of P16-22. mEPSCs result from transmitter release due to spontaneous SV fusion and their frequency measures presynaptic function. Therefore, the similar mEPSC frequencies at BCs from otoferlin mutant and hearing control mice suggest similar properties of endbulb terminals (Wright et al., 2014). Also, the shapes of the mEPSCs were comparable indicating similar subunit compositions and kinetics of AMPA receptors. On the other hand, mEPSCs amplitudes were larger in the mutant that might speak for postsynaptic strengthening due to a higher number of AMPA receptors in BCs of the deaf mice (Wright et al., 2014). At endbulbs of *deafness* mice lacking spontaneous auditory nerve activity due to a mutation in the *transmembrane cochlear-expressed gene 1*, mEPSC frequency was also not significantly different between P7-11 and P13-16.

4.4.2 Alterations of synaptic vesicle pools at endbulb of Held active zones of adult wild-type and *Otof*^{-/-} mice

While in young hearing animals the SV density was unaltered compared to pre-hearing mice, I observed an increase in SV density towards adulthood in wt (Fig. 3.12D). This is consistent with findings from cats (Ryugo et al., 2006). My data showed that two SV populations were mainly affected from this increase, membrane-proximal SVs and SVs 80 to 200 nm away from the AZ. Besides the morphologically docked SVs, several studies also put specific focus on membrane-proximal SVs, which are potentially tethered to the AZ membrane. Within this pool, a clustering of SVs was detected near the AZ at a distance of 5-10 nm after the onset of hearing. This clustering further increased towards adulthood. Similarly, SVs within 10-15 nm were also observed to increase from P10 to 6M (Fig. 3.12E). According to the idea that loosely docked or tethered SVs can be converted into tightly docked and primed SVs (Chang et al., 2018; Neher & Brose, 2018), these SVs near the AZ might be available for priming to sustain the high-frequency firing due to sound evoked activity.

My data show that the development of endbulb AZs in *Otof*^{-/-} mice is accompanied by a decline in the overall number and density of SVs from P22 to 6M (Fig. 3.12C,D). This decrease is mainly caused by SVs of the membrane-proximal pool and SVs within 120-200 nm from the AZ membrane (Fig. 2.12E and 3.14C).

In comparison to all wt and P10 *Otof*^{-/-} AZs, the number of SVs correlated with the respective AZ areas at *Otof*^{-/-} P22 and *Otof*^{-/-} 6M endbulb AZs. This correlation might indicate that complete AZs were smaller and therefore greater parts of AZs with their number of SV were reconstructed at *Otof*^{-/-} P22 and *Otof*^{-/-} 6M endbulbs AZs.

The opposing effect on SV densities during development of wt and *Otof*^{-/-} endbulb AZs result in the drastic decrease of SVs in adult *Otof*^{-/-} animals compared to wt, which is consistent with studies on 7-months-old *shaker-2* mice (Lee et al., 2003). Depletion of SVs was found in the docked and membrane-proximal pool, whereby mainly SVs within 0 and 15 nm from the AZ membrane were decreased at mutant AZs (Fig. 3.12E, 3.13, 3.14). But also SVs farther away from the AZ (40-200nm) were depleted at 6M *Otof*^{-/-} AZs compared to age-matched wt. Together with the functional impairment in endbulbs of *otoferlin* mutant mice at the age of P11 to P60 with most animals aged P16-22 having a stronger depression and higher synaptic failure rates (Wright et al., 2014), these results indicate that synaptic transmission might be less reliable at endbulbs of *Otof*^{-/-} mice.

4.5 SV sizes differ between endbulbs of wild-type and *Otof*^{-/-} mice

Developmental maturation is accompanied by a decline in SV sizes at IHCs as shown by random section analysis of conventionally embedded organs of Corti (Michanski et al., 2019). Similar results were obtained from neuromuscular junctions of zebrafish using HPF/FS and electron tomography (Helmprobst et al., 2015) and motor-sensory neocortex synapses of rats (Markus et al., 1987). However, at endbulbs of Held of normal hearing mice, SV sizes increased from P20 to P100 (Antunes et al., 2020) while in the present study no developmental change in SV sizes could be observed at endbulb AZs of wt mice, neither for all, nor for docked and membrane-proximal SVs (Fig. 3.15). However, at endbulb AZs from *Otof*^{-/-} mice, SVs decreased in size upon development. The phenomenon is not fully understood, but there are a few ideas that might explain the developmental decrease in SV sizes. The SV size is one factor that determines the amount of neurotransmitters and this correlation was demonstrated by overexpressing VGLUT1 in *Drosophila* that resulted in an increased amount of neurotransmitters and SV size (Daniels et al., 2004, 2006). However, a chronic blockade of NMDA receptors, which was shown to increase the neurotransmitter concentration via an elevated expression of VGLUT1 (Wilson et al., 2005) was shown to result in smaller SV sizes in cultured hippocampal neurons (Hu et al., 2008). A possible explanation for this contrasting result could be a compensatory response to unusually elevated neurotransmitter concentrations or regulatory mechanisms specific for NMDA receptors (Qu et al., 2009). However, at endbulb synapses, the expression of NMDA receptors decrease upon maturation as evoked EPSCs were largely mediated by NMDA receptors in P10 mice, but mediated by AMPA receptors in P18 mice (Cao & Oertel, 2010). Further, endbulb synapses of P30 rats lack immunolabeling for the NMDA receptor subunit GluN1 after freeze fracturing (Rubio et al., 2014). It is not known if this downregulation of NMDA receptors also happens in BCs of *Otof*^{-/-} mice or if a NMDA receptor specific mechanism could explain the differences in SV sizes during the development of wt and mutant mice.

Different proteins were also discussed in regulating SV sizes. For instance, in *Drosophila* mutants lacking the clathrin adapter protein AP180, endocytosis of SVs is impaired but SVs were found to be larger (Zhang et al., 1998). Further, in P15-P16 mice with reduced otoferlin levels, larger SVs were observed at IHCs (Strenzke et al., 2016). As exocytosis at IHCs is independent from otoferlin up to P3 (Beurg et al., 2010), it could be suggested that otoferlin might be involved in developmental changes of SVs at IHCs. The present study shows that considering all SVs, immature endbulb AZs of *Otof*^{f/-} mice contain larger SVs compared to age-matched wt, while shortly after hearing onset and at 6M, SVs were comparable in size between mutant and wt mice (Fig. 3.15A). Although these results partially match those of Strenzke et al. (2016), SV size differences cannot be explained by the lack of otoferlin since endbulbs do not express otoferlin.

There are hints that SV diameters at endbulb synapses change upon activity changes. A mild and reversible form of reduced neuronal activity, by occluding the ear canal demonstrated different effects on SV sizes: Endbulbs from monaurally-occluded rats contained smaller SVs compared to hearing rats and after earplug removal, the SV size increased again (Clarkson et al., 2016). Further, the lack of the AMPA receptor subunit GluA3 resulted in impaired ABRs and ultrastructural changes of endbulb synapses (García-Hernández et al., 2017), including smaller SVs (Antunes et al., 2020). These changes in SV sizes were found throughout development from P20 to P100 indicating an important role of GluA3 for the normal developmental increase in SV sizes (Antunes et al., 2020). In contrast, an earlier study reported a negative correlation between SV size and neuronal activity: When afferent activity of electroreceptor nerve of gymnotid fish was blocked by tetrodotoxin injection, an enlargement of SVs was observed with a decline of SV densities adjacent to the membrane (Maler & Mathieson, 1985). Qu and colleagues observed that activity changes due to AMPA receptor blockade or increased K⁺ concentrations did not affect SV sizes in cultured rat hippocampal neurons (Qu et al., 2009).

Speculatively, larger SVs found at immature synapses of *Otof*^{f/-} mice result from an increased amount of glutamate or the expression of SV size-regulatory proteins as a compensatory mechanism which gradually diminishes due to the persistent absence of IHC-driven activity. The larger SVs at mutant AZs do not seem to negatively affect the recruitment to the AZ membrane, as the number and density of docked SVs was comparable between immature wt and *Otof*^{f/-} AZs.

The decrease in SV size observed at endbulbs from *Otof*^{f/-} mice was most prominent for docked SVs, which were found to be significantly smaller at 6M compared to age-matched wt (Fig. 3.15B). Karunanithi et al. reported a linear relationship between quantal size and SV volume at different glutamatergic synapses in *Drosophila* (Karunanithi et al., 2002), indicating

that smaller SVs account for a smaller quantal size. However, quantal contents of wt and deaf *otoferlin*-mutant mice were similar at the age of P16-P22 and mEPSC analyses revealed a potential upregulation of AMPA receptors at the postsynaptic membrane of mutant mice (Wright et al., 2014). These functional parameters were not studied in older animals, thus it is not known whether they change upon adulthood.

4.6 Endbulb active zones contain a variable number of docked synaptic vesicles

In the present study, a highly variable number of docked SVs was observed that could contribute to the variability in P_r observed at endbulb synapses by Oleskevich and colleagues. They reported a moderately high mean P_r of 0.6, but it ranged from 0.3 to almost 1.0 (Oleskevich et al., 2000). However, this variability might also be a result of different activities of the auditory nerve. Differences in ANF activity result in morphological differences between endbulbs as presented by Ryugo et al. for cats. Endbulbs arising from low SR fibers contain less, but larger AZs with a lower number of SVs compared to endbulbs from high SF ANFs (Ryugo et al., 1996). In the present study the distinction between low and high SR fibers was not possible and tomograms were sampled over large AVCN areas. Thus, it is likely that endbulbs arising from ANFs of different activities were included, which in turn might contribute to a higher variability in SV numbers.

4.6.1 The relationship between release probability and number of docked synaptic vesicles

The correlation of P_r and the number of docked SVs was described for cultured hippocampal neurons (Murthy et al., 2001). This correlation was confirmed using electron tomography after HPF/FS by comparing cultured mossy fiber synapses and Schaffer collateral synapses (Maus et al., 2020). Synapses of mossy fibers, which exhibit a lower P_r (Lawrence et al., 2004) compared to Schaffer collateral synapses have a lower density of docked SVs (Maus et al., 2020). This relationship seems not to be a general rule for central synapses as demonstrated by Xu-Friedman et al.: The comparison of two types of synapses that contact cerebellar Purkinje cells revealed that climbing fiber synapses with a high P_r had the same number of docked SVs as synapses of parallel fibers with a low P_r (Xu-Friedman et al., 2001). This suggests that the number of SVs released per AZ is not only defined by the number of morphologically docked SVs.

4.6.2 Changes of release probability during development of endbulb AZs and lack of activity?

By investigating P_r at endbulb AZs of mice in different acoustic conditions, Zhuang et al. observed a dependency of P_r on activity for endbulbs and concluded that changes in P_r are rather a process to adapt to acoustic environments than a developmental process (Zhuang et al., 2020). In the mentioned study, mice of different ages after the hearing onset (from P12 on) were tested, but the P_r was not compared to that of mice of a pre-hearing age. However, McKay and Oleskevich revealed that P_r and RRP size at endbulbs of CBA wt mice were not changed upon onset of hearing (McKay & Oleskevich, 2007), which supports the statement of Zhuang et al. and might further explain the consistent number of docked SVs during maturation of wt mice found in this thesis.

The constant P_r and RRP size between P7-11 and P13-16 *deafness* mice (McKay & Oleskevich, 2007) could further explain the unchanged density of docked SVs that I detected at P10 and P22 *Otof*^{-/-} AZs. In line with my observations comparing P10 wt and *Otof*^{-/-} AZs, the comparison to wt CBA mice revealed normal presynaptic functions of *deafness* mice at the age of P7-11, indicated by similar numbers of AZs, P_r and RRP size (McKay & Oleskevich, 2007). At the age of P13-P16, endbulbs of *deafness* mice revealed a higher P_r compared to age-matched wt mice (McKay & Oleskevich, 2007; Oleskevich & Walmsley, 2002). This is consistent with observations by Zhuang and colleagues who observed higher P_r at endbulb AZs from binaural-occluded CBA/CaJ mice (Zhuang et al., 2017). However, the RRP size was not significantly different between *deafness* and wt mice (McKay & Oleskevich, 2007), which matches comparable numbers of docked SVs at P21/22 wt and *Otof*^{-/-} AZs. These findings support the idea, that the P_r is generally not only defined by the number of docked SVs. So far, there are no such functional studies for adult mice to which the structural findings observed in this study can be compared.

4.6.3 Release probability at endbulbs lacking presynaptic proteins

The relationship between P_r and the structure and organization of AZs at endbulbs of Held was previously investigated using mutant mice. Absence of the large scaffold protein piccolo (Fenster et al., 2000) resulted in a reduced RRP size and fewer SVs at the AZ membrane, while the P_r remained largely unchanged at endbulb synapses (Butola, 2017). In contrast, disruption of *bassoon* (tom Dieck et al., 1998) resulted functionally in an increased P_r at 333 Hz stimulation, while the RRP size decreased. Morphologically, larger AZs with a higher number of SVs within zero to 40 nm from the AZ membrane (normalized to the PSD length) were found. The number of SVs in direct contact to the AZ membrane was unaltered (Mendoza Schulz et al., 2014). RIM-BP2 and Mover are binding partners of bassoon (Davydova et al.,

2014; Kremer et al., 2007) and their roles in the organization of endbulb AZs will be discussed in the following section.

4.7 RIM-BP2 and Mover mediate tethering and docking of synaptic vesicles

Deletion of the CAZ protein RIM-BP2 resulted in an impairment of sound encoding as shown by elevated ABR thresholds and reduced amplitudes of wave I and wave III (Krinner et al., 2017) that are generated by firing of ANFs and neurons within the CN, respectively (Hall, 2007). At endbulbs, a reduced peak onset firing rate and a reduction in evoked EPSC amplitude was found, illustrating that the temporal precision of synaptic transmission was impaired (Butola et al., 2021). In contrast to RIM-BP2, Mover is vertebrate-specific and heterogeneously expressed across brain areas, within brain regions and between synapse types, as shown for e.g. hippocampus, amygdala and cerebellum (Wallrafen & Dresbach, 2018). In the auditory pathway, Mover was found to be expressed in the calyx of Held (Körber et al., 2015) and at excitatory and inhibitory synapses contacting BCs in the AVCN (Mendoza Schulz et al., 2014; Wallrafen, 2019). The functional role of Mover was studied in the calyx of Held of rats (Körber et al., 2015) and mice (Pofantis et al., 2021), where it was found to modulate synaptic transmission by regulating P_r . Its functional role within the AVCN is not known so far, but since disruption of *bassoon* resulted in a downregulation of *Mover* in endbulb terminals (Mendoza Schulz et al., 2014), a role of Mover in regulating synaptic transmission can be suggested.

While Ca^{2+} currents in *RIM-BP2*^{-/-} endbulbs were comparable to that of wt endbulbs (Butola et al., 2021), RIM-BP2 seem to contribute to the organization of VGCCs at endbulb AZs; The number of VGCCs was found to be reduced at *RIM-BP2*-deficient AZs and the distance of VGCCs to AZs, marked by bassoon clusters in freeze-fracture replica immunolabeling was increased (Butola et al., 2021). The altered topography of VGCCs was suggested to cause the reduced P_r at endbulb AZs of mice lacking *RIM-BP2* (Butola et al., 2021).

Similar to maturation from pre-hearing to hearing, the lack of neither *RIM-BP2* nor *Mover* did affect overall SV numbers at endbulb AZs (Fig. 3.17C,D and 3.20B). In contrast to *Mover*, *RIM-BP2* disruption resulted in a lower density of docked SVs at endbulb AZs (Fig. 3.17E), which might contribute to the lower P_r . The reduction of SV docking might also indicate a role of RIM-BP2 in SV priming via its interaction with Munc13-1 (Brockmann et al., 2020). The level of Munc13 was not affected by the disruption of *RIM-BP2* (Butola et al., 2021), but the severe deficits in SV docking observed in *C. elegans* (Weimer et al., 2006) and mice (Imig et al., 2014; Siksou et al., 2009) lacking UNC-13/Munc13 might partially depend on the interaction with RIM-BP2. Inconsistent with the reduced number of docked SVs at *RIM-BP2*^{-/-} AZs, no

difference in the RRP size could be observed (Butola et al., 2021). Only a trend towards a smaller RRP was found when presynaptic Ca^{2+} influx was elevated that in turn restored P_r . However, the first evoked EPSC amplitude was still lower in the absence of *RIM-BP2* suggesting a deficit in superprimed or tightly docked SVs (Butola et al., 2021). The remaining docked SVs seem to localize more randomly at the AZ membrane of *RIM-BP2*^{-/-} endbulbs since they tend to be further away from the estimated AZ center (Fig. 3.18D), possibly due to the missing RIM-BP2-mediated interaction with VGCCs. Besides docked SVs, also the density of membrane-proximal SVs (Table S9) and SVs within 2-20 nm from the AZ membrane were reduced at *RIM-BP2*^{-/-} AZs (Fig. 3.17E). This contrasts the findings on synapses lacking Munc13, in which an increase in SV numbers within 5–20 nm was observed (Imig et al., 2014). Interestingly, I observed a decline of membrane-proximal SVs at *Mover*^{-/-} endbulb AZs (Fig. 3.20C). It needs to be considered that the AVCN of *Mover*^{-/-} mice were chemically fixed, but these findings seem to be quite robust, since similar observations were made at endbulbs of mice that lack the Mover-interaction partner *bassoon* (Mendoza Schulz et al., 2014).

At inhibitory synapses on BCs, the deletion of *bassoon* did not affect the expression of Mover (Mendoza Schulz et al., 2014) suggesting a rather *bassoon*-independent function of Mover. In general, SV numbers at inhibitory synapses were higher than at endbulb AZs, but their number was not dependent on the expression of Mover. Surprisingly, the SV distribution at endbulb AZs and inhibitory synapses was differently affected upon deletion of *Mover*. In contrast to endbulb AZs, a higher fractions of docked SVs and a higher ratio of docked and membrane-proximal SVs was found at inhibitory synapses of *Mover*^{-/-} mice (Fig. 3.20F,G). This suggests a synapse-specific function of Mover.

These findings imply that both, Mover and RIM-BP2, might regulate P_r and contribute to its variability at endbulb AZs. While Mover might function as an adapter protein between SVs and *bassoon* keeping or recruiting SVs in membrane proximity, RIM-BP2 seems to be involved in tethering and docking of SVs to the AZ membrane. In addition, RIM-BP2 might contribute to a tight coupling of VGCCs and the release machinery at endbulbs as shown before for *Drosophila* larval neuromuscular junctions (Liu et al., 2011; Petzoldt et al., 2020) and murine hippocampal as well as calyx of Held synapses (Acuna et al., 2015). At inhibitory synapses, my results suggest a role of Mover in modulating SV docking, but this hypothesis needs to be confirmed with functional studies on inhibitory synapses.

Taken together, the lack of presynaptic proteins disturbs the structural integrity of the release machinery at endbulbs, which might *per se* have an impact on the P_r . For future studies it would be interesting to investigate if P_r changes upon adulthood and depletion of *otoferlin*. Further, the expression and composition of pre- and postsynaptic proteins and the location of

VGCCs at the AZ membrane might determine the maturation of endbulb AZs that allows high-frequency firing with high temporal fidelity.

5 Conclusion and Outlook

In the present thesis, I used HFP/FS followed by electron tomography of freshly sliced AVCN to investigate ultrastructural changes at endbulb synapses in a near-to-native state.

Early maturation of the auditory system from pre-hearing to hearing was not found to be characterized by morphological changes on the level of individual endbulb of Held AZs. Two scenarios are conceivable: (i) The structure of AZs is already so well prepared for sound-evoked activity at the age of P10. (ii) Functional maturation is not reflected by morphological changes. Since it has been shown that functional maturation is completed by P18 (Müller et al., 2019), I would rather exclude the possibility, that morphological changes primarily due to maturation happens after P21. I would suggest that the observed changes in the ultrastructure upon adulthood in wt are not related to the onset of hearing, but rather to advancing auditory experience. To further evaluate the reason for the lack of morphological changes between P10 and P21, the endbulb AZs should be investigated at younger ages. At the calyx of Held, maturation was investigated using immature rats at the age of P5 (Taschenberger et al., 2002) and mice at P7 (Thomas et al., 2019). Although McKay and Oleskevich did not find differences in functional synaptic properties within the P7-11 or the P13-16 age group (McKay & Oleskevich, 2007), differences in the ultrastructure cannot be excluded.

In contrast to the missing changes in SV pools between wt P10 and P21, I detected clear differences in the structure of mitochondria at endbulb terminals that indicate higher energy demands after the hearing onset. A higher ATP production might be necessary for improved temporal fidelity of endbulbs. For future studies it would be interesting to analyze if mitochondrial structure is different in the *Otof*^{-/-} mice. The lack of auditory input might alter neuronal metabolism that might be reflected by decreased CM densities and mitochondrial volumes. This analysis may uncover changes between the P10 and P22 mice that do not show differences regarding their AZ organization.

Similar to the findings on the development of *Otof*^{-/-} mice upon adulthood in the present study, endbulbs of deaf cats were shown to exhibit variable SV densities with some comparable to hearing cats and some with considerably fewer SVs (Ryugo et al., 1997). In addition, distinctly large mitochondria were observed in some endbulbs of deaf cats (Ryugo et al., 1997), although their average size was comparable between deaf and normal hearing cats throughout development (Baker et al., 2010). In endbulbs of deaf 7-months-old *shaker-2* mice, the mean mitochondrial volume fraction was smaller compared to hearing control mice, indicating decreased metabolic activity upon prolonged deafness. For a better understanding of long-term consequences of the absent neuronal activity and deafness on metabolic activity at endbulbs, it is important to investigate mitochondrial ultrastructure also in adult *Otof*^{-/-} mice in comparison to hearing wt mice. Mitochondrial disorders are often associated with hearing

impairments (Chinnery et al., 2000; Scarpelli et al., 2012). Conversely, a disturbed mitochondrial structure could also be a consequence of the lack of activity in the deaf *Otof*^{-/-} mice that in turn could indicate degenerative processes.

To complete the morphological studies, it would be important for future studies to examine the changes during development and the absence of auditory input at the level of complete endbulb terminals. This way, changes on the ultrastructural level reported in this thesis could be related to changes on the overall endbulb morphology. Large volume 3D imaging like FIB- or SBF-SEM would be required to image whole BCs with all their contacting endbulb terminals. FIB-SEM allows a great z-resolution but is limited in x and y dimensions. The imaging of the big BCs with all branches of endbulb was not possible. With SBF-SEM, larger areas can be imaged, but the z-resolution, which is determined by the section thickness, does not allow e.g. segmentation of the SV pool or the mitochondrial CMs. Ideally, the methods need to be combined to get the whole picture of the endbulb morphology, but both, recording and segmentation are expensive and time-consuming processes. There is a lot of effort to improve auto-segmentation based on machine learning, but until now, this does not work reliably for segmentation of different cellular and subcellular structures in tissues.

To understand the reason for the findings on endbulb morphology due to development and lack of auditory activity it would be interesting to move towards more functional investigations. Important questions are for instance if the level and distribution of VGCCs and presynaptic proteins like Munc13, piccolo and bassoon changes throughout development in wt and *Otof*^{-/-} mice. Also, if e.g. the distribution of AMPA receptors in the postsynaptic membrane differs between wt and *Otof*^{-/-} mice at different ages. Immunolabelling techniques like confocal imaging, SDS-freeze-fracture replica immunolabeling or immunogold labeling could help to answer these kinds of questions.

To gain more insights into the structure-function relationship at endbulb terminals, a combination of acute activity induction, immediate freezing and ultrastructural investigations is needed. With the use of channelrhodopsin2 (ChR2), synaptic activity can be induced precisely by light and tissue can be stimulated inside the HPM and frozen immediately afterwards (Watanabe, 2016). This methodology was established by Dr. Rituparna Chakrabarti (Institute for Auditory Neuroscience, University Medical Center Göttingen) for the cochlea. The duration and intensity of the stimulation can be controlled and the freezing timepoint can be calculated. A possible model of this approach is the Ai32xNeurogenin1-Cre mouse that shows ChR2 expression in SGNs (shown by Christian Vogl, Institute for Auditory Neuroscience, University Medical Center Göttingen).

6 Bibliography

- Acuna, C., Liu, X., Gonzalez, A., & Südhof, T. C. (2015). RIM-BPs Mediate Tight Coupling of Action Potentials to Ca²⁺-Triggered Neurotransmitter Release. *Neuron*, *87*(6), 1234–1247.
- Ahmed, S., Wittenmayer, N., Kremer, T., Hoeber, J., Kiran Akula, A., Urlaub, H., Islinger, M., Kirsch, J., Dean, C., & Dresbach, T. (2013). Mover is a homomeric phospho-protein present on synaptic vesicles. *PLoS One*, *8*(5), e63474.
- Akula, A. K., Zhang, X., Viotti, J. S., Nestvogel, D., Rhee, J.-S., Ebrecht, R., Reim, K., Wouters, F., Liepold, T., Jahn, O., Bogeski, I., & Dresbach, T. (2019). The Calmodulin Binding Region of the Synaptic Vesicle Protein Mover Is Required for Homomeric Interaction and Presynaptic Targeting. *Frontiers in Molecular Neuroscience*, *12*.
- Al-Moyed, H., Cepeda, A. P., Jung, S., Moser, T., Kügler, S., & Reisinger, E. (2019). A dual-AAV approach restores fast exocytosis and partially rescues auditory function in deaf otoferlin knock-out mice. *EMBO Molecular Medicine*, *11*(1), e9396.
- Anderson, D. W., Probst, F. J., Belyantseva, I. A., Fridell, R. A., Beyer, L., Martin, D. M., Wu, D., Kachar, B., Friedman, T. B., Raphael, Y., & Camper, S. A. (2000). The motor and tail regions of myosin XV are critical for normal structure and function of auditory and vestibular hair cells. *Human Molecular Genetics*, *9*(12), 1729–1738.
- Antunes, F. M., Rubio, M. E., & Kandler, K. (2020). Role of GluA3 AMPA Receptor Subunits in the Presynaptic and Postsynaptic Maturation of Synaptic Transmission and Plasticity of Endbulb–Bushy Cell Synapses in the Cochlear Nucleus. *The Journal of Neuroscience*, *40*(12), 2471–2484.
- Augustin, I., Rosenmund, C., Südhof, T. C., & Brose, N. (1999). Munc13-1 is essential for fusion competence of glutamatergic synaptic vesicles. *Nature*, *400*(6743), 457–461.
- Babola, T. A., Li, S., Gribizis, A., Lee, B. J., Issa, J. B., Wang, H. C., Crair, M. C., & Bergles, D. E. (2018). Homeostatic control of spontaneous activity in the developing auditory system. *Neuron*, *99*(3), 511–524.e5.
- Bai, J., Wang, P., & Chapman, E. R. (2002). C2A activates a cryptic Ca²⁺-triggered membrane penetration activity within the C2B domain of synaptotagmin I. *Proceedings of the National Academy of Sciences of the United States of America*, *99*(3), 1665–1670.
- Baker, C. A., Montey, K. L., Pongstaporn, T., & Ryugo, D. K. (2010). *Postnatal Development of the Endbulb of Held in Congenitally Deaf Cats*. *4*(19).
- Bellingham, M. C., Lim, R., & Walmsley, B. (1998). Developmental changes in EPSC quantal size and quantal content at a central glutamatergic synapse in rat. *The Journal of Physiology*, *511*(3), 861–869.
- Beltran-Parrazal, L., López-Valdés, H. E., Brennan, K. C., Díaz-Muñoz, M., de Vellis, J., & Charles, A. C. (2006). Mitochondrial transport in processes of cortical neurons is independent of intracellular calcium. *American Journal of Physiology. Cell Physiology*, *291*(6), C1193–1197.
- Beurg, M., Michalski, N., Safieddine, S., Bouleau, Y., Schneggenburger, R., Chapman, E. R., Petit, C., & Dulon, D. (2010). Control of exocytosis by synaptotagmins and otoferlin in auditory hair cells. *The Journal of Neuroscience: The Official Journal of the Society for Neuroscience*, *30*(40), 13281–13290.
- Beyer, L. A., Odeh, H., Probst, F. J., Lambert, E. H., Dolan, D. F., Camper, S. A., Kohrman, D. C., & Raphael, Y. (2000). Hair cells in the inner ear of the pirouette and shaker 2 mutant mice. *Journal of Neurocytology*, *29*(4), 227–240.

- Billups, B., & Forsythe, I. D. (2002). Presynaptic Mitochondrial Calcium Sequestration Influences Transmission at Mammalian Central Synapses. *The Journal of Neuroscience*, 22(14), 5840–5847.
- Birks, R., & MacIntosh, F. C. (2011). ACETYLCHOLINE METABOLISM OF A SYMPATHETIC GANGLION. *Canadian Journal of Biochemistry and Physiology*.
- Brawer, J. R., Morest, D. K., & Kane, E. C. (1974). The neuronal architecture of the cochlear nucleus of the cat. *Journal of Comparative Neurology*, 155(3), 251–299.
- Brenowitz, S., & Trussell, L. O. (2001). Maturation of Synaptic Transmission at End-Bulb Synapses of the Cochlear Nucleus. *The Journal of Neuroscience*, 21(23), 9487–9498.
- Brockmann, M. M., Zarebidaki, F., Camacho, M., Grauel, M. K., Trimbuch, T., Südhof, T. C., & Rosenmund, C. (2020). A Trio of Active Zone Proteins Comprised of RIM-BPs, RIMs, and Munc13s Governs Neurotransmitter Release. *Cell Reports*, 32(5), 107960.
- Brose, N., Petrenko, A. G., Südhof, T. C., & Jahn, R. (1992). Synaptotagmin: A calcium sensor on the synaptic vesicle surface. *Science (New York, N.Y.)*, 256(5059), 1021–1025.
- Brownell, W. E. (1975). Organization of the cat trapezoid body and the discharge characteristics of its fibers. *Brain Research*, 94(3), 413–433.
- Brownell, W. E. (1990). Outer Hair Cell Electromotility and Otoacoustic Emissions. *Ear and Hearing*, 11(2), 82–92.
- Butola, T., Alvanos, T., Hintze, A., Koppensteiner, P., Kleindienst, D., Shigemoto, R., Wichmann, C., & Moser, T. (2021). RIM-Binding Protein 2 Organizes Ca²⁺ Channel Topography and Regulates Release Probability and Vesicle Replenishment at a Fast Central Synapse. *Journal of Neuroscience*, 41(37), 7742–7767.
- Butola, T., Wichmann, C., & Moser, T. (2017). Piccolo Promotes Vesicle Replenishment at a Fast Central Auditory Synapse. *Frontiers in Synaptic Neuroscience*, 9, 14.
- Cant, N. B. (1981). The fine structure of two types of stellate cells in the anterior division of the anteroventral cochlear nucleus of the cat. *Neuroscience*, 6(12), 2643–2655.
- Cant, N. B., & Morest, D. K. (1979). The bushy cells in the anteroventral cochlear nucleus of the cat. A study with the electron microscope. *Neuroscience*, 4(12), 1925–1945.
- Cao, X. J., McGinley, M. J., & Oertel, D. (2008). Connections and synaptic function in the posteroventral cochlear nucleus of deaf jerker mice. *The Journal of Comparative Neurology*, 510(3), 297–308.
- Cao, X.-J., & Oertel, D. (2010). Auditory Nerve Fibers Excite Targets Through Synapses That Vary in Convergence, Strength, and Short-Term Plasticity. *Journal of Neurophysiology*, 104(5), 2308–2320.
- Chakrabarti, R., Michanski, S., & Wichmann, C. (2018). Vesicle sub-pool organization at inner hair cell ribbon synapses. *EMBO Reports*, e44937.
- Chakrabarti, R. (2017). *Investigation of Vesicle Pool Dynamics at Activity Modulated Inner Hair Cell Ribbon Synapses*. Göttingen.
- Chandel, N. S. (2014). Mitochondria as signaling organelles. *BMC Biology*, 12(1), 34.
- Chang, D. T. W., Honick, A. S., & Reynolds, I. J. (2006). Mitochondrial trafficking to synapses in cultured primary cortical neurons. *The Journal of Neuroscience: The Official Journal of the Society for Neuroscience*, 26(26), 7035–7045.
- Chang, S., Trimbuch, T., & Rosenmund, C. (2018). Synaptotagmin-1 drives synchronous Ca²⁺-triggered fusion by C2B-domain-mediated synaptic-vesicle-membrane attachment. *Nature Neuroscience*, 21(1), 33–40.
- Chinnery, P. F., Elliott, C., Green, G. R., Rees, A., Coulthard, A., Trunbull, D. M., Griffiths, T. D. (2000). The spectrum of hearing loss due to mitochondrial DNA defects. *Brain*, vol. 123, no. 1, pp. 82–92.

- Clarkson, C., Antunes, F. M., & Rubio, M. E. (2016). Conductive Hearing Loss Has Long-Lasting Structural and Molecular Effects on Presynaptic and Postsynaptic Structures of Auditory Nerve Synapses in the Cochlear Nucleus. *The Journal of Neuroscience*, 36(39), 10214–10227.
- Clayton, E. L., Evans, G. J. O., & Cousin, M. A. (2008). Bulk Synaptic Vesicle Endocytosis Is Rapidly Triggered during Strong Stimulation. *The Journal of Neuroscience*, 28(26), 6627–6632.
- Cogliati, S., Enriquez, J. A., & Scorrano, L. (2016). Mitochondrial Cristae: Where Beauty Meets Functionality. *Trends in Biochemical Sciences*, 41(3), 261–273.
- Cogliati, S., Frezza, C., Soriano, M. E., Varanita, T., Quintana-Cabrera, R., Corrado, M., Cipolat, S., Costa, V., Casarin, A., Gomes, L. C., Perales-Clemente, E., Salvati, L., Fernandez-Silva, P., Enriquez, J. A., & Scorrano, L. (2013). Mitochondrial cristae shape determines respiratory chain supercomplexes assembly and respiratory efficiency. *Cell*, 155(1), 160–171.
- Cole, A. A., Chen, X., & Reese, T. S. (2016). A Network of Three Types of Filaments Organizes Synaptic Vesicles for Storage, Mobilization, and Docking. *Journal of Neuroscience*, 36(11), 3222–3230.
- Colonnier, M. (1968). Synaptic patterns on different cell types in the different laminae of the cat visual cortex. An electron microscope study. *Brain Research*, 9(2), 268–287.
- Cserép, C., Pósfai, B., Schwarcz, A. D., & Dénes, Á. (2018). Mitochondrial Ultrastructure Is Coupled to Synaptic Performance at Axonal Release Sites. *ENeuro*, 5(1).
- Daniels, R. W., Collins, C. A., Chen, K., Gelfand, M. V., Featherstone, D. E., & DiAntonio, A. (2006). A Single Vesicular Glutamate Transporter Is Sufficient to Fill a Synaptic Vesicle. *Neuron*, 49(1), 11–16.
- Daniels, R. W., Collins, C. A., Gelfand, M. V., Dant, J., Brooks, E. S., Krantz, D. E., & DiAntonio, A. (2004). Increased expression of the *Drosophila* vesicular glutamate transporter leads to excess glutamate release and a compensatory decrease in quantal content. *The Journal of Neuroscience: The Official Journal of the Society for Neuroscience*, 24(46), 10466–10474.
- David, G., & Barrett, E. F. (2003). Mitochondrial Ca²⁺ uptake prevents desynchronization of quantal release and minimizes depletion during repetitive stimulation of mouse motor nerve terminals. *The Journal of Physiology*, 548(Pt 2), 425–438.
- Davies, K. M., Strauss, M., Daum, B., Kief, J. H., Osiewacz, H. D., Rycovska, A., Zickermann, V., & Kühlbrandt, W. (2011). Macromolecular organization of ATP synthase and complex I in whole mitochondria. *Proceedings of the National Academy of Sciences of the United States of America*, 108(34), 14121–14126.
- Davis, A. F., Bai, J., Fasshauer, D., Wolowick, M. J., Lewis, J. L., & Chapman, E. R. (1999). Kinetics of synaptotagmin responses to Ca²⁺ and assembly with the core SNARE complex onto membranes. *Neuron*, 24(2), 363–376.
- Davydova, D., Marini, C., King, C., Klueva, J., Bischof, F., Romorini, S., Montenegro-Venegas, C., Heine, M., Schneider, R., Schröder, M. S., Altmann, W. D., Henneberger, C., Rusakov, D. A., Gundelfinger, E. D., & Fejtova, A. (2014). Bassoon specifically controls presynaptic P/Q-type Ca(2+) channels via RIM-binding protein. *Neuron*, 82(1), 181–194.
- Deng, L., Kaeser, P. S., Xu, W., & Südhof, T. C. (2011). RIM proteins activate vesicle priming by reversing autoinhibitory homodimerization of Munc13. *Neuron*, 69(2), 317–331.
- Denk, W., & Horstmann, H. (2004). Serial block-face scanning electron microscopy to reconstruct three-dimensional tissue nanostructure. *PLoS Biology*, 2(11), e329.

- Denker, A., Kröhnert, K., & Rizzoli, S. O. (2009). Revisiting synaptic vesicle pool localization in the *Drosophila* neuromuscular junction. *The Journal of Physiology*, 587(Pt 12), 2919–2926.
- Denker, A., & Rizzoli, S. O. (2010). Synaptic Vesicle Pools: An Update. *Frontiers in Synaptic Neuroscience*, 2.
- Donaudy, F., Zheng, L., Ficarella, R., Ballana, E., Carella, M., Melchionda, S., Estivill, X., Bartles, J. R., & Gasparini, P. (2006). Espin gene (ESPN) mutations associated with autosomal dominant hearing loss cause defects in microvillar elongation or organisation. *Journal of Medical Genetics*, 43(2), 157–161.
- Dong, W., Radulovic, T., Goral, R. O., Thomas, C., Suarez Montesinos, M., Guerrero-Given, D., Hagiwara, A., Putzke, T., Hida, Y., Abe, M., Sakimura, K., Kamasawa, N., Ohtsuka, T., & Young, S. M. (2018). CAST/ELKS Proteins Control Voltage-Gated Ca²⁺ Channel Density and Synaptic Release Probability at a Mammalian Central Synapse. *Cell Reports*, 24(2), 284–293.e6.
- Ehret, G. (1974). Age-dependent hearing loss in normal hearing mice. *Die Naturwissenschaften*, 61(11), 506–507.
- Faits, M. C., Zhang, C., Soto, F., & Kerschensteiner, D. (2016). Dendritic mitochondria reach stable positions during circuit development. *ELife*, 5, e11583.
- Farsi, Z., Preobraschenski, J., Bogaart, G. van den, Riedel, D., Jahn, R., & Woehler, A. (2016). Single-vesicle imaging reveals different transport mechanisms between glutamatergic and GABAergic vesicles. *Science*, 351(6276), 981–984.
- Fasshauer, D., Sutton, R. B., Brunger, A. T., & Jahn, R. (1998). Conserved structural features of the synaptic fusion complex: SNARE proteins reclassified as Q- and R-SNAREs. *Proceedings of the National Academy of Sciences of the United States of America*, 95(26), 15781–15786.
- Fedchyshyn, M. J., & Wang, L.-Y. (2005). Developmental transformation of the release modality at the calyx of Held synapse. *The Journal of Neuroscience*, 25(16), 4131–4140.
- Fekete, A., Nakamura, Y., Yang, Y.-M., Herlitze, S., Mark, M. D., DiGregorio, D. A., & Wang, L.-Y. (2019). Underpinning heterogeneity in synaptic transmission by presynaptic ensembles of distinct morphological modules. *Nature Communications*, 10(1), 826.
- Fekete, D. M., Rouiller, E. M., Liberman, M. C., & Ryugo, D. K. (1984). The central projections of intracellularly labeled auditory nerve fibers in cats. *The Journal of Comparative Neurology*, 229(3), 432–450.
- Fenster, S. D., Chung, W. J., Zhai, R., Cases-Langhoff, C., Voss, B., Garner, A. M., Kaempfer, U., Kindler, S., Gundelfinger, E. D., & Garner, C. C. (2000). Piccolo, a Presynaptic Zinc Finger Protein Structurally Related to Bassoon. *Neuron*, 25(1), 203–214.
- Fernandez, I., Araç, D., Ubach, J., Gerber, S. H., Shin, O., Gao, Y., Anderson, R. G., Südhof, T. C., & Rizo, J. (2001). Three-dimensional structure of the synaptotagmin 1 C2B-domain: Synaptotagmin 1 as a phospholipid binding machine. *Neuron*, 32(6), 1057–1069.
- Fernández-Busnadiego, R., Asano, S., Oprisoreanu, A.-M., Sakata, E., Doengi, M., Kochovski, Z., Zürner, M., Stein, V., Schoch, S., Baumeister, W., & Lucić, V. (2013). Cryo-electron tomography reveals a critical role of RIM1 α in synaptic vesicle tethering. *The Journal of Cell Biology*, 201(5), 725–740.
- Fernández-Busnadiego, R., Zuber, B., Maurer, U. E., Cyrklaff, M., Baumeister, W., & Lučić, V. (2010). Quantitative analysis of the native presynaptic cytomatrix by cryoelectron tomography. *The Journal of Cell Biology*, 188(1), 145–156.

- Fitzpatrick, D. C., Batra, R., Stanford, T. R., & Kuwada, S. (1997). A neuronal population code for sound localization. *Nature*, 388, 871.
- Frey, T. G., Renken, C. W., & Perkins, G. A. (2002). Insight into mitochondrial structure and function from electron tomography. *Biochimica Et Biophysica Acta*, 1555(1–3), 196–203.
- García-Hernández, S., Abe, M., Sakimura, K., & Rubio, M. E. (2017). Impaired auditory processing and altered structure of the endbulb of Held synapse in mice lacking the GluA3 subunit of AMPA receptors. *Hearing Research*, 344, 284–294.
- Gardner, S. M., Trussell, L. O., & Oertel, D. (1999). Time Course and Permeation of Synaptic AMPA Receptors in Cochlear Nuclear Neurons Correlate with Input. *The Journal of Neuroscience*, 19(20), 8721–8729.
- Gardner, S. M., Trussell, L. O., & Oertel, D. (2001). Correlation of AMPA Receptor Subunit Composition with Synaptic Input in the Mammalian Cochlear Nuclei. *The Journal of Neuroscience*, 21(18), 7428–7437.
- Gerst, J. E. (1999). SNAREs and SNARE regulators in membrane fusion and exocytosis. *Cellular and Molecular Life Sciences: CMLS*, 55(5), 707–734.
- Gilkerson, R. W., Selker, J. M. L., & Capaldi, R. A. (2003). The cristal membrane of mitochondria is the principal site of oxidative phosphorylation. *FEBS Letters*, 546(2–3), 355–358.
- Glendenning, K. K., Baker, B. N., Hutson, K. A., & Masterton, R. B. (1992). Acoustic chiasm V: Inhibition and excitation in the ipsilateral and contralateral projections of LSO. *The Journal of Comparative Neurology*, 319(1), 100–122.
- Glowatzki, E., & Fuchs, P. A. (2002). Transmitter release at the hair cell ribbon synapse. *Nature Neuroscience*, 5(2), 147–154.
- Golding, N. L., & Oertel, D. (2012). Synaptic integration in dendrites: Exceptional need for speed. *The Journal of Physiology*, 590(Pt 22), 5563–5569.
- Gómez-Nieto, R., & Rubio, M. E. (2011). Ultrastructure, synaptic organization, and molecular components of bushy cell networks in the anteroventral cochlear nucleus of the rhesus monkey. *Neuroscience*, 179, 188–207.
- Gracheva, E. O., Hadwiger, G., Nonet, M. L., & Richmond, J. E. (2008). Direct interactions between *C. elegans* RAB-3 and Rim provide a mechanism to target vesicles to the presynaptic density. *Neuroscience Letters*, 444(2), 137–142.
- Grauel, M. K., Maglione, M., Reddy-Alla, S., Willmes, C. G., Brockmann, M. M., Trimbuch, T., Rosenmund, T., Pangalos, M., Vardar, G., Stumpf, A., Walter, A. M., Rost, B. R., Eickholt, B. J., Haucke, V., Schmitz, D., Sigrist, S. J., & Rosenmund, C. (2016). RIM-binding protein 2 regulates release probability by fine-tuning calcium channel localization at murine hippocampal synapses. *Proceedings of the National Academy of Sciences*, 113(41), 11615–11620.
- Gray, E. G. (1959). Axo-somatic and axo-dendritic synapses of the cerebral cortex. *Journal of Anatomy*, 93(Pt 4), 420–433.
- Gray, E. G. (1963). Electron microscopy of presynaptic organelles of the spinal cord. *Journal of Anatomy*, 97(Pt 1), 101–106.5.
- Grüneberg, H., Burnett, J. B., & Snell, G. D. (1941). The Origin of Jerker, a New Gene Mutation of the House Mouse, and Linkage Studies Made with It. *Proceedings of the National Academy of Sciences of the United States of America*, 27(12), 562–565.
- Gulley, R. L., & Reese, T. S. (1981). Cytoskeletal organization at the postsynaptic complex. *The Journal of Cell Biology*, 91(1), 298–302.

- Gundelfinger, E. D., Reissner, C., & Garner, C. C. (2015). Role of Bassoon and Piccolo in Assembly and Molecular Organization of the Active Zone. *Frontiers in Synaptic Neuroscience*, 7, 19.
- Hackenbrock, C. R. (1966). Ultrastructural bases for metabolically linked mechanical activity in mitochondria. I. Reversible ultrastructural changes with change in metabolic steady state in isolated liver mitochondria. *The Journal of Cell Biology*, 30(2), 269–297.
- Hall, J. W. (2007). *New handbook of auditory evoked responses*. Boston: Pearson.
- Han, Y., Kaeser, P. S., Südhof, T. C., & Schneggenburger, R. (2011). RIM Determines Ca²⁺ Channel Density and Vesicle Docking at the Presynaptic Active Zone. *Neuron*, 69(2), 304–316.
- Hannah, M. J., Schmidt, A. A., & Huttner, W. B. (1999). Synaptic vesicle biogenesis. *Annual Review of Cell and Developmental Biology*, 15, 733–798.
- Harris, K. M., & Weinberg, R. J. (2012). Ultrastructure of synapses in the mammalian brain. *Cold Spring Harbor Perspectives in Biology*, 4(5).
- Harrison, J. M., & Irving, R. (1965). The anterior ventral cochlear nucleus. *Journal of Comparative Neurology*, 124(1), 15–41.
- Held, H. (1893). Die centrale gehörleitung. *Arch. Anat. Physiol. Anat. Abt.*, 17, 201–248.
- Helmprobst, F., Frank, M., & Stigloher, C. (2015). Presynaptic architecture of the larval zebrafish neuromuscular junction. *The Journal of Comparative Neurology*, 523(13), 1984–1997.
- Hibino, H., Pironkova, R., Onwumere, O., Vologodskaja, M., Hudspeth, A. J., & Lesage, F. (2002). RIM - binding proteins (RBPs) couple Rab3—Interacting molecules (RIMs) to voltage—Gated Ca²⁺ channels. *Neuron*, 34(3), 411–423.
- Hida, Y., & Ohtsuka, T. (2010). CAST and ELKS proteins: Structural and functional determinants of the presynaptic active zone. *Journal of Biochemistry*, 148(2), 131–137.
- Hillman, H., & Deutsch, K. (1978). Area changes in slices of rat brain during preparation for histology or electron microscopy. *Journal of Microscopy*, 114(1), 77–84.
- Hintze, A., Gültas, M., Semmelhack, E. A., & Wichmann, C. (2021). Ultrastructural maturation of the endbulb of Held active zones comparing wild-type and otoferlin-deficient mice. *iScience*, 24(4), 102282.
- Hoffpauir, B. K., Grimes, J. L., Mathers, P. H., & Spirou, G. A. (2006). Synaptogenesis of the Calyx of Held: Rapid Onset of Function and One-to-One Morphological Innervation. *The Journal of Neuroscience*, 26(20), 5511–5523.
- Hu, Y., Qu, L., & Schikorski, T. (2008). Mean synaptic vesicle size varies among individual excitatory hippocampal synapses. *Synapse (New York, N. Y.)*, 62(12), 953–957.
- Imig, C., Min, S.-W., Krinner, S., Arancillo, M., Rosenmund, C., Südhof, T. C., Rhee, J., Brose, N., & Cooper, B. H. (2014). The morphological and molecular nature of synaptic vesicle priming at presynaptic active zones. *Neuron*, 84(2), 416–431.
- Isaacson, J. S., & Walmsley, B. (1995). Receptors Underlying Excitatory Synaptic Transmission in Slices of the Rat Anteroventral Cochlear Nucleus. *Journal of Neurophysiology*, 73(3), 964–973.
- Ivannikov, M. V., Sugimori, M., & Llinás, R. R. (2013). Synaptic vesicle exocytosis in hippocampal synaptosomes correlates directly with total mitochondrial volume. *Journal of Molecular Neuroscience: MN*, 49(1), 223–230.
- Iwasaki, S., Momiyama, A., Uchitel, O. D., & Takahashi, T. (2000). Developmental changes in calcium channel types mediating central synaptic transmission. *The Journal of Neuroscience: The Official Journal of the Society for Neuroscience*, 20(1), 59–65.

- Iwasaki, S., & Takahashi, T. (1998). Developmental changes in calcium channel types mediating synaptic transmission in rat auditory brainstem. *The Journal of Physiology*, 509 (Pt 2), 419–423.
- Iwasaki, S., & Takahashi, T. (2001). Developmental regulation of transmitter release at the calyx of Held in rat auditory brainstem. *The Journal of Physiology*, 534(Pt 3), 861–871.
- Johnson, C. P., & Chapman, E. R. (2010). Otoferlin is a calcium sensor that directly regulates SNARE-mediated membrane fusion. *The Journal of Cell Biology*, 191(1), 187–197.
- Jonas, E. A., Buchanan, J., & Kaczmarek, L. K. (1999). Prolonged activation of mitochondrial conductances during synaptic transmission. *Science (New York, N.Y.)*, 286(5443), 1347–1350.
- Joris, P. X., & Trussell, L. O. (2018). The Calyx of Held: A Hypothesis on the Need for Reliable Timing in an Intensity-Difference Encoder. *Neuron*, 100(3), 534–549.
- Jung, S., Maritzen, T., Wichmann, C., Jing, Z., Neef, A., Revelo, N. H., Al-Moyed, H., Meese, S., Wojcik, S. M., Panou, I., Bulut, H., Schu, P., Ficner, R., Reisinger, E., Rizzoli, S. O., Neef, J., Strenzke, N., Haucke, V., & Moser, T. (2015). Disruption of adaptor protein 2 μ (AP-2 μ) in cochlear hair cells impairs vesicle reloading of synaptic release sites and hearing. *The EMBO Journal*, 34(21), 2686–2702.
- Kaesler, P. S., Deng, L., Wang, Y., Dulubova, I., Liu, X., Rizo, J., & Südhof, T. C. (2011). RIM proteins tether Ca²⁺ channels to presynaptic active zones via a direct PDZ-domain interaction. *Cell*, 144(2), 282–295.
- Kaesler, P. S., & Regehr, W. G. (2017). The readily releasable pool of synaptic vesicles. *Current Opinion in Neurobiology*, 43, 63–70.
- Kalimo, H. (1976). The role of the blood-brain barrier in perfusion fixation of the brain for electron microscopy. *The Histochemical Journal*, 8(1), 1–12.
- Kandel, E. R., Schwartz, J. H., & Jessell, T. (2012). *Principles of neural science*. McGraw-Hill Medical.
- Kandler, K., Clause, A., & Noh, J. (2009). Tonotopic reorganization of developing auditory brainstem circuits. *Nature Neuroscience*, 12(6), 711–717.
- Kang, J.-S., Tian, J.-H., Pan, P.-Y., Zald, P., Li, C., Deng, C., & Sheng, Z.-H. (2008). Docking of axonal mitochondria by syntrophin controls their mobility and affects short-term facilitation. *Cell*, 132(1), 137–148.
- Karlsson, U., & Schultz, R. L. (1965). FIXATION OF THE CENTRAL NERVOUS SYSTEM FROM ELECTRON MICROSCOPY BY ALDEHYDE PERFUSION. I. PRESERVATION WITH ALDEHYDE PERFUSATES VERSUS DIRECT PERFUSION WITH OSMIUM TETROXIDE WITH SPECIAL REFERENCE TO MEMBRANES AND THE EXTRACELLULAR SPACE. *Journal of Ultrastructure Research*, 12, 160–186.
- Karunanithi, S., Marin, L., Wong, K., & Atwood, H. L. (2002). Quantal Size and Variation Determined by Vesicle Size in Normal and Mutant *Drosophila* Glutamatergic Synapses. *The Journal of Neuroscience*, 22(23), 10267–10276.
- Kaufmann, N., DeProto, J., Ranjan, R., Wan, H., & Vactor, D. V. (2002). *Drosophila* Liprin- α and the Receptor Phosphatase Dlar Control Synapse Morphogenesis. *Neuron*, 34(1), 27–38.
- Keats, B. J., Nouri, N., Huang, J. M., Money, M., Webster, D. B., & Berlin, C. I. (1995). The deafness locus (dn) maps to mouse chromosome 19. *Mammalian Genome: Official Journal of the International Mammalian Genome Society*, 6(1), 8–10.
- Keine, C., & Rübsamen, R. (2015). Inhibition Shapes Acoustic Responsiveness in Spherical Bushy Cells. *Journal of Neuroscience*, 35(22), 8579–8592.

- Kerschensteiner, D. (2014). Spontaneous network activity and synaptic development. *The Neuroscientist: A Review Journal Bringing Neurobiology, Neurology and Psychiatry*, 20(3), 272–290.
- Kiang, N. Y., Pfeiffer, R. R., Warr, W. B., & Backus, A. S. (1965). Stimulus coding in the cochlear nucleus. *Transactions of the American Otological Society*, 53, 35–58.
- Kim, D. O. (1986). Active and nonlinear cochlear biomechanics and the role of outer-hair-cell subsystem in the mammalian auditory system. *Hearing Research*, 22, 105–114.
- Ko, J., Na, M., Kim, S., Lee, J.-R., & Kim, E. (2003). Interaction of the ERC Family of RIM-binding Proteins with the Liprin- α Family of Multidomain Proteins*. *Journal of Biological Chemistry*, 278(43), 42377–42385.
- Koert, E., & Kuenzel, T. (2020). *Small dendritic synapses enhance temporal coding in a model of cochlear nucleus bushy cells* (p. 2020.06.03.131516). bioRxiv. <https://doi.org/10.1101/2020.06.03.131516>
- Kopp-Scheinflug, C., & Tempel, B. L. (2015). Decreased temporal precision of neuronal signaling as a candidate mechanism of auditory processing disorder. *Hearing Research*, 330, 213–220.
- Körber, C., Horstmann, H., Venkataramani, V., Herrmannsdörfer, F., Kremer, T., Kaiser, M., Schwenger, D. B., Ahmed, S., Dean, C., Dresbach, T., & Kuner, T. (2015). Modulation of Presynaptic Release Probability by the Vertebrate-Specific Protein Mover. *Neuron*, 87(3), 521–533.
- Korogod, N., Petersen, C. C., & Knott, G. W. (2015). Ultrastructural analysis of adult mouse neocortex comparing aldehyde perfusion with cryo fixation. *ELife*, 4, e05793. [h](https://doi.org/10.7554/eLife.05793)
- Koster, A. J., Grimm, R., Typke, D., Hegerl, R., Stoschek, A., Walz, J., & Baumeister, W. (1997). Perspectives of molecular and cellular electron tomography. *Journal of Structural Biology*, 120(3), 276–308.
- Koushika, S. P., Richmond, J. E., Hadwiger, G., Weimer, R. M., Jorgensen, E. M., & Nonet, M. L. (2001). A post-docking role for active zone protein Rim. *Nat Neurosci*, 4(10), 997–1005.
- Kremer, J. R., Mastronarde, D. N., & McIntosh, J. R. (1996). Computer visualization of three-dimensional image data using IMOD. *Journal of Structural Biology*, 116(1), 71–76.
- Kremer, T., Kempf, C., Wittenmayer, N., Nawrotzki, R., Kuner, T., Kirsch, J., & Dresbach, T. (2007). Mover is a novel vertebrate-specific presynaptic protein with differential distribution at subsets of CNS synapses. *FEBS Letters*, 581(24), 4727–4733.
- Krinner, S., Butola, T., Jung, S., Wichmann, C., & Moser, T. (2017). RIM-Binding Protein 2 Promotes a Large Number of CaV1.3 Ca²⁺-Channels and Contributes to Fast Synaptic Vesicle Replenishment at Hair Cell Active Zones. *Frontiers in Cellular Neuroscience*, 11, 334.
- Kuenzel, T. (2019). Modulatory influences on time-coding neurons in the ventral cochlear nucleus. *Hearing Research*, 384, 107824. <https://doi.org/10.1016/j.heares.2019.107824>
- Kujawa, S. G., & Liberman, M. C. (2019). Translating animal models to human therapeutics in noise-induced and age-related hearing loss. *Hearing Research*, 377, 44–52.
- Lauer, A. M., Connelly, C. J., Graham, H., & Ryugo, D. K. (2013). Morphological Characterization of Bushy Cells and Their Inputs in the Laboratory Mouse (*Mus musculus*) Anteroventral Cochlear Nucleus. *PLoS ONE*, 8(8), e73308.
- Lawrence, J. J., Grinspan, Z. M., & McBain, C. J. (2004). Quantal transmission at mossy fibre targets in the CA3 region of the rat hippocampus. *The Journal of Physiology*, 554(1), 175–193.

- Lawrence, J. J., & Trussell, L. O. (2000). Long-term specification of AMPA receptor properties after synapse formation. *The Journal of Neuroscience: The Official Journal of the Society for Neuroscience*, *20*(13), 4864–4870.
- Lee, D. J., Cahill, H. B., & Ryugo, D. K. (2003). Effects of congenital deafness in the cochlear nuclei of Shaker-2 mice: An ultrastructural analysis of synapse morphology in the endbulbs of Held. *Journal of Neurocytology*, *32*(3), 229–243.
- Lee, D., Lee, K.-H., Ho, W.-K., & Lee, S.-H. (2007). Target Cell-Specific Involvement of Presynaptic Mitochondria in Post-Tetanic Potentiation at Hippocampal Mossy Fiber Synapses. *Journal of Neuroscience*, *27*(50), 13603–13613.
- Lenn, N. J., & Reese, T. S. (1966). The fine structure of nerve endings in the nucleus of the trapezoid body and the ventral cochlear nucleus. *The American Journal of Anatomy*, *118*(2), 375–389.
- Lewis, T. L., Turi, G. F., Kwon, S.-K., Losonczy, A., & Polleux, F. (2016). Progressive Decrease of Mitochondrial Motility during Maturation of Cortical Axons In Vitro and In Vivo. *Current Biology: CB*, *26*(19), 2602–2608.
- Li, Z., Okamoto, K.-I., Hayashi, Y., & Sheng, M. (2004). The importance of dendritic mitochondria in the morphogenesis and plasticity of spines and synapses. *Cell*, *119*(6), 873–887.
- Liang, Y., Wang, A., Belyantseva, I. A., Anderson, D. W., Probst, F. J., Barber, T. D., Miller, W., Touchman, J. W., Jin, L., Sullivan, S. L., Sellers, J. R., Camper, S. A., Lloyd, R. V., Kachar, B., Friedman, T. B., & Fridell, R. A. (1999). Characterization of the human and mouse unconventional myosin XV genes responsible for hereditary deafness DFNB3 and shaker 2. *Genomics*, *61*(3), 243–258. h
- Lieberman, M. C. (1982). The cochlear frequency map for the cat: Labeling auditory-nerve fibers of known characteristic frequency. *The Journal of the Acoustical Society of America*, *72*(5), 1441–1449.
- Lieberman, M. C., Gao, J., He, D. Z. Z., Wu, X., Jia, S., & Zuo, J. (2002). *Prestin is required for electromotility of the outer hair cell and for the cochlear amplifier*. 419, 5.
- Lieberman, A. R., & Spacek, J. (1997). Filamentous contacts: The ultrastructure and three-dimensional organization of specialized non-synaptic interneuronal appositions in thalamic relay nuclei. *Cell and Tissue Research*, *288*(1), 43–57.
- Limb, C. J., & Ryugo, D. K. (2000). Development of Primary Axosomatic Endings in the Anteroventral Cochlear Nucleus of Mice. *Journal of the Association for Research in Otolaryngology*, *1*(2), 103–119.
- Lin, K.-H., Oleskevich, S., & Taschenberger, H. (2011). Presynaptic Ca²⁺ influx and vesicle exocytosis at the mouse endbulb of Held: A comparison of two auditory nerve terminals. *The Journal of Physiology*, *589*(17), 4301–4320.
- Littleton, J. T., Barnard, R. J. O., Titus, S. A., Slind, J., Chapman, E. R., & Ganetzky, B. (2001). SNARE-complex disassembly by NSF follows synaptic-vesicle fusion. *Proceedings of the National Academy of Sciences*, *98*(21), 12233–12238.
- Liu, K. S. Y., Siebert, M., Mertel, S., Knoche, E., Wegener, S., Wichmann, C., Matkovic, T., Muhammad, K., Depner, H., Mettke, C., Bückers, J., Hell, S. W., Müller, M., Davis, G. W., Schmitz, D., & Sigrist, S. J. (2011). RIM-binding protein, a central part of the active zone, is essential for neurotransmitter release. *Science (New York, N.Y.)*, *334*(6062), 1565–1569.
- Luo, F., Liu, X., Südhof, T. C., & Acuna, C. (2017). Efficient stimulus-secretion coupling at ribbon synapses requires RIM-binding protein tethering of L-type Ca²⁺ channels. *Proceedings of the National Academy of Sciences*, *114*(38), E8081–E8090. h

- Macaskill, A. F., Rinholm, J. E., Twelvetrees, A. E., Arancibia-Carcamo, I. L., Muir, J., Fransson, A., Aspenstrom, P., Attwell, D., & Kittler, J. T. (2009). Miro1 is a calcium sensor for glutamate receptor-dependent localization of mitochondria at synapses. *Neuron*, *61*(4), 541–555.
- Maler, L., & Mathieson, W. B. (1985). The effect of nerve activity on the distribution of synaptic vesicles. *Cellular and Molecular Neurobiology*, *5*(4), 373–387.
- Mannella, C. A. (2006). Structure and dynamics of the mitochondrial inner membrane cristae. *Biochimica Et Biophysica Acta*, *1763*(5–6), 542–548.
- Mannella, C. A., Marko, M., Penczek, P., Barnard, D., & Frank, J. (1994). The internal compartmentation of rat-liver mitochondria: Tomographic study using the high-voltage transmission electron microscope. *Microscopy Research and Technique*, *27*(4), 278–283.
- Mannella, C. A., Pfeiffer, D. R., Bradshaw, P. C., Moraru, I. I., Slepchenko, B., Loew, L. M., Hsieh, C. E., Buttle, K., & Marko, M. (2001). Topology of the mitochondrial inner membrane: Dynamics and bioenergetic implications. *IUBMB Life*, *52*(3–5), 93–100.
- Markus, E. J., Petit, T. L., & LeBoutillier, J. C. (1987). Synaptic structural changes during development and aging. *Brain Research*, *432*(2), 239–248.
- Mastrorarde, D. N. (2005). Automated electron microscope tomography using robust prediction of specimen movements. *Journal of Structural Biology*, *152*(1), 36–51.
- Maus, L., Lee, C., Altas, B., Sertel, S. M., Weyand, K., Rizzoli, S. O., Rhee, J., Brose, N., Imig, C., & Cooper, B. H. (2020). Ultrastructural Correlates of Presynaptic Functional Heterogeneity in Hippocampal Synapses. *Cell Reports*, *30*(11), 3632-3643.e8.
- McGuire, B., Fiorillo, B., Ryugo, D. K., & Lauer, A. M. (2015). Auditory nerve synapses persist in ventral cochlear nucleus long after loss of acoustic input in mice with early-onset progressive hearing loss. *Brain Research*, *1605*, 22–30.
- McKay, S. M., & Oleskevich, S. (2007). The role of spontaneous activity in development of the endbulb of Held synapse. *Hearing Research*, *230*(1–2), 53–63.
- Medler, K., & Gleason, E. L. (2002). Mitochondrial Ca(2+) buffering regulates synaptic transmission between retinal amacrine cells. *Journal of Neurophysiology*, *87*(3), 1426–1439.
- Mendoza Schulz, A., Jing, Z., María Sánchez Caro, J., Wetzelsch, F., Dresbach, T., Strenzke, N., Wichmann, C., & Moser, T. (2014). Bassoon-disruption slows vesicle replenishment and induces homeostatic plasticity at a CNS synapse. *EMBO Journal*, *33*(5), 512–527.
- Mettlen, M., Chen, P.-H., Srinivasan, S., Danuser, G., & Schmid, S. L. (2018). Regulation of Clathrin-Mediated Endocytosis. *Annual Review of Biochemistry*, *87*, 871–896.
- Michalski, N. A., Goutman, J. D., Auclair, S. M., Monvel, J. B. de, Tertrais, M., Emptoz, A., Parrin, A., Nouaille, S., Guillon, M., Sachse, M., Ciric, D., Bahloul, A., Hardelin, J.-P., Sutton, R. B., Avan, P., Krishnakumar, S. S., Rothman, J. E., Dulon, D., Safieddine, S., & Petit, C. (2017). Otoferlin acts as a Ca²⁺ sensor for vesicle fusion and vesicle pool replenishment at auditory hair cell ribbon synapses. *ELife*, *6*, e31013.
- Michanski, S., Smaluch, K., Steyer, A. M., Chakrabarti, R., Setz, C., Oestreicher, D., Fischer, C., Möbius, W., Moser, T., Vogl, C., & Wichmann, C. (2019). Mapping developmental maturation of inner hair cell ribbon synapses in the apical mouse cochlea. *Proceedings of the National Academy of Sciences*, *116*(13), 6415–6424.
- Mikaelian, D., & Ruben, R. J. (1965). Development of Hearing in the Normal Cba-J Mouse: Correlation of Physiological Observations with Behavioral Responses and with Cochlear Anatomy. *Acta Oto-Laryngologica*, *59*(2–6), 451–461.
- Milosevic, I. (2018). Revisiting the Role of Clathrin-Mediated Endocytosis in Synaptic Vesicle Recycling. *Frontiers in Cellular Neuroscience*, *12*, 27.

- Mittelstaedt, T., & Schoch, S. (2007). Structure and evolution of RIM-BP genes: Identification of a novel family member. *Gene*, *403*(1–2), 70–79.
- Moser, T., Neef, A., & Khimich, D. (2006). Mechanisms underlying the temporal precision of sound coding at the inner hair cell ribbon synapse. *The Journal of Physiology*, *576*(1), 55–62.
- Mukherjee, K., Yang, X., Gerber, S. H., Kwon, H.-B., Ho, A., Castillo, P. E., Liu, X., & Südhof, T. C. (2010). Piccolo and bassoon maintain synaptic vesicle clustering without directly participating in vesicle exocytosis. *Proceedings of the National Academy of Sciences of the United States of America*, *107*(14), 6504–6509.
- Müller, M. K., Jovanovic, S., Keine, C., Radulovic, T., Rübsamen, R., & Milenkovic, I. (2019). Functional Development of Principal Neurons in the Anteroventral Cochlear Nucleus Extends Beyond Hearing Onset. *Frontiers in Cellular Neuroscience*, *13*.
- Murthy, V. N., Schikorski, T., Stevens, C. F., & Zhu, Y. (2001). Inactivity Produces Increases in Neurotransmitter Release and Synapse Size. *Neuron*, *32*(4), 673–682.
- Nakamura, N., Miyake, Y., Matsushita, M., Tanaka, S., Inoue, H., & Kanazawa, H. (2002). KIF1B β 2, Capable of Interacting with CHP, Is Localized to Synaptic Vesicles1. *The Journal of Biochemistry*, *132*(3), 483–491.
- Naz, S., Griffith, A., Riazuddin, S., Hampton, L., Battey, J., Khan, S., Riazuddin, S., Wilcox, E., & Friedman, T. (2004). Mutations of ESPN cause autosomal recessive deafness and vestibular dysfunction. *Journal of Medical Genetics*, *41*(8), 591–595.
- Neher, E., & Brose, N. (2018). Dynamically Primed Synaptic Vesicle States: Key to Understand Synaptic Short-Term Plasticity. *Neuron*, *100*(6), 1283–1291.
- Nelson, N., & Lill, H. (1994). Porters and neurotransmitter transporters. *Journal of Experimental Biology*, *196*(1), 213–228.
- Nguyen, T. H., Maucort, G., Sullivan, R. K. P., Schenning, M., Lavidis, N. A., McCluskey, A., Robinson, P. J., & Meunier, F. A. (2012). Actin- and Dynamin-Dependent Maturation of Bulk Endocytosis Restores Neurotransmission following Synaptic Depletion. *PLoS ONE*, *7*(5), e36913.
- Nicol, M. J., & Walmsley, B. (2002). Ultrastructural basis of synaptic transmission between endbulbs of Held and bushy cells in the rat cochlear nucleus. *The Journal of Physiology*, *539*(3), 713.
- Noben-Trauth, K., Zheng, Q. Y., & Johnson, K. R. (2003). Association of cadherin 23 with polygenic inheritance and genetic modification of sensorineural hearing loss. *Nature Genetics*, *35*(1), 21–23.
- Oertner, T. G., Sabatini, B. L., Nimchinsky, E. A., & Svoboda, K. (2002). Facilitation at single synapses probed with optical quantal analysis. *Nature Neuroscience*, *5*(7), 657–664.
- Oghalai, J. S. (2004). The cochlear amplifier: Augmentation of the traveling wave within the inner ear. *Current Opinion in Otolaryngology & Head and Neck Surgery*, *12*(5), 431–438.
- Ohtsuka, T., Takao-Rikitsu, E., Inoue, E., Inoue, M., Takeuchi, M., Matsubara, K., Deguchi-Tawarada, M., Satoh, K., Morimoto, K., Nakanishi, H., & Takai, Y. (2002). Cast: A novel protein of the cytomatrix at the active zone of synapses that forms a ternary complex with RIM1 and munc13-1. *The Journal of Cell Biology*, *158*(3), 577–590.
- Okada, Y., Yamazaki, H., Sekine-Aizawa, Y., & Hirokawa, N. (1995). The neuron-specific kinesin superfamily protein KIF1A is a unique monomeric motor for anterograde axonal transport of synaptic vesicle precursors. *Cell*, *81*(5), 769–780.
- Okerlund, N. D., Schneider, K., Leal-Ortiz, S., Montenegro-Venegas, C., Kim, S. A., Garner, L. C., Gundelfinger, E. D., Reimer, R. J., & Garner, C. C. (2017). Bassoon Controls Presynaptic Autophagy through Atg5. *Neuron*, *93*(4), 897-913.e7.

- Oleskevich, S., Clements, J., & Walmsley, B. (2000). Release probability modulates short-term plasticity at a rat giant terminal. *The Journal of Physiology*, 524(Pt 2), 513–523.
- Oleskevich, S., & Walmsley, B. (2002). Synaptic transmission in the auditory brainstem of normal and congenitally deaf mice. *The Journal of Physiology*, 540(2), 447–455.
- O’Neil, J. N., Connelly, C. J., Limb, C. J., & Ryugo, D. K. (2011). Synaptic morphology and the influence of auditory experience. *Hearing Research, In Press, Corrected Proof*.
- Osen, K. K. (1969). Cytoarchitecture of the cochlear nuclei in the cat. *Journal of Comparative Neurology*, 136(4), 453–483.
- Pangrsic, T., Lasarow, L., Reuter, K., Takago, H., Schwander, M., Riedel, D., Frank, T., Tarantino, L. M., Bailey, J. S., Strenzke, N., Brose, N., Müller, U., Reisinger, E., & Moser, T. (2010). Hearing requires otoferlin-dependent efficient replenishment of synaptic vesicles in hair cells. *Nature Neuroscience*, 13(7), 869–876.
- Pangršič, T., Reisinger, E., & Moser, T. (2012). Otoferlin: A multi-C2 domain protein essential for hearing. *Trends in Neurosciences*, 35(11), 671–680.
- Parthier, D., Kuner, T., & Körber, C. (2018). The presynaptic scaffolding protein Piccolo organizes the readily releasable pool at the calyx of Held. *The Journal of Physiology*, 596(8), 1485–1499.
- Perkins, G. A., Renken, C., Frey, T. G., & Ellisman, M. H. (2001). Membrane architecture of mitochondria in neurons of the central nervous system. *Journal of Neuroscience Research*.
- Perkins, G. A., Song, J. Y., Tarsa, L., Deerinck, T. J., Ellisman, M. H., & Frey, T. G. (1998). Electron tomography of mitochondria from brown adipocytes reveals crista junctions. *Journal of Bioenergetics and Biomembranes*, 30(5), 431–442.
- Perkins, G. A., Tjong, J., Brown, J. M., Poquiz, P. H., Scott, R. T., Kolson, D. R., Ellisman, M. H., & Spirou, G. A. (2010). The Micro-Architecture of Mitochondria at Active Zones: Electron Tomography Reveals Novel Anchoring Scaffolds and Cristae Structured for High-Rate Metabolism. *The Journal of Neuroscience: The Official Journal of the Society for Neuroscience*, 30(3), 1015–1026.
- Perkins, G., Renken, C., Martone, M. E., Young, S. J., Ellisman, M., & Frey, T. (1997). Electron tomography of neuronal mitochondria: Three-dimensional structure and organization of cristae and membrane contacts. *Journal of Structural Biology*, 119(3), 260–272.
- Petzoldt, A. G., Götz, T. W. B., Driller, J. H., Lützkendorf, J., Reddy-Alla, S., Matkovic-Rachid, T., Liu, S., Knoche, E., Mertel, S., Ugorets, V., Lehmann, M., Ramesh, N., Beuschel, C. B., Kuroпка, B., Freund, C., Stelzl, U., Loll, B., Liu, F., Wahl, M. C., & Sigrist, S. J. (2020). RIM-binding protein couples synaptic vesicle recruitment to release sites. *Journal of Cell Biology*, 219(7), e201902059.
- Pofantis, E., Neher, E., & Dresbach, T. (2021). Regulation of a subset of release-ready vesicles by the presynaptic protein Mover. *Proceedings of the National Academy of Sciences of the United States of America*, 118(3).
- Poirier, M. A., Xiao, W., Macosko, J. C., Chan, C., Shin, Y. K., & Bennett, M. K. (1998). The synaptic SNARE complex is a parallel four-stranded helical bundle. *Nature Structural Biology*, 5(9), 765–769.
- Probst, F. J., Fridell, R. A., Raphael, Y., Saunders, T. L., Wang, A., Liang, Y., Morell, R. J., Touchman, J. W., Lyons, R. H., Noben-Trauth, K., Friedman, T. B., & Camper, S. A. (1998). Correction of deafness in shaker-2 mice by an unconventional myosin in a BAC transgene. *Science (New York, N.Y.)*, 280(5368), 1444–1447.
- Pujol, R., Shnerson, A., Lenoir, M., & Deol, M. S. (1983). Early degeneration of sensory and ganglion cells in the inner ear of mice with uncomplicated genetic deafness (dn): Preliminary observations. *Hearing Research*, 12(1), 57–63.

- Qu, L., Akbergenova, Y., Hu, Y., & Schikorski, T. (2009). Synapse-to-synapse variation in mean synaptic vesicle size and its relationship with synaptic morphology and function. *The Journal of Comparative Neurology*, *514*(4), 343–352.
- Raimondi, A., Ferguson, S. M., Lou, X., Armbruster, M., Paradise, S., Giovedi, S., Messa, M., Kono, N., Takasaki, J., Cappello, V., O'Toole, E., Ryan, T. A., & De Camilli, P. (2011). Overlapping Role of Dynamin Isoforms in Synaptic Vesicle Endocytosis. *Neuron*, *70*(6), 1100–1114.
- Redd, E. E., Pongstaporn, T., & Ryugo, D. K. (2000). The effects of congenital deafness on auditory nerve synapses and globular bushy cells in cats. *Hearing Research*, *147*(1), 160–174. h
- Reisinger, E., Bresee, C., Neef, J., Nair, R., Reuter, K., Bulankina, A., Nouvian, R., Koch, M., Bückers, J., Kastrup, L., Roux, I., Petit, C., Hell, S. W., Brose, N., Rhee, J.-S., Kügler, S., Brigande, J. V., & Moser, T. (2011). Probing the functional equivalence of otoferlin and synaptotagmin 1 in exocytosis. *Journal of Neuroscience*, *31*(13), 4886–4895.
- Richmond, J. E., Weimer, R. M., & Jorgensen, E. M. (2001). An open form of syntaxin bypasses the requirement for UNC-13 in vesicle priming. *Nature*, *412*(6844), 338–341.
- Rintoul, G. L., Filiano, A. J., Brocard, J. B., Kress, G. J., & Reynolds, I. J. (2003). Glutamate decreases mitochondrial size and movement in primary forebrain neurons. *The Journal of Neuroscience: The Official Journal of the Society for Neuroscience*, *23*(21), 7881–7888.
- Rizzoli, S. O., & Betz, W. J. (2005). Synaptic vesicle pools. *Nature Reviews. Neuroscience*, *6*(1), 57–69.
- Rodríguez-Ballesteros, M., Reynoso, R., Olarte, M., Villamar, M., Morera, C., Santarelli, R., Arslan, E., Medá, C., Curet, C., Völter, C., Sainz-Quevedo, M., Castorina, P., Ambrosetti, U., Berrettini, S., Frei, K., Tedín, S., Smith, J., Cruz Tapia, M., Cavallé, L., ... del Castillo, I. (2008). A multicenter study on the prevalence and spectrum of mutations in the otoferlin gene (OTOF) in subjects with nonsyndromic hearing impairment and auditory neuropathy. *Human Mutation*, *29*(6), 823–831.
- Rosenmund, C., Sigler, A., Augustin, I., Reim, K., Brose, N., & Rhee, J. S. (2002). Differential control of vesicle priming and short-term plasticity by Munc13 isoforms. *Neuron*, *33*(3), 411–424.
- Rosenmund, C., & Stevens, C. F. (1996). Definition of the readily releasable pool of vesicles at hippocampal synapses. *Neuron*, *16*(6), 1197–1207.
- Rosenmund, C., & Stevens, C. F. (1997). The rate of aldehyde fixation of the exocytotic machinery in cultured hippocampal synapses. *Journal of Neuroscience Methods*, *76*(1), 1–5.
- Rostaing, P., Real, E., Siksou, L., Lechaire, J.-P., Boudier, T., Boeckers, T. M., Gertler, F., Gundelfinger, E. D., Triller, A., & Marty, S. (2006). Analysis of synaptic ultrastructure without fixative using high-pressure freezing and tomography. *European Journal of Neuroscience*, *24*(12), 3463–3474.
- Roth, T. F., & Porter, K. R. (1964). YOLK PROTEIN UPTAKE IN THE OOCYTE OF THE MOSQUITO AEDES AEGYPTI. L. *The Journal of Cell Biology*, *20*, 313–332.
- Rouiller, E. M., Cronin-Schreiber, R., Fekete, D. M., & Ryugo, D. K. (1986). The central projections of intracellularly labeled auditory nerve fibers in cats: An analysis of terminal morphology. *Journal of Comparative Neurology*, *249*(2), 261–278.
- Roux, I., Safieddine, S., Nouvian, R., Grati, M., Simmler, M.-C., Bahloul, A., Perfettini, I., Le Gall, M., Rostaing, P., Hamard, G., Triller, A., Avan, P., Moser, T., & Petit, C. (2006). Otoferlin, defective in a human deafness form, is essential for exocytosis at the auditory ribbon synapse. *Cell*, *127*(2), 277–289.

- Rowland, K. C., Irby, N. K., & Spirou, G. A. (2000). Specialized synapse-associated structures within the calyx of Held. *The Journal of Neuroscience: The Official Journal of the Society for Neuroscience*, 20(24), 9135–9144.
- Royle, S. J. (2006). The cellular functions of clathrin. *Cellular and Molecular Life Sciences: CMLS*, 63(16), 1823–1832.
- Rube, D. A., & van der Bliek, A. M. (2004). Mitochondrial morphology is dynamic and varied. *Molecular and Cellular Biochemistry*, 256–257(1–2), 331–339.
- Rubio, M. E., Fukazawa, Y., Kamasawa, N., Clarkson, C., Molnár, E., & Shigemoto, R. (2014). Target- and input-dependent organization of AMPA and NMDA receptors in synaptic connections of the cochlear nucleus. *The Journal of Comparative Neurology*, 522(18), 4023–4042.
- Ryugo, D. K., Cahill, H. B., Rose, L. S., Rosenbaum, B. T., Schroeder, M. E., & Wright, A. L. (2003). Separate forms of pathology in the cochlea of congenitally deaf white cats. *Hearing Research*, 181(1–2), 73–84.
- Ryugo, D. K., & Fekete, D. M. (1982). Morphology of primary axosomatic endings in the anteroventral cochlear nucleus of the cat: A study of the endbulbs of Held. *Journal of Comparative Neurology*, 210(3), 239–257.
- Ryugo, D. K., Montey, K. L., Wright, A. L., Bennett, M. L., & Pongstaporn, T. (2006). Postnatal development of a large auditory nerve terminal: The endbulb of Held in cats. *Hearing Research*, 216–217, 100–115.
- Ryugo, D. K., Pongstaporn, T., Huchton, D. M., & Niparko, J. K. (1997). Ultrastructural analysis of primary endings in deaf white cats: Morphologic alterations in endbulbs of held. *Journal of Comparative Neurology*, 385(2), 230–244.
- Ryugo, D. k., Rosenbaum, B. t., Kim, P. j., Niparko, J. k., & Saada, A. a. (1998). Single unit recordings in the auditory nerve of congenitally deaf white cats: Morphological correlates in the cochlea and cochlear nucleus. *The Journal of Comparative Neurology*, 397(4), 532–548.
- Ryugo, D. K., & Sento, S. (1991). Synaptic connections of the auditory nerve in cats: Relationship between endbulbs of held and spherical bushy cells. *Journal of Comparative Neurology*, 305(1), 35–48.
- Ryugo, D. K., Wu, M. M., & Pongstaporn, T. (1996). Activity-related features of synapse morphology: A study of endbulbs of Held. *The Journal of Comparative Neurology*, 365(1), 141–158.
- Safieddine, S., & Wenthold, R. J. (1999). SNARE complex at the ribbon synapses of cochlear hair cells: Analysis of synaptic vesicle- and synaptic membrane-associated proteins. *European Journal of Neuroscience*, 11(3), 803–812.
- Sanes, D. H. (1990). An in vitro analysis of sound localization mechanisms in the gerbil lateral superior olive. *Journal of Neuroscience*, 10(11), 3494–3506.
- Sätzler, K., Söhl, L. F., Bollmann, J. H., Borst, J. G. G., Frotscher, M., Sakmann, B., & Lübke, J. H. R. (2002). Three-Dimensional Reconstruction of a Calyx of Held and Its Postsynaptic Principal Neuron in the Medial Nucleus of the Trapezoid Body. *The Journal of Neuroscience*, 22(24), 10567–10579.
- Scarpelli, M., Zappini, F., Filosto, M., Russignan, A., Tonin, P., & Tomelleri, G. (2012). Mitochondrial Sensorineural Hearing Loss: A Retrospective Study and a Description of Cochlear Implantation in a MELAS Patient. *Genetics Research International*, 2012, e287432.
- Schikorski, T., & Stevens, C. F. (1997). Quantitative ultrastructural analysis of hippocampal excitatory synapses. *The Journal of Neuroscience: The Official Journal of the Society for Neuroscience*, 17(15), 5858–5867.

- Schlüter, O. M., Basu, J., Südhof, T. C., & Rosenmund, C. (2006). Rab3 superprimes synaptic vesicles for release: Implications for short-term synaptic plasticity. *The Journal of Neuroscience: The Official Journal of the Society for Neuroscience*, 26(4), 1239–1246.
- Schnee, M. E., Santos-Sacchi, J., Castellano-Muñoz, M., Kong, J.-H., & Ricci, A. J. (2011). Calcium-Dependent Synaptic Vesicle Trafficking Underlies Indefatigable Release at the Hair Cell Afferent Fiber Synapse. *Neuron*, 70(2), 326–338.
- Schneggenburger, R., Meyer, A. C., & Neher, E. (1999). Released Fraction and Total Size of a Pool of Immediately Available Transmitter Quanta at a Calyx Synapse. *Neuron*, 23(2), 399–409.
- Schoch, S., Castillo, P. E., Jo, T., Mukherjee, K., Geppert, M., Wang, Y., Schmitz, F., Malenka, R. C., & Südhof, T. C. (2002). RIM1alpha forms a protein scaffold for regulating neurotransmitter release at the active zone. *Nature*, 415(6869), 321–326.
- Schoch, S., & Gundelfinger, E. D. (2006). Molecular organization of the presynaptic active zone. *Cell and Tissue Research*, 326(2), 379–391. h
- Schoch, S., Mittelstaedt, T., Kaeser, P. S., Padgett, D., Feldmann, N., Chevaleyre, V., Castillo, P. E., Hammer, R. E., Han, W., Schmitz, F., Lin, W., & Südhof, T. C. (2006). Redundant functions of RIM1[alpha] and RIM2[alpha] in Ca²⁺-triggered neurotransmitter release. *EMBO J*, 25(24), 5852–5863.
- Sento, S., & Ryugo, D. K. (1989). Endbulbs of held and spherical bushy cells in cats: Morphological correlates with physiological properties. *The Journal of Comparative Neurology*, 280(4), 553–562.
- Shen, J., Tareste, D. C., Paumet, F., Rothman, J. E., & Melia, T. J. (2007). Selective Activation of Cognate SNAREpins by Sec1/Munc18 Proteins. *Cell*, 128(1), 183–195.
- Shepherd, G. M. G., & Harris, K. M. (1998). Three-Dimensional Structure and Composition of CA3→CA1 Axons in Rat Hippocampal Slices: Implications for Presynaptic Connectivity and Compartmentalization. *Journal of Neuroscience*, 18(20), 8300–8310.
- Siksou, L., Rostaing, P., Lechaire, J.-P., Boudier, T., Ohtsuka, T., Fejtová, A., Kao, H.-T., Greengard, P., Gundelfinger, E. D., Triller, A., & Marty, S. (2007). Three-dimensional architecture of presynaptic terminal cytomatrix. *The Journal of Neuroscience*, 27(26), 6868–6877.
- Siksou, L., Varoqueaux, F., Pascual, O., Triller, A., Brose, N., & Marty, S. (2009). A common molecular basis for membrane docking and functional priming of synaptic vesicles. *European Journal of Neuroscience*, 30(1), 49–56.
- Silva, C. A., Yalnizyan-Carson, A., Fernández Busch, M. V., van Zwieten, M., Verhage, M., & Lohmann, C. (2021). Activity-dependent regulation of mitochondrial motility in developing cortical dendrites. *ELife*, 10, e62091.
- Smith, H. L., Bourne, J. N., Cao, G., Chirillo, M. A., Ostroff, L. E., Watson, D. J., & Harris, K. M. (2016). Mitochondrial support of persistent presynaptic vesicle mobilization with age-dependent synaptic growth after LTP. *ELife*, 5, e15275.
- Smith, J. E., & Reese, T. S. (1980). Use of aldehyde fixatives to determine the rate of synaptic transmitter release. *Journal of Experimental Biology*, 89(1), 19–28.
- Smith, P. H., Joris, P. X., Carney, L. H., & Yin, T. C. T. (1991). Projections of physiologically characterized globular bushy cell axons from the cochlear nucleus of the cat. *The Journal of Comparative Neurology*, 304(3), 387–407.
- Smith, P. H., Joris, P. X., & Yin, T. C. T. (1993). Projections of physiologically characterized spherical bushy cell axons from the cochlear nucleus of the cat: Evidence for delay lines to the medial superior olive. *Journal of Comparative Neurology*, 331(2), 245–260.
- Smit-Rigter, L., Rajendran, R., Silva, C. A. P., Spierenburg, L., Groeneweg, F., Ruimschotel, E. M., van Versendaal, D., van der Togt, C., Eysel, U. T., Heimel, J. A., Lohmann, C.,

- & Levelt, C. N. (2016). Mitochondrial Dynamics in Visual Cortex Are Limited In Vivo and Not Affected by Axonal Structural Plasticity. *Current Biology: CB*, 26(19), 2609–2616.
- Song, D. H., Park, J., Maurer, L. L., Lu, W., Philbert, M. A., & Sastry, A. M. (2013). Biophysical significance of the inner mitochondrial membrane structure on the electrochemical potential of mitochondria. *Physical Review. E, Statistical, Nonlinear, and Soft Matter Physics*, 88(6), 062723.
- Sonntag, M., Englitz, B., Kopp-Scheinflug, C., & Rübsamen, R. (2009). Early postnatal development of spontaneous and acoustically evoked discharge activity of principal cells of the medial nucleus of the trapezoid body: An in vivo study in mice. *The Journal of Neuroscience*, 29(30), 9510.
- Soykan, T., Kaempf, N., Sakaba, T., Vollweiter, D., Goerdeler, F., Puchkov, D., Kononenko, N. L., & Haucke, V. (2017). Synaptic Vesicle Endocytosis Occurs on Multiple Timescales and Is Mediated by Formin-Dependent Actin Assembly. *Neuron*, 93(4), 854-866.e4.
- Spacek, J., & Harris, K. M. (1998). Three-dimensional organization of cell adhesion junctions at synapses and dendritic spines in area CA1 of the rat hippocampus. *Journal of Comparative Neurology*, 393(1), 58–68.
- Spirou, G. A., Rager, J., & Manis, P. B. (2005). Convergence of auditory-nerve fiber projections onto globular bushy cells. *Neuroscience*, 136(3), 843–863.
- Spirou, G. A., Rowland, K. C., & Berrebi, A. S. (1998). Ultrastructure of neurons and large synaptic terminals in the lateral nucleus of the trapezoid body of the cat. *The Journal of Comparative Neurology*, 398(2), 257–272.
- Stalman, U., Franke, A. J., Al-Moyed, H., Strenzke, N., & Reisinger, E. (2021). Otoferlin Is Required for Proper Synapse Maturation and for Maintenance of Inner and Outer Hair Cells in Mouse Models for DFNB9. *Frontiers in Cellular Neuroscience*, 15, 677543.
- Stamatakis, S., Francis, H. W., Lehar, M., May, B. J., & Ryugo, D. K. (2006). Synaptic alterations at inner hair cells precede spiral ganglion cell loss in aging C57BL/6J mice. *Hearing Research*, 221(1–2), 104–118.
- Steel, K. P., & Bock, G. R. (1983). Cochlear dysfunction in the jerker mouse. *Behavioral Neuroscience*, 97(3), 381–391.
- Stevens, R. J., Akbergenova, Y., Jorquera, R. A., & Littleton, J. T. (2012). Abnormal Synaptic Vesicle Biogenesis in Drosophila Synaptogyrin Mutants. *The Journal of Neuroscience*, 32(50), 18054–18067.
- Strenzke, N., Chakrabarti, R., Al-Moyed, H., Müller, A., Hoch, G., Pangrsic, T., Yamanbaeva, G., Lenz, C., Pan, K.-T., Auge, E., Geiss-Friedlander, R., Urlaub, H., Brose, N., Wichmann, C., & Reisinger, E. (2016). Hair cell synaptic dysfunction, auditory fatigue and thermal sensitivity in otoferlin Ile515Thr mutants. *The EMBO Journal*, 35(23), e201694564.
- Stryker, E., & Johnson, K. G. (2007). LAR, liprin alpha and the regulation of active zone morphogenesis. *Journal of Cell Science*, 120(Pt 21), 3723–3728.
- Sun, T., Qiao, H., Pan, P.-Y., Chen, Y., & Sheng, Z.-H. (2013). Motile axonal mitochondria contribute to the variability of presynaptic strength. *Cell Reports*, 4(3), 413–419. /
- Sutton, R. B., Fasshauer, D., Jahn, R., & Brunger, A. T. (1998). Crystal structure of a SNARE complex involved in synaptic exocytosis at 2.4 Å resolution. *Nature*, 395(6700), 347–353.
- Takago, H., Oshima-Takago, T., & Moser, T. (2019). Disruption of Otoferlin Alters the Mode of Exocytosis at the Mouse Inner Hair Cell Ribbon Synapse. *Frontiers in Molecular Neuroscience*, 11.

- Tang, Y., & Zucker, R. S. (1997). Mitochondrial involvement in post-tetanic potentiation of synaptic transmission. *Neuron*, 18(3), 483–491.
- Tao, C.-L., Liu, Y.-T., Sun, R., Zhang, B., Qi, L., Shivakoti, S., Tian, C.-L., Zhang, P., Lau, P.-M., Zhou, Z. H., & Bi, G.-Q. (2018). Differentiation and Characterization of Excitatory and Inhibitory Synapses by Cryo-electron Tomography and Correlative Microscopy. *The Journal of Neuroscience*, 38(6), 1493–1510.
- Taschenberger, H., Leão, R. M., Rowland, K. C., Spirou, G. A., & von Gersdorff, H. (2002). Optimizing synaptic architecture and efficiency for high-frequency transmission. *Neuron*, 36(6), 1127–1143.
- Taschenberger, H., & von Gersdorff, H. (2000). Fine-Tuning an Auditory Synapse for Speed and Fidelity: Developmental Changes in Presynaptic Waveform, EPSC Kinetics, and Synaptic Plasticity. *The Journal of Neuroscience*, 20(24), 9162–9173.
- Taschenberger, H., Woehler, A., & Neher, E. (2016). Superpriming of synaptic vesicles as a common basis for intersynapse variability and modulation of synaptic strength. *Proceedings of the National Academy of Sciences*, 113(31), E4548–E4557.
- Tatsuoka, H., & Reese, T. S. (1989). New structural features of synapses in the anteroventral cochlear nucleus prepared by direct freezing and freeze-substitution. *The Journal of Comparative Neurology*, 290(3), 343–357.
- Thomas, C. I., Keine, C., Okayama, S., Satterfield, R., Musgrove, M., Guerrero-Given, D., Kamasawa, N., & Young, S. M. (2019). Presynaptic Mitochondria Volume and Abundance Increase during Development of a High-Fidelity Synapse. *The Journal of Neuroscience*, 39(41), 7994–8012.
- Tolbert, L. P., & Morest, D. K. (1982a). The neuronal architecture of the anteroventral cochlear nucleus of the cat in the region of the cochlear nerve root: Electron microscopy. *Neuroscience*, 7(12), 3053–3067.
- Tolbert, L. P., & Morest, D. K. (1982b). The neuronal architecture of the anteroventral cochlear nucleus of the cat in the region of the cochlear nerve root: Golgi and Nissl methods. *Neuroscience*, 7(12), 3013–3030.
- tom Dieck, S., Sanmartí-Vila, L., Langnaese, K., Richter, K., Kindler, S., Soyke, A., Wex, H., Smalla, K. H., Kämpf, U., Fränzer, J. T., Stumm, M., Garner, C. C., & Gundelfinger, E. D. (1998). Bassoon, a novel zinc-finger CAG/glutamine-repeat protein selectively localized at the active zone of presynaptic nerve terminals. *The Journal of Cell Biology*, 142(2), 499–509.
- Tritsch, N. X., Yi, E., Gale, J. E., Glowatzki, E., & Bergles, D. E. (2007). The origin of spontaneous activity in the developing auditory system. *Nature*, 450(7166), 50–55.
- Tritsch, N. X., Zhang, Y.-X., Ellis-Davies, G., & Bergles, D. E. (2010). ATP-induced morphological changes in supporting cells of the developing cochlea. *Purinergic Signalling*, 6(2), 155–166.
- Trussell, L. O. (1999). SYNAPTIC MECHANISMS FOR CODING TIMING IN AUDITORY NEURONS. *Annual Review of Physiology*, 61(1), 477–496.
- Uthaiyah, R. C., & Hudspeth, A. J. (2010). Molecular Anatomy of the Hair Cell's Ribbon Synapse. *The Journal of Neuroscience*, 30(37), 12387–12399.
- Valdivia, O. (1971). Methods of fixation and the morphology of synaptic vesicles. *Journal of Comparative Neurology*, 142(3), 257–273.
- Verstreken, P., Ly, C. V., Venken, K. J. T., Koh, T.-W., Zhou, Y., & Bellen, H. J. (2005). Synaptic Mitochondria Are Critical for Mobilization of Reserve Pool Vesicles at *Drosophila* Neuromuscular Junctions. *Neuron*, 47(3), 365–378.

- Vogel, F., Bornhövd, C., Neupert, W., & Reichert, A. S. (2006). Dynamic subcompartmentalization of the mitochondrial inner membrane. *Journal of Cell Biology*, *175*(2), 237–47.
- Vogl, C., Cooper, B. H., Neef, J., Wojcik, S. M., Reim, K., Reisinger, E., Brose, N., Rhee, J.-S., Moser, T., & Wichmann, C. (2015). Unconventional molecular regulation of synaptic vesicle replenishment in cochlear inner hair cells. *Journal of Cell Science*, *128*(4), 638–644.
- Vona, B., Rad, A., & Reisinger, E. (2020). The Many Faces of DFNB9: Relating OTOF Variants to Hearing Impairment. *Genes*, *11*(12), 1411.
- Waites, C. L., Leal-Ortiz, S. A., Okerlund, N., Dalke, H., Fejtova, A., Altroock, W. D., Gundelfinger, E. D., & Garner, C. C. (2013). Bassoon and Piccolo maintain synapse integrity by regulating protein ubiquitination and degradation. *The EMBO Journal*, *32*(7), 954–969.
- Wallrafen, R. (2019). *The presynaptic protein Mover is heterogeneously expressed across brain areas and synapse types*. <https://ediss.uni-goettingen.de/handle/21.11130/00-1735-0000-0003-C13D-F>
- Wallrafen, R., & Dresbach, T. (2018). The Presynaptic Protein Mover Is Differentially Expressed Across Brain Areas and Synapse Types. *Frontiers in Neuroanatomy*, *12*.
- Wang, H. C., Lin, C.-C., Cheung, R., Zhang-Hooks, Y., Agarwal, A., Ellis-Davies, G., Rock, J., & Bergles, D. E. (2015). Spontaneous Activity of Cochlear Hair Cells Triggered by Fluid Secretion Mechanism in Adjacent Support Cells. *Cell*, *163*(6), 1348–1359.
- Wang, Y., Sugita, S., & Südhof, T. C. (2000). The RIM/NIM family of neuronal C2 domain proteins. Interactions with Rab3 and a new class of Src homology 3 domain proteins. *Journal of Biological Chemistry*, *275*(26), 20033–20044.
- Wang, Y.-X., Wenthold, R. J., Ottersen, O. P., & Petralia, R. S. (1998). Endbulb Synapses in the Anteroventral Cochlear Nucleus Express a Specific Subset of AMPA-Type Glutamate Receptor Subunits. *The Journal of Neuroscience*, *18*(3), 1148–1160.
- Watanabe, S. (2016). Flash-and-Freeze: Coordinating Optogenetic Stimulation with Rapid Freezing to Visualize Membrane Dynamics at Synapses with Millisecond Resolution. *Frontiers in Synaptic Neuroscience*, *8*, 24.
- Watanabe, S., Rost, B. R., Camacho-Pérez, M., Davis, M. W., Söhl-Kielczynski, B., Rosenmund, C., & Jorgensen, E. M. (2013). Ultrafast endocytosis at mouse hippocampal synapses. *Nature*, *504*(7479), 242–247.
- Watanabe, S., Trimbuch, T., Camacho-Pérez, M., Rost, B. R., Brokowski, B., Söhl-Kielczynski, B., Felies, A., Davis, M. W., Rosenmund, C., & Jorgensen, E. M. (2014). Clathrin regenerates synaptic vesicles from endosomes. *Nature*, *515*(7526), 228–233.
- Webster, D. B., & Trune, D. R. (1982). Cochlear nuclear complex of mice. *American Journal of Anatomy*, *163*(2), 103–130.
- Wei, Z., Zheng, S., Spangler, S. A., Yu, C., Hoogenraad, C. C., & Zhang, M. (2011). Liprin-mediated large signaling complex organization revealed by the liprin- α /CASK and liprin- α /liprin- β complex structures. *Molecular Cell*, *43*(4), 586–598.
- Weimer, R. M., Gracheva, E. O., Meyrignac, O., Miller, K. G., Richmond, J. E., & Bessereau, J.-L. (2006). UNC-13 and UNC-10/rim localize synaptic vesicles to specific membrane domains. *The Journal of Neuroscience: The Official Journal of the Society for Neuroscience*, *26*(31), 8040–8047. <https://doi.org/10.1523/JNEUROSCI.2350-06.2006>
- Wen, X., Saltzgaber, G. W., & Thoreson, W. B. (2017). Kiss-and-Run Is a Significant Contributor to Synaptic Exocytosis and Endocytosis in Photoreceptors. *Frontiers in Cellular Neuroscience*, *11*.

- Wichmann, C. (2015). Molecularly and structurally distinct synapses mediate reliable encoding and processing of auditory information. *Hearing Research*, 330(Pt B), 178–190.
- Wickesberg, R. E., & Oertel, D. (1988). Tonotopic projection from the dorsal to the anteroventral cochlear nucleus of mice. *The Journal of Comparative Neurology*, 268(3), 389–399.
- Wiedemann, N., & Pfanner, N. (2017). Mitochondrial Machineries for Protein Import and Assembly. *Annual Review of Biochemistry*, 86, 685–714.
- Willard, F. H., & Ryugo, D. K. (1983). Anatomy of the central auditory system. In: *The Auditory Psychobiology of the Mouse*, edited by Willott JF. Springfield, IL: Charles C Thomas, p. 201–304.
- Wilson, J. A., Garry, E. M., Anderson, H. A., Rosie, R., Colvin, L. A., Mitchell, R., & Fleetwood-Walker, S. M. (2005). NMDA receptor antagonist treatment at the time of nerve injury prevents injury-induced changes in spinal NR1 and NR2B subunit expression and increases the sensitivity of residual pain behaviours to subsequently administered NMDA receptor antagonists. *Pain*, 117(3), 421–432.
- Wong, A. B., Rutherford, M. A., Gabrielaitis, M., Pangršič, T., Göttfert, F., Frank, T., Michanski, S., Hell, S., Wolf, F., Wichmann, C., & Moser, T. (2014). Developmental refinement of hair cell synapses tightens the coupling of Ca²⁺ influx to exocytosis. *The EMBO Journal*, 33(3), 247–264.
- Wright, S., Hwang, Y., & Oertel, D. (2014). Synaptic transmission between end bulbs of Held and bushy cells in the cochlear nucleus of mice with a mutation in Otoferlin. *Journal of Neurophysiology*, 112(12), 3173–3188.
- Wu, L. G., & Borst, J. G. (1999). The reduced release probability of releasable vesicles during recovery from short-term synaptic depression. *Neuron*, 23(4), 821–832.
- Wu, S. H., & Oertel, D. (1984). Intracellular injection with horseradish peroxidase of physiologically characterized stellate and bushy cells in slices of mouse anteroventral cochlear nucleus. *The Journal of Neuroscience: The Official Journal of the Society for Neuroscience*, 4(6), 1577–1588.
- Wu, S. H., & Oertel, D. (1987). Maturation of synapses and electrical properties of cells in the cochlear nuclei. *Hearing Research*, 30(1), 99–110.
- Wu, Y., O’Toole, E. T., Girard, M., Ritter, B., Messa, M., Liu, X., McPherson, P. S., Ferguson, S. M., & De Camilli, P. (2014). A dynamin 1-, dynamin 3- and clathrin-independent pathway of synaptic vesicle recycling mediated by bulk endocytosis. *ELife*, 3, e01621.
- Wurm, C. A., & Jakobs, S. (2006). Differential protein distributions define two sub-compartments of the mitochondrial inner membrane in yeast. *FEBS Letters*, 580(24), 5628–5634.
- Xue, R., Ruhl, D. A., Briguglio, J. S., Figueroa, A. G., Pearce, R. A., & Chapman, E. R. (2018). Doc2-mediated superpriming supports synaptic augmentation. *Proceedings of the National Academy of Sciences of the United States of America*, 115(24), E5605–E5613.
- Xu-Friedman, M. A., Harris, K. M., & Regehr, W. G. (2001). Three-Dimensional Comparison of Ultrastructural Characteristics at Depressing and Facilitating Synapses onto Cerebellar Purkinje Cells. *The Journal of Neuroscience*, 21(17), 6666–6672.
- Yang, H., & Xu-Friedman, M. A. (2010). Developmental Mechanisms for Suppressing the Effects of Delayed Release at the Endbulb of Held. *The Journal of Neuroscience*, 30(34), 11466–11475.
- Yasunaga, S., Grati, M., Chardenoux, S., Smith, T. N., Friedman, T. B., Lalwani, A. K., Wilcox, E. R., & Petit, C. (2000). OTOF Encodes Multiple Long and Short Isoforms: Genetic

- Evidence That the Long Ones Underlie Recessive Deafness DFNB9. *American Journal of Human Genetics*, 67(3), 591–600.
- Yasunaga, S., Grati, M., Cohen-Salmon, M., El-Amraoui, A., Mustapha, M., Salem, N., El-Zir, E., Loiselet, J., & Petit, C. (1999). A mutation in OTOF, encoding otoferlin, a FER-1-like protein, causes DFNB9, a nonsyndromic form of deafness. *Nature Genetics*, 21(4), 363–369.
- Yin, T. C., & Chan, J. C. (1990). Interaural time sensitivity in medial superior olive of cat. *Journal of Neurophysiology*, 64(2), 465–488.
- Yizhar, O., & Ashery, U. (2008). Modulating vesicle priming reveals that vesicle immobilization is necessary but not sufficient for fusion-competence. *PLoS One*, 3(7), e2694.
- Yousoufian, M., Couchman, K., Shivdasani, M. N., Paolini, A. G., & Walmsley, B. (2008). Maturation of auditory brainstem projections and calyces in the congenitally deaf (dn/dn) mouse. *The Journal of Comparative Neurology*, 506(3), 442–451.
- Zeng, F. G., Oba, S., Garde, S., Sininger, Y., & Starr, A. (1999). Temporal and speech processing deficits in auditory neuropathy. *Neuroreport*, 10(16), 3429.
- Zhang, B., Koh, Y. H., Beckstead, R. B., Budnik, V., Ganetzky, B., & Bellen, H. J. (1998). Synaptic Vesicle Size and Number Are Regulated by a Clathrin Adaptor Protein Required for Endocytosis. *Neuron*, 21(6), 1465–1475.
- Zheng, J., Shen, W., He, D. Z. Z., Long, K. B., Madison, L. D., & Dallos, P. (2000). Prestin is the motor protein of cochlear outer hair cells. *Nature*, 405(6783), 149–155.
- Zheng, L., Sekerková, G., Vranich, K., Tilney, L. G., Mugnaini, E., & Bartles, J. R. (2000). The deaf jerker mouse has a mutation in the gene encoding the espin actin-bundling proteins of hair cell stereocilia and lacks espins. *Cell*, 102(3), 377–385.
- Zhou, B., Yu, P., Lin, M.-Y., Sun, T., Chen, Y., & Sheng, Z.-H. (2016). Facilitation of axon regeneration by enhancing mitochondrial transport and rescuing energy deficits. *The Journal of Cell Biology*, 214(1), 103–119.
- Zhuang, X., Sun, W., & Xu-Friedman, M. A. (2017). Changes in Properties of Auditory Nerve Synapses following Conductive Hearing Loss. *The Journal of Neuroscience*, 37(2), 323–332.
- Zhuang, X., Wong, N. F., Sun, W., & Xu-Friedman, M. A. (2020). Mechanisms and Functional Consequences of Presynaptic Homeostatic Plasticity at Auditory Nerve Synapses. *The Journal of Neuroscience*, 40(36), 6896–6909.
- Zürner, M., Mittelstaedt, T., tom Dieck, S., Becker, A., & Schoch, S. (2011). Analyses of the spatiotemporal expression and subcellular localization of liprin- α proteins. *The Journal of Comparative Neurology*, 519(15), 3019–3039.
- Zürner, M., & Schoch, S. (2009). The mouse and human Liprin-alpha family of scaffolding proteins: Genomic organization, expression profiling and regulation by alternative splicing. *Genomics*, 93(3), 243–253.

7 Supplemental Figures and Tables

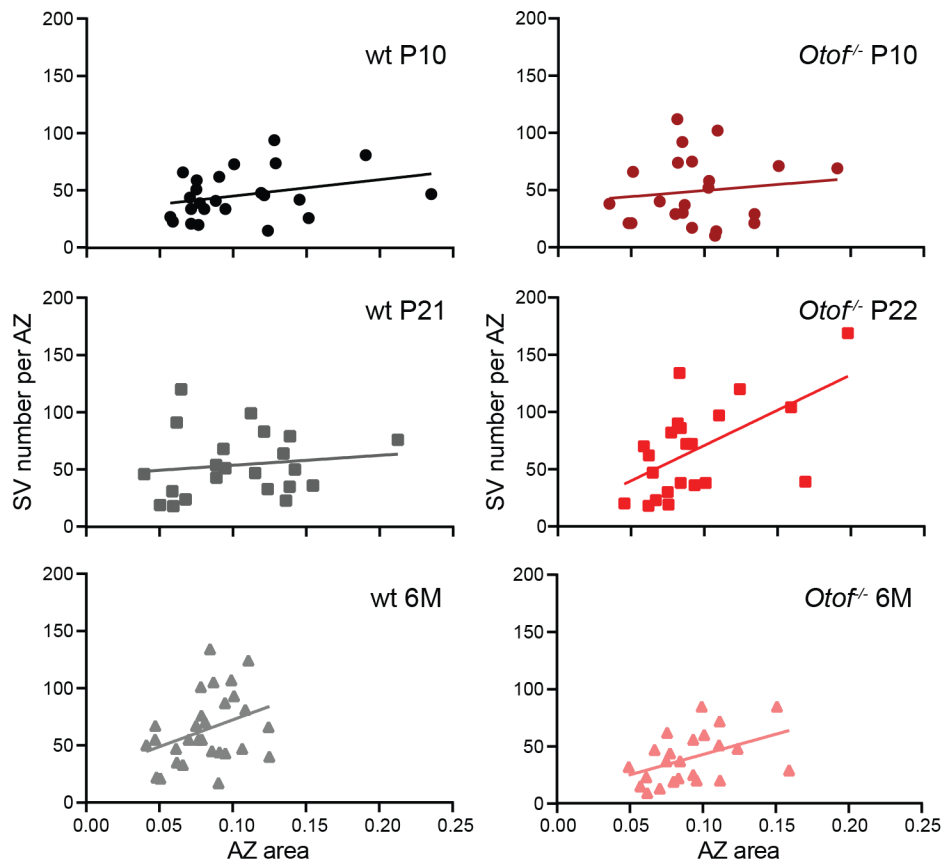


Figure S1: Overall SV numbers do not correlate with the AZ areas. Related to section 3.3.3.

The number of all SVs per AZ within 200 nm distance does not correlate with the AZ area at wt AZs of all ages and at AZs of *Otof*^{-/-} P10 mice. wt P10: $r = 0.3246$; $p = 0.1217$; wt P21: $r = 0.1937$; $p = 0.3878$; wt 6M: $r = 0.3023$; $p = 0.1108$; *Otof*^{-/-} P10: $r = 0.0300$; $p = 0.8947$; Spearman test). At *Otof*^{-/-} P22 and *Otof*^{-/-} 6M endbulb AZs, the SV number correlates with the size of the AZ (*Otof*^{-/-} P22: $r = 0.5599$; $**p = 0.0067$; *Otof*^{-/-} 6M: $r = 0.4658$; $*p = 0.0251$; Spearman test). The continuous line is the linear regression fit to the data.

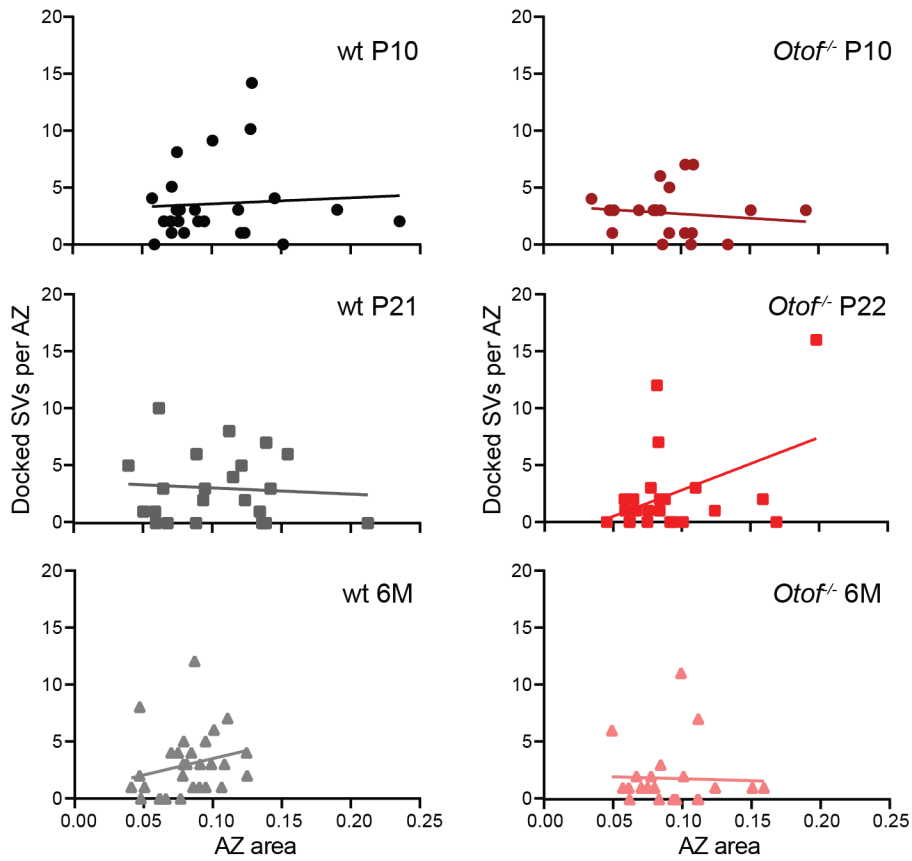


Figure S2: The number of docked SVs and the size of the AZ area do not correlate. Related to section 3.3.4.

Plots demonstrating that the number of docked SVs per AZ and the AZ size do not correlate in any of the analyzed groups. wt P10: $r = 0.1006$; $p = 0.6400$; wt P21: $r = 0.0086$; $p = 0.9698$; wt 6M: $r = 0.3579$; $p = 0.0566$; *Otof*^{-/-} P10: $r = -0.2189$; $p = 0.3276$; *Otof*^{-/-} P22: $r = 0.1897$; $p = 0.3859$; *Otof*^{-/-} 6M: $r = -0.1066$; $p = 0.6282$; Spearman test. The continuous lines are the linear regression fits to the data.

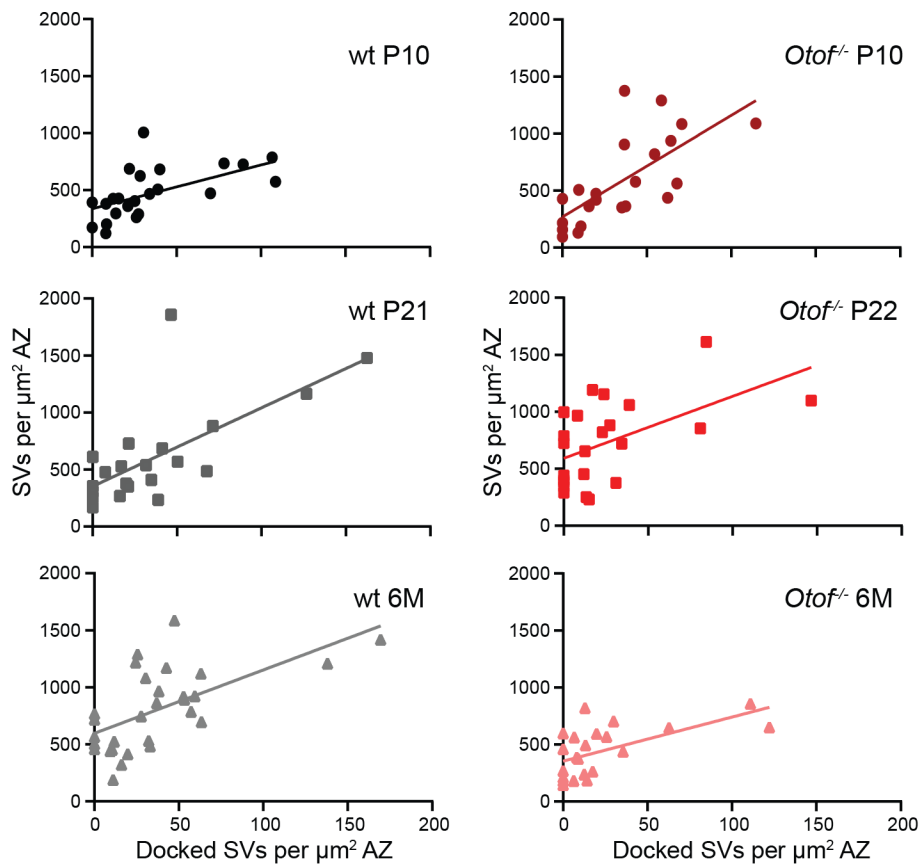


Figure S3: Correlation between the density of all SVs and the density of docked SVs. Related to section 3.3.4.

Plots showing that the density of all SVs within 200 nm from the AZ membrane correlate with and density of docked SVs at AZs from wt and mutant endbulbs of Held of all investigated ages. wt P10: $r = 0.7547$; **** $p < 0.0001$; wt P21: $r = 0.6690$; *** $p = 0.0007$; wt 6M: $r = 0.6158$; *** $p = 0.0004$; *Otof*^{-/-} P10: $r = 0.7622$; **** $p < 0.0001$; *Otof*^{-/-} P22: $r = 0.4880$; * $p = 0.0182$; *Otof*^{-/-} 6M: $r = 0.5993$; ** $p = 0.0025$; Spearman test. The continuous lines show the linear regression fits to the data.

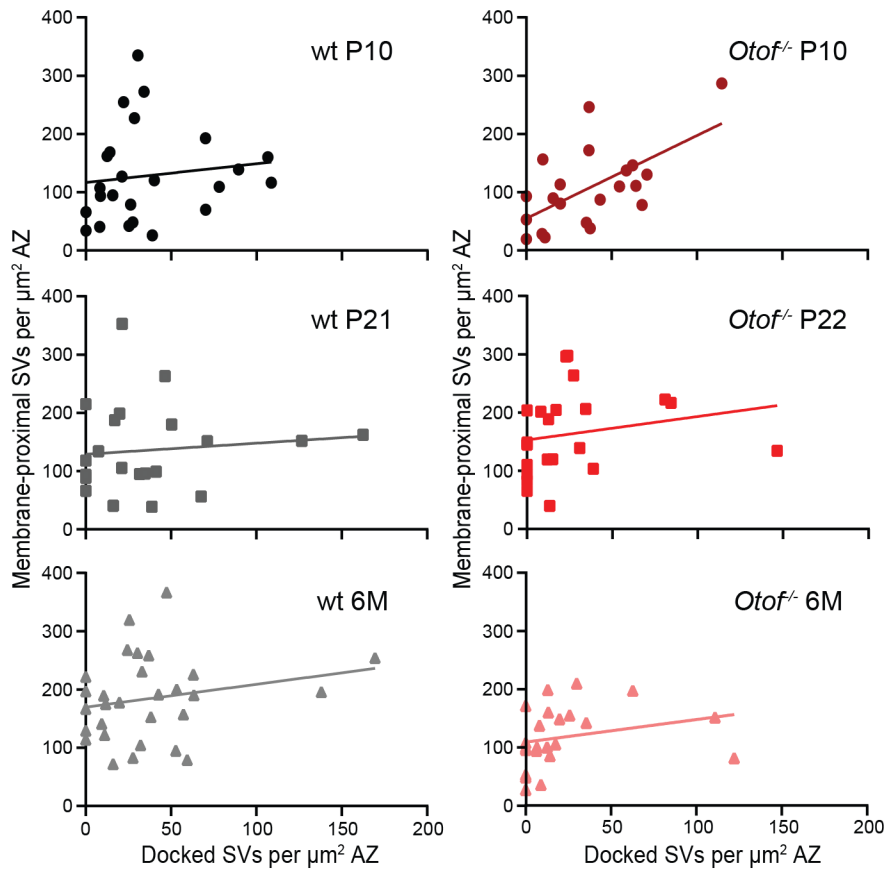


Figure S4: The density of membrane-proximal SVs correlates with the density of docked SVs at mutant AZs. Related to section 3.3.5.

At wt endbulb AZs the densities of membrane-proximal SVs and docked SVs do not correlate. wt P10: $r = 0.3122$; $p = 0.1374$; wt P21: $r = 0.2230$; $p = 0.3185$; wt 6M: $r = 0.2049$; $p = 0.2862$; Spearman test. In *Otof*^{-/-} mice of all ages, the density of membrane-proximal SVs a weak correlation with the density of docked SVs is found. *Otof*^{-/-} P10: $r = 0.5125$; $*p = 0.0147$ *Otof*^{-/-} P22: $r = 0.4285$; $*p = 0.0414$; *Otof*^{-/-} 6M: $r = 0.4580$; $*p = 0.0280$; Spearman test. The continuous lines show the linear regression fits to the data.

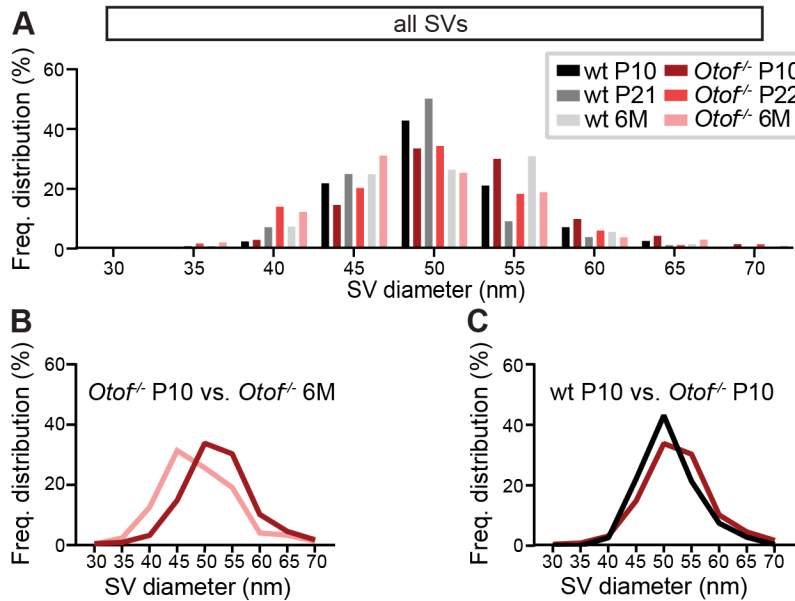


Figure S5: The frequency distributions of individual SV diameters. Related to Fig. 3.15A.

(A) SV diameters were divided in 5 nm bins and the frequency distribution of diameters from all SVs within 200 nm from the AZ membrane is shown as histogram. (B,C) For a better overview, the groups whose averaged diameters were significantly different (see section 3.3.6, Table S3-S7), are depicted in additional graphs showing a clear right shift of SV sizes at *Otof*^{-/-} P10 compared to *Otof*^{-/-} 6M (B). Comparing P10 mice, just a slight shift towards greater SVs can be observed in the mutant (C), although the averaged SV diameters per tomogram were significantly different (Table S4).

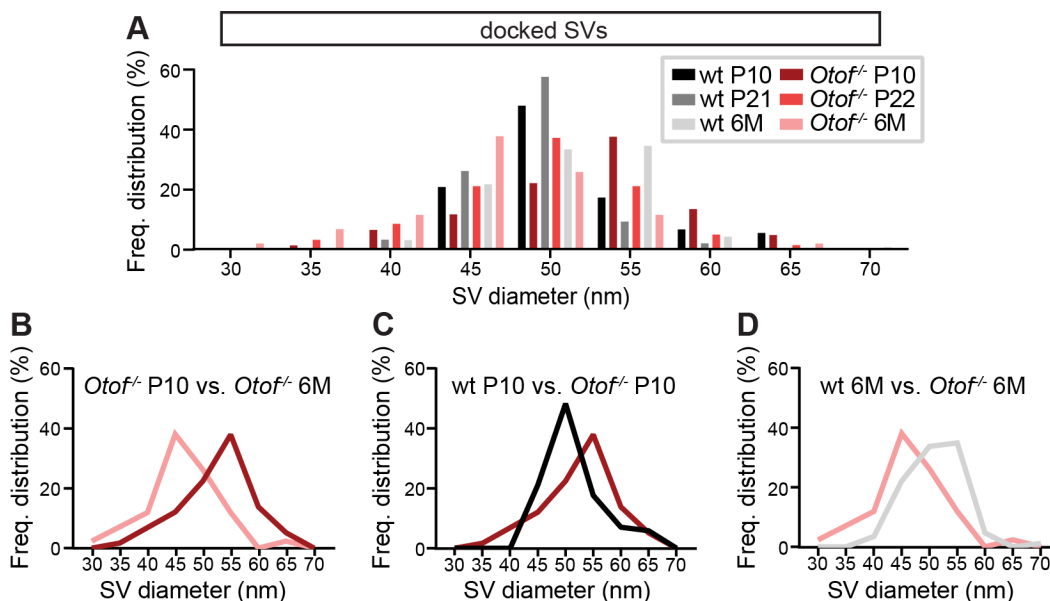


Figure S6: The frequency distributions of individual diameters of morphologically docked SVs. Related to Fig. 3.15B.

(A) Histogram showing the frequency distribution of diameters from just the docked SVs. SV diameters were divided in 5 nm bins. (B-D) Graphs showing the frequency distribution of the groups whose averaged diameters were significantly different (see section 3.3.6, Table S3-S7). The graph of mutant P10 SVs is shifted clearly towards greater SV diameters compared to *Otof*^{-/-} P22 (B) and wt P10 (C). At *Otof*^{-/-} 6M, the graph is shifted to the left compared to age-matched wt (D) illustrating the significant smaller docked SVs at mutant endbulbs.

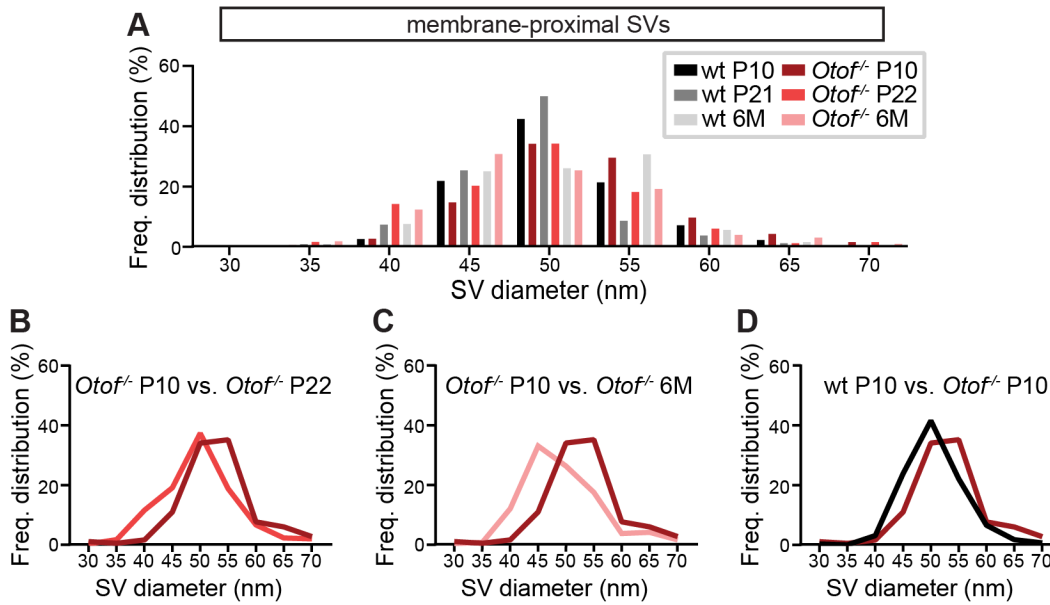


Figure S7: The frequency distributions of individual diameters of membrane-proximal SVs. Related to Fig. 3.15C.

(A) SV diameters were divided in 5 nm bins and the histogram shows the frequency distribution of diameters from membrane-proximal SVs. (B-D) Frequency distributions of groups whose averaged diameters per tomogram were significantly different, are illustrated separately (see section 3.3.6, Table S3-S7). Membrane-proximal SVs of *Otof*^{-/-} P10 are significantly greater compared to that of *Otof*^{-/-} P22 (B), *Otof*^{-/-} 6M (C) and wt P10 (D) which is also reflected by the right shift of the graphs.

Parameter		wt P10	wt P21	Statistical test	p-value
AZ area (μm^2)		0.1040 \pm 0.0089 (0.0892)	0.1044 \pm 0.0090 (0.1036)	W	0.8961 (ns)
No. of SVs	all SVs	45.88 \pm 4.25 (43.00)	54.09 \pm 5.94 (48.50)	T	0.2675 (ns)
	docked SVs	3.54 \pm 0.70 (2.50)	3.05 \pm 0.63 (2.50)	W	0.5897 (ns)
	membrane-proximal SVs	12.17 \pm 1.32 (12.00)	12.86 \pm 1.51 (11.00)	W	0.9045 (ns)
No. of SVs per μm^2 AZ	all SVs	477.4 \pm 44.1 (445.6)	594.2 \pm 89.7 (480.4)	W	0.7111 (ns)
	docked SVs	36.83 \pm 6.64 (26.88)	35.19 \pm 8.93 (21.24)	W	0.5416 (ns)
	membrane-proximal SVs	128.5 \pm 16.55 (112.8)	135.6 \pm 16.18 (111.7)	W	0.6790 (ns)
	0-5 nm	60.22 \pm 9.79 (42.35)	51.89 \pm 10.37 (37.00)	W	0.4195 (ns)
	5-10 nm	13.00 \pm 3.04 (9.17)	29.83 \pm 6.18 (21.09)	W	0.0022 (**)
	10-15 nm	18.01 \pm 4.17 (13.03)	17.70 \pm 3.23 (16.37)	W	0.5709 (ns)
	15-20 nm	10.14 \pm 2.49 (7.34)	15.94 \pm 4.01 (8.47)	W	0.4322 (ns)
	20-25 nm	15.57 \pm 3.70 (12.98)	16.84 \pm 3.67 (14.41)	W	0.5273 (ns)
	25-30 nm	15.10 \pm 3.61 (8.11)	12.88 \pm 3.20 (7.65)	W	0.6790 (ns)
	30-35 nm	13.64 \pm 2.52 (13.24)	13.04 \pm 2.55 (12.87)	W	0.8446 (ns)
	35-40 nm	19.69 \pm 3.00 (17.15)	12.66 \pm 2.94 (9.16)	W	0.0459 (*)
	40-80 nm	115.1 \pm 11.2 (99.4)	142.5 \pm 17.2 (135.2)	W	0.3478 (ns)
	80-120 nm	89.10 \pm 10.28 (82.06)	114.6 \pm 20.4 (82.8)	W	0.6317 (ns)
	120-160 nm	68.29 \pm 11.34 (68.50)	88.30 \pm 16.71 (69.24)	W	0.4322 (ns)
	160-200 nm	39.61 \pm 8.66 (27.61)	78.09 \pm 25.73 (35.87)	W	0.2744 (ns)
Ratio	0-2/0-40 nm	0.23 \pm 0.04 (0.15)	0.19 \pm 0.04 (0.16)	T	0.5241 (ns)
Diameter (nm)	all SVs	51.46 \pm 0.50 (51.65)	50.03 \pm 0.74 (50.28)	T	0.1187 (ns)
	docked SVs	50.32 \pm 0.72 (50.37)	48.15 \pm 1.08 (48.04)	T	0.1074 (ns)
	membrane-proximal SVs	51.58 \pm 0.63 (51.57)	49.73 \pm 0.72 (49.99)	T	0.0579 (ns)

Table S1: Quantitative analysis of tomograms of wild-type P10 P21. Related to Fig. 3.2-3.4.

Data are presented as mean \pm SEM (median in brackets). Normal distribution was assessed with the Jarque-Bera test and equality of variances was assessed with the *F*-test in normally distributed data. Unpaired *t*-test (T) was used to determine statistical significance of normally distributed data. For non-normally distributed data Wilcoxon Rank test (W) was used. *p*-value > 0.05: not significant (ns), **p*-value < 0.05, ***p*-value < 0.01.

Parameter	eb P10	eb P21	Statistical test	p-value
Mitochondrial volume (all; *10 ⁶ nm ³)	5.18 ± 0.30 (4.50)	11.61 ± 0.80 (11.45)	W	< 0.0001 (****)
AZ area (µm ²)	0.0573 ± 0.0049 (0.0552)	0.0643 ± 0.0044 (0.0652)	T	0.2977 (ns)
Distance (Mitochondrion – AZ membrane; nm)	372.3 ± 25.9 (348.2)	380.1 ± 30.2 (331.8)	W	0.8611 (ns)
Mitochondrial volume (*10 ⁶ nm ³)	5.97 ± 0.63 (4.80)	11.49 ± 1.15 (9.99)	W	< 0.0001 (****)
CM surface area (*10 ⁶ nm ²)	0.19 ± 0.02 (0.14)	0.44 ± 0.05 (0.36)	W	0.0001 (***)
CM density (1/nm)	0.0313 ± 0.0018 (0.0302)	0.0362 ± 0.0015 (0.0351)	W	0.0123 (*)
Crista Shape Factor	0.1937 ± 0.0038 (0.1930)	0.1927 ± 0.0044 (0.1892)	W	0.7771 (ns)
Parameter	non-eb P10	non-eb P21	Statistical test	p-value
Mitochondrial volume (all; *10 ⁶ nm ³)	7.74 ± 0.81 (6.31)	9.87 ± 0.85 (8.65)	W	0.0167 (*)
AZ area (µm ²)	0.0469 ± 0.0037 (0.0444)	0.0546 ± 0.0043 (0.0521)	T	0.1825 (ns)
Distance (Mitochondrion – AZ membrane)	251.8 ± 27.3 (212.3)	294.2 ± 25.9 (237.5)	T	0.2638 (ns)
Mitochondrial volume (*10 ⁶ nm ³)	7.96 ± 0.96 (6.56)	10.27 ± 1.14 (8.50)	W	0.0577 (ns)
CM surface area (*10 ⁶ nm ²)	0.23 ± 0.03 (0.19)	0.30 ± 0.03 (0.26)	W	0.0424 (*)
CM density (1/nm)	0.0286 ± 0.0010 (0.0276)	0.0304 ± 0.0012 (0.0311)	T	0.2782 (ns)
Crista Shape Factor	0.1852 ± 0.0035 (0.1843)	0.1957 ± 0.0041 (0.1966)	T	0.0606 (ns)
Parameter	eb P10	non-eb P10	Statistical test	p-value
Mitochondrial volume (all; *10 ⁶ nm ³)	5.18 ± 0.30 (4.50)	7.74 ± 0.81 (6.31)	W	0.0007 (***)
AZ area (µm ²)	0.0573 ± 0.0049 (0.0552)	0.0469 ± 0.0037 (0.0444)	T	0.0987 (ns)
Distance (Mitochondrion – AZ membrane)	372.3 ± 25.9 (348.2)	251.8 ± 27.3 (212.3)	TW	0.0018 (**)
Mitochondrial volume (*10 ⁶ nm ³)	5.97 ± 0.63 (4.80)	7.96 ± 0.96 (6.56)	W	0.0772 (ns)
CM surface area (*10 ⁶ nm ²)	0.19 ± 0.02 (0.14)	0.23 ± 0.03 (0.19)	W	0.2806 (ns)
CM density (1/nm)	0.0313 ± 0.0018 (0.0302)	0.0286 ± 0.0010 (0.0276)	W	0.1681 (ns)
Crista Shape Factor	0.1937 ± 0.0038 (0.1930)	0.1852 ± 0.0035 (0.1843)	W	0.0972 (ns)

Continued on next page

Parameter	eb P21	non-eb P21	Statistical test	p-value
Mitochondrial volume (all; *10⁶ nm³)	11.61 ± 0.80 (11.45)	9.87 ± 0.85 (8.65)	W	0.2034
AZ area (µm²)	0.0643 ± 0.0044 (0.0652)	0.0546 ± 0.0043 (0.0521)	T	0.1221 (ns)
Distance (Mitochondrion – AZ membrane)	380.1 ± 30.2 (331.8)	294.2 ± 25.9 (237.5)	W	0.1983 (ns)
Mitochondrial volume (*10⁶ nm³)	11.49 ± 1.15 (9.99)	10.27 ± 1.14 (8.50)	W	0.3747 (ns)
CM surface area (*10⁶ nm²)	0.44 ± 0.05 (0.36)	0.30 ± 0.03 (0.26)	W	0.1115 (ns)
CM density (1/nm)	0.0362 ± 0.0015 (0.0351)	0.0304 ± 0.0012 (0.0311)	T	0.0046 (**)
Crista Shape Factor	0.1927 ± 0.0044 (0.1892)	0.1957 ± 0.0041 (0.1966)	T	0.6241 (ns)

Table S2: Quantitative analysis of tomograms of mitochondria at presynaptic AZs of P10 and P21 mice. Related to Fig. 3.7-3.10.

Presynaptic mitochondria of endbulb terminals (eb) and of other excitatory, non-endbulb synapses (non-eb) within the AVCN were compared between wt P10 and wt P21. Further, for both age groups, mitochondrial parameters were compared between endbulbs and non-endbulbs. Data are presented as mean ± SEM (median in brackets). Normal distribution was assessed with the Jarque-Bera test and equality of variances was assessed with the *F*-test in normally distributed data. Unpaired *t*-test (T) was used to determine statistical significance of normally distributed data with equal variances, for normally distributed data with unequal variances, unpaired *t*-test with Welch's correction (TW) was used. For non-normally distributed data, Wilcoxon Rank (W) test was used. *p*-value > 0.05: not significant (ns), **p*-value < 0.05, ***p*-value < 0.01, ****p*-value < 0.001, *****p*-value < 0.0001.

Parameter	wt P10	wt P21	wt 6M	Statistics
AZ area (μm^2)	0.1040 \pm 0.0089 (0.0892)	0.1045 \pm 0.0090 (0.1036)	0.0816 \pm 0.0042 (0.0813)	ANOVA: $p = 0.0384$, Tukey's: wt P10 vs. wt P21: $p = 0.9991$ (ns) wt P10 vs. wt 6M: $p = 0.0739$ (ns) wt P21 vs. wt 6M: $p = 0.0759$ (ns)
SVs per AZ	45.88 \pm 4.25 (43.00) 3.54 \pm 0.70 (2.50)	54.09 \pm 5.94 (48.50) 3.05 \pm 0.63 (2.50)	63.52 \pm 5.63 (55.00) 2.97 \pm 0.51 (3.00)	$p = 0.0643$ (ns) $p = 0.8403$ (ns)
membrane-proximal SVs	12.17 \pm 1.32 (12.00)	12.86 \pm 1.51 (11.00)	14.48 \pm 1.18 (13.00)	$p = 0.4544$ (ns)
SVs per μm^2 AZ	477.4 \pm 44.1 (445.6)	594.2 \pm 89.7 (480.4)	801.5 \pm 65.7 (765.5)	wt P10 vs. wt P21: $p = 0.4771$ (ns) wt P10 vs. wt 6M: $p = 0.0026$ (**) wt P21 vs. wt 6M: $p = 0.0850$ (ns)
docked SVs	36.83 \pm 6.64 (26.88)	35.19 \pm 8.93 (21.24)	37.00 \pm 7.15 (30.30)	$p = 0.8077$
membrane-proximal SVs	128.5 \pm 16.56 (112.8)	135.6 \pm 16.2 (111.7)	184.1 \pm 13.4 (189.6)	wt P10 vs. wt P21: $p = 0.9472$ (ns) wt P10 vs. wt 6M: $p = 0.0266$ (*) wt P21 vs. wt 6M: $p = 0.0688$ (ns)
0-5 nm	60.22 \pm 9.19 (42.35)	51.89 \pm 10.37 (37.00)	71.81 \pm 11.68 (49.23)	$p = 0.4217$
5-10 nm	13.00 \pm 3.04 (9.17)	29.83 \pm 6.18 (21.09)	41.31 \pm 5.71 (39.50)	wt P10 vs. wt P21: $p = 0.0236$ (*) wt P10 vs. wt 6M: $p = 0.0002$ (***) wt P21 vs. wt 6M: $p = 0.8236$ (ns)
10-15 nm	18.01 \pm 4.17 (13.03)	17.70 \pm 3.23 (16.37)	31.66 \pm 3.85 (28.60)	wt P10 vs. wt P21: $p > 0.9999$ (ns) wt P10 vs. wt 6M: $p = 0.0171$ (*) wt P21 vs. wt 6M: $p = 0.0500$ (ns)
15-20 nm	10.14 \pm 2.49 (7.34)	15.94 \pm 4.01 (8.47)	18.13 \pm 2.55 (18.42)	$p = 0.1011$ (ns)
20-25 nm	15.57 \pm 3.70 (12.98)	16.84 \pm 3.67 (14.41)	11.79 \pm 2.10 (12.31)	$p = 0.6322$ (ns)
25-30 nm	15.10 \pm 3.61 (8.11)	12.88 \pm 3.20 (7.65)	18.29 \pm 3.29 (11.83)	$p = 0.4572$ (ns)
30-35 nm	13.64 \pm 2.52 (13.24)	13.04 \pm 2.55 (12.87)	15.05 \pm 2.57 (16.15)	$p = 0.8446$ (ns)
35-40 nm	19.69 \pm 3.00 (17.15)	12.66 \pm 2.94 (9.16)	13.1 \pm 2.68 (10.56)	KW: $p = 0.0414$, Dunn's: wt P10 vs. wt P21: $p = 0.0994$ (ns) wt P10 vs. wt 6M: $p = 0.0715$ (ns) wt P21 vs. wt 6M: $p > 0.9999$ (ns)
40-80 nm	115.1 \pm 11.2 (99.4)	142.5 \pm 17.2 (135.2)	152.3 \pm 13.4 (145.3)	$p = 0.1495$
80-120 nm	89.10 \pm 10.28 (82.06)	114.6 \pm 20.4 (82.79)	154.0 \pm 12.56 (165.8)	wt P10 vs. wt P21: $p = 0.4634$ (ns) wt P10 vs. wt 6M: $p = 0.0051$ (**) wt P21 vs. wt 6M: $p = 0.1402$ (ns)
120-160 nm	68.29 \pm 11.34 (68.50)	88.30 \pm 16.71 (69.24)	153.2 \pm 18.75 (130.4)	wt P10 vs. wt P21: $p = 0.6883$ (ns) wt P10 vs. wt 6M: $p = 0.0010$ (**) wt P21 vs. wt 6M: $p = 0.0181$ (*)
160-200 nm	39.61 \pm 8.66 (27.61)	78.09 \pm 25.73 (35.87)	120.9 \pm 16.6 (98.5)	wt P10 vs. wt P21: $p = 0.8539$ (ns) wt P10 vs. wt 6M: $p = 0.0010$ (*) wt P21 vs. wt 6M: $p = 0.0526$ (ns)

Continued on next page

Parameter	wt P10	wt P21	wt 6M	Statistics
Diameter (nm)				
all SVs	51.46 ± 0.50 (51.65)	50.03 ± 0.74 (50.28)	50.62 ± 0.66 (50.37)	$p = 0.3235$ (ns)
docked SVs	50.32 ± 0.72 (50.37)	48.15 ± 1.08 (48.04)	50.29 ± 0.76 (50.28)	$p = 0.1558$ (ns)
membrane-proximal SVs	51.58 ± 0.63 (51.57)	49.73 ± 0.72 (49.99)	50.72 ± 0.76 (50.22)	$p = 0.2212$ (ns)
Ratio	0.23 ± 0.04 (0.15)	0.19 ± 0.04 (0.16)	0.16 ± 0.02 (0.12)	$p = 0.3096$ (ns)

Table S3: Quantitative analysis of tomograms of wild-type AZs. Related to Fig. 3.12-3.15.

Data are presented as mean ± SEM (median in brackets). Normal distribution was assessed with the Jarque-Bera test and equality of variances was assessed with the F -test in normally distributed data. Statistical significance of normally distributed data was determined by one-way ANOVA test followed by Tukey's s test. For non-normally distributed data, Kruskal-Wallis (KW) test followed by Dunn's test was used. p -value > 0.05: not significant (ns), * p -value < 0.05, ** p -value < 0.01, *** p -value < 0.001.

Parameter	Otof ^{-/-} P10	Otof ^{-/-} P22	Otof ^{-/-} 6M	Statistics
AZ area (μm^2)	0.0944 \pm 0.0077 (0.0890)	0.0919 \pm 0.0079 (0.0831)	0.0932 \pm 0.0057 (0.0933)	$p = 0.9415$ (ns)
SVs per AZ	49.00 \pm 6.38 (39.00)	66.64 \pm 8.73 (66.00)	39.61 \pm 4.68 (37.00)	Otof ^{-/-} P10 vs. Otof ^{-/-} P22: $p = 0.1667$ (ns) Otof ^{-/-} P10 vs. Otof ^{-/-} 6M: $p = 0.5874$ (ns) Otof ^{-/-} P22 vs. Otof ^{-/-} 6M: $p = 0.0163$ (*) $p = 0.0891$
docked SVs	2.73 \pm 0.46 (3.00)	2.44 \pm 0.84 (1.00)	1.83 \pm 0.56 (1.00)	Otof ^{-/-} P10 vs. Otof ^{-/-} P22: $p = 0.0104$ (*) Otof ^{-/-} P10 vs. Otof ^{-/-} 6M: $p = 0.6526$ (ns) Otof ^{-/-} P22 vs. Otof ^{-/-} 6M: $p = 0.0886$ (ns)
membrane-proximal SVs	8.86 \pm 1.13 (7.50)	15.39 \pm 2.11 (12.00)	10.78 \pm 1.09 (12.00)	Otof ^{-/-} P10 vs. Otof ^{-/-} P22: $p = 0.3042$ (ns) Otof ^{-/-} P10 vs. Otof ^{-/-} 6M: $p = 0.2959$ (ns) Otof ^{-/-} P22 vs. Otof ^{-/-} 6M: $p = 0.0099$ (**) $p = 0.1140$
SVs per μm^2 AZ	579.5 \pm 81.6 (453.6)	726.0 \pm 76.14 (725.2)	431.3 \pm 46.38 (438.2)	Otof ^{-/-} P10 vs. Otof ^{-/-} P22: $p = 0.0081$ (**) Otof ^{-/-} P10 vs. Otof ^{-/-} 6M: $p = 0.7555$ (ns) Otof ^{-/-} P22 vs. Otof ^{-/-} 6M: $p = 0.0490$ (*) $p = 0.4598$
docked SVs	34.89 \pm 6.40 (35.94)	24.66 \pm 7.39 (13.25)	22.06 \pm 6.95 (12.51)	Otof ^{-/-} P10 vs. Otof ^{-/-} P22: $p = 0.0011$ (**) Otof ^{-/-} P10 vs. Otof ^{-/-} 6M: $p = 0.2319$ (ns) Otof ^{-/-} P22 vs. Otof ^{-/-} 6M: $p = 0.2109$ (ns)
membrane-proximal SVs	103.8 \pm 14.6 (90.8)	162.9 \pm 14.6 (145.5)	117.5 \pm 10.8 (105.1)	$p = 0.2624$ (ns) $p = 0.7388$ (ns) $p = 0.2555$ (ns) $p = 0.1012$ (ns) $p = 0.5094$ (ns) $p = 0.3971$ (ns) $p = 0.0601$ (ns) $p = 0.0560$ (ns)
0-5 nm	42.58 \pm 7.85 (36.33)	33.87 \pm 9.19 (23.80)	32.30 \pm 7.15 (21.43)	Otof ^{-/-} P10 vs. Otof ^{-/-} P22: $p = 0.6934$ (ns) Otof ^{-/-} P10 vs. Otof ^{-/-} 6M: $p = 0.1575$ (ns) Otof ^{-/-} P22 vs. Otof ^{-/-} 6M: $p = 0.0230$ (*)
5-10 nm	12.05 \pm 5.32 (0.00)	30.68 \pm 4.45 (34.05)	20.83 \pm 4.82 (13.33)	Otof ^{-/-} P10 vs. Otof ^{-/-} P22: $p > 0.9999$ (ns) Otof ^{-/-} P10 vs. Otof ^{-/-} 6M: $p = 0.0503$ (ns) Otof ^{-/-} P22 vs. Otof ^{-/-} 6M: $p = 0.0151$ (*)
10-15 nm	12.12 \pm 3.09 (10.05)	29.81 \pm 7.31 (16.16)	18.02 \pm 3.52 (14.96)	
15-20 nm	14.98 \pm 2.93 (12.24)	19.05 \pm 3.93 (13.34)	17.91 \pm 4.28 (12.91)	
20-25 nm	14.17 \pm 2.96 (10.12)	20.79 \pm 3.85 (19.82)	14.28 \pm 2.73 (16.15)	
25-30 nm	15.42 \pm 3.14 (11.98)	23.84 \pm 3.83 (26.69)	13.74 \pm 3.28 (10.44)	
30-35 nm	16.19 \pm 3.80 (13.69)	13.37 \pm 2.23 (12.57)	11.54 \pm 2.23 (10.09)	
35-40 nm	11.23 \pm 2.42 (10.62)	16.13 \pm 2.95 (14.95)	12.53 \pm 2.45 (12.57)	
40-80 nm	129.1 \pm 16.1 (120.5)	158.9 \pm 16.3 (138.9)	108.4 \pm 12.08 (85.71)	
80-120 nm	122.5 \pm 18.3 (93.1)	156.6 \pm 22.7 (171.7)	92.95 \pm 13.17 (77.47)	
120-160 nm	106.1 \pm 19.4 (66.7)	124.9 \pm 18.58 (109.0)	63.03 \pm 8.99 (62.64)	
160-200 nm	83.14 \pm 17.60 (52.28)	92.32 \pm 16.93 (62.86)	33.19 \pm 8.12 (16.15)	

Continued on next page

Parameter	Otof ^{-/-} P10	Otof ^{-/-} P22	Otof ^{-/-} 6M	Statistics
Diameter (nm)				
all SVs	54.87 ± 0.90 (55.15)	52.23 ± 1.11 (52.28)	50.63 ± 1.03 (49.94)	Otof ^{-/-} P10 vs. Otof ^{-/-} P22: <i>p</i> = 0.1698 (ns) Otof ^{-/-} P10 vs. Otof ^{-/-} 6M: <i>p</i> = 0.0128 (*) Otof ^{-/-} P22 vs. Otof ^{-/-} 6M: <i>p</i> = 0.5060 (ns)
docked SVs	54.99 ± 1.52 (56.10)	51.00 ± 1.83 (49.70)	46.23 ± 1.03 (47.70)	Otof ^{-/-} P10 vs. Otof ^{-/-} P22: <i>p</i> = 0.1517 (ns) Otof ^{-/-} P10 vs. Otof ^{-/-} 6M: <i>p</i> = 0.0003 (***) Otof ^{-/-} P22 vs. Otof ^{-/-} 6M: <i>p</i> = 0.0811 (ns)
membrane-proximal SVs	55.36 ± 1.14 (55.35)	51.28 ± 0.98 (51.65)	50.87 ± 1.09 (49.91)	Otof ^{-/-} P10 vs. Otof ^{-/-} P22: <i>p</i> = 0.0247 (*) Otof ^{-/-} P10 vs. Otof ^{-/-} 6M: <i>p</i> = 0.0119 (*) Otof ^{-/-} P22 vs. Otof ^{-/-} 6M: <i>p</i> = 0.9588 (ns)
Ratio				
0-2/0-40 nm	0.23 ± 0.03 (0.27)	0.11 ± 0.03 (0.07)	0.12 ± 0.03 (0.08)	Otof ^{-/-} P10 vs. Otof ^{-/-} P22: <i>p</i> = 0.0168 (*) Otof ^{-/-} P10 vs. Otof ^{-/-} 6M: <i>p</i> = 0.0308 (*) Otof ^{-/-} P22 vs. Otof ^{-/-} 6M: <i>p</i> = 0.9699 (ns)

Table S4: Quantitative analysis of tomograms of Otof^{-/-} AZs. Related to Fig. 3.12-3.15.

Data are presented as mean ± SEM (median in brackets). Normal distribution was assessed with the Jarque-Bera test and equality of variances was assessed with the *F*-test in normally distributed data. Statistical significance of normally distributed data was determined by one-way ANOVA test followed by Tukey's *s* test. For non-normally distributed data, Kruskal-Wallis (KW) test followed by Dunn's test was used. *p*-value > 0.05: not significant, **p*-value < 0.05, ***p*-value < 0.01, ****p*-value < 0.001.

Parameter		wt P10	<i>Otof</i> ^{-/-} P10	Statistical test	p-value
AZ area (μm ²)		0.1040 ± 0.0089 (0.0892)	0.0944 ± 0.0077 (0.0890)	W	0.8107 (ns)
No. of SVs	all SVs	45.88 ± 4.25 (43.00)	49.00 ± 6.38 (39.00)	T	0.6860 (ns)
	docked SVs	3.54 ± 0.70 (2.50)	2.73 ± 0.46 (3.00)	W	0.7224 (ns)
	membrane-proximal SVs	12.17 ± 1.32 (12.00)	8.86 ± 1.13 (7.50)	T	0.0631 (ns)
No. of SVs per μm ² AZ	all SVs	477.4 ± 44.1 (445.6)	579.5 ± 81.6 (453.6)	TW	0.2790 (ns)
	docked SVs	36.83 ± 6.64 (26.88)	34.89 ± 6.40 (35.94)	W	0.8961 (ns)
	membrane-proximal SVs	128.5 ± 16.56 (112.8)	103.8 ± 14.6 (90.8)	W	0.2943 (ns)
	0-5 nm	60.22 ± 9.19 (42.35)	42.58 ± 7.85 (36.33)	T	0.1514 (ns)
	5-10 nm	13.00 ± 3.04 (9.17)	12.05 ± 5.32 (0.00)	W	0.2744 (ns)
	10-15 nm	18.01 ± 4.17 (13.03)	12.12 ± 3.09 (10.05)	W	0.4650 (ns)
	15-20 nm	10.14 ± 2.49 (7.34)	14.98 ± 2.93 (12.24)	W	0.2123 (ns)
	20-25 nm	15.57 ± 3.70 (12.98)	14.17 ± 2.96 (10.12)	W	0.9479 (ns)
	25-30 nm	15.10 ± 3.61 (8.11)	15.42 ± 3.11 (11.98)	W	0.6950 (ns)
	30-35 nm	13.64 ± 2.52 (13.24)	16.19 ± 3.80 (13.69)	W	0.7357 (ns)
	35-40 nm	19.69 ± 3.00 (17.15)	11.23 ± 2.42 (10.62)	W	0.0187 (*)
	40-80 nm	115.1 ± 11.2 (99.4)	129.1 ± 16.1 (120.5)	T	0.4794 (ns)
	80-120 nm	89.10 ± 10.28 (82.06)	122.5 ± 18.3 (93.1)	TW	0.1210 (ns)
	120-160 nm	68.29 ± 11.34 (68.50)	106.1 ± 19.4 (66.7)	TW	0.5737 (ns)
	160-200 nm	39.61 ± 8.66 (27.61)	83.14 ± 17.60 (52.28)	W	0.0497 (*)
Diameter (nm)	all SVs	51.46 ± 0.50 (51.65)	54.87 ± 0.90 (55.15)	TW	0.0022 (**)
	docked SVs	50.32 ± 0.72 (50.37)	54.99 ± 1.52 (56.10)	TW	0.0104 (*)
	membrane-proximal SVs	51.58 ± 0.63 (51.57)	55.36 ± 1.14 (55.35)	TW	0.0066 (**)
Ratio	0-2/0-40 nm	0.23 ± 0.04 (0.15)	0.23 ± 0.03 (0.27)	T	0.9011

Table S5: Quantitative analysis of tomograms of P10 wild-type and *Otof*^{-/-} mice. Related to Fig. 3.12-3.15.

Data are presented as mean ± SEM (median in brackets). Normal distribution was assessed with Jarque-Bera test and equality of variances was assessed with *F*-test in normally distributed data. Unpaired *t*-test (T) was used to determine statistical significance of normally distributed data with equal variances, for normally distributed data with unequal variances, unpaired *t*-test with Welch's correction (TW) was used. For non-normally distributed data, Wilcoxon Rank test (W) was used. *p*-value > 0.05: not significant (ns), **p*-value < 0.05, ***p*-value < 0.01.

Parameter		wt P21	<i>Otof</i> ^{-/-} P22	Statistical test	p-value
AZ area (µm ²)		0.1045 ± 0.0090 (0.1036)	0.0919 ± 0.0079 (0.0831)	W	0.2496 (ns)
No. of SVs	all SVs	54.09 ± 5.94 (48.50)	66.64 ± 8.73 (66.00)	T	0.2423 (ns)
	docked SVs	3.05 ± 0.63 (2.50)	2.44 ± 0.84 (1.00)	W	0.2216 (ns)
	membrane-proximal SVs	12.86 ± 1.51 (11.00)	15.39 ± 2.11 (12.00)	W	0.5578 (ns)
No. of SVs per µm ² AZ	all SVs	594.2 ± 89.7 (480.4)	726.0 ± 76.14 (725.2)	W	0.1474 (ns)
	docked SVs	35.19 ± 8.93 (21.24)	24.66 ± 7.39 (13.25)	W	0.2591 (ns)
	membrane-proximal SVs	135.6 ± 16.2 (111.7)	162.9 ± 14.6 (145.5)	W	0.1234 (ns)
	0-5 nm	51.89 ± 10.37 (37.00)	33.87 ± 9.19 (23.80)	W	0.0655 (ns)
	5-10 nm	29.83 ± 6.18 (21.09)	30.68 ± 4.45 (34.05)	W	0.4109 (ns)
	10-15 nm	17.70 ± 3.23 (16.37)	29.81 ± 7.31 (16.16)	W	0.6692 (ns)
	15-20 nm	15.94 ± 4.01 (8.47)	19.05 ± 3.93 (13.34)	W	0.5286 (ns)
	20-25 nm	16.84 ± 3.67 (14.41)	20.79 ± 3.85 (19.82)	W	0.3919 (ns)
	25-30 nm	12.88 ± 3.20 (7.65)	23.84 ± 3.83 (26.69)	W	0.0379 (*)
	30-35 nm	13.04 ± 2.55 (12.87)	13.37 ± 2.23 (12.57)	W	0.8573 (ns)
	35-40 nm	12.66 ± 2.94 (9.16)	16.13 ± 2.95 (14.95)	W	0.3211 (ns)
	40-80 nm	142.5 ± 17.2 (135.2)	158.9 ± 16.3 (138.9)	W	0.4174 (ns)
	80-120 nm	114.6 ± 20.4 (82.79)	156.6 ± 22.7 (171.7)	W	0.1350 (ns)
120-160 nm	88.30 ± 16.71 (69.24)	124.9 ± 18.58 (109.0)	W	0.0931 (ns)	
160-200 nm	78.09 ± 25.73 (35.87)	92.32 ± 16.93 (62.86)	W	0.1976 (ns)	
Diameter (nm)	all SVs	50.03 ± 0.74 (50.28)	52.23 ± 1.11 (52.28)	T	0.1079 (ns)
	docked SVs	48.15 ± 1.08 (48.04)	51.00 ± 1.83 (49.70)	T	0.1937 (ns)
	membrane-proximal SVs	49.73 ± 0.72 (49.99)	51.28 ± 0.98 (51.65)	T	0.2073 (ns)
Ratio	0-2/0-40 nm	0.19 ± 0.04 (0.16)	0.11 ± 0.03 (0.07)	W	0.1646 (ns)

Table S6: Quantitative analysis of tomograms of P21/22 wild-type and *Otof*^{-/-} mice. Related to Fig. 3.12-3.15.

Data are presented as mean ± SEM (median in brackets). Normal distribution was assessed with the Jarque-Bera test and equality of variances was assessed with the *F*-test in normally distributed data. Unpaired *t*-test was used to determine statistical significance of normally distributed data. For non-normally distributed data, Wilcoxon Rank test was used. *p*-value > 0.05: not significant (ns), **p*-value < 0.05.

Parameter		wt 6M	Otof ^{-/-} 6M	Statistical test	p-value
AZ area (µm ²)		0.0816 ± 0.0042 (0.0813)	0.0932 ± 0.0057 (0.0933)	T	0.1980 (ns)
No. of SVs	all SVs	63.52 ± 5.63 (55.00)	39.61 ± 4.68 (37.00)	T	0.0020 (**)
	docked SVs	2.97 ± 0.51 (3.00)	1.83 ± 0.56 (1.00)	W	0.0379 (*)
	membrane-proximal SVs	14.48 ± 1.18 (13.00)	10.78 ± 1.09 (12.00)	W	0.0695 (ns)
No. of SVs per µm ² AZ	all SVs	801.5 ± 65.67 (765.5)	431.3 ± 46.38 (438.2)	TW	< 0.0001 (****)
	docked SVs	37.00 ± 7.15 (30.30)	22.06 ± 6.95 (12.51)	W	0.0317 (*)
	membrane-proximal SVs	184.1 ± 13.4 (189.6)	117.5 ± 10.8 (105.1)	T	0.0003 (***)
	0-5 nm	71.81 ± 11.68 (49.23)	32.30 ± 7.15 (21.43)	W	0.0036 (**)
	5-10 nm	41.31 ± 5.71 (39.50)	20.83 ± 4.82 (13.33)	W	0.0110 (*)
	10-15 nm	31.66 ± 3.85 (28.60)	18.02 ± 3.52 (14.96)	T	0.0117 (*)
	15-20 nm	18.13 ± 2.55 (18.42)	17.91 ± 4.28 (12.91)	W	0.4929 (ns)
	20-25 nm	11.79 ± 2.10 (12.31)	14.28 ± 2.73 (16.15)	W	0.5104 (ns)
	25-30 nm	18.29 ± 3.29 (11.83)	13.74 ± 3.28 (10.44)	W	0.3364 (ns)
	30-35 nm	15.05 ± 2.57 (16.15)	11.54 ± 2.23 (10.09)	T	0.3071 (ns)
	35-40 nm	13.1 ± 2.68 (10.56)	12.53 ± 2.45 (12.57)	W	0.8623 (ns)
	40-80 nm	152.3 ± 13.4 (145.3)	108.4 ± 12.1 (85.7)	W	0.0231 (*)
	80-120 nm	154.0 ± 12.6 (165.8)	92.95 ± 13.17 (77.47)	T	0.0016 (**)
	120-160 nm	153.2 ± 18.8 (130.4)	63.03 ± 8.99 (62.64)	TW	< 0.0001 (****)
	160-200 nm	120.9 ± 16.6 (98.5)	33.19 ± 8.12 (16.15)	W	< 0.0001 (****)
Diameter (nm)	all SVs	50.62 ± 0.66 (50.37)	50.63 ± 1.03 (49.94)	T	0.9924 (ns)
	docked SVs	50.29 ± 0.76 (50.28)	46.23 ± 1.03 (47.70)	T	0.0035 (**)
	membrane-proximal SVs	50.72 ± 0.76 (50.22)	50.87 ± 1.09 (49.91)	W	0.8194 (ns)
Ratio	0-2/0-40 nm	0.16 ± 0.02 (0.13)	0.12 ± 0.03 (0.08)	W	0.1713 (ns)

Table S7: Quantitative analysis of tomograms of 6M wild-type and Otof^{-/-} mice. Related to Fig. 3.12-3.15.

Data are presented as mean ± SEM (median in brackets). Normal distribution was assessed with Jarque-Bera test and equality of variances was assessed with *F*-test in normally distributed data. Unpaired *t*-test (T) was used to determine statistical significance of normally distributed data with equal variances, for normally distributed data with unequal variances, unpaired *t*-test with Welch's correction (TW) was used. For non-normally distributed data, Wilcoxon Rank test (W) was used. *p*-value > 0.05: not significant (ns), **p*-value < 0.05, ***p*-value < 0.01, ****p*-value < 0.001, *****p*-value < 0.0001.

Docked SVs	Adjusted <i>p</i>-value
wt P10 vs. wt P21	$p = 0.6397$
wt P10 vs. wt 6M	$p = 0.4507$
wt P21 vs. wt 6M	$p = 0.7755$
<i>Otof</i> ^{-/-} P10 vs. <i>Otof</i> ^{-/-} P22	$p = 0.0809$
<i>Otof</i> ^{-/-} P10 vs. <i>Otof</i> ^{-/-} 6M	$p = 0.4507$
<i>Otof</i> ^{-/-} P22 vs. <i>Otof</i> ^{-/-} 6M	$p = 0.2475$
wt P10 vs. <i>Otof</i> ^{-/-} P10	$p = 0.2475$
wt P21 vs. <i>Otof</i> ^{-/-} P22	$p = 0.4232$
wt 6M vs. <i>Otof</i> ^{-/-} 6M	$p = 0.8987$
Membrane-proximal SVs	
wt P10 vs. wt P21	$p = 0.7749$
wt P10 vs. wt 6M	$p = 0.9717$
wt P21 vs. wt 6M	$p = 0.7297$
<i>Otof</i> ^{-/-} P10 vs. <i>Otof</i> ^{-/-} P22	* $p = 0.0300$
<i>Otof</i> ^{-/-} P10 vs. <i>Otof</i> ^{-/-} 6M	$p = 0.9717$
<i>Otof</i> ^{-/-} P22 vs. <i>Otof</i> ^{-/-} 6M	* $p = 0.0300$
wt P10 vs. <i>Otof</i> ^{-/-} P10	$p = 0.5343$
wt P21 vs. <i>Otof</i> ^{-/-} P22	$p = 0.3084$
wt 6M vs. <i>Otof</i> ^{-/-} 6M	$p = 0.5343$

Table S8: Comparison of the number of docked and membrane-proximal SVs. Related to Fig. 3.13 and 3.14.

Variances of the AZ containing 0 to 16 docked SVs, or 0 to 44 membrane-proximal SVs were compared using *F*-test. The corresponding *p*-values were corrected for multiple comparisons. *p*-value > 0.05: not significant, **p*-value < 0.05.

Parameter		wt	<i>RIM-BP2</i> ^{-/-}	Statistical test	p-value
AZ area (μm ²)		0.0820 ± 0.0052 (0.0809)	0.1031 ± 0.0039 (0.0981)	T	0.0022 (**)
No. of SVs	all SVs	49.81 ± 4.49 (46.50)	51.57 ± 4.63 (41.00)	T	0.7857 (ns)
No. of SVs per μm ² AZ	all SVs	662.3 ± 77.4 (543.1)	523.7 ± 53.4 (443.2)	W	0.1374 (ns)
	docked SVs	27.52 ± 5.24 (18.58)	14.64 ± 4.77 (1.72)	W	0.0152 (*)
	membrane-proximal SVs	167.7 ± 15.2 (167.4)	117.8 ± 10.5 (113.4)	W	0.0041 (**)
	2-20 nm	109.1 ± 12.8 (98.4)	68.16 ± 9.22 (59.32)	W	0.0056 (**)
	20-40 nm	58.59 ± 7.14 (45.26)	49.68 ± 5.40 (45.20)	W	0.6063 (ns)
	40-60 nm	83.25 ± 8.23 (82.21)	53.59 ± 5.36 (53.69)	W	0.0042 (**)
	60-80 nm	79.81 ± 10.62 (64.31)	55.80 ± 6.26 (48.54)	W	0.0899 (ns)
	80-100 nm	70.43 ± 10.52 (54.67)	59.51 ± 7.92 (43.09)	W	0.3898 (ns)
	100-120 nm	61.41 ± 11.08 (43.38)	51.56 ± 9.16 (36.31)	W	0.5137 (ns)
	120-140 nm	50.51 ± 10.47 (41.23)	48.79 ± 7.41 (41.68)	W	0.6428 (ns)
	140-160 nm	55.12 ± 11.25 (42.14)	47.62 ± 6.21 (38.58)	W	0.8234 (ns)
	160-180 nm	37.59 ± 7.70 (25.56)	40.12 ± 8.33 (27.80)	W	0.9178 (ns)
	180-200 nm	29.68 ± 8.40 (15.05)	33.26 ± 4.97 (31.13)	W	0.1958 (ns)
Diameter (nm)	all SVs	50.99 ± 0.59 (51.68)	52.14 ± 0.68 (52.44)	T	0.7324 (ns)

Table S9: Quantitative analysis of tomograms of P22 wild-type and *RIM-BP2*^{-/-} mice. Related to Fig. 3.17.

Data are presented as mean ± SEM (median in brackets). Normal distribution was assessed with the Jarque-Bera test and equality of variances was assessed with the *F*-test in normally distributed data. Unpaired *t*-test (T) was used to determine statistical significance of normally distributed data. For non-normally distributed data, Wilcoxon Rank test (W) was used. *p*-value > 0.05: not significant (ns), **p*-value < 0.05, ***p*-value < 0.01.

Parameter		wt exc.	<i>Mover</i> ^{-/-} exc.	Statistical test	p-value
No. of SVs	all SVs	31.74 ± 2.24 (29.00)	36.50 ± 2.18 (38.50)	T	0.1309 (ns)
Rel. SV number per AZ (%)	docked SVs	8.06 ± 1.37 (4.71)	7.05 ± 1.15 (6.25)	W	0.8905 (ns)
	2-40 nm	31.96 ± 2.06 (28.64)	24.52 ± 1.72 (22.22)	T	0.0073 (**)
	40-80 nm	24.17 ± 1.13 (23.75)	28.57 ± 1.24 (28.57)	W	0.0145 (*)
	80-120 nm	17.04 ± 1.21 (18.14)	17.41 ± 1.27 (18.42)	T	0.8338 (ns)
	120-160 nm	10.58 ± 1.35 (9.88)	12.57 ± 1.02 (12.50)	T	0.2439 (ns)
	160-200 nm	8.20 ± 1.21 (7.79)	10.32 ± 1.34 (9.52)	W	0.2243 (ns)
Ratio	0-2/0-40 nm	0.1874 ± 0.0269 (0.1429)	0.2131 ± 0.0318 (0.2000)	T	0.5407 (ns)
Diameter (nm)	all SVs	51.73 ± 0.40 (51.61)	52.58 ± 0.39 (52.09)	W	0.2352 (ns)
Parameter		wt inh.	<i>Mover</i> ^{-/-} inh.	Statistical test	p-value
No. of SVs	all SVs	57.44 ± 8.53 (61.00)	54.77 ± 5.53 (53.00)	T	0.7709 (ns)
Rel. SV number per AZ (%)	docked SVs	4.68 ± 1.34 (4.35)	9.21 ± 1.52 (9.09)	T	0.0364 (*)
	2-40 nm	22.80 ± 2.71 (22.22)	18.19 ± 2.89 (16.98)	T	0.3364 (ns)
	40-80 nm	25.00 ± 2.16 (25.00)	20.16 ± 1.70 (20.97)	T	0.0965 (ns)
	80-120 nm	19.59 ± 1.96 (21.74)	22.33 ± 1.44 (20.83)	T	0.2759 (ns)
	120-160 nm	18.09 ± 2.76 (19.15)	15.64 ± 1.60 (16.67)	T	0.4556 (ns)
	160-200 nm	9.84 ± 2.83 (10.00)	13.77 ± 2.09 (13.51)	T	0.2811 (ns)
Ratio	0-2/0-40 nm	0.1632 ± 0.0448 (0.2000)	0.3365 ± 0.0518 (0.3000)	T	0.0199 (*)
Parameter		wt exc.	wt inh.	Statistical test	p-value
No. of SVs	all SVs	31.74 ± 2.24 (29.00)	57.44 ± 8.53 (61.00)	TW	0.0169 (*)
Parameter		<i>Mover</i> ^{-/-} exc.	<i>Mover</i> ^{-/-} inh.	Statistical test	p-value
No. of SVs	all SVs	36.50 ± 2.18 (38.50)	54.77 ± 5.53 (53.00)	TW	0.0065 (**)

Table S10: Quantitative analysis of tomograms of adult wild-type and *Mover*^{-/-} mice. Related to Fig. 3.20.

Excitatory endbulb AZs (exc.) and inhibitory synapses on BCs (inh.) were compared between *Mover*^{-/-} mice and their wt littermates. In addition, SV numbers were compared between exc. and inh. AZs within the genotypes. Data are presented as mean ± SEM (median in brackets). Normal distribution was assessed with Jarque-Bera test and equality of variances was assessed with *F*-test in normally distributed data. Unpaired *t*-test (T) was used to determine statistical significance of normally distributed data with equal variances, for normally distributed data with unequal variances, unpaired *t*-test with Welch's correction (TW) was used. For non-normally distributed data, Wilcoxon Rank test (W) was used. *p*-value > 0.05: not significant (ns), **p*-value < 0.05, ***p*-value < 0.01.

Acknowledgements

I would like to express my gratitude to the people who supported me during my PhD.

Above all, I want to thank my supervisor Prof. Dr. Carolin Wichmann who accepted me in her group and introduced me to the world of electron microscopy. I am grateful for her guidance, trust, valuable suggestions and encouragement throughout my PhD.

Next, I would like to thank my thesis committee members Prof. Dr. Thomas Dresbach and Dr. Benjamin Cooper, who provided great advice and valuable input on the progress of my work. Also, I would like to thank Prof. Dr. Silvio. O. Rizzoli, Prof. Dr. Stefan Jakobs and Prof. Frauke Alves for taking the time to be my additional members of my examination board.

I would also like to thank the following people for collaborations: Dr. Rebecca Wallrafen and Prof. Dr. Thomas Dresbach from the Institute for Anatomy and Embryology, Göttingen, my “endbulb buddy” Theoharis Alvanos and Prof. Dr. Tobias Moser from the Institute for Auditory Neuroscience, Göttingen and Dr. Felix Lange and Prof. Dr. Stefan Jakobs from the Research Group Mitochondrial Structure and Dynamics, MPI for Multidisciplinary Sciences, Göttingen. Further, I am grateful for the collaborations and discussions on large volume 3D imaging: Dr. Anna Maria Steyer and Dr. Wiebke Möbius from the Electron Microscopy Core Unit, MPI for Multidisciplinary Sciences, Göttingen and Dr. Christian Wrede and Dr. Jan Hegermann from the Research Core Unit Electron Microscopy, Hannover Medical School, Hannover.

I would like to acknowledge the Deutsche Forschungsgemeinschaft, for the funding through the SFB 1286 A4 project (AG Wichmann) and the Sensory and Motor Neuroscience (SMN) program at the Göttingen Graduate School for Neurosciences, Biophysics, and Molecular Biosciences (GGNB) for the variety of methods and soft skill courses that made it possible to gain insight into other scientific fields and to exchange ideas with other PhD students.

Many thanks to Anna Goldak, Christiane Senger-Freitag, Sandra Gerke and Sina Langer for their technical assistance in the experimental work. Many thanks to Omar Lautaro Diaz for solving all my problems with computers. Thanks to Dr. Michael Hoppert for his support whenever there was a problem with the microscopes. Thanks to Patricia Räke-Kügler for her help with bureaucratic questions and problems. Many thanks to Prof. Dr. Mehmet Gültas for his patience and help with the statistics.

Thanks to Esther Anna Semmelhack, Lisa-Marie Müller and Celine Straßner for their excellent work during their lab rotations.

Thanks to all current and former people of 1st floor of the green side (BIN) for a nice working atmosphere and the delicious birthday cakes in the kitchen, which are far too long ago.

In particular, I would like to thank all current and former members of the Wichmann group: Dr. Jana Kroll, Dr. Rituparna Chakrabarti, Dr. Susann Michanski, Loujin Slitin and Magdalena Redondo Canales. Thanks for always offering help, your valuable suggestions and fruitful discussions. I am really happy that our paths have met.

I am grateful to Ritu, Susi, Magda and Johanna for their comments and helpful suggestions to improve this thesis.

I want to thank my family and friends. I am grateful to my parents, who never hesitated to support me and my plans. Thanks to Anja, Alex, Lena, Steffen and the Schmitz' for the time out that have simply brought me to other thoughts. Thanks to Sarah for the yoga sessions. Finally, I am extremely grateful to my husband, Jan. Thanks for his patience and understanding. He left me alone when I needed it, but also made me go outside and made me laugh when I didn't really feel like it. Thanks for walking through this time with me.

List of publications

Butola T, Alvanos T, **Hintze A**, Koppensteiner P, Kleindienst D, Shigemoto R, Wichmann C, Moser T. RIM-Binding Protein 2 Organizes Ca²⁺ Channel Topography and Regulates Release Probability and Vesicle Replenishment at a Fast Central Synapse. J Neurosci. 2021 Sep 15;41(37):7742-7767. doi: 10.1523/JNEUROSCI.0586-21.2021.

Hintze A, Gültas M, Semmelhack EA, Wichmann C. Ultrastructural maturation of the endbulb of Held active zones comparing wild-type and otoferlin-deficient mice. iScience. 2021 Mar 8;24(4):102282. doi: 10.1016/j.isci.2021.102282.